

MULTIDIMENSIONAL MAGNETOTELLURIC IMAGING OF CRUSTAL
AND UPPERMOST MANTLE STRUCTURES OF THE ATLAS
MOUNTAINS OF MOROCCO

DUYGU KIYAN

B.Sc., Istanbul Technical University, 2005

M.Sc., Istanbul Technical University, 2009

NUI Galway Student Number: 09233814

The thesis is submitted to the Faculty of Science,
National University of Ireland, Galway
in fulfilment of the requirements for the degree of
DOCTOR OF PHILOSOPHY



Faculty of Science, Department of Earth and Ocean Sciences
National University of Ireland, Galway,
Galway, Ireland

SUPERVISED BY:

Prof. Dr. Alan G. Jones, Dublin Institute for Advanced Studies, Dublin, Ireland

Dr. Colin Brown, National University of Ireland, Galway, Ireland

April 2015

Duygu Kiyan: *Multidimensional Magnetotelluric imaging of crustal and uppermost mantle structures of the Atlas Mountains of Morocco,*

© April 2015

CONTENTS

Table of Contents	v
List of Figures	xiv
List of Tables	xv
List of Symbols	xvi
List of Acronyms	xix
Summary	xxi
Preface	xxiii
Declaration	xxiv
Statement of Co-Authorship	xxv
Publications	xxvi
Acknowledgements	xxviii
Dedication	xxxi
I INTRODUCTION, THEORY, AND BACKGROUND INFORMATION	1
1 INTRODUCTION	2
2 MAGNETOTELLURIC THEORY	8
2.1 From Maxwell's Equation to the Diffusion Equations	9
2.2 The Assumptions of the MT Method	10
2.3 The Magnetotelluric Transfer Functions	14
2.3.1 The Impedance Tensor	14
2.3.2 The Geomagnetic Transfer Function	15
2.4 Natural Source Fields of MT Signals	16
2.4.1 Sources in the Magnetosphere	16
2.4.2 Sources in the Atmosphere – lightning activity	23
2.4.3 Source Field Effects on MT Responses	24
2.5 Electrical Properties of Earth Materials	26
2.5.1 Electrical Conductivity	26
2.5.2 Electrical Charge Transport Mechanisms	26
2.5.3 Two-Phase Mixing Systems	28
2.6 Dimensionality	32
2.6.1 The 1-D Earth	32
2.6.2 The 2-D Earth	33
2.6.3 The 3-D Earth	35
2.6.4 The Anisotropic Earth	35

2.7	The Distortion Problem	37
2.8	Data Processing, Analysis, Modelling and Inversion	40
2.8.1	From Time Series to Frequency Domain Transfer Functions	40
2.8.2	Distortion Analysis and Removal	43
2.8.3	D^+ and ρ^+	49
2.8.4	Forward Modelling and Inversion of MT Data	50
3	WESTERN MEDITERRANEAN FIELD AREA	53
3.1	Geological and Tectonic Background of Atlas Mountains of Morocco	53
3.1.1	The Atlantic Domain	56
3.1.2	The Tethyan Domain	58
3.1.3	Overall Shortening in the Atlas System	60
3.1.4	The Cenozoic Volcanic History of the Atlas System	60
3.2	Previous Geophysical Work in the Atlas System of Morocco	62
3.2.1	Magnetotelluric Studies	62
3.2.2	Active Source Seismology	66
3.2.3	Seismic Tomography	66
3.2.4	Receiver Functions	70
3.2.5	Seismic Anisotropy – shear-wave splitting measurements	70
3.2.6	Surface Heat Flow Data and Thermal Models	73
3.2.7	Seismicity	73
3.2.8	Integrated Geophysical and Petrological Modelling	75
II THE MAGNETOTELLURIC EXPERIMENT ACROSS THE ATLAS MOUNTAINS OF MOROCCO		79
4	DATA ACQUISITION, PROCESSING AND ANALYSIS	80
4.1	The TopoMed-PICASSO Project	80
4.2	Broad-Band and Long-Period MT Data Acquisition	83
4.3	Instrumentation	84
4.3.1	Broad-Band MT System	84
4.3.2	The Long-Period Magnetotelluric Instrumentation (LMTI, LEMI-417M)	85
4.4	Time Series Data Processing	86
4.4.1	Time Series Data	86
4.4.2	Data Processing	86
4.5	Data Analysis – dimensionality and directionality	89
4.5.1	Phase Tensor	89
4.5.2	Strike Analysis	91
5	2-D INVERSION OF TOPOMED MT DATA	100
5.1	Inversion Parameters	100
5.2	Crustal Structures, MEK Profile – crustal strike direction	102

5.3	Mantle Structures, MEK Profile – lithospheric mantle strike direction	107
5.4	Interpretation	111
6	3D MODELLING OF OBLIQUE STRUCTURES	118
6.1	Abstract	118
6.2	Introduction	118
6.3	Synthetic Data: Test Model	119
6.4	3-D Inverse Modelling	120
6.4.1	Model Set-up	121
6.4.2	Smoothing Parameter	122
6.4.3	3-D Inversion Results	122
6.5	Conclusions	125
7	3-D INVERSION OF TOPOMED MT DATA	134
7.1	Modular Electromagnetic Inversion System	134
7.2	Coast Effect	137
7.3	Inversion of MEK Profile Data Set	140
7.4	Inversion of MAR Profile Data Set	150
III DISCUSSION, CONCLUSIONS AND REFERENCES		155
8	DISCUSSION	156
8.1	Comparison with Seismic Results	156
8.2	Origin of High Conductivity in the Lower Crust and Uppermost Mantle	157
8.2.1	Temperature Regime in the Crust – crustal geotherm calculations	160
8.2.2	Estimates of Melt Fraction	161
8.3	Geodynamic Implications	168
9	CONCLUSIONS AND OUTLOOK	170
9.1	Modelling and Interpretation of both the MEK and the MAR Profile Data	170
9.1.1	Insights into the Crustal and Mantle Structures of the Atlas Mountains of Morocco	170
9.2	3-D MT Inversion	171
9.3	Suggestions for Future Work	172
References		200
IV APPENDICES		201
A	FORWARD MODELLING RESULTS OF OBLIQUE CONDUCTOR	202
A.1	Comparison of 2-D and 3-D Forward Responses	202
B	PICASSO/TOPOMED - SUPPLEMENTARY FIGURES	204
B.1	TopoMed Magnetotelluric Data	204

LIST OF FIGURES

Figure 1.1	Tectonic setting of the western Mediterranean	3
Figure 2.1	Schematic view of the Earth's magnetosphere; <i>from</i> (Lapenta, 2011). . . .	17
Figure 2.2	(a) The layers of the ionosphere with their electron density and predominant ion populations; <i>modified from</i> Andersen & Fuller-Rowell (1999). (b) Electrical conductivities based on typical day-time ionosphere (Parkinson, 1983).	21
Figure 2.3	Equivalent currents of solar daily variations S_q on quiet days. The magnetic field of these currents reproduce the mean global S_q field for September equinoxes 1957/1958: for the external part (on the left) and for the internal part (on the right). Total current is given by the numbers while the flow direction is shown by the arrows; <i>from</i> Schmucker (1985).	21
Figure 2.4	Monthly (blue) and monthly smoothed (red) sunspot numbers since April 1749 till May 2012; <i>Data obtained from the Solar Influence Data Analysis Center (SIDC), Royal Observatory of Belgium</i>	23
Figure 2.5	Figure showing the distribution of lightning flashes around the world; <i>from</i> NASA	24
Figure 2.6	A graphical description of a simple 2-D model composed of 2 quarter-space model with different conductivities σ_1 and σ_2	33
Figure 2.7	Illustration of basic anisotropy parameters	36
Figure 2.8	Sketch of current channelling and deflection	38
Figure 2.9	Groom–Bailey twist, shear and anisotropy distortion of a unit vector; <i>modified from</i> Simpson & Bahr (2005)	45
Figure 2.10	Graphical representation of the phase tensor	47
Figure 3.1	Structural map of Morocco	54
Figure 3.2	The break-up of the Pangea super-continent and further plate tectonics of the Atlantic and Tethyan domains; <i>modified from</i> Stampfli & Borel (2002).	55
Figure 3.3	The Triassic to Middle Jurassic West Moroccan Arch and surrounding areas. A: Paleogeography during the Late Triassic. B: Paleogeography during the Early and Middle Jurassic; <i>modified from</i> de Lamotte et al. (2008).	56

Figure 3.4	Structural map of the Western High Atlas onshore and offshore; <i>from Hafid et al. (2006)</i>	57
Figure 3.5	Tectonic map of Middle Atlas region showing main faults and Quaternary basalt; <i>from Gomez et al. (1996)</i>	58
Figure 3.6	Geodynamic evolution of the Anti-Atlas domain during Neoproterozoic times; <i>modified from Ennih & Lie (2001)</i>	61
Figure 3.7	Details of Moroccan Atlas system (Middle Atlas, High Atlas and Anti-Atlas) and location of Cenozoic volcanic centers	63
Figure 3.8	Map of the northwest African plate (A) and flow of Canary mantle plume material under northwest Africa through a subcontinental lithospheric corridor in a 3-D model (B)	64
Figure 3.9	Figure showing the first electrical resistivity model derived from forward modelling of 5-component MT data along the Profile S, (<i>Schwarz et al., 1992</i>)	65
Figure 3.10	Crustal section for the SSE-NNW profile from the Middle Atlas through High Atlas towards the Anti-Atlas; <i>from Wigger et al. (1992)</i>	66
Figure 3.11	Body wave tomography of the western Mediterranean upper mantle with improved resolution through the use of a large teleseismic dataset, and a crustal velocity structure derived from surface wave modelling (<i>Palomeras et al., 2014</i>). Location of the seismic stations used in the modelling are shown with black solid circles; <i>modified from Bezada et al. (2013)</i>	68
Figure 3.12	Body wave tomography of the western Mediterranean upper mantle with improved resolution through the use of a large teleseismic data set	69
Figure 3.13	Absolute shear velocity maps at crustal and mantle depths	71
Figure 3.14	Crustal and lithospheric thickness in the Western High Atlas derived from receiver function study	72
Figure 3.15	Station-averaged SK(K)S splitting plotted centered at the station location from the <i>Wustefeld et al. (2009)</i> updated database which includes the studies of <i>Buontempo et al. (2008)</i> and <i>Diaz et al. (2010)</i> (dark blue), new SK(K)S (orange), and direct S results from the deep (>600 km) focus earthquake, that occurred beneath Grenada on April 11, 2010). The bar azimuth denotes the direction of fast polarization, with delay time proportional to bar length. The dashed green line shows the approximate location of the West African Craton; <i>from Miller et al. (2013)</i>	74
Figure 3.16	Average crustal geotherms: Alboran Basin, Rif, Middle Atlas, High Moulouya Plain, High Atlas, Anti-Atlas, Western High Atlas and Anti-Atlas; <i>redrawn after Rimi (1999)</i>	75
Figure 3.17	Density map of seismicity in the Mediterranean-Atlantic transition zone	76

Figure 3.18	Structure of the lithosphere of the Atlantic-Mediterranean Transition Region derived from topography, geoid anomalies, surface heat flow data, and seismic data modelling; <i>from Fullea et al. (2010)</i> . A) Maps of the Moho depths. Isolines every 2 km. B) LAB depth maps superimposed to the structural map with the main tectonic units and volcanism. Isolines every 20 km.	77
Figure 3.19	Lithospheric model from <i>Fullea et al. (2010)</i> (thick solid line) along the profile P3 (coincides with the MT profile MEK, see Figure 3.7 or Figure 4.1). Superimposed on the right-hand figure are the crust-mantle boundary and LAB geometries from previous works: dashed line (<i>Zeyen et al., 2005</i>), dash-dotted line (<i>Missenard et al., 2006</i>); <i>modified from Fullea et al. (2010)</i>	78
Figure 4.1	Overview of all PICASSO-TopoMed MT and seismic site locations	82
Figure 4.2	Daily international sunspot numbers for the period during the acquisition of the long-period MT data. Sunspot data obtained from the Sunspot Index Data Centre maintained by the Royal Observatory of Belgium.	84
Figure 4.3	Phoenix V5-2000 MT system. From left to right: non-polarizing lead, lead-chloride (Pb - PbCl) electrodes, induction coil cables, MTC-50 induction coils, battery, recording unit, case for the unit, and GPS antenna. Photo courtesy Phoenix Geophysics.	85
Figure 4.4	Schematic layout of the broad-band MT recording system used during the TopoMed fieldwork campaigns.	86
Figure 4.5	The Long-period Magnetotelluric Instrument (LMTI) LEMI-417M. From left to right: fluxgate magnetometer with 10 m cable and installation platform, electronic unit (black box), the lead-free non-polarizing copper, copper-sulphide (Cu - CuSO ₄) electrodes, electric lines terminal, and GPS antenna.	87
Figure 4.6	Simultaneous time series data of magnetic and electric fields at station MEK012 (red) in Middle Atlas and at station MEK016 (black) in High Moulouya Plain.	88
Figure 4.7	Phase tensor ellipse pseudo-sections for each periods of each sites (except 4 sites: mek010, mek004, mek002 and mek001 due to poor data quality) along the MAR profile of measurements across the Middle Atlas. The axes of ellipses are normalized by Φ_{max} and the colours represent the skew angle β (on the top) and the geometric mean $\Phi_2 (\sqrt{\Phi_{max}\Phi_{min}})$ (on the bottom). The ellipses are plotted so that the horizontal axis corresponds to an east-west orientation.	92

Figure 4.8	Phase tensor ellipse pseudo-sections for each periods of each sites (except 4 sites: mar015, mar016, mar019 and mek020 due to poor data quality) along the MAR profile of measurements across the Middle Atlas. The axes of ellipses are normalized by Φ_{max} and the colours represent the skew angle β (on the top) and the geometric mean $\Phi_2 (\sqrt{\Phi_{max}\Phi_{min}})$ (on the bottom).The ellipses are plotted so that the horizontal axis corresponds to an east-west orientation.	93
Figure 4.9	Rms misfit values from decomposition models for each MT stations along the MEK profile with varying the geo-electric strike direction at the Niblett-Bostick depth ranges of 3 - 10 km, 10 - 28 km, 40 - 90 km, and 90 - 150 km. The optimal common geo-electric strike direction clockwise from North calculated for all stations for crustal and lithospheric depths; indicated by black dashed line on the plots. Also, the optimal geo-electric strike directions calculated for stations excluding the stations in the Tabular Middle Atlas (mek006 and mek008) and the stations in the northern part of the profile (mek01a, mek02a, and mek03a); indicated by black dotted line on the plots. Empty columns are due to insufficient data for this depth range at the respective station.	95
Figure 4.10	Figure showing (a) rms misfit values from decomposition models for each MT stations along the MEK profile with varying the geo-electric strike direction for crustal (5 - 35 km) and lithospheric (50 - 150 km) depth ranges, respectively. The dashed line indicate overall strike directions for crustal and lithospheric depths. Empty columns are due to insufficient data for this depth range at the respective station. (b) a table of the different strike angles for crustal and lithospheric depth ranges and for different areas of the MEK profile.	96
Figure 4.11	Figures showing the comparison between the results of unconstrained (a & b) and constrained (c-50° & d-22°) single-site strike analysis along MEK profile (a & c) for crustal depth ranges (5-35 km) and (b & d) for lithospheric depth ranges (50 - 150 km). Double-headed arrows show 2-D geo-electric strike direction, scaled in length by phase difference between the XY and YX modes. A large phase indicates a stronger degree of dimensionality. Coloured squares show the rms misfit error, normalized by the observational errors in the observed MT response, at each site. By normalizing the rms error by observational errors, higher quality data with low errors are weighted more heavily in the decomposition. Low rms errors ($< \sim 2$) indicate MT responses in which the sub-surface structure is described as 2-D.	97

Figure 4.12	Rms misfit values from decomposition models for each MT stations along the MAR profile with varying the geo-electric strike direction at Niblett-Bostick depth ranges of 300 m - 3 km, 3 - 10 km, 10 - 30 km, and 35 - 90 km. The dashed lines indicate overall strike direction for requested depth range. Empty columns are due to insufficient data for this depth range at the respective station.	98
Figure 4.13	Rms misfit values from decomposition models for each MT stations along the MAR profile with varying the geo-electric strike direction for crustal depth ranges (3 - 30 km). The dashed line indicates overall strike direction.	99
Figure 5.1	Rms misfit versus τ trade-off curves for the crustal and the whole data sets	102
Figure 5.2	An example of inversion results using three different values 0.1 (a), 2 (b) and 100 (c) for τ	103
Figure 5.3	Comparison of isotropic and anisotropic 2-D inversion results for the MEK profile data set	105
Figure 5.4	The apparent resistivity and phase pseudo-sections of TM (on the top) and TE data (on the bottom)	106
Figure 5.5	2-D isotropic inversion results of individual components of MT data for crustal MEK profile	108
Figure 5.6	Comparison of isotropic and anisotropic 2-D inversion results for the southern part of the MEK profile data set	109
Figure 5.7	The apparent resistivity and phase pseudo-sections of TM (on the top) and TE data (on the bottom)	110
Figure 5.8	2-D isotropic inversion results of individual components of MT data for crustal MEK profile	112
Figure 5.9	The apparent resistivity and phase pseudo-sections of TM (on the top) and TE data (on the bottom)	113
Figure 5.10	Isotropic 2-D crustal resistivity model of the MEK profile across the Atlas Mountains are derived from inversion of joint TM and TE mode MT data. The main features of the resistivity model are the high conductivity of the middle to lower crust in the Middle Atlas and the High Moulouya Plain and the resistive Anti-Atlas. The Moho depth is highlighted by red dashed lines (Ayarza et al., 2005) and black dashed lines (Miller & Becker, 2014). NHAF: North High Atlas Fault; SHAF: South Atlas Fault.	115
Figure 5.11	Figure showing the first electrical resistivity model derived from forward modelling of 5-component MT data along the Profile S, (Schwarz et al., 1992).	115

Figure 5.12	Previous 2-D electrical resistivity model across the Atlas Mountains of Morocco (Ledo et al., 2011)	116
Figure 5.13	Previous 2-D electrical resistivity model across the Atlas Mountains of Morocco (Anahnah et al., 2011)	117
Figure 6.1	(a) Plan view of the synthetic model used to generate MT data and (b) resistivity and phase curves calculated at site A009 in both strike aligned and geographic coordinate systems	120
Figure 6.2	Impedance magnitude rotation diagram for site A009 is at 100s	121
Figure 6.3	3-D inversion results of the test model using different smoothing parameters	123
Figure 6.4	3-D inversion results of the test model obtained in geographic coordinate system	124
Figure 6.5	Observed and predicted pseudo-sections from the only off-diagonal 3-D inversion and the full-tensor 3-D inversion	126
Figure 6.6	Inversion results obtained using off-diagonal ($\mathbf{Z}_{x'y'}$, $\mathbf{Z}_{y'x'}$) tensor components after aligning both the 3-D mesh and the data with predominant strike direction.	127
Figure 6.7	Apparent resistivity and phase pseudo-sections for observed data, and the predicted data for the final 3-D inversion result obtained by fitting off-diagonal components	128
Figure 6.8	Inversion results from three parallel profiles using only off-diagonal elements of the impedance tensor	128
Figure 6.9	Inversion results from three parallel profiles using complete impedance tensor elements	129
Figure 6.10	Apparent resistivity and phase pseudo-sections for observed data, and the predicted data for the final 3-D inversion result obtained by fitting off-diagonal components	130
Figure 6.11	Apparent resistivity and phase pseudo-sections for observed data, and the predicted data for the final 3-D inversion result obtained by fitting full-tensor components for the left-hand side profile	131
Figure 6.12	As in Figure 6.11, but for the centre profile.	132
Figure 6.13	As in Figure 6.11 & Figure 6.12, but for the right-hand side profile.	133
Figure 7.1	Schematic overview of the Modular Electromagnetic Inversion (ModEM) system	137
Figure 7.2	(a) Plan view of the large-scale regional model used for the study of the ocean effect for the MEK profile, including the bathymetry and (b) the coast effect in the apparent resistivity and phase curves	138

Figure 7.3	(a) Plan view of the large-scale regional model used for the study of the ocean effect for the MAR profile, including the bathymetry and (b) the coast effect in the apparent resistivity and phase curves	139
Figure 7.4	Plan view of the preferred 3-D resistivity model obtained from the final 3-D inversion, which is the result of fitting only the components, at depths middle crust, lower crust and lithospheric mantle	143
Figure 7.5	Representative cross-section from the representative 3-D resistivity model and 2-D electrical resistivity model of Ledo et al. (2011) along the MEK profile	144
Figure 7.6	Phase pseudo-sections of observed data, and the corresponding predicted data for the final 3-D inversion of the off-diagonal components only	145
Figure 7.7	Perspective view of 3-D inversion model, which is obtained from 3-D inversion of the southern part of the MEK profile data set, fitting only the off-diagonal impedance tensor components, with E-W slices across the modelled space	146
Figure 7.8	Sensitivity test for 3-D MEK profile model Figure 7.5	147
Figure 7.9	(a) S-receiver function profile across Atlas mountains from north to south and (b) Differences in apparent resistivities and phases of best fitting model and altered model response curves	148
Figure 7.10	Variation of rms error value with varying the LAB depth and the electrical resistivity value of the zone below the LAB depth.	149
Figure 7.11	Plan view of the preferred 3-D resistivity model obtained from the final 3-D inversion, which is the result of fitting full impedance tensor elements, at depths upper crust, middle crust, lower crust and lithospheric mantle . .	151
Figure 7.12	2-D profile of the MAR transect extracted from preferred 3-D inversion model shown Figure 7.11	152
Figure 7.13	Comparison of the observed data and the response curves of the final 3-D inversion model of MAR profile	153
Figure 7.14	Figure showing 2-D profile of the MAR transect extracted from preferred 3-D inversion model and the isotropic 2-D model obtained from joint inversion of TE and TM data using the NLCG algorithm of Rodi & Mackie (2001) along the MAR profile.	154

Figure 8.1	<p>Crustal resistivity models compared with the crustal velocity model obtained from long offset wide-angle seismic reflection data under the framework of SIMA seismic experiment. Top: Velocity model with the tectonic interpretation; <i>modified from Ayarza et al. (2014)</i>. The area of interest, which coincides with the MEK profile, is outlined by a black box. On the velocity model, contours and semi-transparent colours represent the resistivity model by <i>Ledo et al. (2011)</i>: while the outer contour indicates $\rho < 25 \Omega\text{m}$, the inner one indicates $\rho < 2 \Omega\text{m}$ (on the bottom). Bottom: Depth slice of electrical resistivity extracted from the final 3-D inversion model. The grey dashes indicate interpreted crust-mantle boundary (Moho) by <i>Ayarza et al. (2014)</i>.</p>	158
Figure 8.2	<p>Top: Cross sections showing shear wave velocity through the Atlas Mountains extracted from the 3-D shear wave velocity model; <i>from (Palomeras et al., 2014)</i>. The area of interest, which coincides with the MEK profile, is outlined by a red box. Bottom: Depth slice of electrical resistivity extracted from the final 3-D inversion model. The black and grey dashes indicate interpreted crust-mantle boundary (Moho) by <i>Miller & Becker (2014)</i> and <i>Ayarza et al. (2014)</i>, respectively. Lithosphere-asthenosphere boundary (LAB), based on S Receiver Function (SRF) analysis (<i>Miller & Becker, 2014</i>) and from <i>Fullea et al. (2010)</i> are indicated with red dashes and blue solid line, respectively.</p>	159
Figure 8.3	Crustal geotherms for the Middle Atlas and the High Moulouya Plain . . .	162
Figure 8.4	Electrical conductivity of saline fluids compared with wet and dry partial melt	163
Figure 8.5	Figure showing a modelled geotherm with a modelled geotherm corresponds to a lithospheric structure that matches with the measured surface heat flow and topography in the study area. Phase diagram emphasizing the role of water in magma source rock showing a comparison between the dry and water-saturated solidi for granite and basalt, and 1-D MT models	166
Figure 8.6	Electrical conductivity of a partially molten rock as a function of melt fraction for various mixing models	167
Figure A.1	Comparison of the rotated 2-D and 3-D responses. Resistivity and phase curves for all four components calculated at stations A006, A009, A012, and A016 (for station locations see Figure 6.1a in Section 6.3) The blue circles represent the rotated 2-D responses into strike angle of 45° and the red stars are the 3-D responses.	203

Figure B.1	PICASSO/TopoMed MEK profile original data for plotted for all four components (XX, XY, YX and YY) of the impedance tensor.	205
Figure B.2	PICASSO/TopoMed MEK profile original data for plotted for all four components (XX, XY, YX and YY) of the impedance tensor.	206
Figure B.3	PICASSO/TopoMed MEK profile original data for plotted for all four components (XX, XY, YX and YY) of the impedance tensor.	207
Figure B.4	PICASSO/TopoMed MAR profile original data for plotted for all four components (XX, XY, YX and YY) of the impedance tensor.	208
Figure B.5	PICASSO/TopoMed MAR profile original data plotted for all four components (XX, XY, YX and YY) of the impedance tensor.	209

LIST OF TABLES

Table 2.1	Classification of geomagnetic fluctuations reproduced from (Schmucker, 1985)	17
Table 2.2	Summary of different geometric models to describe melt distribution; σ_{eff} = effective conductivity, X_m = melt fraction, σ_m = fluid phase conductivity, C and n = Archie's law empirical coefficients, β = partitioning between tube and cube distribution; <i>after</i> ten Grotenhuis et al. (2005) and Partzsch et al. (2000).	30
Table 2.2	Continued from previous page.	31
Table 8.1	Properties of the different crustal bodies used in the geotherm calculation.	161
Table 8.2	Parameters (i.e., melt composition, temperature, pressure and water content) used for the computation of electrical conductivity of pure melt – Effect of each parameter on the electrical conductivity of melt are tested, respectively. For the melt compositions, nephelinites, basanites, alkali basalts, and subalkaline basalts are used, respectively, (El Azzouzi et al., 2010; Bosch et al., 2014). Melt conductivity values of 0.796 and 1.564 are used in the melt fraction estimates.	165

LIST OF SYMBOLS

Following is a list of symbols used in this thesis. Their meanings (and typical units if appropriate) are indicated. Vectors are denoted by a single underline, whereas tensors and matrices with double underlines.

Symbol	Description (Units)
\underline{B}	magnetic induction (nT)
C	Schmucker-Weidelt transfer function
$\underline{\underline{C}}$	galvanic distortion matrix (electric effects)
\underline{D}	electric displacement ($\frac{C}{m^2}$)
$\underline{\underline{D}}$	galvanic distortion matrix (magnetic effects)
δ	skin depth
\underline{E}	electric field ($\frac{V}{m}$)
E_x, E_y, E_z	elements of \underline{E} Cartesian coordinates
$\varepsilon = \varepsilon_0 \cdot \varepsilon_r$	electrical permittivity ($\frac{As}{Vm}$)
ε_0	electrical permittivity of the vacuum (8.854×10^{-12})
ε_r	relative electric permittivity
q	electric charge density ($\frac{C}{m^3}$)
\underline{j}	electric current density (A/m ²)
\underline{j}_f	electric current density of free charges ($\frac{A}{m^2}$)
f	frequency (Hz)
\underline{H}	magnetic intensity ($\frac{A}{m}$)
H_x, H_y, H_z	elements of \underline{H} Cartesian coordinates
I	current (A)
$\underline{\underline{M}}$	complex magnetotelluric tensor ($\frac{mV}{km}/nT$)
$M_{xx}, M_{xy},$ M_{yx}, M_{yy}	elements of $\underline{\underline{M}}$ Cartesian coordinates ($\frac{mV}{km}/nT$)

continued on next page

continued from previous page

Symbol	Description (units)
μ	magnetic permeability ($\frac{Vs}{Am}$)
μ_0	magnetic permeability of the vacuum ($4\pi \times 10^{-7} \frac{Vs}{Am}$)
$\underline{\underline{R}}$	rotation matrix
ρ	electric resistivity (Ωm)
ρ_a	apparent electric resistivity (Ωm)
σ	electric conductivity (S/m)
σ_{eff}	effective conductivity (S/m)
σ_f	electrolyte conductivity (S/m)
σ_m	melt conductivity (S/m)
σ_s	conductivity of the solid rock; surface conductivity (S/m)
T	period (s); temperature ($^{\circ}C$ or K); Tesla
\underline{T}	geomagnetic transfer function/tipper
T_x, T_y	elements of \underline{T} in Cartesian coordinates
τ_c	closeness parameter
τ_s	smoothness parameter
V_p	P wave velocity (m/s)
V_s	shear wave velocity (m/s)
ω	angular frequency ($\frac{1}{s}$)
x, y, z	Cartesian coordinates (z positive downwards)
X_m	melt fraction
$\underline{\underline{Z}}$	complex impedance tensor ($\Omega = \frac{V}{A}$)
$Z_{xx}, Z_{xy},$ Z_{yx}, Z_{yy}	elements of $\underline{\underline{Z}}$ in Cartesian coordinates (Ω)
z	depth (m or km)
ϕ	impedance tensor phase; volume fraction of the conductive material; porosity
Φ	objective function
$\underline{\underline{\Phi}}$	phase tensor

continued on next page

continued from previous page

Symbol	Description (units)
i	complex number
\Re	real part of a complex number
\Im	imaginary part of a complex number
$\frac{\partial}{\partial t}$	time derivative
∇	nabla operator
Δ	delta operator
∞	infinite
$ \cdot $	absolute value
$\ \cdot\ $	norm
\underline{X}	vector
$\underline{X}, \underline{X}^T$	matrix X , and transpose matrix X
\underline{I}	identity matrix

LIST OF ACRONYMS AND ABBREVIATIONS

Following is a list of acronyms and abbreviations used in this thesis. Their definition and explanations are indicated.

Acronym	Description (Units)
1-D	one-dimensional
2-D	two-dimensional
3-D	three-dimensional
AA	Anti-Atlas
AAMF	Anti-Atlas Major Fault
ANMA	North Middle Atlas Fault
ASMA	South Middle Atlas Fault
BBMT	broad-band magnetotellurics
dd	dip equator region on the day-side
DP1	polar magnetic storms with centre of disturbance in the night-time auroral zone
DP2	polar magnetic storms with correlated irregular variations in low latitudes
DS	disturbance local time inequality of smoothed storm-time variations
Dst	storm time-dependent part of smoothed storm-time variations
EM	electromagnetics
ERC	equatorial ring current in the radiation belt of the magnetosphere
FMA	Folded Middle Atlas
HA	High Atlas
HMPA	High Moulouya Plain
LAB	lithosphere-asthenosphere boundary
LEMI	long-period magnetotellurics
MA	Middle Atlas

continued on next page

continued from previous page

Acronym	Description (units)
MLD	mid-lithospheric discontinuity
MT	magnetotellurics
NHAF	North High Atlas Fault
NLCG	non-linear conjugate gradient
PC	principal component
Pc1 — Pc5	regular continuous ultralow frequency waves (pulsations)
PEJ	polar electrojet in the ionosphere
Pi1, Pi2	irregular transient ultralow frequency waves (pulsations)
PICASSO	program to investigate convective Alboran Sea system overturn
rms	root mean square
S_D	solar daily variation, enhanced on disturbed days
sfe	solar flare effect
SHAF	South Atlas Fault
SIMA	seismic investigations of the Moroccan Atlas
ssc	sudden storm commencement
Sq	solar daily variation on quiet days
TE	transverse electric (TE) mode / E-polarisation
TM	transverse magnetic (TM) mode / B-polarisation
TMA	Tabular Middle Atlas
TopoMed	plate re-organization in the western Mediterranean: lithospheric causes and topographic consequences
ULF	ultralow frequency (bands / waves)
VLF	very low frequency (bands / waves)

SUMMARY

The primary goal of the PICASSO (Program to Investigate Convective Alboran Sea System Overturn) project, and the concomitant TopoMed (Plate reorganization in the western Mediterranean: Lithospheric causes and topographic consequences - an ESF EUROSCORES TOPO-EUROPE Collaborative Research Project) project, is to provide new constraints on the crustal and lithospheric structures of the Alboran Sea, Betics, Rif, Atlas Mountain belt and surrounding areas in the western Mediterranean. A component of both PICASSO and TopoMed is electromagnetic imaging using the magnetotelluric method. The land-based magnetotelluric survey's main objectives are to image the electrical conductivity structure of the Atlas Mountains of Morocco, as well as to test the hypotheses for explaining the observation of a "missing" mantle root inferred from the integrated geophysical-petrological forward modelling that combines elevation, gravity, geoid, surface heat flow and seismic data.

Two-dimensional (2-D) and three-dimensional (3-D) inversion of magnetotelluric data, acquired along two profiles (the so-called MEK and MAR profile), are conducted to obtain enhanced insight into the subsurface geology of the Atlas Mountains. 2-D and 3-D isotropic modelling results from the approximately 220 km long MEK profile, crossing the Tabular (TMA) and the Folded (FMA) Middle Atlas, the High Moulouya Plain (HMP), the High Atlas (HA) and the eastern Anti-Atlas (AA), indicate that the TMA, FMA and the HMP are characterized by a low conductivity (3 - 10 Ωm) lower crust underlain by relatively normal ($\sim 150 \Omega\text{m}$) upper mantle structure. In order to account for the observed low resistivities in the lower crust 3.3 - 10% of partial melt fraction is required. The interpreted lower crustal partial melt beneath the Middle Atlas and the HMP may have been formed by mantle-derived $\text{CO}_2\text{-H}_2\text{O}$ rich supercritical fluids, which originate from the metasomatic alteration of the lherzolitic Atlas lithosphere during the partial melting process. On the other hand, 3-D isotropic inversion results of the southernmost MT data sites located on Paleozoic outcrops of the eastern Anti-Atlas system showed a homogeneous and high electrical resistivity crustal and lithospheric structure. Investigation of the approximately 225 km long MAR profile, crossing the Haouz Basin, the Western High Atlas, the Souss Basin and the Anti-Atlas, shows that the conductive Western High Atlas is confined by two resistive ($>500 - 750 \Omega\text{m}$) basins, the Souss basin to the south and the Haouz basin to the north. The enhanced conductivity structure is mainly parallel to the early Mesozoic rifting structures and can be attributed to the presence of fluids, the presence of clay ions or possible mineralization along the fault zones.

During the 3-D inverse modelling of the MEK profile MT data, new 3-D inversion results confirm the high conductive zones of the 2-D inversion results except for one, which is found at the middle to lower crustal depth beneath the Anti-Atlas. Based on a synthetic data set from a single MT profile, in the presence of a regional, elongated 2-D conductive structure, the importance of including the

diagonal components of the impedance tensor in 3-D inversion is demonstrated. Moreover, in the case of using only the off-diagonal components of the impedance tensor, the model mesh and the data set must be aligned with quasi 2-D geo-electrical strike in order to map the right geometry and shape of the oblique conductive structures.

PREFACE

This thesis is based on the results of the PICASSO Phasell/TopoMed projects and a collection of one journal article written in collaboration with *Alan G. Jones* and *Jan Vozar* at *Dublin Institute for Advanced Studies*. The content of this article was unaltered to conform with Journal copyrights.

The results presented were generated using programs written mostly in Fortran and Matlab, as well as Perl and shell-scripts. The figures were produced almost entirely using Matlab and Generic Mapping Tools (GMT; [Wessel & Smith, 2005](#)), with minor use of Adobe Illustrator, and Corel Draw.

DECLARATION

I, the **Candidate**, certify that the Thesis is all my own work and that I have not obtained a degree in this University or elsewhere on the basis of any of this work.

Duygu Kiyani
Galway, Ireland,
April 2015

STATEMENT OF CO-AUTHORSHIP

Chapter 6 was published with *Alan G. Jones and Jan Vozar* at *Dublin Institute for Advanced Studies*. I generated the test model with input from *Alan G. Jones and Jan Vozar*, performed the analysis, and made the interpretation. I wrote the manuscript with input from *Alan G. Jones and Jan Vozar*.

PUBLICATIONS

Some of the ideas, results, and figures of generated through the course of this thesis have been presented to the scientific community, as follows:

PEER REVIEWED PAPERS:

Kiyan, D., Jones, A. G., and Vozar, J., 2014. The inability of magnetotelluric off-diagonal impedance tensor elements to sense oblique conductors in 3-D inversion. *Geophysical Journal International*, 196, pp. 1351-1364, 10.1093/gji/ggt470.

Jones, A. G., **Kiyan, D.**, Fullea, J., Ledo, J., Queralt, P., Marcuello, A., Siniscalchi, A., and Romano, G., 2012. Comment on "Deep resistivity cross section of the intraplate Atlas Mountains (NW Africa): New evidence of anomalous mantle and related Quaternary volcanism" by Anahnah et al. (2011). *Tectonics*, 31, TC5011, 10.1029/2011TC003051.

Ledo, J., Jones, A. G., Siniscalchi, A., Campanya, J., **Kiyan, D.**, Romano, G., Rouai, M., and the TopoMed MT Team, 2011. Electrical signature of modern and ancient tectonic processes in the crust of the Atlas mountains of Morocco. *Physics of the Earth and Planetary Interiors*, 185, 82-88, 10.1016/j.pepi.2011.01.008.

ORAL PRESENTATIONS:

Kiyan, D., A. G. Jones, J. Fullea, J. Ledo, A. Siniscalchi, G. Romano. Crustal and uppermost mantle structures of the Atlas Mountains of Morocco inferred from electromagnetic imaging. AGU Fall Meeting 2012, San Francisco. 3 - 7 December.

Kiyan, D., A.G. Jones, J. Ledo, J. Fullea, A. Siniscalchi, G. Romano, J. Campanyà, and the TopoMed MT Team. 3D structures of the crust and upper mantle in the Atlas Mountains of Morocco from magnetotelluric data. EGU General Assembly 2012, Vienna, Austria, 22 - 27 May.

Kiyan, D., A. G. Jones, J. Fullea, J. Ledo, A. Siniscalchi, M. Rouai, J. Campanya, G. Romano, P. Moretti, and TOPOMED Team. Crustal and lithospheric imaging beneath the Atlas Mountain of Morocco. TOPOMED Workshop 2011, Institute of Earth Sciences Jaume Almera – CSIC Barcelona, 19 - 20 September.

Kiyan, D., A. G. Jones, J. Fullea, C. Hogg, J. Ledo, A. Siniscalchi, M. Rouai, J. Campanya, P.P. Moretti, G. Romano, and the PICASSO Phase II Team. Magnetotelluric data from the Atlas Mountains of Morocco as part of TopoMed: preliminary results. 6th TOPO-EUROPE Workshop 2010, Honefoss, Norway, 4 - 6 November.

POSTER PRESENTATIONS:

Kiyan, D., A. G. Jones, J. Ledo, J. Fullea, A. Siniscalchi, and G. Romano. Multi-dimensional crustal and lithospheric structure of the Atlas Mountains of Morocco by magnetotelluric imaging. AGU Fall Meeting 2014, San Francisco, USA, 15 - 19 December.

Kiyan, D., A. G. Jones, J. Ledo, J. Fullea, A. Siniscalchi, and G. Romano. Three-dimensional crustal and lithospheric structures of Atlas Mountains of Morocco inferred from magnetotelluric imaging as part of the PICASSO/TopoMed Project. 21st Electromagnetic Induction Workshop 2014, Weimar, Germany, 24 - 30 August.

Kiyan, D., A. G. Jones, J. Ledo, J. Fullea, A. Siniscalchi, G. Romano. Crustal and lithospheric structures of Atlas Mountains of Morocco revealed through three-dimensional magnetotelluric imaging as part of the PICASSO/TopoMed Project. IGRM 2014, Dublin, Ireland, 28 February - 2 March.

Kiyan, D., A. G. Jones, J. Fullea, J. Ledo, A. Siniscalchi, and G. Romano. Crustal and uppermost mantle structure of the Atlas Mountains of Morocco revealed from three-dimensional inversion of magnetotelluric data. AGU Fall Meeting 2013, San Francisco, USA, 9 - 13 December.

Kiyan, D., A. G. Jones, J. Fullea, J. Ledo, A. Siniscalchi, and G. Romano. Three-dimensional magnetotelluric imaging of crustal and uppermost mantle structures of the Atlas Mountains of Morocco. EGU General Assembly 2013, Vienna, Austria, 7 - 12 April.

Kiyan, D., A. G. Jones, J. Ledo, J. Fullea, A. Siniscalchi, G. Romano. Crustal and uppermost mantle three-dimensional resistivity structure of the Atlas Mountains of Morocco revealed by magnetotelluric data. IAGA 2013, Merida Yucatan, Mexico, 26 - 31 August.

Kiyan, D., A. G. Jones, J. Ledo, J. Fullea, A. Siniscalchi, G. Romano. Crustal and lithospheric structures of Atlas Mountains, Morocco: constraints from magnetotelluric data. IGC 2012, Brisbane, Australia, 5 - 10 August.

Kiyan, D., A. G. Jones, J. Fullea and Anne Pommier. Crustal and lithospheric structures of Atlas Mountains of Morocco: insights from magnetotelluric data. 21st EM Induction Workshop 2012, Darwin, Australia. 25 - 31 July.

Kiyan, D., A. G. Jones, J. Fullea, C. Hogg, J. Ledo, A. Siniscalchi, J. Campanyà, G. Romano, P. Moretti, M. Rouai, and the The TopoMed MT Team. Lithospheric-scale geometry of the Atlas Mountains of Morocco revealed by magnetotelluric surveying. EGU General Assembly 2011, Vienna, 3 - 8 April.

Kiyan, D., A. G. Jones, C. Hogg, J. Ledo, A. Siniscalchi, and the PICASSO Phase II Team. MT investigations over the Atlas Mountains of Morocco: preliminary results. 20th Electromagnetic Induction Workshop 2010, Egypt, 18 - 24 September.

ACKNOWLEDGEMENTS

First and foremost, I would like to thank my supervisors, Prof. Alan Jones and Prof. Colin Brown, for their patient guidance and support over the past five years. I am thankful for the opportunities Prof. Jones has given me to discuss my work at many international conferences and workshops, to participate in magnetotelluric field campaigns in Canada and Ireland, and to be involved in training courses, such as in New Mexico (SAGE 2011) and at the University of Copenhagen (Elite PhD course, 2011).

I would like to sincerely thank Dr. Mark Muller, Dr. Jan Vozar, Dr. Javier Fulla and Dr. Volker Rath for their constructive advice, guidance and encouragement. I would particularly like to thank to Dr. Vozar for the invaluable discussions that we had on general aspects of 3-D MT inversion and the 3-D results from the TopoMed/Picasso MT data set. I would like to acknowledge Dr. Andrew Schaeffer, Dr. Florian Le Pape, Prof. Sergei Lebedev, Dr. Celine Tirel, Dr. Eric Mandolesi, Dr. Ebru Bozdogan, and Ms. Fatma Gulmez for their helpful advice and encouragement during the writing process.

With regards to the PICASSO Phase II/TopoMed fieldwork campaigns in Morocco, I would like to sincerely thank all of the team members who helped me collect the magnetotelluric data set and made the campaigns such a great experience: Colin Hogg, Florian Le Pape, Gerardo Romano, Jan Schmoldt, Jan Vozar, Javier Fulla, Joan Campaña, Matthew Drew, Pierpaolo Moretti, Shane Carey, and Perla Pina. I am especially grateful to Prof. Mohamed Raoui and his PhD students from Meknes University, Morocco, namely Yousef Seddas, Khaoula Qarqori, and Fetah Kourchi for their collaboration and help during the fieldwork seasons.

My time at DIAS was made enjoyable in large part due to the many friends and colleagues who became part of my life. I would like to thank all of my colleagues, past and present, in the Geophysics Section of DIAS for creating such a friendly and inspiring work atmosphere. Warmest thanks go to my fantastic office mates in the front room and the blue room: Sarah Blake, Robert Delhaye, Thomas Farrell, David Khoza, Eric Mandolesi, Florian Le Pape, Jan Schmoldt, and Pieter Share. A big thanks must also go to DIAS' technical and support staff members for their continuous assistance throughout: Anna Sewielska, Clare Horan, Louise Collins, Philippe Grange, Jean Francois Bucas, and Sean O'Sullivan.

I would like to acknowledge Irish Research Council for Science, Engineering and Technology (IRCSET). Their funding made my PhD work possible and for this I am very grateful. I also would also like to thank the Irish Centre for High-End Computing (ICHEC) for the provision of computational facilities and support.

Prof. Jones organized three TopoMed working group meetings in Montpellier in the past three years. I would like to sincerely thank all of the TopoMed MT group members: Prof. Juanjo Ledo,

Dr. Javier Fulla, Prof. Agata Siniscalchi and Dr. Gerardo Romano for their collaboration on the project and for the helpful discussions we had during our time in Montpellier.

Lastly, I would like to thank my family, especially my Mum, Dad and brother, for all of their love, faith and encouragement. A special thanks must also go to my friends at home in Turkey: Karolin Firtina, Tuba Kiyani, Nevra Aydogan, Fatma Gulmez, Gulsah Karahasan, Dilek Inkun, Pinar Gutsuz, Sertan Kiyani, Doga Dusunur Dogan, Huseyin Yildirim, Sema Germen, Ayse Yaltirim, Murat Germen, Bilge Buhar, and Nihat Musa for their love and support. A very special thank you goes to my friend and colleague Colin Hogg, who has been supportive and encouraging in every way. And most of all for my loving, supportive and patient boyfriend Barry—thank you simply for everything.

Dedicated to my beloved family: *my mum, dad, and brother...*

Part I

INTRODUCTION, THEORY, AND BACKGROUND INFORMATION

INTRODUCTION

The opening and closing of oceanic basins is an integral process of Earth dynamics, and constitutes the main component of the Wilson cycle (Wilson, 1966). The complete conceptual Wilson cycle involves the creation of new oceanic crust at mid-ocean ridges, followed by its eventual consumption at subduction zones around the basin's margins. The end of the cycle is typically marked by continent-continent collision, which occurs after all intervening oceanic lithosphere is subducted. The western Mediterranean region presents an ideal natural laboratory to study the 3-D structures and dynamics associated with this final stage of the plate tectonic cycle.

Since the Oligocene, the geodynamic evolution of the western Mediterranean region stretching—from the northern Apennines to southern Iberia, including the Calabrian and Gibraltar Arcs—has been characterized by the slow convergence (6 to 4 mm/year) of Africa (Nubia) towards Eurasia (in a N to NW direction). Simultaneously, the rapid roll-back of narrow slabs of subducting African oceanic lithosphere (e.g., Jolivet & Faccenna, 2000; Faccenna et al., 2004; Rosenbaum et al., 2002) resulted in the extension and formation of young oceanic back-arc basins (namely, the Alboran Sea, Algerian Basin, Liguro-Provençal Basin and Tyrrhenian Sea) (Figure 1.1). To understand the geologic evolution of the Calabrian arc in the east and Gibraltar arc in the west, we require information not only from their internal deformation zones (i.e., Betics in Spain, Rif in Morocco, Tell in Algeria and Tunisia, and Apennines in Italy), but also external constraints from their bordering intra-continental chains (i.e., Iberian Range and the Pyrenees in Europe, and the Atlas Mountains in North Africa).

The Atlas Mountains of North Africa (the Middle Atlas, the High Atlas and the Anti-Atlas in Morocco, the Saharan Atlas in Algeria and the Tunisian Atlas in Tunisia) are an important and ideal natural laboratory for studying complex tectonic processes. Since the start of the early Miocene, the Atlas Mountains have accommodated a significant fraction (17 - 45%) of the western Mediterranean plate convergence between Africa and Iberia (Gomez et al., 2000). Furthermore, considering the relatively youthful age (Neogene to present) tectonism, Gomez et al. (2000) suggest that the Atlas system should be regarded as an integral part of the African-Eurasian plate-boundary zone in the western Mediterranean. The opening of north Atlantic and the western Tethys in the early Mesozoic and the Africa-Eurasia continent-continent collision in the early Cenozoic (e.g., Schaer, 1987; Jacobshagen et al., 1988) are two major events that affected the geologic history and present-day tectonics of Morocco. In contrast with major orogens such as the Himalayas, Andes or the

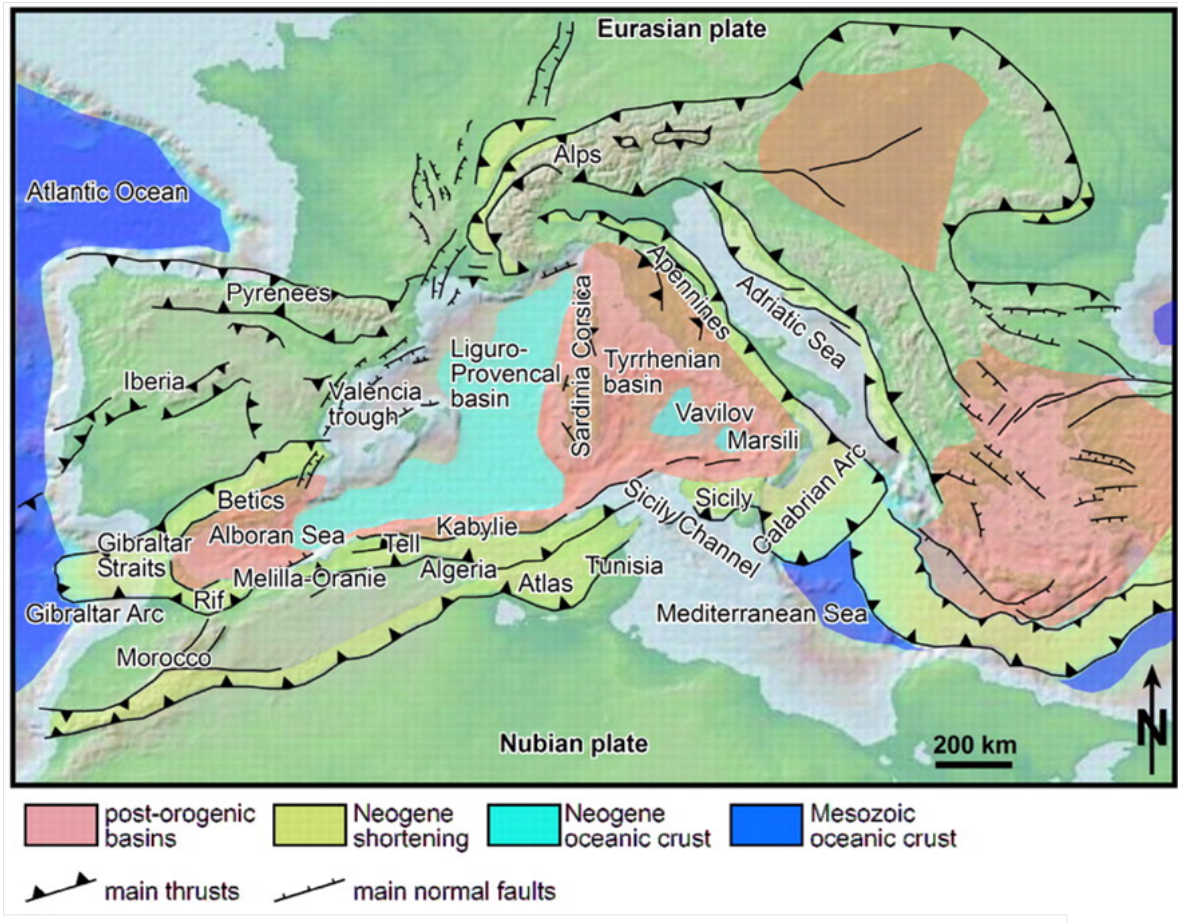


Figure 1.1.: Tectonic setting of the western Mediterranean; *from* Calvert et al. (2000).

Alps, which are also located along convergent/collisional plate boundaries, the Atlas Mountains of Morocco lack many of the observed diagnostic geological features of intraplate mountains, such as flyschs, nappes, regional metamorphism, ophiolites, granitoid intrusions and large-scale asymmetric deformation (Seber et al., 1996). Furthermore, unlike the eastern Atlas Mountain range (Saharan and Tunisian Atlas), the western mountain range (Middle Atlas, High Atlas and Anti-Atlas) has much higher topography even though they underwent a similar amount of convergence close to the same amount of convergence (de Lamotte et al., 2000). The overall shortening estimates are of 15 - 24% for the High Atlas (Teixell et al., 2003) and less than 15% for the Middle Atlas (Gomez et al., 1998; Arboleya et al., 2004); Moho thickness is a modest ~ 35 km across the Atlas, and does not isostatically reflect the elevation and recent uplift history (Teixell et al., 2003, 2005; Ayarza et al., 2005; Babault et al., 2008). While inversion tectonics and crustal thickening are thought to be responsible for the moderate uplift in the eastern Atlas, a thermal component has been considered a requirement to explain the relief of Atlas Mountains of Morocco (Ayarza et al., 2005; Teixell et al., 2005; Zeyen et al., 2005; Missenard et al., 2006; de Lamotte et al., 2009; Fullea et al., 2010).

Previous geophysical studies that combined geoid, gravity, heat flow and topography data concluded that a roughly NE-trending elongated zone of lithospheric thinning, proposed to be called the Morocco Hot Line by de Lamotte et al. (2009), lies beneath the Atlas Mountains of Morocco (Missenard et al., 2006). The authors also emphasized the consistency of a NE-trending thinned domain that is marked by a strip of late Miocene-Quaternary alkaline magmatism. The publications by Teixell et al. (2005); Zeyen et al. (2005); and Fullea et al. (2010) all modelled an anomalously thin lithosphere beneath the Atlas Mountains, based primarily on fitting the gravity and topographic elevation, although the estimates of its magnitude, shape, and exact location of this lithospheric thinning vary considerably between the authors. To explain the modelled lithospheric thinning, several models are proposed that invoke: (i) lithospheric mantle delamination of the Middle and High Atlas as a consequence of lithospheric thickening caused by Africa/Eurasia converge (Ramdani, 1998); (ii) delamination of the Atlas lithosphere caused by Canary mantle plume material (Duggen et al., 2009); (iii) thermal erosion of the Atlas lithosphere caused by lateral flow of asthenospheric mantle associated with roll-back of the Tethys slab (Teixell et al., 2005); (iv) a large scale mantle plume with a deep reservoir extending from the Canary Islands to the western Mediterranean (Hornle et al., 1995; Goes et al., 1999; Fullea et al., 2010); (v) a small Cenozoic asthenospheric plume, which causes thermal erosion of the Atlas lithosphere, similar to those mapped under the French Massif Central or the Eifel in Germany (Zeyen et al., 2005); (vi) small-scale convection involving the deep mantle reservoir or baby-plume (Fullea et al., 2010); (vii) edge-driven convection due to a significant difference in lithosphere-asthenosphere boundary (LAB) depth between the west African craton and the Moroccan lithosphere (King & Ritsema, 2000; Missenard & Cadoux, 2012).

In 2007, two international studies of the western Mediterranean field area, which includes the Betics in Spain, the Alboran Basin, the Rif Mountains of Morocco, and the Atlas (the Middle and High Atlas) and the Anti-Atlas to the south, were initiated to understand the tectonic evolution and lithospheric structure of the western Mediterranean. The first was named Program to Inves-

investigate Convective Alboran Sea System Overturn (PICASSO), whereas the second was the Plate re-organization in the western Mediterranean: Lithospheric causes and topographic consequences (TopoMed). The PICASSO and TopoMed projects were designed to collect high resolution, multi-disciplinary lithospheric scale data in order to distinguish between the proposed tectonic models of the region. To achieve this goal, the PICASSO and TopoMed projects proposed the acquisition of active and passive seismic data, land and marine magnetotelluric (MT) data collection, geochemical sampling, structural geology studies, and geodynamic modelling.

During the past decade, deep-probing electromagnetic imaging techniques, such as magnetotellurics, have been employed to study the crustal and upper mantle structure and evolution of orogenic belts. Several examples include the Himalayan Orogen and Tibetan Plateau formed in response to the collision between India and Asia (*e.g.*, Unsworth *et al.*, 2005a; Le Pape *et al.*, 2012), as well as the Anatolian-Iranian Plateau resulting from the collision of Arabia with Eurasia (Türkoğlu *et al.*, 2008). The geo-electric structure of Atlas Mountains of Morocco was first investigated by Schwarz *et al.* (1992) in 1983 and the authors concluded that a high conductivity zone existed at crustal depths beneath the Middle and High Atlas. Since the late-1980s new generation long-period magnetotelluric (LMT) systems have been developed, initially by the Geological Survey of Canada (Andersen *et al.*, 1988), and, more recently followed by new generation, low noise, 24-bit, highly-sensitive systems (Lviv long-period LEMI-417M recording system; Lviv Centre of Institute for Space Research, 2009). In addition to precise, high-quality field instrumentation, major developments in advanced processing methods and multi-dimensional modelling and inversion codes have occurred over the last decade.

A number of questions regarding the tectonics of the western Mediterranean remain, including the cause for the elevation of the Atlas Mountains, given observations of a missing lithospheric root (Teixell *et al.*, 2005; Zeyen *et al.*, 2005; Missenard *et al.*, 2006; de Lamotte *et al.*, 2009; Fulla *et al.*, 2010). Therefore, within the broad PICASSO and TopoMed Collaborative Research projects framework, with its overarching goal of understanding the tectonics of the western Mediterranean, this study—the MT component of the PICASSO and TopoMed projects—will focus its research activities on the Atlas Mountains of Morocco with the specific aims of:

1. Imaging and characterizing the deep crustal and mantle structure
2. Unravelling the role of the Atlas Mountains on the evolution of the western Mediterranean

The subsurface resistivity structure can provide crucial information that aids understanding of similar tectonic processes (*e.g.*, Solon *et al.*, 2005; Spratt *et al.*, 2005; White *et al.*, 2005; Türkoğlu *et al.*, 2008; Le Pape *et al.*, 2012). Moreover, MT can constrain fluid content and thermal structure, which are key parameters for defining the rheology of the crust and upper mantle of the orogens (Unsworth, 2010). Magnetotellurics is a passive-source electromagnetic sounding technique that measures time variations of natural electric and magnetic fields of the Earth to derive the lateral and vertical variations of the Earth's subsurface electrical resistivity. In the Earth's crust there are several sources of enhanced electrical conductivity (reduced resistivity), including aqueous fluids

(e.g., Li et al., 2003), graphite (e.g., Mareschal et al., 1992; Khoza et al., 2013b), sulphides (e.g., Jones et al., 1997; Ritter et al., 2003), iron oxides (e.g., Heinson et al., 2006), and in active tectonic regions like Tibet, partial melt (e.g., Unsworth et al., 2005a; Le Pape et al., 2012). Mantle conductivity is primarily sensitive to temperature variation and water content (Jones et al., 2012a; Evans, 2012), and to a lesser extent chemical composition and pressure. Therefore, MT is the perfect geophysical technique for the imaging the LAB that will provide new constraints on the lithospheric structure of the Atlas Mountains as well as on the crustal structures, and will aid discrimination between competing models describing the tectonics of the region.

This thesis constitutes the first 3-D geo-electrical subsurface characterization of the Atlas Mountains of Morocco. Moreover, the electromagnetic investigations described in this thesis are the first ones ever carried out in the Western High Atlas. The objectives of this thesis are the following:

1. The geo-electrical characterization of the deep crustal and the mantle structure of the Atlas Mountains of Morocco
 - a) Obtain isotropic and anisotropic two-dimensional (2-D) electrical resistivity models
 - b) Obtain isotropic three-dimensional (3-D) electrical resistivity models
 - c) Estimate partial melt fraction from bulk resistivity obtained through 2-D and 3-D MT inverse modelling

2. Unravelling the role of the Atlas Mountains on the evolution of the western Mediterranean
 - a) Correlation of electrical resistivity models with seismic models derived from modelling of a wide-angle reflection seismic line under the framework of SIMA (Seismic Imaging of the Moroccan Atlas) project (Ayarza et al., 2014) for characterization of deep crustal structure
 - b) Correlation of electrical resistivity models with seismic velocity models (i.e., obtained through surface-wave (Palomeras et al., 2014) and body-wave tomography (Bezada et al., 2014; Bonnin et al., 2014) for characterization of mantle structure
 - c) Test the lithospheric thinning models of Teixell et al. (2005), Zeyen et al. (2005), and Fulla et al. (2010) by employing 3-D MT forward modelling

In 2009-2010, broad-band and long-period MT data were recorded at 42 and 25 stations respectively across the Atlas Mountains of Morocco as part of the PICASSO and TopoMed projects. The TopoMed MT data were acquired by the Dublin Institute for Advanced Studies, in collaboration with University of Barcelona and University of Bari, and their processing, modelling and interpretation form the basis of this thesis. Measurements were made along two profiles: an approximately 500 km long N-S oriented 2-D profile crossing the Middle Atlas, the High Atlas and the eastern Anti-Atlas (called the MEK profile) to the east and an approximately 225 km long NE-SW oriented 2-D profile through the Western High Atlas to the west (called the MAR profile). Due to very limited road access across the Atlas Mountains, no other options were possible.

OUTLINE

In the framework of this thesis, the acquisition, analysis, 2-D isotropic and anisotropic and isotropic 3-D inverse modelling, and interpretation of the TopoMed MT data set are presented. The details of the thesis are outlined here under.

The thesis is divided into three parts, namely Introduction, Theory and Background Information (Part I), The Magnetotelluric Experiment Across the Atlas Mountains of Morocco (Part II), Discussion and Conclusions (Part III). Appendices follow.

Part I consists of two chapters: Magnetotelluric Theory, and western Mediterranean Field Area. **Chapter 2** provides an introduction to the basic theory of the MT method. Natural source fields of MT signals and the electromagnetic properties of Earth materials are discussed. MT transfer functions are introduced, and their characteristics that depend on dimensionality are reviewed. Causes and effects of distortion are also reviewed in this chapter. Lastly, the data acquisition and strategies of data processing, analysis and inversion are described. **Chapter 3** provides information about the tectonic and geological setting of the Atlas Mountains of Morocco, followed by review of previous geophysical work undertaken in the western Mediterranean.

Part II focuses on the work undertaken during this thesis. **Chapter 4** details the PICASSO/-TopoMed Project and associated data acquisition and instrumentation. This chapter also includes a brief description of data processing of the TopoMed MT data set ([Section 4.4](#)) and discussion of dimensionality and directionality of the MT data set ([Section 4.5](#)). **Chapter 5** discusses the 2-D inversion results of the MEK profile data set. The new 2-D models for crustal and lithospheric mantle are compared with three other resistivity models ([Schwarz et al., 1992](#); [Ledo et al., 2011](#); [Anahnah et al., 2011](#)). **Chapter 6** makes use of synthetic single MT profile data set in the presence of a regional 2-D structure with a strongly oblique strike direction (45°) to the adopted 3-D grid in order to examine the influence of inversion and data coordinate system in 3-D modelling. Furthermore, the influence of the model smoothing parameter of the Modular system for ElectroMagnetic inversion (ModEM; [Egbert & Kelbert \(2012\)](#) and [Kelbert et al. \(2014\)](#)) in the inversion process is explored. **Chapter 7** applies the inversion strategy used in the previous chapter to the TopoMed MT data set. 3-D inversion results of both the MAR and MEK profiles data set are presented and discussed, and compared with other available information, (i.e., geology and previous geophysical work). A brief description of the 3-D inversion code, ModEM, used in the framework of this thesis is also included in this chapter.

Part III summarizes the main contributions of this thesis to the tectonic understanding of the western Mediterranean field area and makes some brief concluding remarks and suggestions for further work.

MAGNETOTELLURIC THEORY

Magnetotellurics (MT) is a natural-source (passive) geophysical imaging technique to image the electrical conductivity structure of the subsurface, which uses the recorded time variation of natural electric and magnetic fields at the surface of the Earth. Measurement of these naturally occurring electromagnetic fields allows us to derive the vertical and lateral subsurface electrical conductivity distribution within the crust and mantle. The fundamental theory of the method was first introduced in the 1950s by [Tikhonov \(1950\)](#), and independently in more detail by [Cagniard \(1953\)](#). [Wait \(1954\)](#) and [Price \(1962\)](#) challenged the validity of the assumption, which is that the incident electromagnetic fields satisfy a plane wave approximation at the surface. More than a decade later, computer modelling studies by [Madden & Nelson \(1964\)](#) and [Swift \(1967\)](#) proved the validity of Tikhonov's model, and showed that the plane wave source assumption is valid for periods up to 10^3 s; at mid-geomagnetic latitudes it is even valid for periods up to 10^5 s ([Srivastava, 1965](#); [Swift, 1967](#)). The scalar representation of the magnetotelluric response ([Tikhonov, 1950](#); [Cagniard, 1953](#)) was inadequate in areas of lateral conductivity variation. [Neves \(1957\)](#) instead recognized the tensor nature of the relationship between the electric and magnetic fields and defined a finite-difference algorithm for solving the 2-D MT forward problem ([Chave & Jones, 2012b](#)). Since 1980s, the use of the MT method has been rapidly increasing in both academia and industry. This rapid growth of the MT technique, especially over the last decade or so, is due to: (i) the significant improvements that have taken place in MT data collection, processing, modelling (from one-dimensional to three-dimensional) and interpretation, (ii) the application of the method in areas where other exploration methods (seismics, gravity, magnetic) cannot be practically and economically applied, and (iii) the realization that MT and seismics can provide complementary information about the electrical conductivity and velocity structure of the subsurface on similar scales and resolutions ([Unsworth, 2005b](#)).

Detailed descriptions of the MT method and many technical aspects of the method can be found in textbooks devoted to electromagnetic methods in geophysics (e.g., [Kaufman & Keller, 1981](#); [Berdichevsky & Zhdanov, 1984](#); [Zhdanov & Keller, 1994](#); [Vozoff, 1991](#)). More comprehensive description of the MT theory and application principles of the method can be found in [Simpson & Bahr \(2005\)](#) and [Chave & Jones \(2012a\)](#).

This chapter will present the basic concepts of MT theory including the natural source fields and the electrical properties of the Earth's materials as well as data processing, analysis, distortion effects and strategies for handling with them, and modelling.

2.1 FROM MAXWELL'S EQUATION TO THE DIFFUSION EQUATIONS

The fundamental equations of MT theory are Maxwell's equations that describe the behaviour of both electric and magnetic fields and their interaction at any frequency:

- Gauss' Law for the electric field: The electric field (or the electric displacement $\underline{D} = \varepsilon_0 \underline{E}$) is a field with the charge density as its source. The electric displacement through a closed surface of a volume is equal to the electric charges inside the volume,

$$\nabla \cdot \underline{E} = \frac{q}{\varepsilon_0} . \quad (2.1)$$

- Gauss' Law for the magnetic field: The magnetic field is source free. There are no free magnetic charges (i.e., magnetic monopoles do not exist),

$$\nabla \cdot \underline{B} = 0 . \quad (2.2)$$

- Faraday's Law: Time variations in the magnetic field induce corresponding fluctuations in the electric field flowing in a closed loop with the axis oriented in the direction of the inducing field,

$$\nabla \times \underline{E} = -\frac{\partial \underline{B}}{\partial t} . \quad (2.3)$$

- Ampère-Maxwell's Law: The magnetic field depends on the electrical current density of free charges and the time variation of the electric displacement. The magnetic field along the edges of a surface is equal to the sum of the electric currents and the time variations of the current displacement through surface,

$$\nabla \times \underline{H} = \underline{j}_f + \frac{\partial \underline{D}}{\partial t} . \quad (2.4)$$

In the equations, \underline{E} is the electric field (in V/m), \underline{B} is magnetic induction (in T), \underline{H} is the magnetic intensity (A/m), \underline{D} is electric displacement (in C/m²), q is the electric charge density owing to the free charges (C/m³), \underline{j}_f is the electric current density owing to free charges (A/m²), and ε_0 is the electrical permittivity of free-space and is equal to 8.854×10^{-12} F/m. In addition, the quantities are linked by the constitutive relations:

$$\underline{B} = \mu_0 \mu_r \underline{H} = \mu \underline{H} \quad (2.5)$$

$$\underline{D} = \varepsilon_0 \varepsilon_r \underline{E} = \varepsilon \underline{E} \quad (2.6)$$

and

$$\underline{j} = \sigma \underline{E} \quad (2.7)$$

where ε_r is the relative electric permittivity, μ_0 is the magnetic permeability of the free-space ($\mu_0 = 1.2566 \times 10^{-6}$). According to Ohm's law, electric current density \underline{j} can be defined by Equation 2.7 where σ is the electrical conductivity (in S/m) which is the inverse of the resistivity ρ (in Ωm).

2.2 THE ASSUMPTIONS OF THE MT METHOD

There are a number of simplifying assumptions that are applied when considering electromagnetic induction in the Earth. These assumptions have been discussed in several publications (e.g., Cagniard, 1953; Price, 1962; Vozoff, 1991; Simpson & Bahr, 2005) and are summarized below (modified from Simpson & Bahr (2005)):

- i Maxwell's equations are obeyed.
- ii The Earth does not generate electromagnetic energy, it only absorbs or dissipates it.
- iii Away from their sources, all fields may be presumed to be conservative and analytic.
- iv The electromagnetic source fields utilised by the MT method may be treated as being uniform, plane-polarised electromagnetic waves, which are generated at a relatively distant source and have near-vertical angle of incidence to the Earth's surface. This is commonly known as the plane wave assumption and may be violated in polar and equatorial regions.
- v No accumulation of free charges is expected to be sustained in a layered Earth. However, in a multi-dimensional earth (2-D or 3-D), non-inductive static shift effects can be caused by charges that are accumulated and dissipated along conductivity discontinuities.
- vi The Earth behaves as an ohmic conductor, and charge is conserved, i.e., $\underline{j} = \sigma \underline{E}$ and $\frac{\partial \rho}{\partial t} + \nabla \cdot \underline{j} = 0$, where \underline{j} is the total electric current density, ρ is the charge density, σ is the conductivity of the medium, and \underline{E} is the electric field.
- vii The Quasi-stationary approximation: Time-varying displacement currents are negligible compared to the time-varying conduction currents for the period range, 10^{-5} s - 10^5 s. This approximation allows us to treat induction in the Earth as a diffusion process.
- viii Any variations in the electrical permittivities and magnetic permeabilities of rocks are negligible compared with variations in bulk conductivities of rocks.

Electromagnetic fields in the Earth must not only obey Maxwell's equations, but also the appropriate conditions to be applied at boundaries between the homogeneous regions involved in the problem. Therefore, the boundary conditions are listed below, given two regions, medium 1 and medium 2 (Ward & Hohmann, 1987):

- The normal component B_n of the magnetic field \underline{B} is continuous across an interface separating medium 1 and medium 2, i.e.,

$$B_{n1} = B_{n2} \quad . \quad (2.8)$$

- Due to accumulation of surface charge density, ρ_s , the normal component \underline{D}_n of the displacement current D , is discontinuous across an interface separating the two media, i.e.,

$$D_{n2} - D_{n1} = \rho_s \quad . \quad (2.9)$$

- The tangential component \underline{E}_t of electric field \underline{E} , is continuous across an interface separating medium 1 and medium 2, i.e.,

$$E_{t1} = E_{t2} \quad . \quad (2.10)$$

- The tangential component \underline{H}_t of magnetic field \underline{H} , is continuous across an interface separating medium 1 and medium 2 if there is no surface current, i.e.,

$$H_{t1} = H_{t2} \quad . \quad (2.11)$$

- The normal component \underline{J}_n of current density \underline{J} , is continuous across an interface separating medium 1 and medium 2, i.e.,

$$J_{n1} = J_{n2} \quad . \quad (2.12)$$

- The scalar potentials, appropriate to static fields only, V and U defined by: $\underline{E} = -\nabla V$, and $\underline{H} = -\nabla U$, are continuous across an interface, i.e.,

$$V_1 = V_2 \text{ and } U_1 = U_2 \quad . \quad (2.13)$$

Considering all of these assumptions, the modified Maxwell's Equations can be written in the frequency domain as follow:

$$-\frac{\partial \underline{B}(t)}{\partial t} = -i\omega \underline{B}(\omega) \quad . \quad (2.14)$$

Applying the assumption (vi) and Ohm's law (Equation 2.7) to Ampère-Maxwell's Law (Equation 2.4) and taking the divergence of Equation 2.4 (Note that $\nabla \cdot (\nabla \times \underline{A}) = 0$ for any vector field \underline{A}) gives

$$\mu_0 \nabla \cdot (\sigma \underline{E}) = \mu_0 (\sigma \nabla \cdot \underline{E} + \underline{E} \cdot \nabla \sigma) = 0 \quad . \quad (2.15)$$

Substituting with Gauss' Law for the electric field (Equation 2.1) gives

$$\frac{q}{\varepsilon_0} = -\underline{E} \frac{\nabla \sigma}{\sigma} \Rightarrow \frac{q}{\varepsilon_0} = -\underline{E} \nabla \ln \sigma \quad . \quad (2.16)$$

Using Equation 2.14 and Equation 2.16, and applying Equation 2.5 and Equation 2.6 and Ohm's Law (Equation 2.7), the Maxwell's Equations can be written as in the frequency domain:

$$\nabla \cdot \underline{E} = -\underline{E} \nabla \ln \sigma \quad (2.17)$$

$$\nabla \cdot \underline{B} = 0 \quad (2.18)$$

$$\nabla \times \underline{E} = -i\omega \underline{B} \quad (2.19)$$

and

$$\nabla \times \underline{B} = \mu_0 \sigma \underline{E} \quad . \quad (2.20)$$

To derive the diffusion equations in terms of the electrical and magnetic fields, the curl of Equation 2.19 and Equation 2.20 to be taken, respectively. By making use of the following proven vector field identity:

$$\nabla \times (\nabla \times \underline{A}) = (\nabla \cdot \nabla \cdot \underline{A}) - \nabla^2 \underline{A} \quad (2.21)$$

where \underline{A} is any vector field. The diffusion equation of the electrical and magnetic fields are given by:

$$\nabla^2 \underline{E} = i\omega \mu_0 \sigma \underline{E} - \nabla (\underline{E} \nabla \ln \sigma) \quad (2.22)$$

and

$$\nabla^2 \underline{B} = i\omega \mu_0 \sigma \underline{B} + \mu_0 \underline{E} \times \nabla \sigma \quad . \quad (2.23)$$

In the case of an isotropic and homogeneous half space, the conductivity σ is constant ($\nabla\sigma = 0$), and therefore diffusion equations (Equation 2.22 and Equation 2.23) simplify to

$$\nabla^2 \underline{E} = i\omega\mu_0\sigma \underline{E} \quad (2.24)$$

and

$$\nabla^2 \underline{B} = i\omega\mu_0\sigma \underline{B} \quad (2.25)$$

These second order differential equations with solutions of the form

$$\underline{E} = \underline{E}_1 e^{i\omega t - qz} + \underline{E}_2 e^{i\omega t + qz} \quad (2.26)$$

and

$$\underline{B} = \underline{B}_1 e^{i\omega t - qz} + \underline{B}_2 e^{i\omega t + qz} \quad (2.27)$$

The second term on the right-hand side increases with depth z . Since the Earth does not generate EM energy, but only dissipates or absorbs it (assumption ii), the amplitudes of \underline{E}_2 and \underline{B}_2 should be set to zero. In the case of homogeneous half space ($\frac{\partial \underline{E}}{\partial x} = \frac{\partial \underline{E}}{\partial y} = 0$), applying the solution Equation 2.26 to the left side of Equation 2.24 produces,

$$\nabla^2 \underline{E} = \frac{\partial^2 \underline{E}}{\partial z^2} = q^2 \underline{E}_1 e^{i\omega t - qz} = q^2 \underline{E} \quad (2.28)$$

therefore Equation 2.24 becomes

$$q = \sqrt{i\omega\mu_0\sigma} = \sqrt{i}\sqrt{\omega\mu_0\sigma} = \frac{\pm(1+i)}{\sqrt{2}}\sqrt{\omega\mu_0\sigma} = \pm\left(\sqrt{\frac{\mu_0\sigma\omega}{2}} + i\sqrt{\frac{\mu_0\sigma\omega}{2}}\right) \quad (2.29)$$

using

$$\sqrt{i} = \frac{\pm(1+i)}{\sqrt{2}} \Rightarrow i = \frac{(\pm(1+i))^2}{2} = \frac{1+2i+i^2}{2} = \frac{1+2i-1}{2} \quad (2.30)$$

The real part of q governs the attenuation, and the inverse of the real part is known as the frequency dependent, EM skin depth:

$$\delta = \frac{1}{\text{Re}(q)} = \sqrt{\frac{2}{\mu_0\sigma\omega}} \quad (2.31)$$

and the inverse of q is known as the Schmucker-Weidelt transfer function (Weidelt, 1972; Schmucker, 1973)

$$C = \frac{1}{q} \quad (2.32)$$

Using the assumption of a homogeneous half space and Faraday's law, the Schmucker-Weidelt transfer function establishes a linear relationship between the different electric and magnetic field components

$$-\frac{\partial E_y}{\partial z} = -\frac{\partial B_x}{\partial t} \Rightarrow qE_y = -i\omega B_x \quad , \quad (2.33)$$

$$-\frac{\partial E_x}{\partial z} = -\frac{\partial B_y}{\partial t} \Rightarrow qE_x = -i\omega B_y \quad . \quad (2.34)$$

Therefore, C also can be calculated from the electric and magnetic field components in the frequency domain

$$C = \frac{1}{q} = \frac{E_x}{i\omega B_y} = -\frac{E_y}{i\omega B_x} \quad . \quad (2.35)$$

Combining [Equation 2.34](#) and [Equation 2.35](#) with [Equation 2.29](#) yields,

$$\rho = \frac{1}{\sigma} = \frac{1}{|q|^2(\omega)} \mu_0 \omega = |C|^2 \mu_0 \omega \quad , \quad (2.36)$$

where ρ and σ are the resistivity and conductivity of a half space, respectively. Furthermore, a phase ϕ can be derived and written as

$$\phi = \tan^{-1} \frac{\Im C}{\Re C} \quad . \quad (2.37)$$

2.3 THE MAGNETOTELLURIC TRANSFER FUNCTIONS

A magnetotelluric transfer function is defined as a function that relates the measured EM fields at a given frequency. It depends only on the electrical properties of the material not the nature of the EM source. The most common MT transfer functions are represented by the impedance tensor or MT tensor and the geomagnetic transfer function. The geomagnetic transfer function is also known as the tipper or the vertical magnetic transfer function.

2.3.1 The Impedance Tensor

The impedance tensor \underline{Z} describes a linear relationship between the horizontal electric (E_x and E_y) and magnetic (H_x and H_y or B_x/μ_0 , B_y/μ_0) fields for each frequency. It is a complex second-rank tensor, frequency-dependent matrix and described as follows:

$$\begin{pmatrix} E_x \\ E_y \end{pmatrix} = \begin{pmatrix} Z_{xx} & Z_{xy} \\ Z_{yx} & Z_{yy} \end{pmatrix} \begin{pmatrix} \frac{B_x}{\mu_0} \\ \frac{B_y}{\mu_0} \end{pmatrix} \quad . \quad (2.38)$$

Weaver et al. (2000) introduced the term $\underline{\underline{M}}$, the MT tensor, which is an identical description of the transfer function, except that uses the $\underline{\underline{B}}$ instead of the \underline{H} field:

$$\begin{pmatrix} E_x \\ E_y \end{pmatrix} = \begin{pmatrix} M_{xx} & M_{xy} \\ M_{yx} & M_{yy} \end{pmatrix} \begin{pmatrix} B_x \\ B_y \end{pmatrix} . \quad (2.39)$$

Both tensors ($\underline{\underline{Z}}$ and $\underline{\underline{M}}$) are complex, and thus each matrix component contains real and imaginary parts (i.e., each component not only has a magnitude, but also a phase).

2.3.2 The Geomagnetic Transfer Function

The geomagnetic transfer function, also known as the tipper vector, is a dimensionless quantity, which describes the relationship between the horizontal and the vertical magnetic field components:

$$H_z = (T_x, T_y) \begin{pmatrix} H_x \\ H_y \end{pmatrix} . \quad (2.40)$$

The geomagnetic transfer function is commonly represented as induction arrow, the concept of which was first introduced by Parkinson (1959), Parkinson (1962) and Wiese (1962). Induction arrows are two real, dimensionless vectors

$$\underline{T}_{\Re} = (\Re T_x, \Re T_y) \quad (2.41)$$

and

$$\underline{T}_{\Im} = (\Im T_x, \Im T_y) \quad (2.42)$$

which represent the real and imaginary parts of the geomagnetic transfer function on the xy plane. Since vertical magnetic fields are generated by lateral conductivity gradients, induction arrows can be used to infer the presence or absence of lateral variations in conductivity (Jones & Price, 1970; Jones, 1986; Simpson & Bahr, 2005). There are two conventions used for plotting the induction arrows: the Parkinson convention (Parkinson, 1959) and the Wiese convention (Wiese, 1962). The Parkinson convention, where the induction arrows point *towards* the anomalous current concentration, is more commonly used by most MT practitioners (Jones, 1986; Simpson & Bahr, 2005). The Wiese convention is opposed to the Parkinson convention, in other words, where induction arrows point *away* from the anomalous current concentration.

2.4 NATURAL SOURCE FIELDS OF MT SIGNALS

Natural electromagnetic (EM) signals are generated by different sources ranging from the core of the earth to distant galaxies and they are originated in different processes (Vozoff, 1991). In MT exploration, the period range of interest is $10^4 - 10^{-5}$ Hz. There are two important source regions for this frequency range: (i) at frequencies greater than 1 Hz, EM waves are produced by electric lightning discharge, and (ii) at frequencies lower than 1 Hz, EM waves are generated by the interactions between the solar wind and the Earth's magnetic field. The basic assumption in MT studies of the Earth's conductivity structure is that the primary field originating from the ionosphere and the magnetosphere is laterally sufficiently uniform and it is described as plane waves (Tikhonov, 1950; Cagniard, 1953). While this assumption is acceptable at mid-latitudes (geomagnetic latitudes below 50°), it is questionable near auroral or equatorial latitudes, particularly at periods longer than about a minute. For this reason, a number of theoretical (e.g., Mareschal, 1986; Osipova et al., 1989; Pirjola, 1992) and experimental (e.g., Padilha et al., 1997; Padilha, 1999; Jones & Spratt, 2002) studies have discussed the possible source effects at auroral and equatorial zones where concentrated ionospheric currents are present.

The spatial and the temporal variations of the source fields as well as their effects on MT measurements are briefly discussed in the following sections.

2.4.1 Sources in the Magnetosphere

The Earth's magnetosphere is the region which is produced by the interaction between the solar wind and earth's magnetic field (Figure 2.1), and includes the ionosphere and the atmosphere. The ionosphere, the region of relatively high conductivity, extends approximately from ~ 50 km to 1,000 km above Earth's surface and shows a strong solar-cycle dependency. It is divided into several regions designated by the letters D, E, and F (in the order of increasing elevation) and the latter region is subdivided into F1 and F2 (in the order of increasing electron density). F2 region has the greatest electron density and decreases upward out to several Earth radii (Garcia & Jones, 2002a).

There are four different types of electrical conductivities defined in the ionosphere: direct, Pedersen, Hall and Cowling conductivities. Figure 2.2b shows those conductivities based on calculated distributions of plasma densities and ion-neutral particle collisions at mid-latitudes. The definitions of the conductivities are as follows:

Direct conductivity: The conductivity in a direction parallel to both electric field \mathbf{E} , and magnetic field \mathbf{B} , which can only exist if there is a voltage drop along magnetic field-lines and generates a priori field-aligned currents.

Pedersen conductivity (σ_P): If \mathbf{E} is perpendicular to \mathbf{B} , the conductivity direction parallel to \mathbf{E} and thus perpendicular to \mathbf{B} . These currents are dissipative in the ionosphere, because $\mathbf{J} \cdot \mathbf{E} > 0$.

Hall conductivity (σ_H): It regulates the current flowing orthogonal to both the electric and magnetic fields.

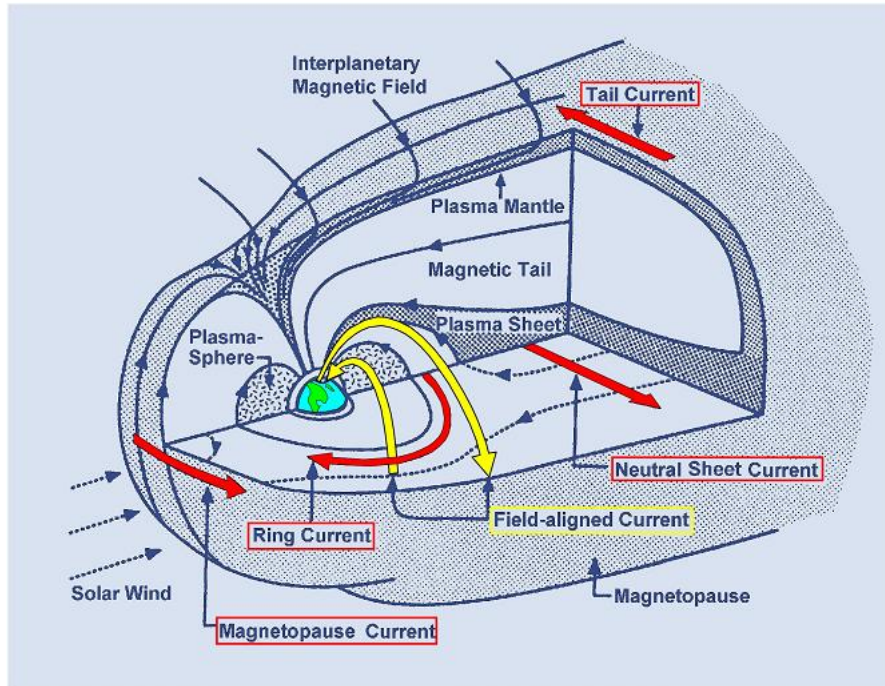


Figure 2.1.: Schematic view of the Earth's magnetosphere; *from* (Lapenta, 2011).

Cowling conductivity (σ_C): Close to the equator, the geomagnetic field is nearly horizontal so that the current density in the direction perpendicular to the geomagnetic field is determined by the Cowling conductivity (Viljanen, 2012). The Cowling conductivity is larger than Pedersen and Hall conductivities and in the case of the electrojet, it can be given by the following equation

$$\sigma_C^2 = \sigma_P^2 + \sigma_H^2 . \quad (2.43)$$

A list of the contributing signals together with their characteristics and sources are summarized in Table 2.1 and their detailed descriptions are given in the following subsections.

Table 2.1.: Classification of geomagnetic fluctuations reproduced from (Schmucker, 1985) with ULF part updated from (McPherron, 2005). **A**: Peak-to-peak amplitude or maximum departure from undisturbed level; **ERC**: equatorial ring current in the radiation belt of the magnetosphere; **EEJ**: equatorial electrojet; **PEJ**: Polar electrojet; **a**: auroral zone latitudes; **m**: mi-latitudes; **l**: low latitudes; **dd**: dip equator region on the day-side.

Type	Symbol	Period	A (nT)	Source
Solar cycle variations		11 years	20	ERC modulation by sunspot cycle
Annual variations		1 year	5	Ionospheric sources

continued on next page

Table2.1 – continued from previous page

Type	Symbol	Period	A (nT)	Source
Semi-annual variations		6 months	5	ERC modulation within the earth's orbit around the sun
Smoothed storm-time variations				Enhanced ERC after magnetic storms
storm-time-dependent part	Dst	2 - 27 days	100	
disturbance level time inequality	DS	12 - 24 h	100	
Solar daily variations	S			Ionospheric current
on quiet days	Sq	1 day	30 - 60 (m,l)	loops on day-side
	EEJ	1 day	60 - 120 (dd)	sectors of the both
enhancement on disturbed days	S_D	1 day	10 - 20	hemispheres
Lunar daily variation	L	1 lunar day	1 - 3	Dual ionospheric current loops on both hemispheres
Polar magnetic storms and short-lived substorms	DP			Polar electrojet PEJ in the ionosphere
centre of disturbance in the night-time auroral zone	DP1	10 mn - 2 h	1000 (a) 100 (m,l)	with connecting field-aligned
with correlated irregular variations in low latitudes	DP2	10 mn - 2 h	100 (a) 10 (m,l) 100 (dd)	currents to plasma regions of the magnetosphere
Special effects connected to polar magnetic storms				see DP1
bays = substorms as observed in mid-latitudes	b	30 mn - 2 h	20 - 100 (a,m) 5 - 25 (l)	

continued on next page

Table2.1 – continued from previous page

Type	Symbol	Period	A (nT)	Source
Solar flare effect	sfe	10 - 20 mn	10	Short-lived enhancement of Sq currents in the ionosphere
Sudden storm commencement	ssc	2 - 5 mn	10 - 100	Impact of intense solar particle stream on magnetopause
Ultra Low Frequency pulsations	ULF	0.2 - 600 s		Standing and propagating
regular continuous pulsations	Pc5	150 - 600 s	100 (a) 10 (m)	hydromagnetic waves in the magnetosphere
	Pc4	45 - 150 s	2	
	Pc3	10 - 45 s	0.5	
	Pc2	5 - 10 s	0.5	
	Pc1	0.2 - 5 s	1	
irregular transient pulsations	Pi2	45 - 150 s	1	
	Pi1	1 - 45 s	1	
Schumann resonance oscillations		1/7.8 s	<0.1	Cavity resonance earth-ionosphere for electromagnetic waves
Extra Low Frequency emissions	ELF	10^{-3} - 0.2 s	<0.1	Propagating electromagnetic waves in the earth-ionosphere wave guide (ELF) and propagating hydromagnetic waves in the magnetosphere (VLF and ELF)

continued on next page

Table 2.1 – continued from previous page

Type	Symbol	Period	A (nT)	Source
Very Low frequency Emissions, including whistlers	VLF	$10^{-5} - 10^{-3}$ s		

Solar daily variations (S)

Solar daily variations are defined as regular variations in local mean solar system (Schmucker, 1985). Below, their definitions are briefly summarized.

Quiet solar (S_q) variations; Solar disturbance daily (S_D) variations; equatorial electrojet: They are mainly generated by the currents in the E region of the Earth's ionosphere (Figure 2.2). The S_q current system consists of two loops confined within the dayside of the hemisphere, the northern loop being counter clockwise and the southern one being clockwise with the foci around 35° magnetic latitude and about 11 hours longitude (Figure 2.3). The variations in S_q currents are associated with solar activity cycle, seasonal/hemispherical differences, 27-day cycle as well as due to solar flare are considered to be due to the changes in E layer ionization density caused by the changes in the solar ionizing radiations (Rastogi, 1992). The size of S_q variations changes from maximum peak-to-peak amplitudes of 60 nT in the summer to minimum amplitudes of 20 nT in the winter (Schmucker, 1985). The variation S_D is part of the disturbance variation, D. The equatorial electrojet is the intense eastward current flow centred at the magnetic equator in the E-region (Figure 2.2) of the ionosphere about 600 km wide. It is the result of the abnormal enhancement in the S_q variation caused by the differential mobility ions which in turn cause the vertical Hall polarization field to generate eastward currents normal to the electric and magnetic fields (Rastogi, 1992). Changes in the equatorial electrojet and associated effects originate at the magnetosphere due to the interaction of solar wind with interplanetary magnetic fields (Rastogi & Iyer, 1976). Sizova (2002) showed that part of the geomagnetic field variations at the equator can be associated with the auroral electric fields and that Inter-planetary Magnetic Field and the H-component variations are interrelated. Furthermore, the electric fields from field aligned currents penetrate to equatorial regions resulting in H-component variations at the magnetic equator.

Lunar (L) daily variations

Lunar daily variations result from lunar tides in the ocean and atmosphere. In comparison with S_q , L variations have very small amplitude (maximum peak-to-peak amplitudes are 3 nT), so it is very difficult to notice them in the magnetic records (Schmucker, 1985).

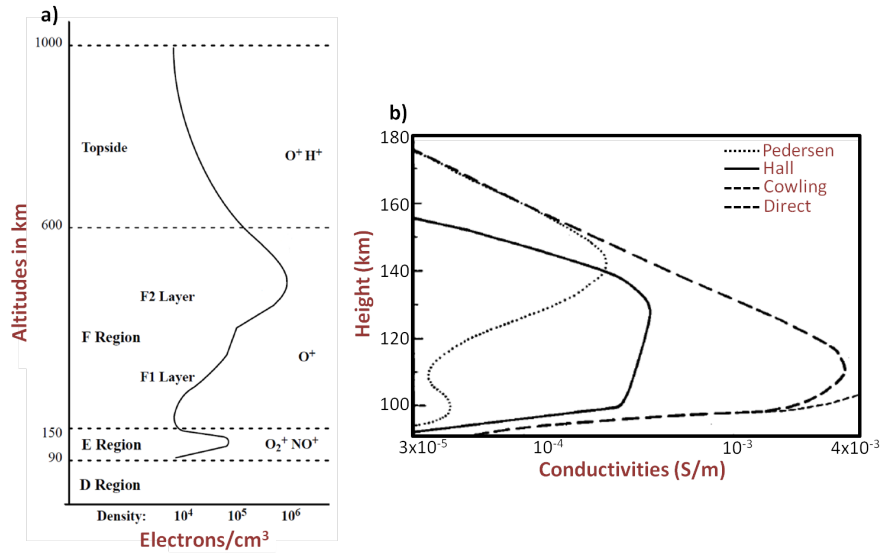


Figure 2.2.: (a) The layers of the ionosphere with their electron density and predominant ion populations; modified from Andersen & Fuller-Rowell (1999). (b) Electrical conductivities based on typical day-time ionosphere (Parkinson, 1983).

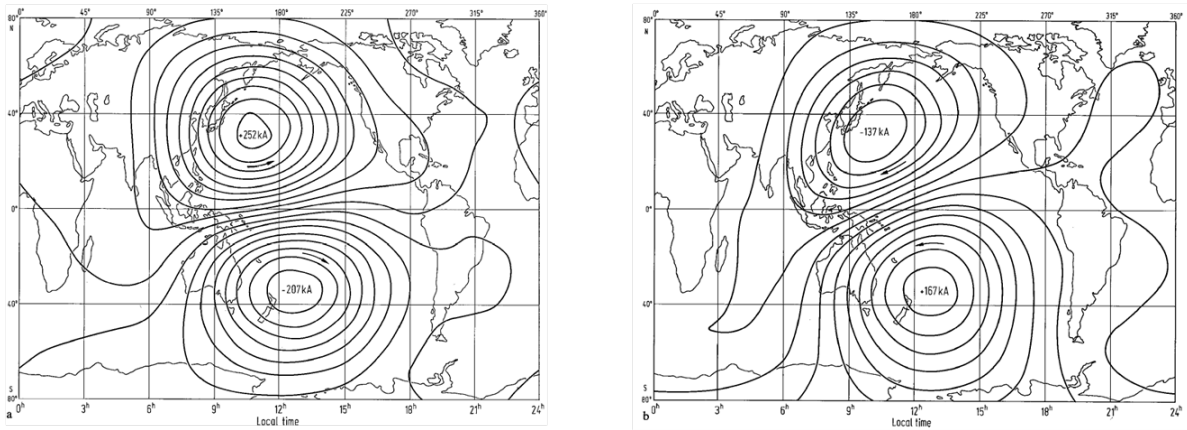


Figure 2.3.: Equivalent currents of solar daily variations S_q on quiet days. The magnetic field of these currents reproduce the mean global S_q field for September equinoxes 1957/1958: for the external part (on the left) and for the internal part (on the right). Total current is given by the numbers while the flow direction is shown by the arrows; from Schmucker (1985).

Magnetic storms (D)

Magnetic storms are the strongest geomagnetic variations caused by the Sun, producing 50-300 nT changes in the Earth's magnetic field at the equator. They start when enhanced energy transfer from the interplanetary magnetic field (IMF) of the solar wind into the magnetosphere leads to an intensification of the magnetospheric ring current at distance of 3 - 8 R_E (Viljanen, 2012). Storms can be divided into three main phases, initial, main and recovery phases, respectively. The initial phase can be represented by a sudden change called a *storm sudden commencement* (ssc) which marks the beginning of a geomagnetic storm or an increase activity lasting at least an hour. The main phase lasts from half an hour to several hours, and the horizontal component of geomagnetic field reaches its maximum decrease. Storms end with a slow recovery phase which may last from tens of hours to a week.

D_{st} is a geomagnetic index which has been introduced to characterize the worldwide magnetic storm levels on an hourly basis since 1957 (Sugiura, 1964, 1991). It is constructed by averaging the horizontal component of the geomagnetic field by using low- and mid-latitude magnetograms. The D_{st} index responds most strongly to the ring current and the magnetopause current (Burton et al., 1975; Rangarajan, 1989).

Polar magnetic storms and sub-storms; auroral electrojet

McPherron (1979) defines a sub-storm as "a transient process initiated on the night side of the Earth, in which a significant amount of energy derived from the solar wind magnetosphere interaction, is deposited in the auroral ionosphere and in the magnetosphere." The sub-storm is characterized by three phases: growth, expansion, and recovery (Akasofu, 1968; McPherron, 1970). The sub-storm starts with a growth phase when the energy transfer from the solar wind to the magnetosphere is enhanced. This happens when IMF B_z component turns negative. Part of the solar wind energy flows directly through the magnetosphere and part of it is stored in the form of magnetic energy in the lobes of the magnetotail. The sub-storm expansion phase starts with an onset, where the westward electrojet intensifies rapidly and the whole auroral oval expands poleward and equatorward. At the end of the expansion phase, the westward electrojet reaches its maximum and begins to recover toward the quiet-time level. During the recovery phase, the magnetosphere returns back to its quiet-time state (Tanskanen, 2002).

Ultra low frequency waves; Pc disturbances

Ultra low frequency (ULF) waves incident on the Earth are produced by processes in the magnetosphere and solar wind. These processes produce a wide variety of ULF hydromagnetic wave types that are classified on the ground as either Pi (irregular) or Pc (continuous) pulsations (McPherron, 2005).

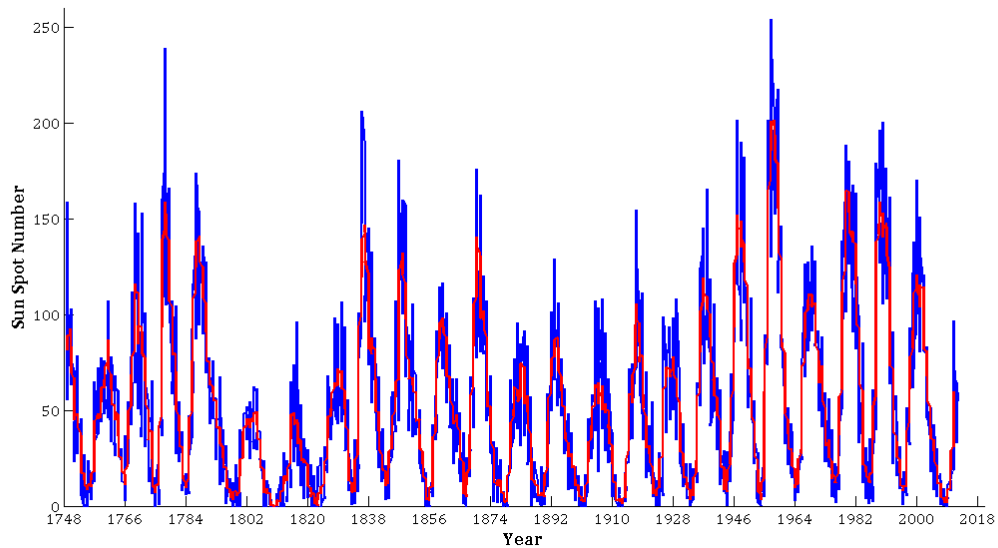


Figure 2.4.: Monthly (blue) and monthly smoothed (red) sunspot numbers since April 1749 till May 2012; Data obtained from the Solar Influence Data Analysis Center (SIDC), Royal Observatory of Belgium

Solar cycle variations

In the long time trend of the earth's magnetic field over years the modulation of geomagnetic activity with the sunspot cycle produces regular solar cycle variations with a fundamental period of 11 years (Schmucker, 1985). Sunspots are dark regions on solar disk with magnetic field strengths greater than 1500 gauss. During the period from 1645 to 1715, the sun entered a low activity known as the 'Maunder Minimum'. Figure 2.4 shows the monthly sunspot numbers since January 1749 till May 2012. We are currently over the minimum of the twenty-third 11 year cycle.

2.4.2 Sources in the Atmosphere – lightning activity

In the previous sections origin of the long period variations (>1 s) are discussed. At shorter periods (<1 s), natural source time-varying EM waves are originated from the distant lightning activity and these waves propagate within the Earth-ionosphere waveguide whose properties show diurnal, seasonal and 11 year solar cycle fluctuations (Garcia & Jones, 2002a). Distant lightning activity can be classified in two frequency bands ranging from 7.8 Hz to 1 kHz and 5 kHz to 30 kHz. The frequency range of 1 - 5 kHz characterizes the *AMT dead band*, where significant signal amplitude attenuation occurs that are caused by those temporal fluctuations (Garcia & Jones, 2002a). Sferics are defined as the impulse or wavelet characterizing the return-stroke of lightning. Sferics having origins in the equatorial regions propagate around the world within a waveguide bounded by ionosphere and the Earth's surface. The Earth-ionosphere cavity enables electromagnetic resonances

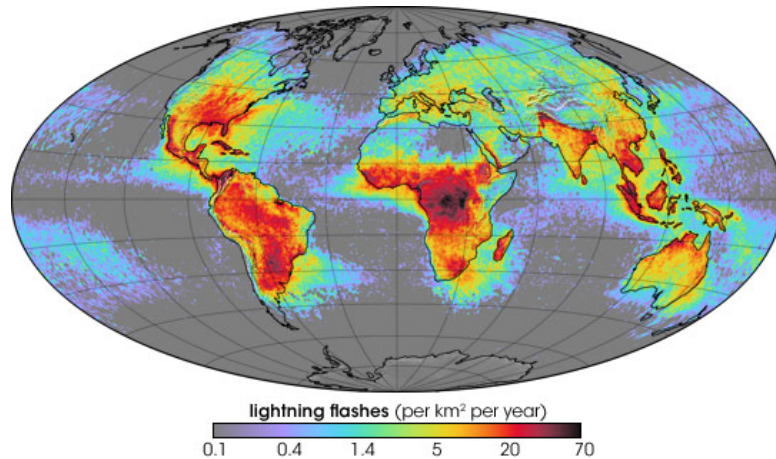


Figure 2.5.: Figure showing the distribution of lightning flashes around the world; *from NASA*

called Schumann resonances which is mainly excited by the lightning discharges. The fundamental mode of the Schumann resonances is 7.8 Hz (Garcia & Jones, 2002a), which defines the upper limit of the MT dead band (Vozoff, 1991). The Schumann resonances' fundamental mode and its multiples belongs to the extremely low frequency (ELF) band of the Earth's EM field spectrum. The very low frequency (VLF) emissions take part in the highest frequencies EM spectrum (extends up to 30 kHz) and cover lightning impulses as well as wavelets, which propagates through the magnetosphere and ionosphere (Schmucker, 1985). During sferics' travel time away from the Earth, they undergo dispersion through the ionosphere and magnetosphere, before returning to the Earth along magnetic field lines. These dispersed lightning impulses are observed at the Earth's surface as whistlers in the VLF spectrum (Schmucker, 1985). Figure 2.5 shows the distribution of lightning flashes around the world. The highest lightning activity is localized around the tropics. Sferics are absorbed in the D layer and disappear during the nighttime. Furthermore, lightning activity will vary from summer to winter in each hemisphere. Due to presence of major lightning activity and the less attenuation of atmospheric electric field, AMT data recordings should be made during the nighttime and the summer months in order to obtain high quality AMT data.

2.4.3 Source Field Effects on MT Responses

Low-latitude zones

Padilha et al. (1997) considered the source effects due to the presence of EEJ in a broad-band MT survey of 8 sites distributed along a 1,000 km profile across the dip equator, in central part of South America. The high quality MT data were collected between the period range of 0.0006 - 2,048 s during both daytime (in the presence of the EEJ) and nighttime (in the absence of the EEJ). What the authors observed that there were no significant differences between the daytime and nighttime soundings. Besides this, they demonstrated that the usual plane wave approach

can provide reliable subsurface conductivity structures, at least in this region up to periods of 2000 s. The authors compared the observed data with the response of non-uniform source models (line current and Gaussian model) and uniform source model (plane wave). The modelling results showed that a line current model generates departures from the results of plane wave modelling that were not observed in practice, and that a Gaussian model agreed with the data up to 1,000 s when the most conductive limit was considered. On the other hand, both non-uniform source model responses showed deviations from the observed data after the period of 100 s when the most resistive limit was considered.

Additional to this study, Padilha (1999) used the magnetic data obtained from four temporary stations, which were in the same region of the previously described broad-band MT survey (Padilha et al., 1997), and two near-equatorial and mid-latitude permanent observatories. It was observed that the amplitude of the geomagnetic variations was horizontally uniform within the interval of $\pm 3^\circ$ of geomagnetic latitude, indicating that the primary field in the analyzed period range (0.0001 - 2,048 s) satisfied the plane wave criterion. As a result of theoretical modelling, source effects would just appear at periods longer than 1,000 s (resistive regions) and 10,000 s (conductive regions).

High-latitude zones

Garcia et al. (1997) examined long-period MT data from northern Canada acquired during September and October, 1994. The data were influenced by auroral electrojet and especially by auroral episodes. They observed that the largest effect on the estimate of MT impedance tensor was during interval of highest magnetic activity during the local nighttime. To extract stable uniform field impedance estimates, the data were processed using a robust processing algorithm. A non-robust processing algorithm was also applied to the entire data set. The non-robust processing results using all of the data were controlled by the nighttime data, which were dominated by non-uniform source effects. The authors showed that the non-robust method failed to recover a useful result from all of the daytime data. The robust processing results using all the data and only daytime data provided that the fraction of auroral activity was not large. The strongest bias in the response function was observed during the initial quarter of an auroral event.

Jones & Spratt (2002) introduced a simple technique using the vertical component of the magnetic field time series in order to identify intervals of low contamination by auroral sources. Times were chosen when the variations stay within prescribed limits defined on the basis of a histogram of the variations for the whole recording interval. The authors highlighted that the local source distortion associated with the polar electrojet can lead to an increase in apparent resistivity responses and a decrease in phase responses at longer periods, and will then cause misinterpretation of the resulting models (i.e., an underestimated lithosphere-asthenosphere boundary (LAB) depth).

Lezaeta et al. (2007) studied the spatial variation of source field effects on magnetic fields from long-period MT and GDS data due to the presence of auroral currents. The high quality MT and GDS responses were obtained between the period range of 80 and 2,000 s. Principal component

(PC) analysis was applied to the power spectral density matrix of the magnetic field components. It was demonstrated that the power spectra of the magnetic fields over monthly and daily intervals have maxima during summer time at periods over 1,000 s. It was observed that the geomagnetic north component was dominant by one or two orders of magnitude with respect to east component at long periods. In contrast, short period power spectra have east components that are as large as the north ones. This observation was interpreted as it may be the reflection of 2-D nature of ionospheric currents related to geomagnetic pulsations and other rapid variations, where no preferred direction of the horizontal current flow prevails.

2.5 ELECTRICAL PROPERTIES OF EARTH MATERIALS

2.5.1 *Electrical Conductivity*

Electrical conductivity σ is the measure of the ability for a material to conduct electrical current. The electrical conductivity, or reciprocal resistivity, of a rock contains information about its composition and structure. In order to understand the conductivity of crustal and upper mantle rocks, it is first necessary to consider the conductivity of minerals that make up these rocks (Unsworth & Rondenay, 2012). Of all the physical properties of rocks and minerals, such as density, elastic wave velocity, and radioactive content, the electrical conductivity is the one that varies over orders of magnitude. For example, while the electric conductivity of metallic minerals are 10^5 S/m, that of close-grained rocks, like gabbro as large as 10^{-6} S/m (Telford et al., 1990). The SI unit of electrical conductivity is Siemens/meter (S/m) and that of electrical resistivity is ohm-meters (Ωm).

The electrical resistivity of a pure mineral depends on two factors: (1) the density of charge carriers, typically electrons and ions and (2) the ease with which these charge carriers can move through the mineral (mobility). An extreme example is Cu, which has a very high density of charge carriers (electrons) that are weakly attached to atoms in a lattice and move very easily, resulting in a very high conductivity (low resistivity, $\rho = 10^{-10}$ Ωm). In contrast, in diamond the C atoms are too rigidly attached to the crystal to carry electric current. This makes the electric resistivity of diamond very high, typically more than 10^{10} Ωm .

There are four different electrical charge transport processes within rocks and minerals, which are presented in the following section.

2.5.2 *Electrical Charge Transport Mechanisms*

Electrolytic conduction

Within the upper crust, most rocks exhibit a porous and fissured structure which is partially or totally filled with fluid electrolytes. Electrolytic conduction is the dominant electrical charge transport mechanism in these rocks. The mechanism in those fluid saturated rocks depends on composition,

microstructure and interfacial effects. While the first term determines the bulk properties of the constituents, microstructure considers the geometrical arrangement of the constituents. The last term, interfacial effects, are due to mineral/fluid interactions which forms the electrochemical double layer (DL). This layer has a significant effect on the clay bearing rocks and in low-porous, low-permeable rocks (Nover, 2005). In this case, the bulk conductivity of a rock can be characterized by a sum of three different conductivities:

$$\sigma_{bulk} = \sigma_f + \sigma_m + \sigma_s \quad (2.44)$$

where σ_f is the electrolyte conductivity, σ_m is the matrix conductivity of the rock forming minerals and σ_s is the surface conductivity caused by polarisation of ions or hydrated ions at the inner surface of the pore system.

Electronic conduction

In the presence of interconnected highly conducting phases such as graphite and ores, in a rock matrix, electronic conduction enhances the electrical conductivity by orders of magnitude. The conductivity of this system simply obeys Ohm's law (Equation 2.7). The conductivity of rock depends on the degree of interconnection and the specific conductance of the metallic conducting phases (Nover, 2005). Graphite is commonly suggested as a contributor to continental crust and lithospheric mantle level conductors, particularly in sheared zones (faults, planes and so forth). Depending on the shear direction, high conductivities in the crustal shear zones can also be interpreted as a result of presence of electrical anisotropy (Evans, 2012; Wannamaker et al., 2008). Using the upper bound formula of Hashin & Shtrikman (1962), Duba & Shankland (1982) calculated that a volume fraction of graphite of only 5×10^{-6} is needed to enhance the bulk conductivity to values ~ 0.1 S/m.

Semiconduction

Temperature-induced semiconduction is the dominant transport mechanism at lower crustal and upper mantle pressure and temperature conditions. At room temperature, most rock forming minerals are poor conductors and thus the electrical conductivity of those rocks are low. However, with increasing temperature, the mobility of lattice defects and impurities (e.g., hydrogen, ferric iron) will be enhanced, and thus semiconduction will take place. The conductivity of a pure mineral depends on both the density of the charge carriers and the mobility of those charge carriers (Nover, 2005).

Since the temperature-induced semiconduction depends on temperature, pressure and oxygen fugacity, the bulk conductivity of the minerals in the mantle can be described by the solid-state Arrhenius equation:

$$\sigma = \sigma_0 \exp\left(\frac{-E_a - P\Delta V}{k_B T}\right) \quad (2.45)$$

where σ_0 is a pre-exponential factor (S/m), E_a is the activation energy (J/mol), P is the pressure (MPa), ΔV is the activation volume (cm^3/mol), k_B is the Boltzmann constant (1.38×10^{-23} J/K), and T is the temperature (K) (Nover, 2005; Pommier et al., 2008; Yoshino, 2010).

Partial melts

Charge transport related to partial melts occurs in high temperature gradient areas or at greater depths in the Earth's mantle where the temperatures are sufficiently high to form a melt phase (Nover, 2005). The temperature at which partial melts may form depends on not only the presence of hydrous mineral phases or the presence of free water, but also the chemistry of the rocks. Partial melts are often thought to be responsible for the high conductivity anomalies observed in the lower crust and uppermost mantle (e.g., Park et al., 1996; Türkoğlu et al., 2008; Le Pape et al., 2012). In a partially molten rock, the electrical conductivity of the melt phase is much higher than the surrounding solid rock. Once an interconnected network of melt is formed, the overall conductivity of the rock is enhanced by several orders of magnitude (e.g., Shankland & Waff, 1977; Schilling et al., 1997; Roberts & Tyburczy, 1999; Partzsch et al., 2000).

The electrical conductivity in amorphous silicates (glasses and melts) is mainly controlled by the ionic mobility which is related to diffusive transport of charge carriers within the melt and can be expressed by the following Nerst-Einstein equation:

$$\sigma_i = \frac{D_i q_i^2 N_i}{k_B T H_r} \quad (2.46)$$

where D_i is the coefficient of diffusion of a ion i (m^2/s), q_i is its charge (C), N_i is the concentration of i (m^{-3}), k_B is the Boltzmann constant (1.38×10^{-23} J/K), T is the temperature (K), and H_r is the Haven ratio characterizing the ion migration mechanisms into the melt (Pommier et al., 2008).

2.5.3 Two-Phase Mixing Systems

The overall conductivity of a rock is dominated by the conductivities of available fluid phases (aqueous fluids and partial melts), the amount of fluid phases, and their geometric distribution within the rock matrix. Based on geometrical considerations, numerous two-phase mixing geometrical models have been proposed to calculate the effective conductivity (σ_{eff}) of a partially molten rock sample as a function of the melt fraction (X_m), conductivity of the solid phase (σ_s) and conductivity of the melt phase (σ_m). Most commonly used solid-fluid mixing geometrical models for electrical

conductivity are summarized in [Table 2.2](#) after [ten Grotenhuis et al. \(2005\)](#) and [Partzsch et al. \(2000\)](#).

[Hashin & Shtrikman \(1962\)](#) defined the upper and lower boundaries of the effective conductivity of a two-phase medium as

$$\sigma_f + (1 - \phi) \left(\frac{1}{(\sigma_s - \sigma_f)} + \frac{\phi}{3\sigma_f} \right)^{-1} > \sigma_{eff} > \sigma_s + \phi \left(\frac{1}{(\sigma_f - \sigma_s)} + \frac{(1 - \phi)}{3\sigma_s} \right)^{-1} \quad (2.47)$$

where σ_f is the most conductive material, ϕ is the volume fraction of the conductive material. While the Hashin-Shtrikman upper bound, which is denoted HS+ ([Table 2.2](#)), describes the case that the conductive material is perfectly interconnected, the lower bound, denoted HS-, describes the case that conductive material is confined within isolated pockets ([Simpson & Bahr, 2005](#); [ten Grotenhuis et al., 2005](#)).

Under crustal (brittle) conditions, the electrical conductivity of rock depends on the volume fraction of pore fluid and its degree of connectivity ([Evans, 2012](#)). An empirical expression, which relates fluid phase conductivity to bulk conductivity, is given by

$$\sigma_{eff} = A\sigma_f\phi^{-m} \quad (2.48)$$

where σ_f is the fluid phase conductivity, ϕ is the porosity and A and m are Archie's law empirical coefficients. A is commonly used to describe the degree of saturation and m defines the degree of interconnection of pore fluid. A value of 1 (i.e., $m = 1$) reflects good interconnection with crack shaped pores while $m = 2$ implies poor interconnection with spherical shaped pores. Values $1.5 < m < 2.5$ are common for sedimentary rocks containing saline aqueous fluids in upper crustal basins ([Glover et al., 2000](#)), and also values of 2 - 3 are not uncommon for crustal rocks (e.g., [Evans et al., 1994](#)).

Using Archie's law, which is in the form of [Equation 2.52](#) (in [Table 2.2](#)), [ten Grotenhuis et al. \(2005\)](#) found that the electrical conductivity of partially molten olivine samples is best described with the Archie's law with parameters $C = 1.47$ and $n = 1.30$ (C and n are used in the place of A and m , respectively).

Table 2.2.: Summary of different geometric models to describe melt distribution; σ_{eff} = effective conductivity, X_m = melt fraction, σ_m = fluid phase conductivity, C and n = Archie's law empirical coefficients, β = partitioning between tube and cube distribution; *after ten Grotenhuis et al. (2005) and Partzsch et al. (2000)*.

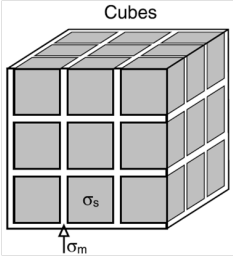
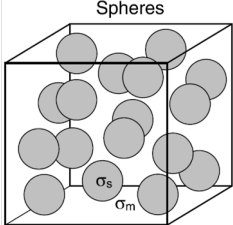
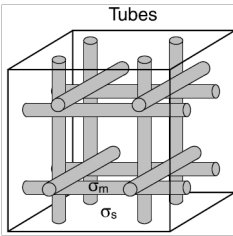
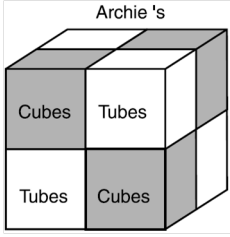
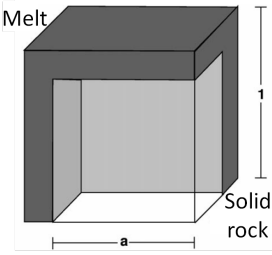
Melt distribution	Description
	<p>In this model, cubic grains with a low conductivity are all the same size and are surrounded by a high conductivity melt layer of uniform thickness (Waff, 1974). This model represents the case that melt is distributed in layers along the grain boundaries. The effective conductivity is given by</p> $\sigma_{eff} = (1 - (1 - X_m)^{\frac{2}{3}})\sigma_m \quad (2.49)$
	<p>In this model, the spherical grains are isolated from each other by the melt, so this model is representative for melt distributed along grain boundary and filling triple junctions. The sphere model is usually called Hashin-Shtrikman upper bound(HS+) or Maxwell model, (Hashin & Shtrikman, 1962).</p> $\sigma_{eff} = \sigma_m + \frac{(1 - X_m)}{1/(\sigma_s - \sigma_m) + X_m/3\sigma_m} \quad (2.50)$ <p>The Hashin-Shtrikman lower bound (HS-) represents a model in which spheres represent isolated pockets of melt in a more resistive matrix.</p>
	<p>In this model, the melt is assumed to be distributed in equally spaced tubes with a rectangular network. The model is representative for melt distributed in a network along the triple junctions, but with unwetted two-grain junctions (Grant & West, 1965; Schmeling, 1986). The effective conductivity is given by</p> $\sigma_{eff} = \frac{1}{3}X_m\sigma_m + (1 - X_m)\sigma_s \quad (2.51)$

Table 2.2.: Continued from previous page.

Melt distribution	Description
	<p>In this model, the melt connectivity changes with the melt fraction (Watanabe & Kurita, 1993), and it is written by</p> $\sigma_{eff} = CX_m^n \sigma_m \quad (2.52)$ <p>It can also be considered as a mixture between the Tubes and Cubes or Spheres models and can be determined by the following equation:</p> $\sigma_{eff} = \sigma_{tubes}^{1-\beta} * \sigma_{cubes}^{1-\beta} \quad (2.53)$
	<p>In this model a resistor network approximates melt films on the surfaces of a cube. The lengths of the edges of the entire cube are set equal to one. A smaller solid cube with edge length a is located in the center of the entire cube. The melt films are interconnected through the faces of the cube. The effective conductivity is given by the following equation, (Partzsch et al., 2000):</p> $\sigma_{eff} = \frac{1}{\frac{1-a}{\sigma_m} + \frac{a}{\sigma_m(1-a^2) + \sigma_s a^2}} \quad (2.54)$ <p>with $a = (1 - X_m)^{\frac{1}{3}}$.</p>

Moreover, a simple model for a two-phase mixing medium can be represented with a stack of layers with two conductivities, σ_1 and σ_2 with respective volume fractions (ϕ). Conduction perpendicular and parallel to the layers gives the familiar parallel and series conduction relations (Evans, 2012):

$$\sigma_{eff}^{series} = \left(\frac{\phi}{\sigma_1} - \frac{(1-\phi)}{\sigma_2} \right)^{-1} \quad (2.55)$$

$$\sigma_{eff}^{parallel} = \phi\sigma_1 + (1-\phi)\sigma_2 \quad (2.56)$$

2.6 DIMENSIONALITY

2.6.1 The 1-D Earth

For a one-dimensional, isotropic layered Earth (i.e., the conductivity changes only with depth), the diagonal components (Z_{xx} and Z_{yy}) of the impedance tensor, which are related to the horizontal electric and magnetic fields, are zero. Since there are no lateral conductivity variations, the off-diagonal components (Z_{xy} and Z_{yx}) are equal, but of opposite sign to preserve the right-hand rule. Thus, the impedance tensor for 1-D Earth can be presented by:

$$\underline{Z}_{1-D}(\omega) = \begin{pmatrix} 0 & Z_{xy}(\omega) \\ -Z_{xy}(\omega) & 0 \end{pmatrix} . \quad (2.57)$$

Applying the 1-D assumption of the impedance tensor to [Equation 2.38](#) yields

$$\begin{pmatrix} E_x \\ E_y \end{pmatrix} = \begin{pmatrix} 0 & Z_{xy} \\ Z_{yx} & 0 \end{pmatrix} \begin{pmatrix} \frac{B_x}{\mu_0} \\ \frac{B_y}{\mu_0} \end{pmatrix} \quad (2.58)$$

or, written as components,

$$E_x = \frac{1}{\mu_0} Z_{xy} B_y \quad \text{and} \quad E_y = -\frac{1}{\mu_0} Z_{yx} B_x . \quad (2.59)$$

Solving those equations for Z_{xy} gives

$$Z_{xy} = \mu_0 \frac{E_x}{B_y} = -\mu_0 \frac{E_y}{B_x} . \quad (2.60)$$

This result is analogous to the Schmucker-Weidelt transfer function ([Equation 2.35](#)) and therefore can also be derived from Maxwell's Equations for the 1-D case. In the case of the Schmucker-Weidelt transfer function $C = 1/q$, whereas the impedance tensor is $Z = i\omega\mu_0/q$. Therefore, Z can be re-written as

$$Z = i\omega\mu_0 C . \quad (2.61)$$

The apparent resistivity can be written as

$$\rho_a(\omega) = \frac{1}{\mu_0\omega} |Z(\omega)|^2 = \rho_{a(1-D)} , \quad (2.62)$$

where ρ_a is defined as the average resistivity of an equivalent homogeneous half space. Since the real and imaginary parts of the impedance tensor elements have the same magnitude and are the

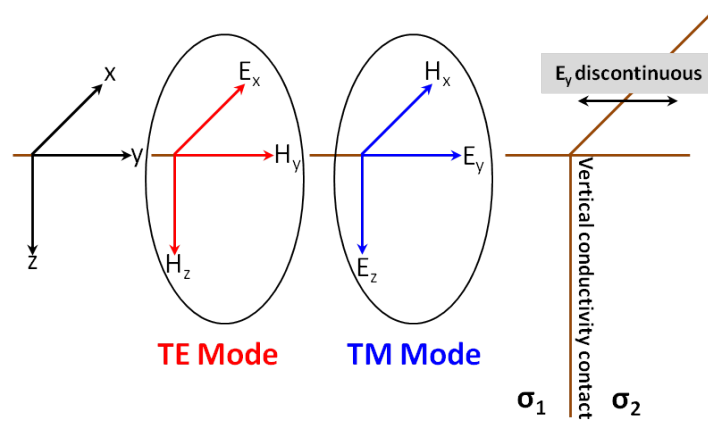


Figure 2.6.: A graphical description of a simple 2-D model composed of 2 quarters-space model, with different conductivities σ_1 and σ_2 . Due to conservation of current across the vertical discontinuity, the y-component of the electrical field E_y is discontinuous across the contact. In this ideal 2-D case, the EM fields can be decoupled into two modes, known as TE and TM modes; *redrawn and modified from Simpson & Bahr (2005)*.

same for both of the off-diagonal elements, the impedance phase is equal to 45° for all ω values for a half space.

$$\phi_{1-D}(\omega) = \tan^{-1} \left(\frac{\Im Z(\omega)}{\Re Z(\omega)} \right) . \quad (2.63)$$

2.6.2 The 2-D Earth

In the 2-D case, the conductivity not only varies with depth but also with lateral extent. Jones (1983b) explored the conditions under which structure may be treated as 2-D and when a 3-D approach is required. Requirement for 2-D or 3-D approach depends largely on the length extent of the body (L) and the skin depth of the periods of interest in the host rock (δ_h). If the ratio $\frac{L}{\delta_h}$ is far greater than 1 for the period of interest, then a 2-D interpretation of the structure should give approximately the correct conductivity structure. If the ratio is smaller than 1 (i.e., the body is too small or the period is too long), then a full 2-D interpretation will not be valid and a 3-D interpretation will be necessary. In the 2-D case, as shown in Figure 2.6, the fields do not vary in the along-strike direction (defined as the x-direction). For the ideal 2-D case, electric and magnetic fields are mutually orthogonal, with electric fields (E_x) parallel to the strike direction inducing magnetic fields perpendicular to strike (H_y , H_z or B_y , B_z), and magnetic fields (H_x or B_x) parallel to strike direction induces electrical fields in the vertical plane perpendicular to strike (E_y , E_z). Under these circumstances, Maxwell's equations can be decoupled into two modes. One mode, which describes electric currents flowing parallel to the strike direction (x direction in

Figure 2.6), is called the Transverse Electric (TE) Mode or E-Polarisation and is composed of E_x , B_y and B_z :

$$\left. \begin{aligned} \frac{\partial E_x}{\partial y} &= \frac{\partial B_z}{\partial t} = i\omega B_z, \\ \frac{\partial E_x}{\partial z} &= \frac{\partial B_y}{\partial t} = -i\omega B_y, \\ \frac{\partial B_z}{\partial y} - \frac{\partial B_y}{\partial z} &= \mu_0 \sigma E_x, \end{aligned} \right\} \text{TE mode} \quad (2.64)$$

The other mode, which describes currents flowing perpendicular to the strike direction, is called the Transverse Magnetic (TM) Mode or B-Polarisation and is composed of B_x , E_y and E_z :

$$\left. \begin{aligned} \frac{\partial B_x}{\partial y} &= \mu_0 \sigma E_z, \\ -\frac{\partial B_x}{\partial z} &= \mu_0 \sigma E_y, \\ \frac{\partial E_z}{\partial y} - \frac{\partial E_y}{\partial z} &= -i\omega B_x, \end{aligned} \right\} \text{TM mode} \quad (2.65)$$

In the ideal 2-D case, strike-aligned coordinate system, the impedance tensor can be described as:

$$\underline{\underline{Z}}_{2-D}(\omega) = \begin{pmatrix} 0 & Z_{xy}(\omega) \\ Z_{yx}(\omega) & 0 \end{pmatrix} = \begin{pmatrix} 0 & Z_{TE}(\omega) \\ Z_{TM}(\omega) & 0 \end{pmatrix}. \quad (2.66)$$

Since the electric components are related to orthogonal magnetic components only (and vice versa), the diagonal elements are zero. The off-diagonal elements (Z_{xy} and Z_{yx}) represent essentially the TE and TM modes respectively. They are normally of opposite sign, and have different magnitudes. Having opposite sign results in the phase of xy in the first quadrant and the phase of yx in the third quadrant (if a positive time dependency $e^{i\omega t}$ is used).

In the 2-D case, if the impedance tensor is not in the electrical strike coordinates, as is generally the case for most recorded data, the diagonal components of the impedance tensor will not be zero, and the two modes will be mixed in the tensor. However, for an ideal 2-D structure and noise-free data it is possible to rotate the impedance tensor by an angle θ around a vertical axis using a Cartesian rotation matrix $\underline{\underline{R}}_\theta$ (Equation 2.68) until the diagonal elements are zero. The impedance tensor $\underline{\underline{Z}}_{2-D}$, which is in a strike-aligned coordinate system, can be calculated as follows:

$$\underline{\underline{Z}}_{2-D} = \underline{\underline{R}}_\theta \underline{\underline{Z}}_{obs} \underline{\underline{R}}_\theta^T \quad (2.67)$$

where

$$\underline{\underline{R}}_\theta = \begin{pmatrix} \cos\theta & \sin\theta \\ -\sin\theta & \cos\theta \end{pmatrix} \quad \text{and} \quad \underline{\underline{R}}_\theta^T = \begin{pmatrix} \cos\theta & -\sin\theta \\ \sin\theta & \cos\theta \end{pmatrix} \quad (2.68)$$

are the rotation matrix (\underline{R}_θ) and its transpose (\underline{R}_θ^T), and \underline{Z}_{obs} is the impedance tensor in the observational reference frame.

2.6.3 The 3-D Earth

If the conductivity distribution changes in all directions, the problem becomes 3-D. In this case there is no angle that can reduce the diagonal elements of the impedance tensor to zero. Also decoupling into two separate modes is no longer valid. The 3-D Earth requires the determination of four elements of the full impedance tensor.

2.6.4 The Anisotropic Earth

Electrical anisotropy denotes the dependency of the electric current density ($\underline{j} = \sigma \underline{E}$) on the direction of the electric field (\underline{E}), and the direction of current is not always parallel to the electric field direction, as opposed to isotropy, which implies the electric field and the current density are always parallel (Wannamaker, 2005; Chave & Weidelt, 2012). In anisotropic problems, the electrical resistivity of a body or layer at each point is defined by a full 3×3 tensor,

$$\rho(x,y,z) = \begin{pmatrix} \rho_{xx} & \rho_{xy} & \rho_{xz} \\ \rho_{yx} & \rho_{yy} & \rho_{yz} \\ \rho_{zx} & \rho_{zy} & \rho_{zz} \end{pmatrix} \quad (2.69)$$

which is a symmetric (i.e., $\rho_{xy} = \rho_{yx}$, $\rho_{xz} = \rho_{zx}$ and $\rho_{zy} = \rho_{yz}$) for purely ohmic condition and non-negative definite tensor (Pek & Verner, 1997). The symmetric and non-negative defined conditions allow the matrix to be written as a diagonal matrix of the three principal resistivities (ρ_1 , ρ_2 and ρ_3 , all positive) and three rotation angles (Pek & Verner, 1997; Pek & Santos, 2002; Heise et al., 2006). Pek & Verner (1997) use these three rotation angles, which are anisotropy strike (α_S), dip (α_D) and slant (α_L), in the Cartesian coordinate system, to describe the anisotropic resistivity as follows:

$$\rho(x, y, z) = \underline{R}_z^T(\alpha_S) \underline{R}_{x'}^T(\alpha_D) \underline{R}_{z'}^T(\alpha_L) \begin{pmatrix} \rho_1 & 0 & 0 \\ 0 & \rho_2 & 0 \\ 0 & 0 & \rho_3 \end{pmatrix} \underline{R}_{z'}(\alpha_L) \underline{R}_{x'}(\alpha_D) \underline{R}_z(\alpha_S) \quad (2.70)$$

where \underline{R} is the Cartesian rotation matrix and \underline{R}^T its transpose. The subscript of the rotation matrix and its transpose represents the respective rotation axis as shown in Figure 2.7.

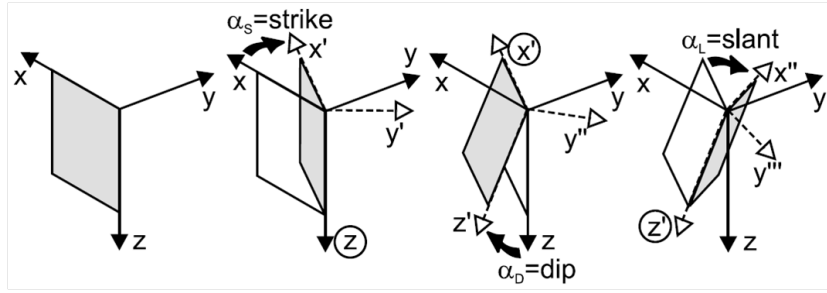


Figure 2.7.: Illustration of basic anisotropy parameters: transformation of conductive dike into general position by successively applying the three elementary Cartesian rotations α_S (anisotropic strike), α_D (anisotropic dip), and α_L (anisotropic slant); from Pek & Santos (2002).

The elementary rotation matrices around the z- and x- axis are given by

$$\underline{\underline{R}}_z(\alpha) = \begin{pmatrix} \cos\alpha & \sin\alpha & 0 \\ -\sin\alpha & \cos\alpha & 0 \\ 0 & 0 & 1 \end{pmatrix}, \quad (2.71)$$

and

$$\underline{\underline{R}}_x(\alpha) = \begin{pmatrix} 1 & 0 & 0 \\ 0 & \cos\alpha & \sin\alpha \\ 0 & -\sin\alpha & \cos\alpha \end{pmatrix}. \quad (2.72)$$

As illustrated in Figure 2.7, the rotation starts with around the z-axis by the anisotropic strike angle (α_S), then a rotation around the x' -axis by the anisotropic dip angle (α_D), and lastly a rotation around the z' -axis by the anisotropic slant angle (α_L).

Under the plane wave assumption, there is no vertical magnetic field for induction in a 1-D Earth. Horizontally varying magnetic fields diffusing downwards in the Earth will induce horizontal electric fields at right angles, which will drive the telluric currents. Therefore, the primary current induced in a 1-D Earth has only horizontal components. As a consequence, without any additional information available, it is not possible to reconstruct the full resistivity tensor in a 1-D Earth as it is not allowed by the MT field of a plane wave (Pek & Santos, 2002). This means that only the projection of the principal resistivities onto the horizontal plane can be resolved, and consequently, if the principal axes of the resistivity tensor are not parallel and perpendicular to the surface (i.e., $\alpha_D \neq 0$) the MT response cannot be distinguished from a lateral anisotropic resistivity (i.e., with zero dip and slant) (Heise et al., 2006). As the MT response is a product of the resistivity in a volume around the measurement with a radius comparable to the corresponding detection depth, it is impossible to distinguish between intrinsic or microscopic anisotropy and aligned macroscopic or aligned km scale resistivity heterogeneities at greater depths (Wannamaker, 2005).

Electrical anisotropy in the Earth can be classified according to their size into three categories: atomic, microscopic and macroscopic. The first two refer to intrinsic and fabric anisotropy (i.e., preferred orientation within lattices and crystals, respectively), whereas the latter is associated with the structural anisotropy. In the upper crust, electrical anisotropy is likely to be originated from macroscopic effects related to preferred orientations of fracture porosity, or lithologic layering, or oriented heterogeneity, whilst in the lower crust preferred orientations of fluidized/melt-bearing or graphitized shear zones might give rise to anisotropic responses. However, the observed responses might not necessarily reflect a current state of stress but could also characterize a signature of past deformation embedded in the rock or an existing fabric that might control fluid distribution (Wannamaker, 2005). Such crustal features can be found in the areas where active collisional, extensional, and fossil collisional regimes are present. Examples include collisional belts such as the New Zealand Southern Alps (Wannamaker et al., 2002) and Tibet (Le Pape et al., 2012), extension such as the Great Basin-Colorado Transition Zone (Wannamaker et al., 2008), and fossil collision such as the studies in the Canadian Precambrian Shield terranes, especially those of the Abitibi-Grenville provinces (Jones, 1992; Kellet et al., 1992; Kurtz et al., 1993; Mareschal et al., 1994, 1995; Boerner et al., 2000) and the studies in the North American Central Plains within the Proterozoic Trans Hudson orogen (e.g., Jones et al., 1997, 2005). In the lithospheric mantle, anisotropy can result from strain-induced crystal preferred orientation of minerals, hydrogen diffusivity in mantle minerals (e.g., Simpson, 2002; Evans et al., 2005), or the presence of partial melt (e.g., Yoshino et al., 2006; Gaillard et al., 2008; Poe et al., 2010).

2.7 THE DISTORTION PROBLEM

Distortion involves small-scale, near-surface conductivity inhomogeneities that can affect the MT impedance tensor. These distorted impedance tensor data can be misleading and usually result in erroneous subsurface models, therefore tectonic interpretation of these subsurface models cannot be believed. Berdichevsky et al. (1973) classified the complex process of distortion into two major effects: galvanic and inductive effects, although these effects are not entirely separate. The galvanic effect is caused by the primary electric field that produce electrical charges where conductivity variations occur, i.e., at distinct boundaries (similar to that described in Section 2.6, the 2-D Earth and fault model) or at continuous transitions. These excess charges result in secondary electric fields which add to the primary electric field. The inductive effect follows Faraday's law, which is associated with the time-varying primary magnetic field that induces currents. These vortex currents flowing in closed loops produce secondary magnetic fields which add vectorially to the primary magnetic field (Jiracek, 1990). Galvanic distortion is also known as vertical and horizontal current gathering, current deflection around resistive bodies, current leakage, current concentration into conductive zones or current channelling (Jones, 1983b; Park, 1985). For a conductive inclusion, the boundary charges cause a secondary field, that is anti-parallel to the primary along the side of the body and over it. The total field is reduced directly over the body, it

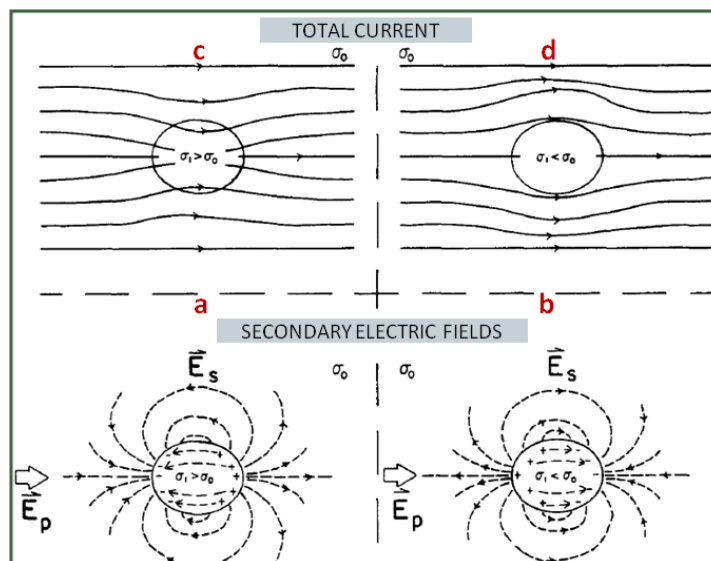


Figure 2.8.: Boundary charges from the surface of conductive inclusion (a) and resistive inclusion (b) producing secondary electric fields E_s . Primary (or regional) field E_p and secondary fields E_s add vectorially to produce total electric field \mathbf{E} resulting in current channelling (c) and current deflection (d); *modified from Jiracek (1990)*.

is enhanced off the ends of the body, and it is diminished along the sides of the body. For a resistive case, the total field is increased directly over the body and along its sides, and decreased off the ends. [Figure 2.8](#) illustrates the galvanic effects of an anomalous body. The galvanic electric field effectively channels currents into conductive inhomogeneities and around resistive inhomogeneities ([Smith, 1997](#)). [Figure 2.8c](#) and [Figure 2.8d](#) present the resulting patterns of total current flow illustrating the classic cases of 'current channelling' and 'current deflection' around conductive and resistive inhomogeneities, respectively. Therefore, MT sounding curves are shifted upward when measuring directly above surficial resistive bodies and are depressed over conductive patches ([Jiracek, 1990](#)). This upward or downward shift is asymptotically a constant (or static) shift of the MT log-log apparent resistivity versus period sounding curves. This effect is known as static shift. No distortion occurs in impedance phase curves over the period range. Furthermore, [Jiracek \(1990\)](#) showed that the galvanic effects are not only produced by resistive or conductive inclusions but also by 2-D topography that can cause the so-called galvanic topographic effect. In 2-D, the topographic galvanic effect, which mainly affects the TM mode, occurs when the primary electric field is perpendicular to the trend of the topography. The maximum charge concentration will occur for the steepest topography ([Jiracek, 1990](#)).

The inductive distortion effect is unlike the galvanic effect, where the secondary field is in phase with the causative primary electric field. For the inductive case, the phase of the secondary magnetic field varies between 0 (the resistive limit) and $\pi/2$ (the inductive limit) relative to the primary magnetic field. There are two major differences in the two effects. The first one is that the inductive effect increases to saturation as frequency increases, whereas the galvanic effect increases to saturation as frequency decreases. The second is that the magnetic field has the leading role

in the induction case, whereas the electric field plays the more important role in the galvanic case (Jiracek, 1990).

The galvanic distortion does not only affect the electric field, but also the magnetic field. Jones & Groom (1993), Chave & Smith (1994) and Smith (1997) accounted for the magnetic field term in their galvanic distortion of MT data. Using an example of data collected in Canada, Chave & Smith (1994) demonstrated that the electric galvanic distortion decomposition does not sufficiently describe the distortion model at higher frequencies, and therefore it is necessary to incorporate both the electric and magnetic galvanic distortion into the model in order to adequately address how the distortion affects the MT responses. The need for attention to the galvanic distortion of the magnetic field is particularly important for seafloor MT data.

Chave & Smith (1994) and Smith (1997) described the galvanic distortion mathematically as follows:

$$\underline{\underline{E}}_{obs} = \underline{\underline{C}} \underline{\underline{E}}_{2-D} \quad (2.73)$$

where $\underline{\underline{E}}_{obs}$ is the observed electric field, $\underline{\underline{C}}$ is the real and frequency-independent 2×2 electric galvanic distortion matrix, and $\underline{\underline{E}}_{2-D}$ is the regional 2-D electric field. Since the magnetic fields of the galvanically distorted currents $\underline{\underline{B}}_g$ are proportional to and in phase with the currents, which are proportional to and in phase with the regional electric field, they can be written as

$$\underline{\underline{B}}_g = \underline{\underline{D}} \underline{\underline{E}}_{2-D} \quad (2.74)$$

where $\underline{\underline{D}}$ is a real and frequency-independent magnetic distortion matrix. The observed magnetic field $\underline{\underline{B}}_{obs}$ which is the sum of the regional magnetic field $\underline{\underline{B}}_{2-D}$ and the galvanic distorted magnetic field $\underline{\underline{B}}_g$:

$$\underline{\underline{B}}_{obs} = \underline{\underline{B}}_{2-D} + \underline{\underline{B}}_g = \underline{\underline{B}}_{2-D} + \underline{\underline{D}} \underline{\underline{E}}_{2-D} \quad (2.75)$$

An observed impedance matrix Z_{obs} relates field measurements of $\underline{\underline{E}}_{obs}$ and $\underline{\underline{B}}_{obs}$:

$$\underline{\underline{E}}_{obs} = Z_{obs} \underline{\underline{B}}_{obs} \quad (2.76)$$

The regional impedance matrix Z_{2-D} can be defined by the similar relation

$$\underline{\underline{E}}_{2-D} = Z_{2-D} \underline{\underline{B}}_{2-D} \quad (2.77)$$

In Equation 2.76, expanding $\underline{\underline{E}}_{obs}$, $\underline{\underline{B}}_{obs}$, and $\underline{\underline{E}}_{2-D}$ using Equation 2.73, Equation 2.75, and Equation 2.77, one obtains

$$\underline{\underline{C}} Z_{obs} \underline{\underline{B}}_{2-D} = Z_{obs} \underline{\underline{B}}_{2-D} + Z_{obs} \underline{\underline{D}} Z_{2-D} \underline{\underline{B}}_{2-D} \quad (2.78)$$

This holds for all polarizations of the regional magnetic field \underline{B}_{2-D} , so

$$\underline{C} \underline{Z}_{2-D} = \underline{Z}_{obs} + \underline{Z}_{obs} \underline{D} \underline{Z}_{2-D} = \underline{Z}_{obs} (I + \underline{D} \underline{Z}_{2-D}) . \quad (2.79)$$

A measured impedance matrix \underline{Z}_{obs} can be written in terms of the regional impedance matrix \underline{Z}_{2-D} , and electric and magnetic galvanic distortion matrices, \underline{C} and \underline{D} as follows:

$$\underline{Z}_{obs} = \underline{C} \underline{Z}_{2-D} (I + \underline{D} \underline{Z}_{2-D})^{-1} \quad (2.80)$$

where \underline{I} is the identity matrix. Assuming that the EM fields are observed in an arbitrary coordinate system that is not aligned with the strike angle of the regional structures, the observed impedance matrix becomes

$$\underline{Z}_{obs}(\theta) = \underline{R}(\theta) \underline{C} \underline{Z}_{2-D} (\underline{I} + \underline{D} \underline{Z}_{2-D})^{-1} \underline{R}^T(\theta) \quad (2.81)$$

where θ is the azimuth angle respect to the regional strike, \underline{R} is the Cartesian rotation matrix. The galvanic magnetic distortion matrix is given by the frequency-dependent, which is due to the frequency dependence of \underline{Z} , product of $\underline{D} \underline{Z}_{2-D}$ and vanishes for low frequencies. For this reason magnetic galvanic distortion is usually neglected [Garcia & Jones \(2002b\)](#) and [Equation 2.81](#) can be rewritten as:

$$\underline{Z}_{obs}(\theta) = \underline{R}(\theta) \underline{C} \underline{Z}_{2-D} \underline{R}^T(\theta) . \quad (2.82)$$

Several distortion identification and removal techniques have been proposed, some of which will be discussed in a later section ([Section 2.8.2](#)). These techniques have used mathematically, statistically, and physically based approaches (for more details on the different approaches see *e.g.*, [Groom & Bahr \(1992\)](#), [Jiracek \(1990\)](#), and [Jones \(2012c\)](#)).

2.8 DATA PROCESSING, ANALYSIS, MODELLING AND INVERSION

2.8.1 From Time Series to Frequency Domain Transfer Functions

Time series processing involves the reduction of measured time series data to estimates of the electromagnetic impedance transfer functions in the frequency domain. However, since measured MT data contain noise, a more robust processing scheme needs to be applied to the data ([Jones et al., 1989](#)). [Jones et al. \(1989\)](#) describe several methods of deriving transfer function estimates. All those processing schemes described in [Jones et al. \(1989\)](#) involve the following steps: pre-conditioning of the data in the time domain, conversion from time to frequency domain and estimation of the transfer functions.

Pre-conditioning is done to reduce the effects of trends and to remove severe noise (spikes). The ultimate goal is to reduce the bias of the final estimate. The pre-conditioning subdivides the time

series into sets of segments of different length and the length of each segment will depend on the period calculated. Using more segments leads to better statistical results later in the processing sequence. Since the segments are of finite length, a Fourier Transform would cause spectral distortion by permitting 'leakage' of power (Jones, 1977). To avoid spectral distortion, a window function (e.g., Parzen window or Hamming window) is generally applied to the time segments.

Once pre-conditioned, the windowed data are converted into the frequency domain using a Fourier Transform or a wavelet transform. Each of the measured field components must be calibrated with respect to the particular instrument's sensitivity. Calibration is achieved by applying the instrument calibration functions that are either frequency dependent (e.g., induction coil sensor) or frequency independent (e.g., fluxgate magnetometer). Since the dispersion relation of Weidelt (1972) predicts similar results for neighbouring frequencies, evaluating six to ten frequencies per decade would give reasonable results. On the other hand, using fewer frequencies could lead to aliasing effects in the frequency domain (Simpson & Bahr, 2005).

Once in the frequency domain, raw power spectrum for each time segment for each channel (E_x , E_y , B_x , B_y , and B_z) are used to calculate the auto and cross spectra, which are the products of the field components and their complex conjugates for each evaluation frequency (ω). These spectra are stored in the so-called special matrix for each evaluation frequency:

B_x	B_y	B_z	E_x	E_y	
$B_x \cdot B_x^*$	$B_y \cdot B_x^*$	$B_z \cdot B_x^*$	$E_x \cdot B_x^*$	$E_y \cdot B_x^*$	B_x
	$B_y \cdot B_y^*$	$B_z \cdot B_y^*$	$E_x \cdot B_y^*$	$E_y \cdot B_y^*$	B_y
		$B_z \cdot B_z^*$			B_z
			$E_x \cdot E_x^*$	$E_y \cdot E_x^*$	E_x
				$E_y \cdot E_y^*$	E_y

For the same evaluation frequency, a number of spectral matrices, which result from each time segment that is processed, will be stacked, and potentially will be manually edited or weighted using statistical techniques.

The next step is the estimation of the transfer functions (also known as earth response functions) - the impedance tensor and the tipper vector:

$$E_x(\omega) = Z_{xx}(\omega) \cdot H_x(\omega) + Z_{xy}(\omega) \cdot H_y(\omega) + \delta Z(\omega) \quad , \quad (2.83)$$

$$E_y(\omega) = Z_{yx}(\omega) \cdot H_x(\omega) + Z_{yy}(\omega) \cdot H_y(\omega) + \delta Z(\omega) \quad , \quad (2.84)$$

and

$$H_z(\omega) = T_x(\omega) \cdot H_x(\omega) + T_y(\omega) \cdot H_y(\omega) + \delta Z(\omega) \quad , \quad (2.85)$$

where $\delta Z(\omega)$ and $\delta T(\omega)$ represent uncorrelated noise.

Goubau et al. (1978) and Gamble et al. (1979) introduced remote reference processing methods to avoid biased errors due to noise. This method involves measuring two extra channels at a station remote from the local MT station to be used as remote references for each other. Therefore, Equation 2.83, Equation 2.84, and Equation 2.85 can be solved using the following equations whose parameters are elements of the special matrix calculated previously:

$$Z_{xx} = \frac{\langle E_x R_x^* \rangle \langle H_y R_y^* \rangle - \langle E_x R_y^* \rangle \langle H_y R_x^* \rangle}{DET}, \quad (2.86)$$

$$Z_{xy} = \frac{\langle E_x R_y^* \rangle \langle H_x R_x^* \rangle - \langle E_x R_x^* \rangle \langle H_x R_y^* \rangle}{DET}, \quad (2.87)$$

$$Z_{yx} = \frac{\langle E_y R_x^* \rangle \langle H_y R_y^* \rangle - \langle E_y R_y^* \rangle \langle H_y R_x^* \rangle}{DET}, \quad (2.88)$$

$$Z_{yy} = \frac{\langle E_y R_y^* \rangle \langle H_x R_x^* \rangle - \langle E_y R_x^* \rangle \langle H_x R_y^* \rangle}{DET}, \quad (2.89)$$

and the tipper elements are given by

$$T_x = \frac{\langle H_z R_x^* \rangle \langle H_y R_y^* \rangle - \langle H_z R_y^* \rangle \langle H_y R_x^* \rangle}{DET}, \quad (2.90)$$

$$T_y = \frac{\langle H_z R_y^* \rangle \langle H_x R_x^* \rangle - \langle H_z R_x^* \rangle \langle H_x R_y^* \rangle}{DET}, \quad (2.91)$$

where $DET = \langle H_x R_x^* \rangle \langle H_y R_y^* \rangle - \langle H_x R_y^* \rangle \langle H_y R_x^* \rangle$. The complex conjugate quantities R_x^* and R_y^* theoretically are either local or remote electric or magnetic field components. In practice, using horizontal magnetic fields from a remote site is favoured, because horizontal magnetic fields are usually less affected by noise and more homogeneous than the electric fields.

There are several commercial as well as free processing codes available (Egbert & Booker, 1986; Egbert, 1997; Smirnov, 2003; Chave & Thomson, 2004). These processing codes will perform with varying degrees of success depending on the nature and quantity of the noise contained within the recorded signal. Common applications of robust processing include bounded influence estimator, M-estimators (Huber, 1981), or Jack-knife processing and iterative rejection of estimates to either increase the coherence of the estimates or decrease the variance of the resulting impedance estimate. Errors of the resulting estimates are then calculated on a statistical basis using Bootstrap analysis. The basic measure of the robustness of an estimator is its breakdown point, ϵ^* , that is, the fraction

(up to 50%) of outlying data points that can corrupt the estimator (Hampel et al., 1986). Least-squares solution has a break down point equal to zero, which means that even a small amount of noise may seriously bias the final estimate (Smirnov, 2003). The stablest of M-estimators have breakdown points approaching 30% in the case of a simple regression. A method with the highest possible breakdown point ($\epsilon^* = 50\%$) was proposed by Siegel (1982) using a repeated median algorithm, and Smirnov (2003) has developed an application for MT processing.

2.8.2 Distortion Analysis and Removal

The distortion problem was discussed in Section 2.7. In order to remove distortion effects, and to gain a better understanding of the geo-electric dimensionality and directionality inherent in the data, different approaches of distortion analysis and decomposition or correction can be applied to the data. The most widely used decomposition technique is the one proposed by Groom & Bailey (1989). There are also many other techniques available, (e.g., Swift, 1967; Bahr, 1988; Weaver et al., 2000; Marti et al., 2005), which will not be discussed in here. All these methods are based on the underlying assumption that the subsurface resistivity structure is 2-D. Utada & Munekane (2000), Garcia & Jones (2002a) and Becken et al. (2008) attempted to solve the problem of distortion removal in a 3-D environment. Another approach allowing for a 3-D background structure is the phase tensor approach proposed by Caldwell et al. (2004), although not a decomposition technique, but is a diagnostic and characterisation technique that will be described later in this section.

Groom-Bailey decomposition

Proposed by Bailey & Groom (1987), Groom (1988) and Groom & Bailey (1989), the Groom-Bailey distortion decomposition approach addresses purely real and independent electric galvanic distortion and neglects the magnetic galvanic distortion. The aim of the approach is to factorise the measured impedance tensor \underline{Z}_{obs} into a rotation matrix \underline{R} , the distortion matrix \underline{C} , and a scaled regional 2-D impedance tensor, \underline{Z}_{2-D} , as given by Equation 2.82, and therefore to separate the local 3-D distortion from the regional 1-D and 2-D response.

Parameterisation of the distortion tensor used by Groom (1988) and Groom & Bailey (1989) not only has a physical meaning, but also naturally separates the distortion tensor into determinable and indeterminate parts. The distortion tensor is factorised into a product of a scaling factor, and three tensors:

$$\underline{C} = g \underline{T} \underline{S} \underline{A} \quad (2.92)$$

where g is called scaling or gain factor, \underline{T} is called the twist, \underline{S} is shear, and \underline{A} is anisotropy. These matrices are:

$$\underline{\underline{T}} = \frac{1}{\sqrt{1+t^2}} \begin{pmatrix} 1 & -t \\ t & 1 \end{pmatrix}, \quad (2.93)$$

$$\underline{\underline{S}} = \frac{1}{\sqrt{1+e^2}} \begin{pmatrix} 1 & e \\ e & 1 \end{pmatrix}, \quad (2.94)$$

and

$$\underline{\underline{A}} = \frac{1}{\sqrt{1+s^2}} \begin{pmatrix} 1+s & 0 \\ 0 & 1-s \end{pmatrix}. \quad (2.95)$$

Twist and shear are the determinable parts of the distortion tensor, while anisotropy and the gain factor are the indeterminable parts of the tensor. [Figure 2.9](#) illustrates the effects of twist, shear and anisotropy by the delocation and/or deformation of a group of unity vectors. The twist tensor functions as a rotation operator ([Jones, 2012c](#)). The local electric fields are rotated through a clockwise twist angle, $\phi_{twist} = \tan^{-1}t$. The magnitude of shear is characterised by the shear angle, $\phi_{shear} = \tan^{-1}e$. [Groom & Bailey \(1989\)](#) showed that in general two solutions exist, but only one is meaningful. One solution results in $|e| < 1$ and the other one in $|e| > 1$. If we consider intuitively the effect of shear operator [Equation 2.94](#) indicates that a shear greater than 45° is not meaningful, and thus it is reasonable to require that $|e| \leq 1$. The anisotropy tensor, also known as splitting tensor, stretches the two field components by different factors. The shear tensor imposes anisotropy on axes that bisect the principal axes of the regional induction. Finally, the gain performs an overall scaling of the electric field.

The distortion problem is underdetermined, as it has nine unknowns (namely the 2 complex regional impedances Z_{xy} and Z_{yx} , the geo-electric strike direction, and the four parameters describing the galvanic distortion, g , t , s and a) and eight knowns, the four complex observed impedances. Both the gain and anisotropy parameters cannot be determined separately from $\underline{\underline{Z}}_{2-D}$, i.e., $\underline{\underline{Z}}'_{2-D} = g \underline{\underline{A}} \underline{\underline{Z}}_{2-D}$ both look like equally valid ideal 2-D impedance tensors. The fact that gain and anisotropy cannot be separated results in apparent resistivity curves that are shifted by an unknown scaling factor, while the shapes of the apparent resistivity and impedance phase curves remain unchanged.

[McNeice & Jones \(2001\)](#) proposed an extension to the Groom-Bailey decomposition method, in which a global minimum is sought to determine the most appropriate strike direction and distortion parameters for a range of frequencies and a set of MT stations, within a statistical framework. This multi-site, multi-frequency analysis is very useful to find an appropriate strike direction over the whole profile length to be modelled in 2-D. A freely available computer program developed by [McNeice & Jones \(2001\)](#) is called Strike. The latest version of the strike code has the functionality

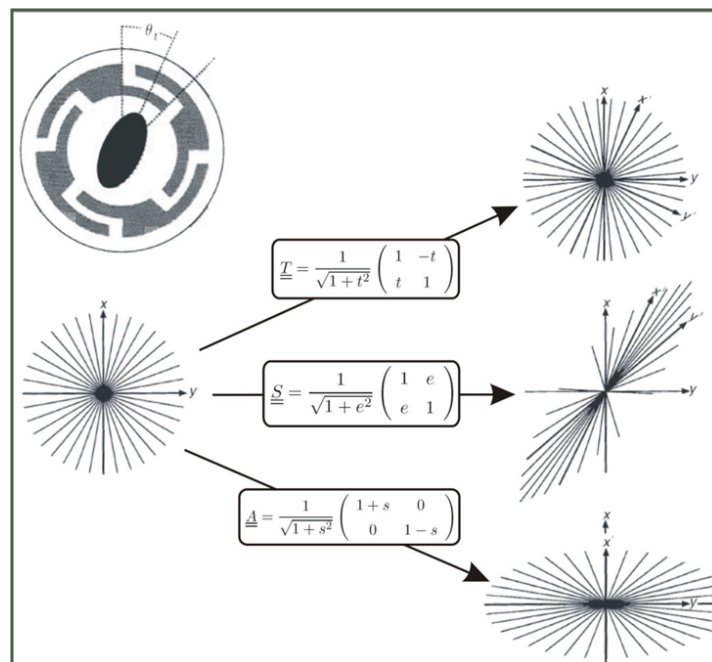


Figure 2.9.: **Top:** A contrived example of distortion. Conductive overburden (grey), on an insulating substratum (white). Inside the circular region of overburden is an elliptical and highly conducting region (black), such as swamp. Measurements are made at the centre of the swamp. The swamp first twists the telluric currents through an angle θ_t , its local strike. The anomalous environment then imposes shear and anisotropy effects on the data. **Bottom:** A group of unit vectors (on the left-hand side) which have had the twist, shear and anisotropy tensors applied to them (on the right-hand side); *modified from Simpson & Bahr (2005)*.

to work in depth bands (using the Niblett-Bostick depth transformation) rather than periods to accommodate the fact that penetration depth of neighbouring sites can vary significantly along a profile (e.g., Miensopust et al., 2011).

Phase tensor analysis

The concept of a 'phase tensor' was introduced by Caldwell et al. (2004). The authors demonstrated that the regional phase information can be recovered directly from the observed impedance tensor, where in both the near-surface inhomogeneity and the regional conductivity structures can be 3-D. Heise et al. (2008) modelled a 3-D resistivity structure with the use of the phase tensor estimates by performing forward modelling tests and they demonstrated that the phase tensor method has the potential to obtain a reliable regional subsurface structure. Most recently, inversion of phase tensor data has been implemented by 3-D inversion schemes such as WSINV3DMT (Siripunvaraporn et al., 2005a) and ModEM (Kelbert et al., 2014), which are freely available 3-D MT inversion codes to the academic community (Tietze, 2012; Patro et al., 2012). Tietze (2012), Patro et al. (2012) demonstrated that 3-D inversion of phase tensor data proved to be a valuable asset for obtaining subsurface structure more reliably compared to that obtained from the impedance tensor inversion, in the presence of galvanic distortion.

The phase tensor approach is based on the fact that in the presence of purely galvanic distortion, only the amplitudes of the observed electric field are distorted by near-surface inhomogeneities. Therefore, the phase relationship between the horizontal electric and magnetic field vectors will be almost unaffected. (Caldwell et al., 2004) proves that as follow:

The real, second-rank phase tensor $\underline{\Phi}$ is defined as the ratio of the real \underline{X} and imaginary part of \underline{Y} of the complex impedance tensor, $\underline{Z} = \underline{X} + i\underline{Y}$, i.e.,

$$\underline{\Phi} = \underline{X}^{-1}\underline{Y} \quad . \quad (2.96)$$

In the presence of galvanic distortion, the observed impedance tensor is $\underline{Z} = \underline{C} \underline{Z}_R$, where $\underline{Z}_R = \underline{X}_R + i\underline{Y}_R$ is the regional impedance impedance and \underline{C} is the distortion tensor. Thus, the distorted real part may be written as $\underline{X} = \underline{C} \underline{X}_R$, and the distorted imaginary part may be written as $\underline{Y} = \underline{C} \underline{Y}_R$. Based on these relations, one can prove that the observed and regional phase tensors are identical and independent of galvanic distortion tensor as follows:

$$\underline{\Phi} = \underline{X}^{-1}\underline{Y} \quad (2.97)$$

$$= (\underline{C} \underline{X}_R)^{-1} (\underline{C} \underline{Y}_R) \quad (2.98)$$

$$= \underline{X}_R^{-1} \underline{C}^{-1} \underline{C} \underline{Y}_R \quad (2.99)$$

$$= \underline{X}_R^{-1} \underline{Y}_R \quad (2.100)$$

$$= \underline{\Phi}_R \quad . \quad (2.101)$$

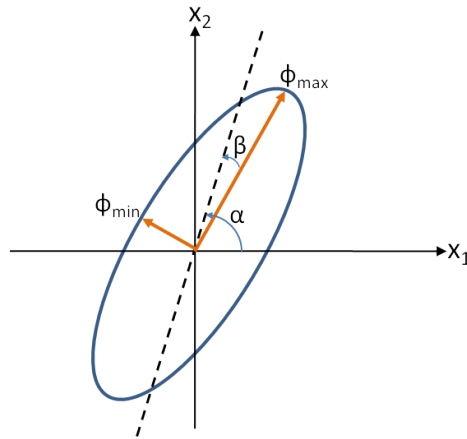


Figure 2.10.: Graphical representation of the phase tensor. Φ_{max} and Φ_{min} are used to scale major and minor ellipse axis, respectively. If the phase tensor is non-symmetric, a third coordinate invariant is needed to characterize the tensor: the skew angle β . The angle $\alpha - \beta$, which gives the orientation of the major axis of the ellipse, defines the relationship between the tensor and the observational reference frame (x_1 and x_2); redrawn from Caldwell et al. (2004)

In a Cartesian coordinate system, the phase tensor can be written in terms of real and imaginary parts of the impedance tensor $\underline{\underline{Z}}$

$$\begin{pmatrix} \Phi_{11} & \Phi_{12} \\ \Phi_{21} & \Phi_{22} \end{pmatrix} = \frac{1}{\det(\underline{\underline{X}})} \begin{pmatrix} X_{yy}Y_{xx} - X_{xy}Y_{yx} & X_{yy}Y_{xy} - X_{xy}Y_{yy} \\ X_{xx}Y_{yx} - X_{yx}Y_{xx} & X_{xx}Y_{yy} - X_{yx}Y_{xy} \end{pmatrix} \quad (2.102)$$

with $\det(\underline{\underline{X}}) = X_{xx}X_{yy} - X_{yx}X_{xy}$ the determinant of $\underline{\underline{X}}$.

The phase tensor is characterized by a direction and three scalar coordinate invariants. Caldwell et al. (2004) define the three coordinate invariants of the phase tensor as maximum (Φ_{max}) and minimum (Φ_{min}) tensor values and the skew angle β . The direction is given by the angle α , which expresses the tensor's dependence on the coordinate system (x_1 and x_2). The phase tensor can be plotted graphically as an ellipse, as shown in Figure 2.10. The major and minor axes of the ellipse represent the principal values of the tensor with the orientation of the major axis specified by the angle $\alpha - \beta$. The phase tensor can be written as a product of its invariants, Φ_{max} , Φ_{min} , and β :

$$\underline{\underline{\Phi}} = \underline{\underline{R}}^T(\alpha - \beta) \begin{pmatrix} \Phi_{max} & 0 \\ 0 & \Phi_{min} \end{pmatrix} \underline{\underline{R}}(\alpha + \beta) , \quad (2.103)$$

where $\underline{\underline{R}}^T$ is the transpose or inverse of the rotation matrix and the rotation matrix $\underline{\underline{R}}(\alpha + \beta)$ is as follow:

$$\underline{\underline{R}}(\alpha + \beta) = \begin{pmatrix} \cos(\alpha + \beta) & \sin(\alpha + \beta) \\ -\sin(\alpha + \beta) & \cos(\alpha + \beta) \end{pmatrix} . \quad (2.104)$$

The principals Φ_{max} and Φ_{min} of the tensor are given by

$$\Phi_{max} = (\Phi_1^2 + \Phi_3^2)^{1/2} + (\Phi_1^2 + \Phi_3^2 - \Phi_2^2)^{1/2} , \quad (2.105)$$

and

$$\Phi_{min} = (\Phi_1^2 + \Phi_3^2)^{1/2} - (\Phi_1^2 + \Phi_3^2 - \Phi_2^2)^{1/2} . \quad (2.106)$$

The two angles α and β can be written as,

$$\beta = \frac{1}{2} \tan^{-1} \left(\frac{\Phi_3}{\Phi_1} \right) , \quad (2.107)$$

and

$$\alpha = \frac{1}{2} \tan^{-1} \left(\frac{\Phi_{12} - \Phi_{21}}{\Phi_{11} + \Phi_{22}} \right) , \quad (2.108)$$

where Φ_1 , Φ_2 and Φ_3 are related to the trace ($tr(\Phi)$), the determinant ($det(\Phi)$) and the skew ($sk(\Phi)$) of the tensor respectively,

$$\Phi_1 = \frac{tr(\Phi)}{2} = \frac{\Phi_{11} + \Phi_{22}}{2} ,$$

$$\Phi_2 = det(\underline{\underline{\Phi}})^{1/2} = (\Phi_{11}\Phi_{22} - \Phi_{12}\Phi_{21})^{1/2} ,$$

and

$$\Phi_3 = \frac{sk(\Phi)}{2} = \frac{\Phi_{12} - \Phi_{21}}{2} .$$

In the simplest case of a uniform conductivity half space, the phase tensor will be represented by a circle of unit radius at all periods. For an isotropic, 1-D case, $\Phi_{max} - \Phi_{min}$ should be zero, and the phase tensor will be represented by circles in which the radius will vary with period according to the variation of the conductivity with depth. For instance, the radius of the circle will increase, if the conductivity increases with depth (Caldwell et al., 2004). For a 2-D case, $\Phi_{max} - \Phi_{min}$ will not be zero, and the phase tensor will be represented by an ellipse. Furthermore, a necessary but not sufficient condition for a 2-D regional conductivity structure is $\beta = 0$ and therefore the phase tensor is symmetric. For a 3-D case, the phase tensor is not symmetric and accordingly, β will be

non-zero. In the work of Caldwell et al. (2004), the authors used a 3D structure of a small 10 m, near-surface cube and a much larger (regional) 1 m body at depth, both embedded in a 100 m half space. Although the resistivity structure is clearly 3D, most of the skew angles obtained are relatively small ($\beta < 3^\circ$). Caldwell et al. (2004) suggested that a small value of β does not necessarily mean that the regional structure is 2-D, and it is necessary to look at the constancy of the direction of the principal axes of the phase tensor with period and with location as a much more reliable indicator of two-dimensionality.

In summary, although the phase tensor method cannot be used to recover an undistorted impedance tensor, it has potential as a data imaging and modelling tool, since the principle axes of the phase tensor ellipse (Φ_{max}, Φ_{min}) indicate the horizontal directions of the maximum and minimum induction current, which reflects lateral variations in the conductivity structure (Caldwell et al., 2004). The phase tensor skew angle (β), and the variation of the direction of the major axis of the tensor ellipse can help us to determine the dimensionality of the structure.

2.8.3 D^+ and ρ^+

The distortion-corrected regional MT response estimates can be tested for internal consistency of the phase and resistivity curves using D^+ and ρ^+ algorithms. The D^+ algorithm of Parker (1980) and Parker & Whaler (1981) is based on the fact that the MT response of any one-dimensional conductivity profile can be matched arbitrarily well at a finite number of frequencies by the response of finite systems of a delta function (Parker & Booker, 1996). Determination of the D^+ solutions can also be used as a simple test that verifies the accuracy of the 1-D modelling assumption on a particular data set. As a further development of the D^+ approach, Parker & Booker (1996)'s ρ^+ algorithm uses the logarithm of the admittance, $\log(c)$, rather than the admittance itself. The measured apparent resistivity ρ_a and the impedance phase ϕ are related to the admittance by

$$\rho_a = \mu_0 \omega |c|^2 \quad (2.109)$$

and

$$c = |c| e^{i(\phi - \pi/2)} \quad (2.110)$$

The ρ^+ algorithm can be used to test mutual consistency between the apparent resistivity and phase data by predicting one from the other, and therefore gives a helpful guidance for the selection or rejection of apparent resistivity and/or phase data at certain frequencies. An example of an application of this consistency approach can be found in the work of Spratt et al. (2005).

2.8.4 Forward Modelling and Inversion of MT Data

Once MT data are processed, analysed, decomposed (removal of distortion effects and rotation into strike direction), and the D^+ and ρ^+ consistency check (removal of bad data points) are performed, the next step is to apply a modelling and inversion method suitable for the particular data set. Depending on the data set, 1-D, 2-D or 3-D subsurface models can be produced using forward modelling and inversion codes in order to determine the subsurface conductivity structure. The resulting models help to relate the resistivity structure of the subsurface to geology and other geophysical models in order to gain a better understanding of the Earth processes.

The procedure using a physical theory for predicting the results of observations is called forward modelling. The reciprocal situation, using the results of measurements to infer the values of the parameters representing a system, is called inverse modelling (Tarantola, 2006).

The forward operator of the inversion process can be described by the following equation:

$$\mathbf{d} = \mathbf{f}(\mathbf{m}) \quad , \quad (2.111)$$

leading to the general inverse operator given by

$$\mathbf{m} = \mathbf{f}^{-1}(\mathbf{d}) + \delta \quad , \quad (2.112)$$

where, the observed data, $\mathbf{d} = d^1, d^2, \dots, d^N$, are reproduced within their error by a forward modelling operator, \mathbf{f} , which is a function of model parameters, $\mathbf{m} = m^1, m^2, \dots, m^M$. Depending on the dimensionality of the data, 1-D, 2-D or 3-D, the conductivity model can be discretized into cells that form the model mesh. In order to define the model mesh, there are different approximations, such as finite element, finite difference and integral equation methods. Previously described Maxwell's equations as well as appropriate boundary conditions are then solved for each cell of the mesh. The exact formulation of the equation system will depend on the approximation used. Once we know the electric and magnetic fields, we can easily estimate the impedance (or resistivity and phase or tipper) values at an observation location. The synthetic data derived from forward modelling are compared with the actual observed data, and their difference is usually presented by an rms misfit. During the inversion process, one tries to find the 'best' values of the model parameters that fits the observed data by applying changes to the forward models which are driven by the minimisation of the misfit between the predictions and the actual observations.

1-D and 2-D inversions are currently the standard approach for modelling MT data and a number of algorithms have been developed. Those algorithms include REBOCC (Siripunvaraporn & Egbert, 2000), OCCAM 1-D and 2-D (Constable et al., 1987), ABIC (Uchida, 1993), and RLM2DI (Rodi & Mackie, 2001), of which an updated version implemented in Geosystem's commercial software WingLink®. In this thesis, 2-D resistivity models were generated using the code by Rodi & Mackie (2001) implemented in WinGLink® (or rather using its modified version (Mackie, 2002; Baba et al., 2006) applying isotropic and anisotropic inversion settings). The forward part of the code is

described by Mackie et al. (1988), which is based on a finite difference approximation of the Maxwell Equations and uses a rectangular mesh to discretize the model. The inversion part of the code is based on a non-linear conjugate gradient algorithm to minimize a regularized objective function (Tikhonov regularization (Tikhonov & Arsenin, 1977)). An extension of the Rodi & Mackie (2001) 2-D MT inversion code has been created in order to include a diagonalized resistivity tensor for seafloor MT data (Baba et al., 2006). The 2-D anisotropic version of the code operates similarly to the isotropic version, but assumes that the axes of anisotropy are known, (i.e., the resistivity varies along anisotropy axes defines as parallel and perpendicular to the main axis of the regional geo-electric strike). Therefore, the resistivity matrix is characterized by a diagonal second rank tensor and the anisotropic modelling is defined by three models: xx - horizontal resistivity across the profile, yy- horizontal resistivity along the profile, and zz - vertical resistivity. The TE and TM modes are now governed by

$$\frac{\partial^2 E_x}{\partial^2 y} + \frac{\partial^2 E_x}{\partial^2 z} + i\omega\mu \frac{E_x}{\rho_{xx}} = 0 \quad (2.113)$$

and

$$\frac{\partial}{\partial y} \left(\rho_{zz} \frac{\partial H_x}{\partial y} \right) + \frac{\partial}{\partial z} \left(\rho_{yy} \frac{\partial H_x}{\partial z} \right) + i\omega\mu H_x = 0 \quad , \quad (2.114)$$

respectively, where x, y, z are the along-strike, cross-strike, and vertical (positive downward) directions, $E_x(H_x)$ are the x components of the electric(magnetic) field, ω is angular frequency, μ is the magnetic permeability of free space, and σ is the electrical conductivity (ρ is the resistivity which is the inverse of conductivity) which has three direction dependent elements. The objective function to be minimised is defined as (as presented in Baba et al. (2006)),

$$\Phi(m) = (\mathbf{d} - F(\mathbf{m}))^t \mathbf{V}^{-1} (\mathbf{d} - F(\mathbf{m})) + \tau_s (\mathbf{m} - \mathbf{m}_0)^t \mathbf{L}_s^t \mathbf{L}_s (\mathbf{m} - \mathbf{m}_0) + \tau_c \mathbf{m}^t \mathbf{L}_c^t \mathbf{L}_c \mathbf{m} \quad (2.115)$$

where \mathbf{d} is the observed data vector, F is the forward modelling operator, \mathbf{m} is the unknown model, \mathbf{m}_0 is a priori model vector, \mathbf{V} is the error covariance matrix, \mathbf{L}_s and \mathbf{L}_c are linear operators expressing the imposed constraints, and τ_s and τ_c are regularization parameters for the smoothness and degree of anisotropy, respectively. The model vector, which we are seeking for, is the log of the anisotropic resistivity as a function of position:

$$\mathbf{m}(y, z) = \ln \begin{bmatrix} \rho_{xx}(y, z) \\ \rho_{yy}(y, z) \\ \rho_{zz}(y, z) \end{bmatrix} \quad . \quad (2.116)$$

Two types of regularization have been imposed, as given by the second and third terms in the objective function. While the second term controls the model smoothness, the third objective term controls the closeness of ρ_{xx} , ρ_{yy} , and ρ_{zz} models. As τ_s grows, the inversion is forced to find

a smoother model. For an isotropic inversion, the closeness parameter, τ_c , is set to a large value (e.g., $\tau_c = 100,000$) resulting in three models are identical. If the $\tau_c = 0$, the three models become completely independent. More information about the parameters used in the 2-D inversion codes of [Rodi & Mackie \(2001\)](#) and [Mackie \(2002\)](#) can be found in [Chapter 5](#).

The 3-D forward and inverse modelling codes and practical aspects of 3-D MT inversion are briefly described and discussed in [Chapter 6](#) and [Chapter 7](#).

WESTERN MEDITERRANEAN FIELD AREA

This chapter provides an overview and background information about the Atlas System in Morocco. The magnetotelluric experiment (TopoMed-PICASSO) is briefly described as well as previous geophysical work, together with an overview of the regional geology and tectonics.

3.1 GEOLOGICAL AND TECTONIC BACKGROUND OF ATLAS MOUNTAINS OF MOROCCO

The Atlas system of North Africa is an intra-continental orogenic domain extending for more than 2000 km through Morocco, Algeria and Tunisia (Figure 3.1). In Morocco, the system comprises four mountain belts: Rif, Middle Atlas, High Atlas and Anti-Atlas. The east-trending High Atlas mountains constitute the highest elevated region in this mountain chain with summits of 4165 m (Mt. Toubkal), framed between the Meseta domains (Morocco Meseta and Oran Meseta) to the north, and the northern boundary of West African Craton (Anti-Atlas) to the south. The Meseta domains are rigid blocks exhibiting tabular thin meso-Cenozoic cover sandwiched between the Rif, the Atlas belts and the Atlantic Margin (Missenard et al., 2006), (Figure 3.1).

The geodynamic evolution of the Atlas system encompasses two major episodes that initiated with rift basin formation during the Mesozoic, evolving into compressional and inverted belts from Cenozoic to present times (e.g., Jacobshagen et al., 1988; Brede, 1992; de Lamotte et al., 2000). During the Alpine orogenic cycle, the different domains crossed by TopoMed-PICASSO transects were affected by both Central Atlantic and Tethyan rifting (de Lamotte et al., 2000), (Figure 3.2). While the Western High Atlas is connected to the Central Atlantic rifting, the NW-SE trending Middle Atlas and E-W trending Central and Eastern High Atlas are inherited from the latter.

Late in the Paleozoic Era, the final assembly of Pangea resulted from the combined continental collisions of the Gondwana, Laurentian and Baltic cratons, as well as the intervening microcontinents, caused the Hercynian, Variscan-Alleghanian and Uralian orogenies. The beginning of the Mesozoic-Cenozoic cycle is dominated by the rifting causing Pangea break-up, followed with the opening of the Central Atlantic and Alpine Tethys Oceans, and ending with Tethys closure and Alpine belt formation (de Lamotte et al., 2008), (Figure 3.2).

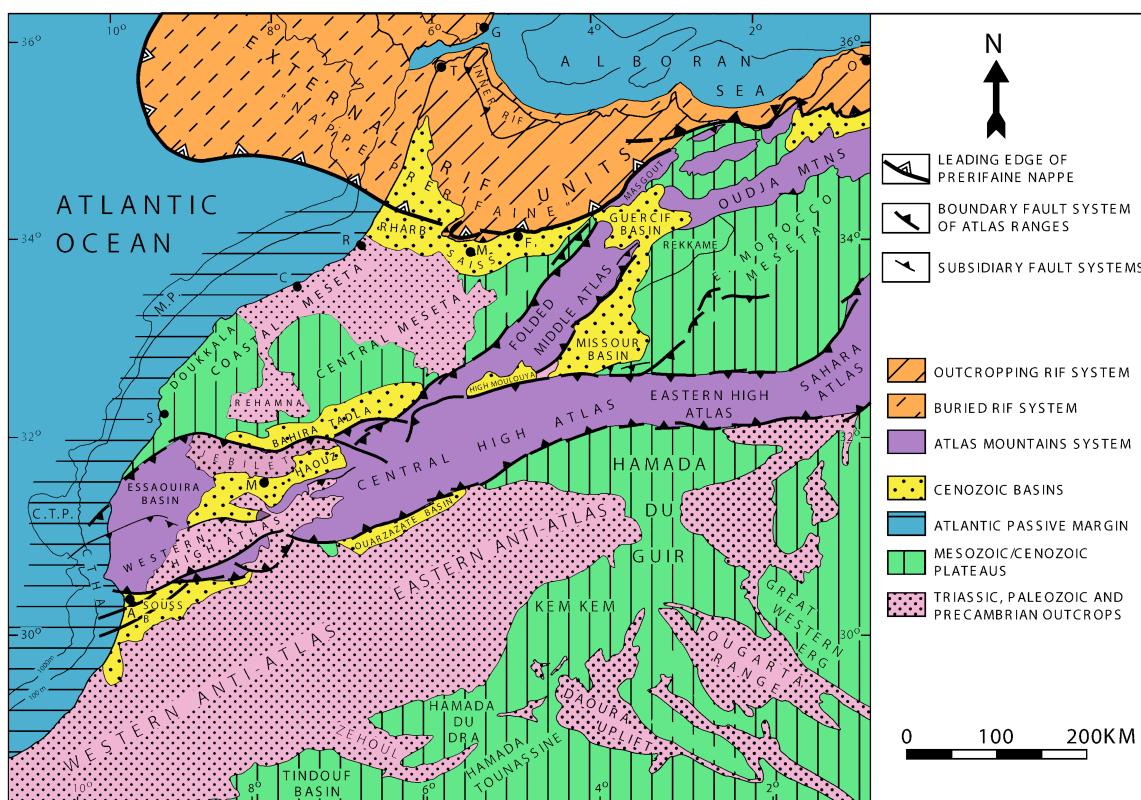


Figure 3.1.: Schematic structural map of Morocco showing the extension of the Atlas system; *modified from Hafid et al. (2006).*

3.1 GEOLOGICAL AND TECTONIC BACKGROUND OF ATLAS MOUNTAINS OF MOROCCO

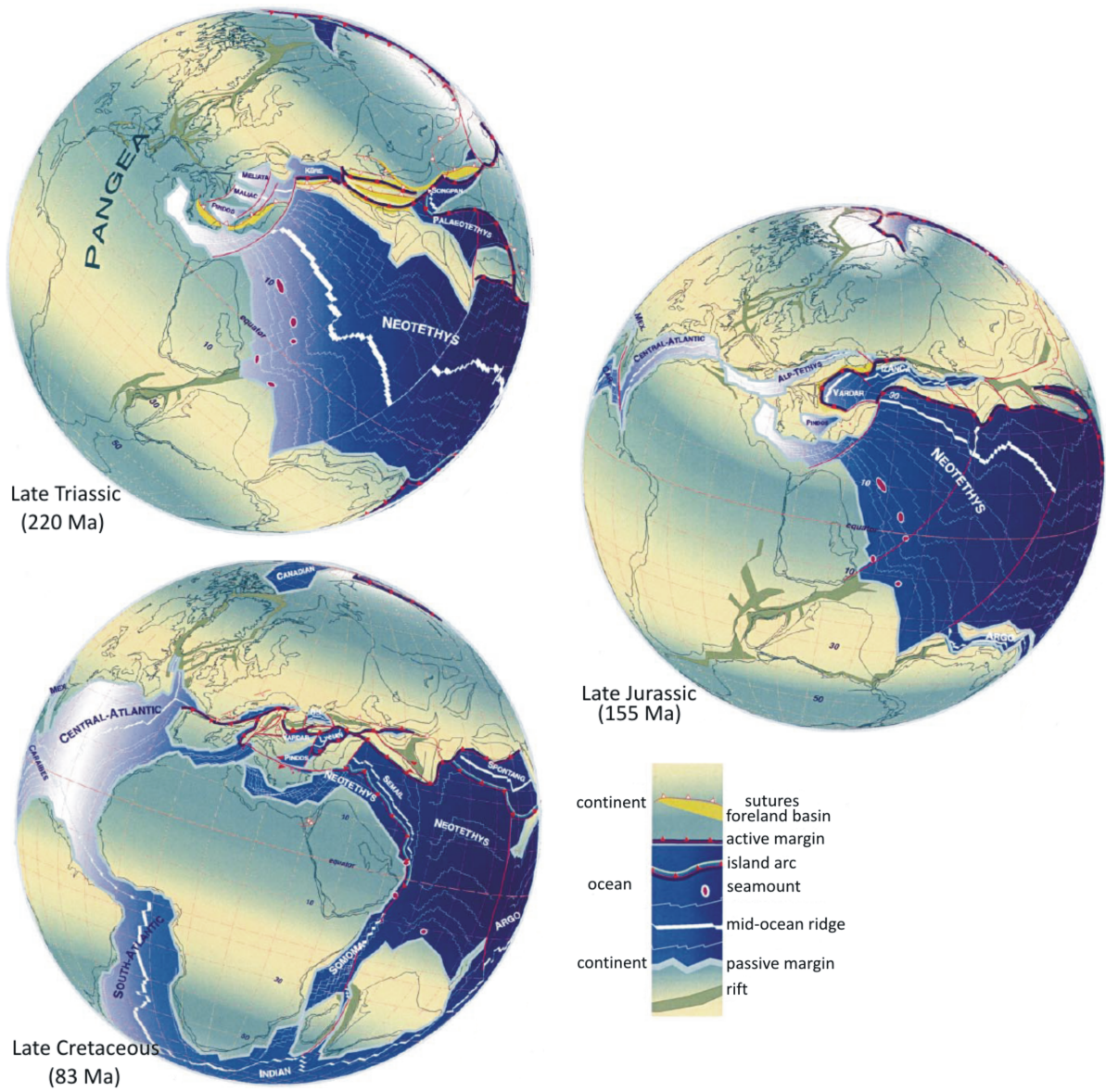


Figure 3.2.: The break-up of the Pangea super-continent and further plate tectonics of the Atlantic and Tethyan domains; *modified from Stampfli & Borel (2002)*.

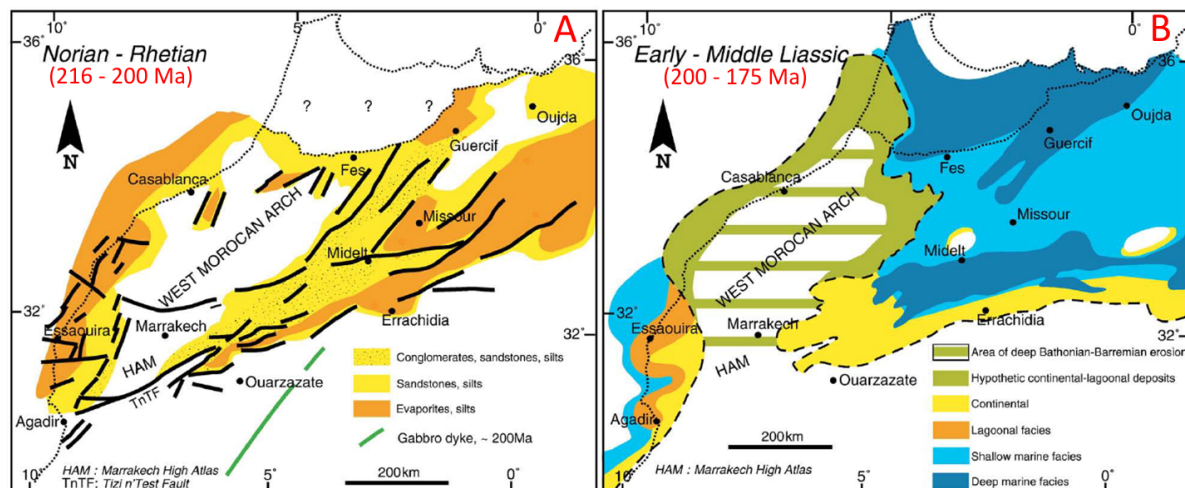


Figure 3.3.: The Triassic to Middle Jurassic West Moroccan Arch and surrounding areas. **A**: Paleogeography during the Late Triassic. **B**: Paleogeography during the Early and Middle Jurassic; *modified from de Lamotte et al. (2008)*.

3.1.1 The Atlantic Domain

The Western High Atlas

The Western High Atlas is a subset of the Atlantic domain and is separated from the Tethyan geological region by the West Moroccan Arch (Figure 3.3). It extends over several Atlantic coastal basins and their adjacent Atlantic shelf segments (Figure 3.4). During the Triassic to Lower Cretaceous, the Western High Atlas region, along with the remainder of the Atlas belt, evolved from a proximal shallow-water platform of the Atlantic passive margin to the present day north-south to NNW-SSE directed compression due to the tectonic convergence between Africa and Europe. The resulting compression yielded significant folding of the evaporite based detachment, reverse faulting and the inversion of Triassic to Jurassic syn-rift structures (de Lamotte et al., 2000; Hafid et al., 2006).

The Haouz Basin (Figure 3.1 and Figure 3.4) is interpreted as an intra-mountain basin as it is thought to be part of the orogenic system. The basin comprises thin Mesozoic and Cenozoic units, with the stratigraphy yielding poorly dated Miocene-Pliocene molassed deposits, that are overlapping the Jebilet range to the North (Missenard et al., 2007; de Lamotte et al., 2008). The 'Mio-Pliocene' molasses are coarser and thicker in the southern part of the basin than in the north.

Similar to the Haouz Basin, the deposits are also preserved in the Souss Basin, which represents the southern foreland of the Atlas system (Figure 3.1 and Figure 3.4). The basin extends over 150 km from the Atlantic coast to the western side of the Siroua Plateau. As a result of tectonic activity, the northern border of the basin along the Western High Atlas is steeper than the southern slope along the Anti-Atlas. It is bordered to the north by the South Atlas Fault Zone. During Atlantic rifting, the basin infill was controlled by an active reverse fault zone (Sebrier et al., 2006).

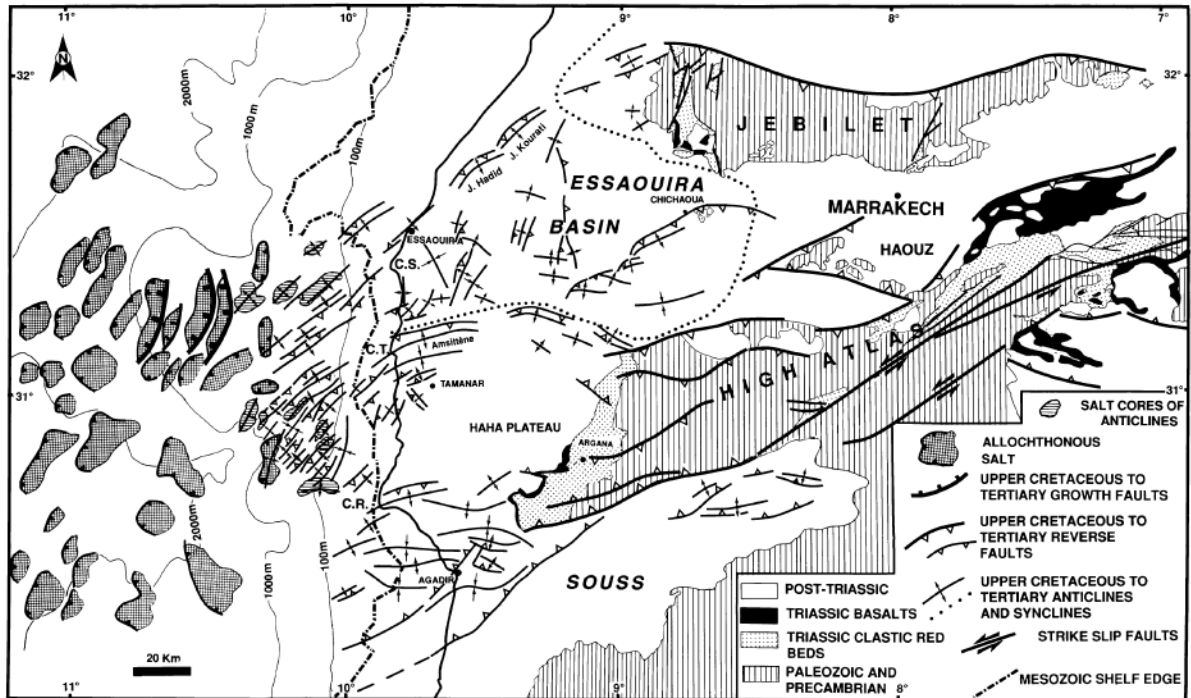


Figure 3.4.: Structural map of the Western High Atlas onshore and offshore; from Hafid et al. (2006).

Based on seismic profiles results by Mustaphi et al. (1997), two other NE-SW major faults, the El Klea and Abou Grai faults, accommodated crustal thinning inside the basin, and controlled the basin's triangular geometry. The sedimentary sequence is characterized by syntectonic Triassic sandstones and conglomerates and Jurassic to Upper Cretaceous sediments. The total thickness of the Cenozoic cover does not exceed 1300 m (Mustaphi et al., 1997).

The Western High Atlas mountains comprise Precambrian basement geology, which is mainly found in the Ouzellarh Block. This geology is composed of metamorphic rocks and granitoids succeeded by a late Precambrian volcanic succession. The Paleozoic geology ranges from Lower Cambrian to Carboniferous and is dominantly clastic rocks that were deformed during Variscan orogeny. Tight folding associated with metamorphism and granite intrusions occurred during the Later Visean-Early Westphalian tectonic event (Michard et al., 2008). The folding indicates a NE-SW to N-S axes and sub-vertical to generally E-dipping axial planes and developed a dominant axial plane cleavage. However ENE-WSW major dextral fault zones (e.g., Tizi n'Test Fault) dominate the Variscan structural pattern which also broke up the Western High Atlas into several structural blocks (Proust et al., 1977; Ouanaimi & Petit, 1992; Houari & Hoepffner, 2003; Hoepffner et al., 2005).

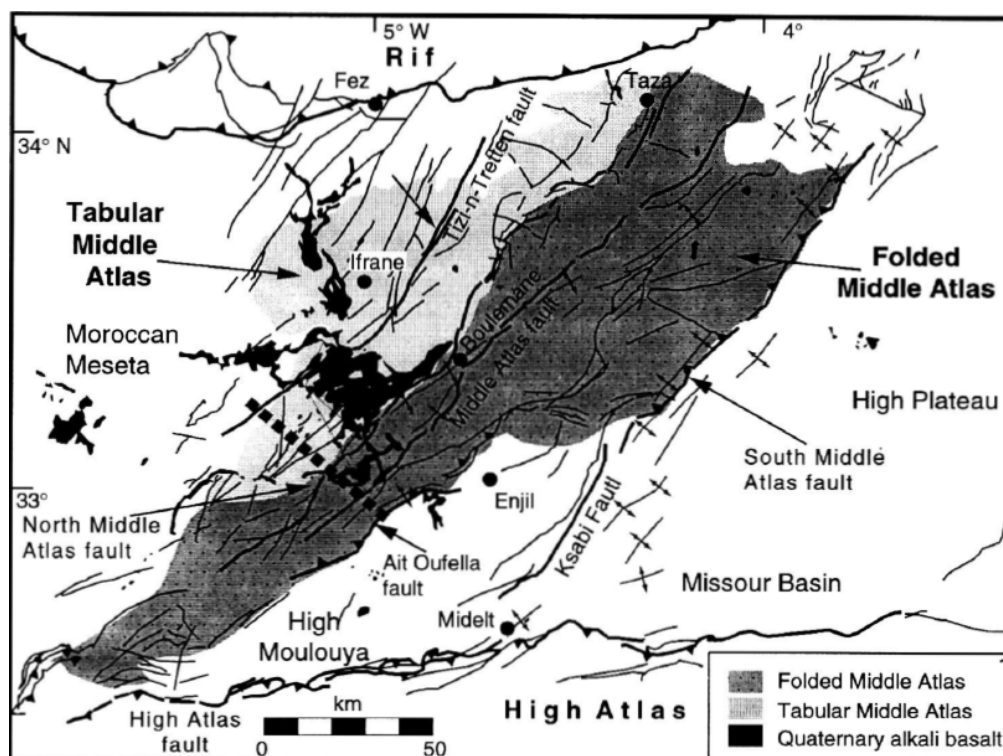


Figure 3.5.: Tectonic map of Middle Atlas region showing main faults and Quaternary basalt; *from Gomez et al. (1996)*.

3.1.2 The Tethyan Domain

The Middle Atlas

The Middle Atlas region comprises three structural zones: the Tabular Middle Atlas in the northwest, the Folded Middle Atlas in the southeast and the High Moulouya Basin (Martin, 1981; Dresnay, 1988), (Figure 3.5). The Folded Middle Atlas is bordered by the North Middle Atlas (NMAF) and the South Middle Atlas faults (SMAF), which mark the boundaries of the Mesozoic rift zone (Fedan, 1988), and the Ait Oufella fault (AOF). The Tabular Middle Atlas is characterized by generally sub-horizontal calcareous rocks of Jurassic and Cretaceous age and much of this part of the Middle Atlas is covered by Quaternary alkali basalts (Gomez et al., 1996). The High Moulouya Basin is a flat region characterized by sub-horizontal strata, exhibiting mostly tabular Mesozoic-Cenozoic sediments (Gomez et al., 1998; de Lamotte et al., 2008). It is bordered by the Ksabu fault and the High Plateau/Missour Basin to the east.

The Central High Atlas

The Mesozoic succession of the High Atlas belt began with the Late Permian-Triassic red beds (conglomerates, sandstones, siltstones and mudstones), unconformably resting on the Lower Pale-

ozoic rocks or on the Precambrian basement. The detrital infilling of basins developed during the Late Permian-Triassic Atlantic pre-rifting phase (when the Variscan shear zones were reactivated as normal and strike-slip faults) was represented with these continental deposits, which are capped by the tholeiitic basalt flows of the CAMP¹ (Ellero et al., 2012).

The transgressive Lower Liassic platform was represented by the limestones and dolomites. The sedimentary succession within the Liassic evolved from massive carbonates into a layered stratigraphy of marls and limestones. This geology would infer a platform basin boundary setting that documents the progressive disruption and submergence of the Liassic platform. The Lower Dogger unit of the Upper Liassic are found to be multicoloured marls and reefal limestones. This geology is underlain by Bathonian red sandstones and silty shales that indicates continental sedimentation. The Cretaceous geology comprises red sandstones, silty shales and conglomerates evolving to a platform of white limestone of Cenomanian-Turonian in age. This marks the overall, global transgression, which the entire Atlas domain experienced.

According to many authors (Görler et al., 1988; Jacobshagen et al., 1988; Giese & Jacobshagen, 1992; de Lamotte et al., 2000; Harfi et al., 2001, 2006; Missenard et al., 2007), the Alpine tectonic evolution of the High Atlas fold and thrust belt has been considered to be characterized by two main deformation steps spanning in age from Late Eocene to Oligocene-Miocene and from Pliocene to Early Quaternary, respectively. A thick-skinned model was proposed to characterize the overall tectonic style of High Atlas (e.g., de Lamotte et al., 2000; Teixell et al., 2003; Harfi et al., 2006). However, a thin-skinned style of deformation has been proposed for structures of its southern border (e.g., Beauchamp et al., 1999; Benammi et al., 2001; Teixell et al., 2003).

Anti-Atlas

The older Anti-Atlas mountain range runs roughly parallel to the High Atlas. It is a large Paleozoic foreland fold belt that has been impacted by the Pan-African, Hercynian and Alpine orogenies, although the latter two only affected it mildly. A slightly folded late Precambrian-Paleozoic sedimentary succession covers Precambrian crystalline basement in the area, which includes ancient subduction zones, marginal basins, magmatic arcs and rift margins juxtaposed on the Eburnian-aged (~2 Ga) West African Craton (WAC) (Villeneuve & Cornee, 1994; Ennih & Lie, 2001). Due to its location in the vicinity of the Central Atlantic Rift, the Anti-Atlas belt was intruded by a huge quantity of dykes and sills of Triassic-Early Liassic gabbros and dolerites. Following a long period of erosion, the former mountain belt was partly overlain by Cretaceous-Tertiary deposits that now form the Hamada Plateau (Figure 3.1). For various geological but also rheological and isotopic reasons, Ennih & Lie (2001) proposed that the actual northern boundary between the WAC (south of the Anti-Atlas Major Fault (AAMF)) and the High Atlas mountain range is the South Atlas Fault.

¹ The first magmatic event is linked to the Triassic rifting, which led to the opening of the Central Atlantic and Western Tethys oceans. Central Atlantic Magmatic Province (CAMP) is characterized by this event, which affected all of Morocco from the Anti-Atlas to the External Rif domain.

Figure 3.6 is a simplified model illustrating the geodynamic evolution of the Anti-Atlas domain during the Neoproterozoic. Ennih & Lie (2001)'s tectonic scenario assumes a north-dipping subduction from ~760-685 Ma (Figure 3.6B). At ~685 Ma, collision of the northern border of the WAC with an oceanic convergent margin resulted in ophiolite remnants in Saghro and Bou Azzer (Figure 3.6C). Between 685 and 585 Ma, no apparent tectonic, metamorphic, or magmatic events occurred in the Anti-Atlas resulting from the free movement of the rigid WAC. At 650-630 Ma, Avalonia-Cadomia collided with the WAC craton and moved afterwards along a sinistral shear zone corresponding to the craton boundary currently marked by the SAF (Figure 3.6C). In the 585-560 Ma age range, high-K alkaline magmatism occurred due to transpressive deformation of the WAC margin (Figure 3.6D-E). During the Adoudounian (prior to 544 Ma)-Early Cambrian, the tectonic regime progressively changed from transpressive to transtensive, and thus the magmatism became more alkaline (Michard et al., 2008).

3.1.3 Overall Shortening in the Atlas System

Shortening in the whole Atlas system began during the Late Cretaceous due to convergence between Europe and Africa (e.g., de Lamotte et al., 2000). Although the amount of tectonic shortening and relief associated with the Alpine compression are controversial, moderate tectonic shortening was defined across the Atlas Mountains by Teixell et al. (2003). Teixell et al. (2003) calculated total shortening ranging from 15% to 24% along transects of the High Atlas, which indicates that not all the observed topography relates to tectonic convergence and crustal thickening alone. Gomez et al. (1998) and Arboleya et al. (2004) estimated total orogenic shortening of <15% for the Middle Atlas (with altitudes up to 3000 m), and of <1% for Anti-Atlas. Therefore, as a consequence of only moderate shortening many authors argue that a thermal factor is involved in the Atlas uplift, being related to an oblique NE-SW strip of the thinned lithosphere (Teixell et al., 2003, 2005; Zeyen et al., 2005; de Lamotte et al., 2009).

3.1.4 The Cenozoic Volcanic History of the Atlas System

The Cenozoic volcanism of the Atlas system is exclusively composed of intraplate alkaline type (alkali basalts, basanites, nephelinites, associated intermediate and evolved lavas, and carbonatites), whereas in the Rif it evolved through time from calc-alkaline to shoshonitic and finally alkaline (El Azzouzi et al., 1999, 2010). The Atlas volcanism forms a SW-NE directed strip, which extends from the Siroua stratavolcano in the Anti-Atlas to the Mediterranean coast near Oujda, underlain by proposed thinned lithosphere (Teixell et al., 2005; Zeyen et al., 2005; Missenard et al., 2006; Fullea et al., 2010) (Figure 3.7).

The Middle Atlas basaltic province is the largest and youngest volcanic field in Morocco (Figure 3.7). Based on a hundred new major and trace element analyses, El Azzouzi et al. (2010) distinguished four types of mafic lavas: 1) Nephelinites ($\text{SiO}_2 = 37\text{-}41 \text{ wt}\%$) usually form small

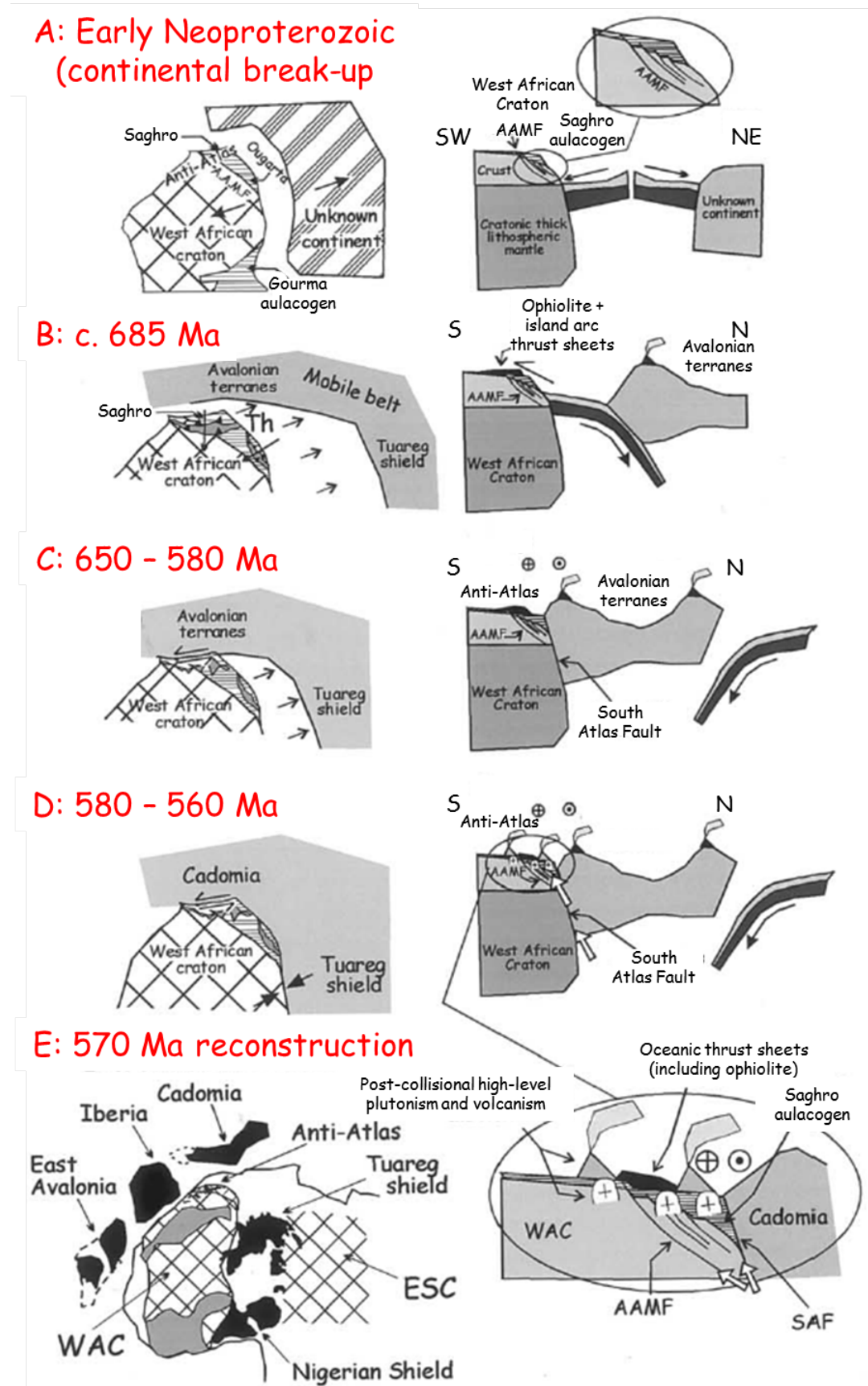


Figure 3.6.: Geodynamic evolution of the Anti-Atlas domain during Neoproterozoic times; *modified from Ennih & Lie (2001).*

strombolian cones and associated lava flows located along the borders of the volcanic plateau. Although they represent 20% of the sampling, they cover only 1.2% of the total surface of volcanic units. 2) Basanites ($\text{SiO}_2 = 42\text{-}45 \text{ wt}\%$), which make up most of the well-preserved cones located between Azrou and Itzer and represent 30% of the sample set. 3) Alkali basalts ($\text{SiO}_2 = 47\text{-}51 \text{ wt}\%$), which represent the dominant petrographic type (46% of the sampling). 4) Subalkaline basalts ($\text{SiO}_2 = 52 \text{ wt}\%$), which is richer in silica compared to the other lava types and form 4% of the sampling. Most of the Middle Atlas alkali basalts, basanites and nephelinites display a Mg-rich character and enriched incompatible elements and their geochemical signatures are hardly distinguishable from those of ocean island alkali basalts and related rocks. The authors observed progressive enrichment in the most compatible elements from alkali basalts to nephelinites, which they considered is consistent with decreasing degrees of partial melting of heterogeneous mantle sources. These sources are thought to be associated with enriched pargasite, spinel and garnet lherzolites, located at depths $\sim 70 \text{ km}$. The authors concluded that partial melting resulted from a high thermal flux linked to the asthenospheric uprise. This asthenospheric uprise induced dehydration melting of pargasite-bearing enriched peridotites, which were metasomatised during an earlier Cenozoic plume-related magmatic event.

An alternative scenario was proposed by [Duggen et al. \(2009\)](#) based on the similarities between the isotopic signatures of Canary Islands, Middle Atlas, Guilliz, and Gourougou Neogene lavas. In order to explain this similarity, the authors suggested that the Canary plume materials would have been channelled beneath the thinned African lithosphere through a subcontinental lithospheric corridor and would have flowed more than 1500 km to the western Mediterranean ([Figure 3.8](#)). In this interpretation, the lithospheric corridor formed through the delamination ([Ramdani, 1998](#)) of subcontinental lithosphere beneath the northwest African Atlas system in response to African and European collision at $\sim 42 \text{ Ma}$, and its formation preceded and enabled inflow of plume mantle material. [Bouabdellah et al. \(2010\)](#) supported [Duggen et al. \(2009\)](#)'s model by studying the Eocene Tamazert alkaline complex of the central High Atlas range of Morocco which hosts the largest outcropping occurrences of carbonatites in northern Africa. The authors pointed out that similarity in carbonatite composition between the Cape Verde and Canary Islands and Tamazert suggests a common sublithospheric source for these carbonatites.

3.2 PREVIOUS GEOPHYSICAL WORK IN THE ATLAS SYSTEM OF MOROCCO

3.2.1 *Magnetotelluric Studies*

In 1983 and 1988, MT data at more than 50 stations were collected along three profiles: two main profiles start from the Rif Mountains and go through the Anti-Atlas (coincident with the MEK profile shown in [Figure 3.9](#), and the third E-W oriented profile runs from the High Atlas towards the Moroccan Meseta ([Schwarz et al., 1992](#)). The final electrical resistivity model (based on stitched 1-D inversion or in 2-D using only the MT phases and induction vector data following

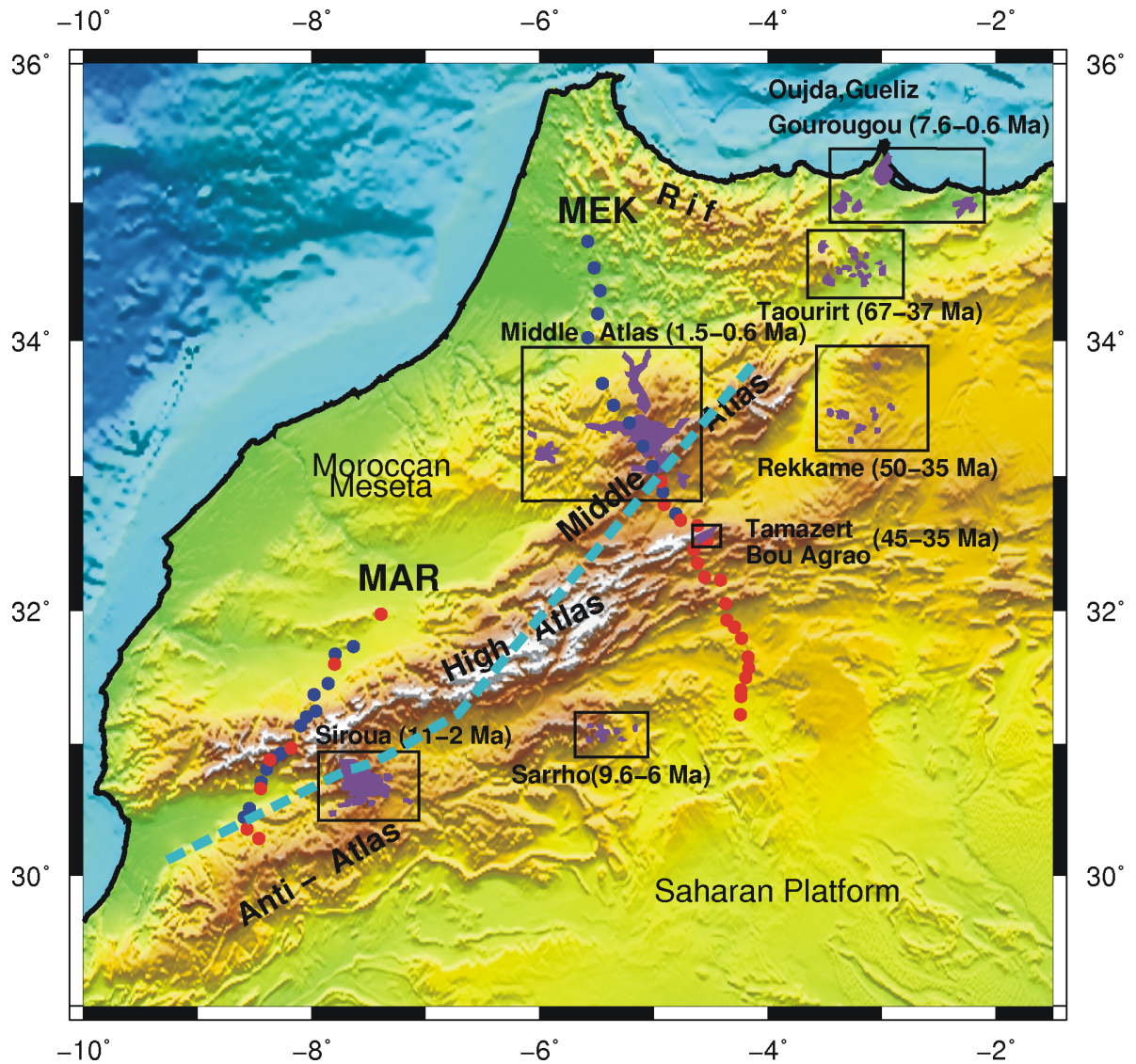


Figure 3.7.: Details of Moroccan Atlas system (Middle Atlas, High Atlas and Anti-Atlas) and location of Cenozoic volcanic centers (purple polygons). Periods of volcanic activity are compiled from [Missenard & Cadoux \(2012\)](#). Blue dashed line shows the axis of lithospheric thinning as evidenced by [Missenard et al. \(2006\)](#), [Fullea et al. \(2010\)](#) and the so-called *Morocco Hot Line* ([de Lamotte et al., 2009](#)). The red solid circles represent broad-band only MT stations and blue ones represent both broad-band and long-period MT stations.

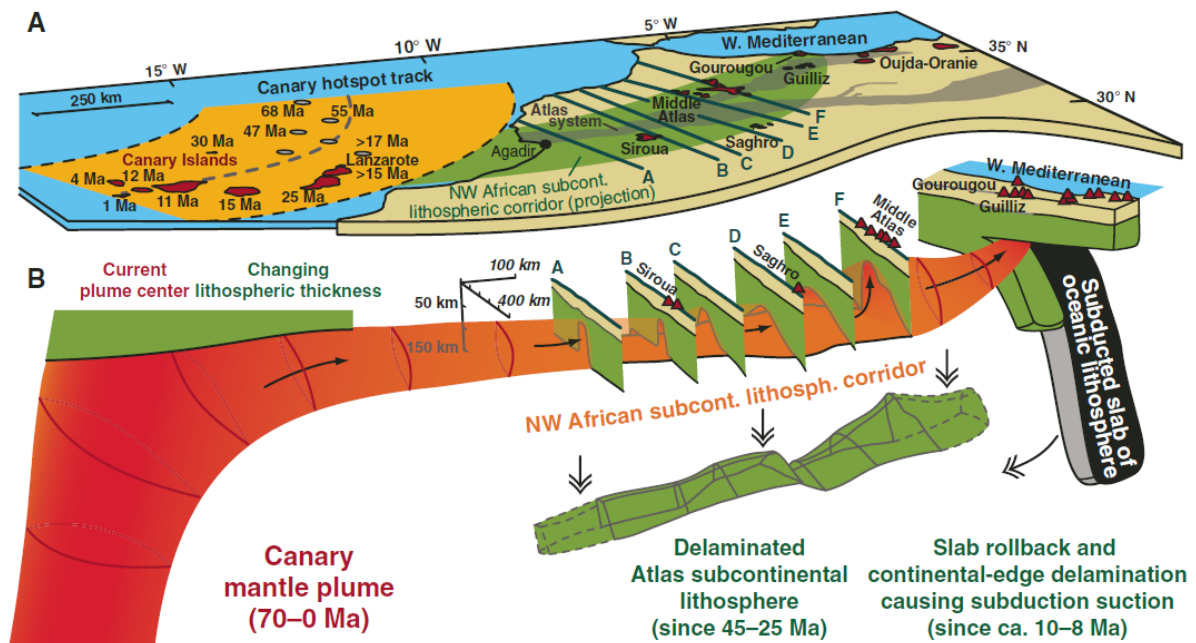


Figure 3.8.: Map of the northwest African plate (**A**) and flow of Canary mantle plume material under northwest Africa through a subcontinental lithospheric corridor in a 3-D model (**B**). **A**: The orange area represents the Canary hotspot track on the oceanic side of the northwest African plate with ages of the oldest lavas from each island (red areas), indicating a southwest-directed age progression and the location of the current plume center beneath the western Canary islands. **B**: The 3-D model illustrates how Canary mantle plume material flows along the base of the oceanic lithosphere that thins to the east and into the subcontinental lithospheric corridor beneath the Atlas system, reaching the western Mediterranean. Plume push, eastward-thinning lithosphere, delamination of northwest African subcontinental lithosphere, and subduction suction related to rollback of the subducting slab in the Mediterranean are proposed to be the main mechanisms for causing Canary plume material to flow ≥ 1500 km to the northeast; *from Duggen et al. (2009).*

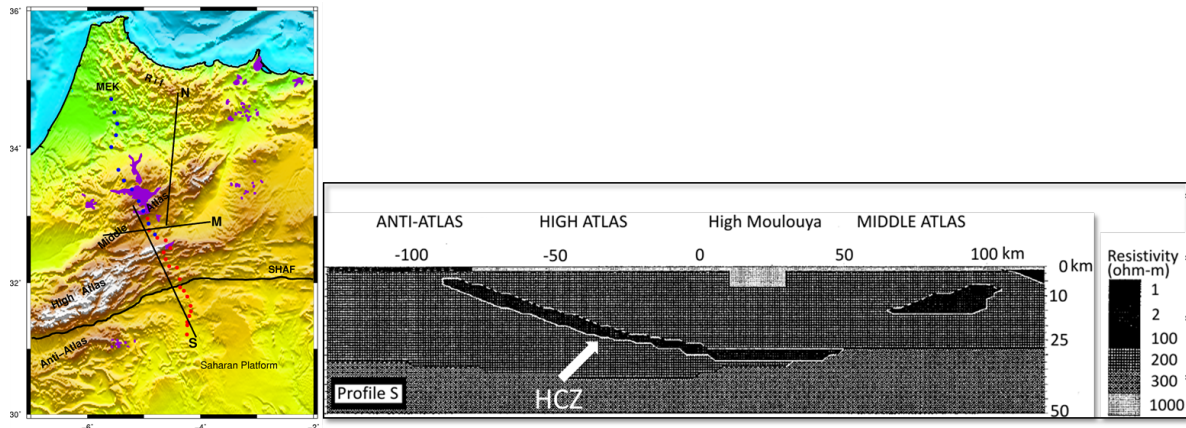


Figure 3.9.: Figure showing the first electrical resistivity model derived from forward modelling of 5-component MT data along the Profile S. (MT data acquired along three profiles: Profiles N (Rif - Middle Atlas), M (High Moulouya - Meseta), and S (Middle Atlas - Anti-Atlas)). Electrical resistivity of the middle and lower crust beneath the Anti-Atlas was determined to about $200 \Omega\text{m}$, the same as for the lower crust of the High and Middle Atlas. The model has a highly resistive ($1000 \Omega\text{m}$) uppermost mantle. The model shows a rather steeply dipping high electrical conductivity zone (HCZ), stretching from the southern border of the High Atlas almost down to Moho depth (36 km) beneath the Moulouya Plain; *modified from Schwarz et al. (1992)*.

a forward trial-and-error approach) shows a crustal low resistivity with total conductance of 2,000 Siemens which extends from the southern border of the High Atlas towards the Middle Atlas (Figure 3.9). As a possible explanation for observed high conductivity in the middle to lower crust, the authors favour of fluids and volatiles that originated due to ancient rifting (early Mesozoic) and associated magmatic activity at the transition from crust to the upper mantle.

More recently in 2009, as part of Topolberia/IberArray project², Anahnah et al. (2011) conducted a lithospheric-scale study along a 380 km long profile with a site spacing of 10 km to 30 km. The NNW-SSE oriented profile also coincides with our MEK profile, because there is only one road over the Atlas Mountains at this longitude. At lower and intermediate crustal-scale ($\sim 15 - 35$ km), the authors imaged resistive bodies, which were attributed to presence of granite batholiths, beneath the Rif and the Middle Atlas. At lithospheric-scale (35 - 100 km), the authors claim that an anomalous mantle with resistivity of $\sim 250 \Omega\text{m}$ is located below the High Atlas inbetween the resistive ($>500 \Omega\text{m}$) Rif lithosphere and that of the resistive ($>2000 \Omega\text{m}$) Anti-Atlas mountains. Observed conductivity anomalies within the first 10 km below the Middle Atlas were inferred to be linked to magma chambers located at the top of the anomalous mantle beneath the Moulouya Plain. However, Jones et al. (2012b) contend that the mantle part of their model is highly suspect

² Topolberia/IberArray project aims to understand the interaction between deep, surficial and atmospheric processes, by integrating research on geology, geophysics, geodesy and geotechnology. The knowledge on the relief changes and its causes is of great social impact concerning the climate change and the evaluation of natural resources and hazards. The southern and northern borders of the Iberian plate (the Betic-Rif system and the Pyrenean-Cantabrian system) and its central core (Meseta and Central-Iberian systems) are the three main domains of research have been identified.

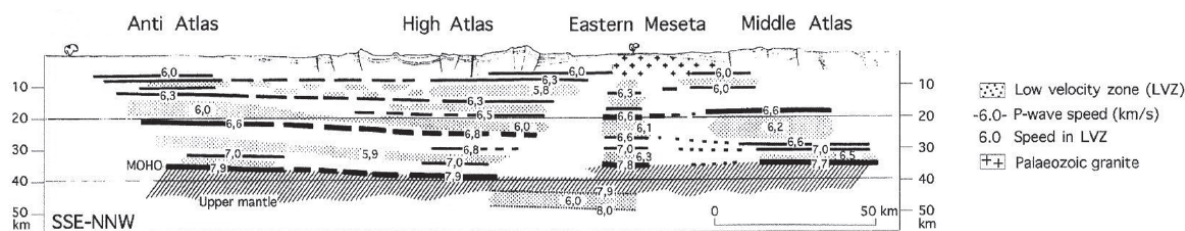


Figure 3.10.: Crustal section for the SSE-NNW profile from the Middle Atlas through High Atlas towards the Anti-Atlas; from Wigger et al. (1992).

and that the evidence for thinned lithosphere is simply non-existent in their data. The reasons for the contentions of Jones et al. (2012b) are outlined in Section 5.2 (Chapter 5).

3.2.2 Active Source Seismology

Seismic refraction studies provided the first estimates of crustal thickness across the Atlas Mountain range. Tadili et al. (1986) modelled refraction and wide-angle data concluding that the crustal thickness varies from 25 km along the Atlantic coast of Morocco to 40 km in the central High Atlas. To the east, crustal thickness in the Midelt-Rich area was estimated to be 38 km, decreasing to 35 km near Errachidia (Figure 3.9). Wigger et al. (1992) carried out a seismic refraction study of the crustal structure beneath the High Atlas and surrounding region. The resulting model shows that the crust is thickest beneath the northern border of High Atlas near Midelt, reaching 38 - 39 km, and thins to the south and north to 35 km (Figure 3.10). The authors obtained relatively low Pn velocities, 7.7 - 7.9 km/s, in the upper mantle.

The most recent wide-angle reflection results by Ayarza et al. (2014) show that crust-mantle boundary (Moho) is modelled with the shallowest depth beneath the Middle Atlas, approximately 31 km, and a crustal root places this boundary at a maximum depth of 40 - 41 km beneath the High Moulouya Plain (i.e., north of the High Atlas) and it shallows progressively up to a depth of 35 km to the Anti-Atlas. The authors reported low V_p values in the lower crust (6.4 km/s and 6.6 km/s characterize the top and bottom of the lower crust in the High Moulouya Plain and in the Middle Atlas) and uppermost mantle of the Middle Atlas and High Atlas (<7.8 km/s).

3.2.3 Seismic Tomography

The most recent P-wave tomography results (Figure 3.11) show a localized low velocity anomaly (approx. 3%) at 75 km beneath the Middle Atlas that extends to ~200 km depth (Bezada et al., 2013), in agreement with Rayleigh wave tomography results (Palomeras et al., 2014). A deep (390 - 530 km) high velocity anomaly beneath the Middle Atlas is interpreted to be evidence for a delamination event beneath the region. The authors' interpretation is that the low velocity anomaly

could be associated with asthenosphere at shallow depth, whereas the fast anomaly could represent the delaminated lithosphere.

With additional seismic stations in the study area, [Bezada et al. \(2014\)](#) have updated the model of [Bezada et al. \(2013\)](#) ([Figure 3.11](#)). The velocity structure for the whole Atlas range, except the Anti-Atlas below 90 km, is dominated by low velocity anomalies. Observed low wave-speed material beneath the Middle Atlas (extends to ~ 200 km) and the High Atlas (extends to ~ 120 km). [Bezada et al. \(2014\)](#) interpreted these zones of lower wave speeds as corresponding to the location of shallow asthenosphere that replaced portions of the lithospheric root following its removal (between 45 - 25 Ma). Below the low velocity zone, [Bezada et al. \(2013, 2014\)](#) imaged a high velocity body at ~ 400 km that was attributed to delamination of the local lithosphere. Unlike [Ramdani \(1998\)](#) and [Duggen et al. \(2009\)](#), [Bezada et al. \(2014\)](#) proposed discontinuous, piecewise delamination of an intrinsically unstable Atlas lithosphere, enabled by combination of tectonic shortening (since the early Miocene and most likely since ~ 45 Ma, ([Gomez et al., 2000](#))) and eclogite loading during Mesozoic rifting and Cenozoic magmatism, and impingement of hot mantle. The presence of hot mantle was thought to be sourced either from regional upwellings in North Africa ([Lustrino & Wilson, 2007](#)), or the Canary Islands hotspot ([Duggen et al., 2009](#)), enhanced the instability of the Atlas lithosphere. Another low velocity anomaly was imaged near the Atlantic coast, which has larger amplitudes at depths >150 km and extends to depths >400 km. In order to investigate if that slow feature at lithospheric depths connects to the Middle Atlas in, or underlies the Siroua and Sahro volcanic fields ([Figure 3.7](#)) in the Anti-Atlas (as proposed by [Missenard et al. \(2006\)](#) and [Duggen et al. \(2009\)](#)), [Bezada et al. \(2014\)](#) conducted a synthetic test. For the synthetic test, a model with a 200 km wide, 5% slow corridor, which follows the lithospheric thinning trend ([Figure 3.7](#)) was constructed. Inverting generated synthetic delays did not fully recover the full extent of the slow corridor, including the areas where the real data did not support slow anomalies. The test results suggest that the lithosphere under the Anti-Atlas is not thinned.

The previous tomography results of [Seber et al. \(1996\)](#), based on teleseismic P-wave-travel-time observations, were also taken to support the proposal that the lithosphere beneath the mountains is abnormally thin.

[Palomeras et al. \(2014\)](#) present the crustal and mantle 3-D shear velocity structure from Rayleigh wave tomography modelling, as shown in [Figure 3.13](#). The Middle and High Atlas and the Western High Atlas are characterized by different shear velocities. The shear velocity beneath the High and Middle Atlas is ~ 3.4 km/s and increases to ~ 3.7 km/s at 25 km. Below the Moho (~ 35 km), the authors define a ~ 10 km thick mantle lid with a velocity of ~ 4.3 km/s. A prominent low shear wave velocity anomaly (~ 4.1 km/s) between $\sim 45 - 100$ km is observed beneath the central High Atlas. In comparison to the central Atlas, the Western High Atlas is defined by a relatively high shear velocity below the Moho (~ 35 km) increasing to almost ~ 4.5 km/s at 65 km depth. The authors suggest that the lithosphere is thinned beneath the Atlas, particularly beneath the Middle

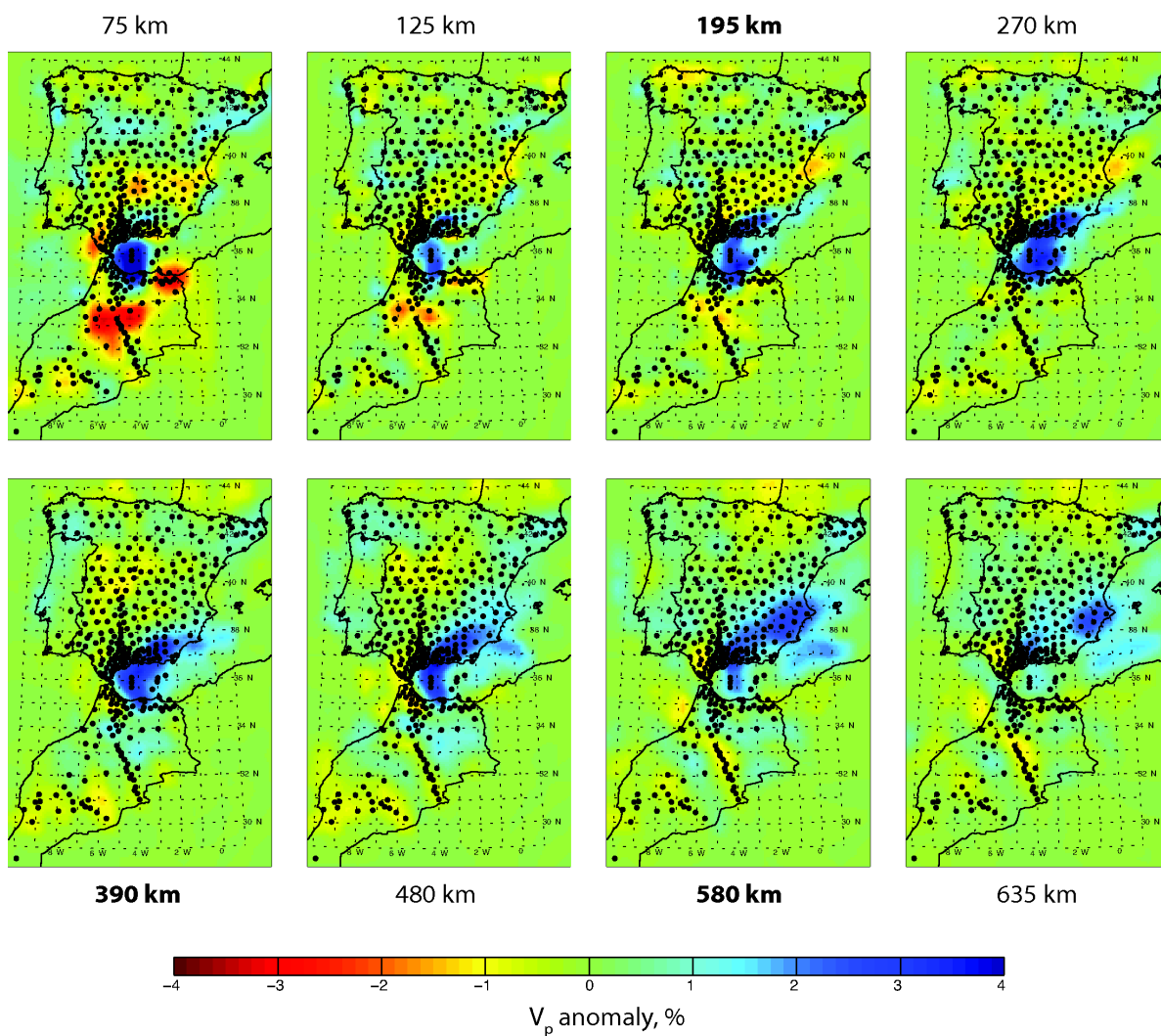


Figure 3.11.: Body wave tomography of the western Mediterranean upper mantle with improved resolution through the use of a large teleseismic dataset, and a crustal velocity structure derived from surface wave modelling (Palomeras et al., 2014). Location of the seismic stations used in the modelling are shown with black solid circles; *modified from Bezada et al. (2013)*.

3.2 PREVIOUS GEOPHYSICAL WORK IN THE ATLAS SYSTEM OF MOROCCO

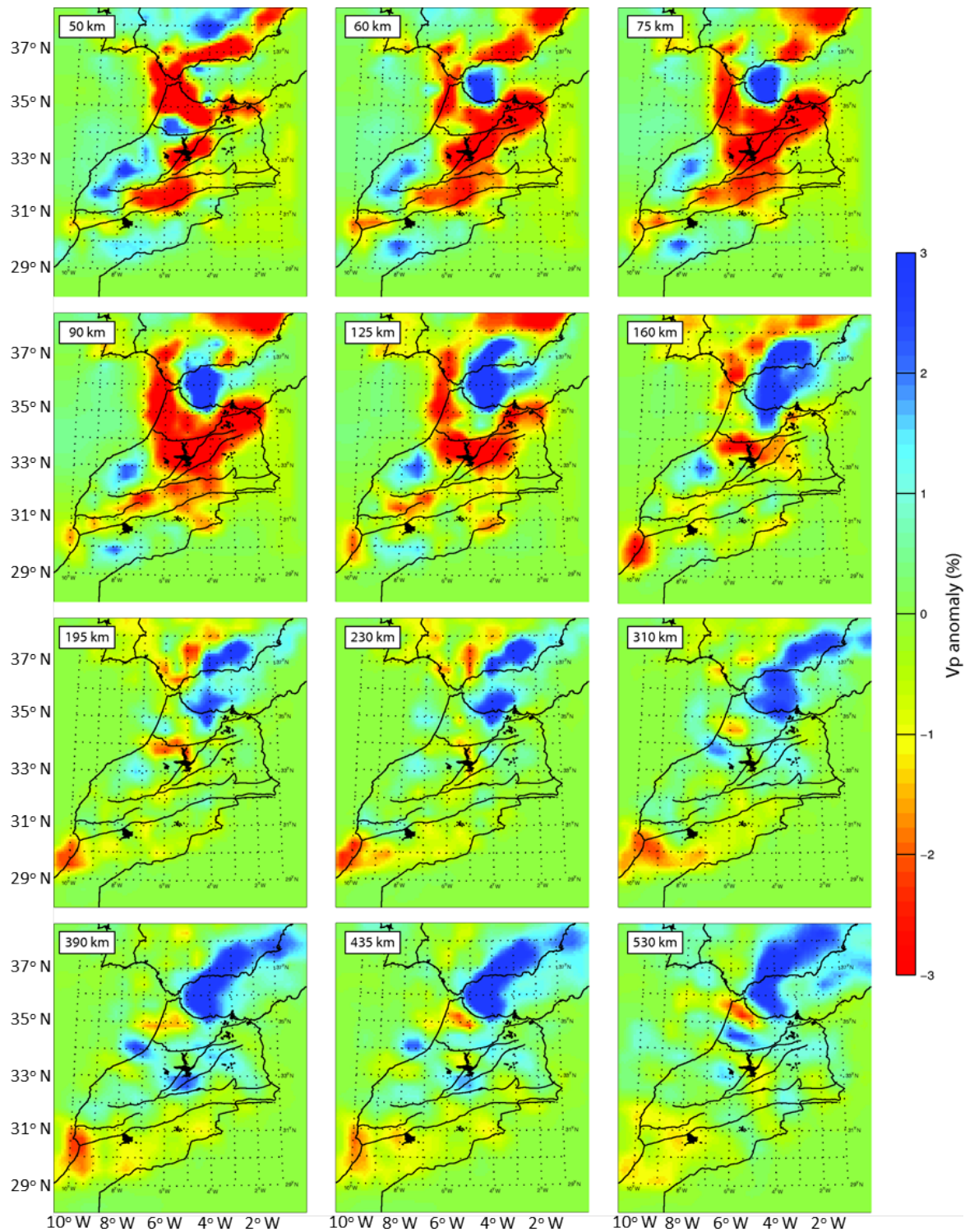


Figure 3.12.: Body wave tomography of the western Mediterranean upper mantle with improved resolution through the use of a large teleseismic dataset and a crustal velocity structure derived from surface wave modelling (Palomeras et al., 2014). Aside from the Alboran slab, the Atlas range is dominated by low velocity anomalies above 160 km. High velocity anomalies are observed beneath the Middle Atlas region below 390 km; *modified from* Bezada et al. (2014).

Atlas and High Atlas, where the LAB may be as shallow as 45 - 50 km, whereas the LAB is found to be 85 - 90 km under the Western High Atlas.

3.2.4 Receiver Functions

Most recent crustal thickness estimates based on S receiver functions by Miller et al. (2013) showed an average of 35 km, which is in agreement with prior seismic refraction and reflection results (Wigger et al., 1992; Ayarza et al., 2005, 2014). Unlike the previous observations though, the crustal thickness beneath the High Moulouya Platform was defined as the thinnest portion of the crust (~ 25 km) by the authors. For the Middle and High Atlas the authors derive a sLABrf (a seismic LAB from receiver functions) depth of ~ 70 km and deepening towards the southern and northern margins of the Atlas mountain belt (~ 100 km).

Earlier receiver function studies of Sandvol et al. (1998) and van der Meijde et al. (2003) showed that the Moho depth beneath the junction between Middle and High Atlas ranges between 36 km and 39 km, which also suggests that there is no significant crustal root beneath the region.

To the south-west, according to S receiver function studies of Spieker et al. (2014), the lithosphere thickness ranges between 70 km and 95 km. The velocity model of Spieker et al. (2014) demonstrated that the lithosphere beneath the western Anti-Atlas is shallower than the central High Atlas. Furthermore, the authors obtained a second interface with velocity reduction at approximately 130 km to 180 km depth. Moho and sLABrf depths are shown in Figure 3.14. Since having ~ 34 km thick crust does not compensate for the high topography, but having strong evidence for a thinned lithosphere, therefore the authors do support the hypothesis of thermal compensation (Teixell et al., 2005; Missenard et al., 2006) beneath the south-western part of the mountains.

3.2.5 Seismic Anisotropy – shear-wave splitting measurements

A shear-wave splitting measurement relies on the observation that when a shear wave with an initial linear polarization enters an anisotropic medium, it is split into two orthogonal components, one of which is oriented parallel to the fast direction of the anisotropic medium. The two orthogonal shear waves propagate through the anisotropic region at different speeds. Therefore, they accumulate a time delay. The azimuth of the fast polarization axis (Φ), and the delay time (δt) contain information about the geometry and the strength (product of percent anisotropy and thickness of the anisotropic layer), respectively, of the anisotropic medium. SKS and direct S are most commonly used phases in the splitting measurement methods. SKS splitting is particularly popular as its initial polarization (before encountering the upper mantle on the receiver side) is controlled by the P-to-S conversion at the core–mantle boundary and is well known. The lateral resolution below the stations is defined by the Fresnel zone of the seismic rays that are analysed. On the contrary, the major limitation of the shear-wave splitting measurements is insensitive to the depth

3.2 PREVIOUS GEOPHYSICAL WORK IN THE ATLAS SYSTEM OF MOROCCO

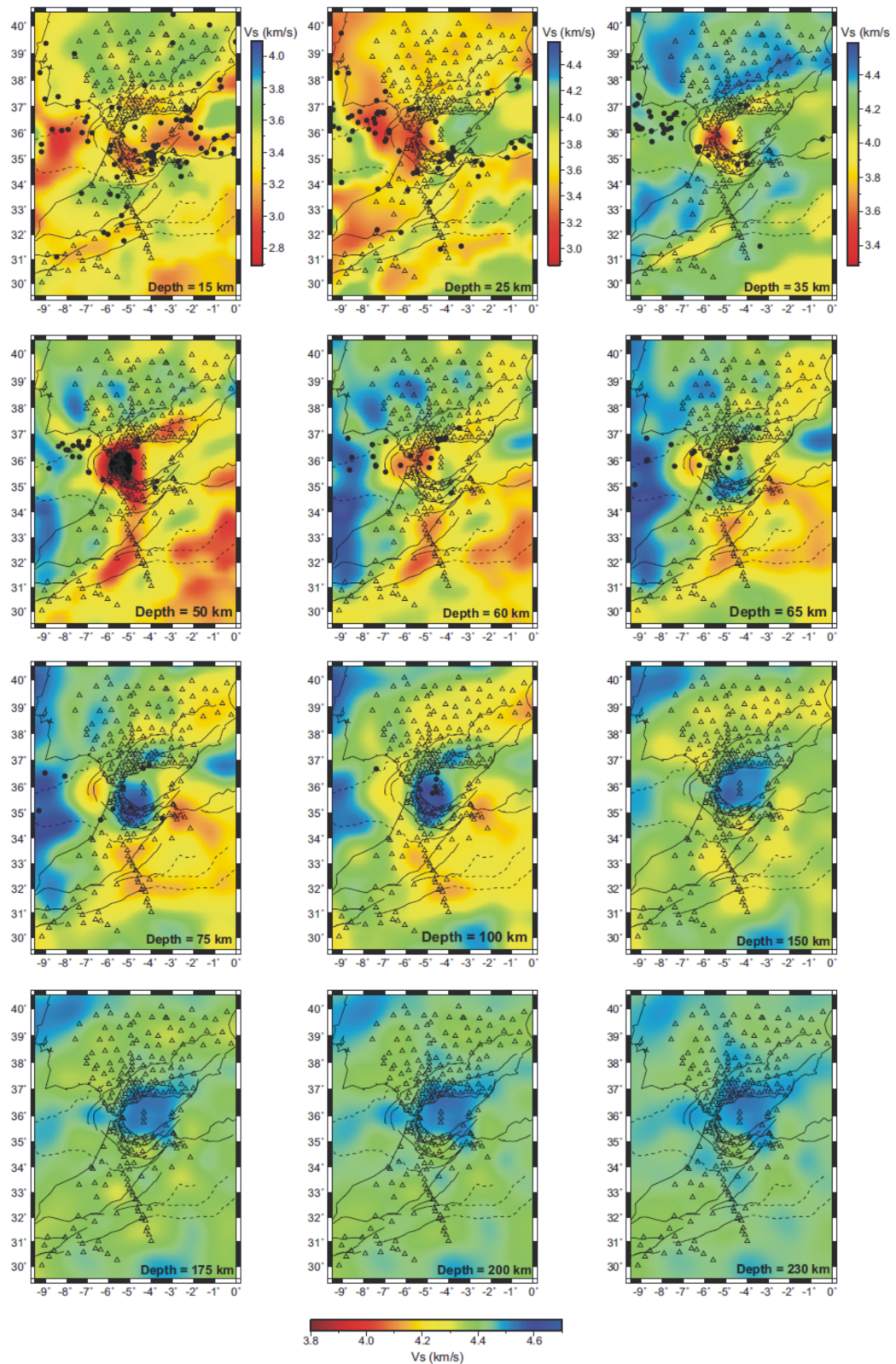


Figure 3.13.: Absolute shear velocity maps at crustal and mantle depths. Triangles represent the station location, and black solid dots are the epicenter locations for earthquakes with $M_w \geq 4.0$ (IGN catalog); *from Palomeras et al. (2014).*

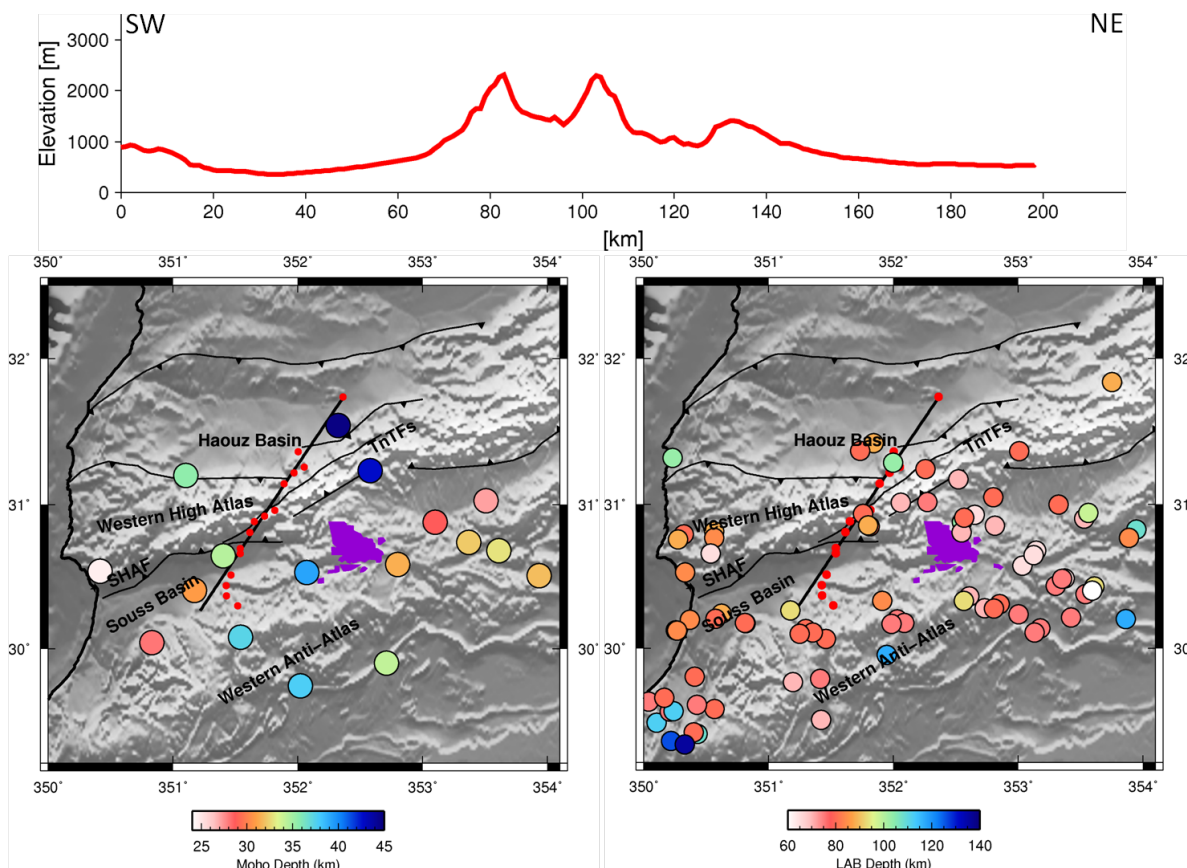


Figure 3.14.: **Bottom-left:** Crustal thickness in the Western High Atlas as derived from P-wave receiver function analysis. Moho depths are given by colour scale. **Bottom-right:** LAB depth (sLABrf) in the study area based on S-wave receiver function. sLABrf depths are given by colour scale. Small red circles in both figures represent the TopoMed magnetotelluric data, and top panel shows the elevation profile along the black solid line. The purple polygon shows the location of Siroua Cenozoic volcanic center. Moho and sLABrf depths information were provided by Kathrin Spieker.

extent and vertical position of the anisotropic layer, since they are path-integrated measurements (Long & Becker, 2010; Miller et al., 2013; Diaz & Gallart, 2014).

Most recently, Miller et al. (2013), as part of PICASSO project, analysed shear-wave delay time for S and SKS phases at 105 densely spaced broadband seismic stations from Iberia to southern Morocco (Figure 3.15). The splitting results for both the S and SKS phases confirm that the peak (~ 3 s average for S and ~ 1.5 s for SKS) in magnitude of delay time occurs along the axis of High Atlas, and descending on the flanks of each side of the mountain range. The results were interpreted to reflect possible channelized flow along the orogen, which could be the result of variation in lithospheric thickness across Morocco, given that the largest inferred anisotropy coincides with domains where thinned lithosphere has been suggested (e.g., Teixell et al., 2005; Zeyen et al., 2005; Missenard et al., 2006; Fullea et al., 2010). Similar to the southernmost splitting results for stations on the edge of the West African Craton, delay times in the Anti-Atlas and Western High Atlas are less than 1 s, which is attributed to frozen-in anisotropy closer to West African Craton. Observed apparent fast polarization directions are approximately parallel to the axis of the mountain range.

3.2.6 Surface Heat Flow Data and Thermal Models

Rimi (1999) constructed 1-D crustal heat generation models and geotherms for the major Moroccan geological domains extending from the Precambrian units in the south to the Alpine units in the north. The author used two types of heat flow data: (i) classical thermal profiles and (ii) conductivities measured in a range of shallow depths (100 - 500 m) and conductivity estimations in oil exploration wells at greater depths (1 - 5 km). The Anti-Atlas is characterized by low surface heat flow density (40 mW/m^2), and it increases from 70 mW/m^2 in the junction between the High and Middle Atlas to 83 mW/m^2 in the Middle Atlas. The calculated temperature-depth profiles for the main Moroccan structural domains (Figure 3.16) show divergent trends in Morocco. Whereas the Alboran basin, the Rif, and the Middle Atlas represent regions of high crustal temperatures, the temperature distribution within the Anti-Atlas, which belongs to the West African Craton, is characterized by a low-temperature ($370 \text{ }^\circ\text{C}$ at the Moho, 35 km) depth dependence. The highest temperature profile ($890 \text{ }^\circ\text{C} \pm 84$ at the Moho) is calculated below the Middle Atlas, whereas the thermal regime in the High Atlas domain remains "normal" ($511 \text{ }^\circ\text{C} \pm 87$ at the Moho). For the High Moulouya Plain, temperature of $695 \text{ }^\circ\text{C} \pm 48$ at a depth of 35 km was estimated.

3.2.7 Seismicity

Figure 3.17 demonstrates that seismicity occurs concentrated in NE-SW trending zone, covering Middle Atlas, Central High Atlas and western part of Anti-Atlas. Seismic activity in the Atlas system in north-western Africa is associated with the plate boundary between Eurasia and Africa and with the transform faults reaching from the Mid-Atlantic ridge to the Azores and farther into

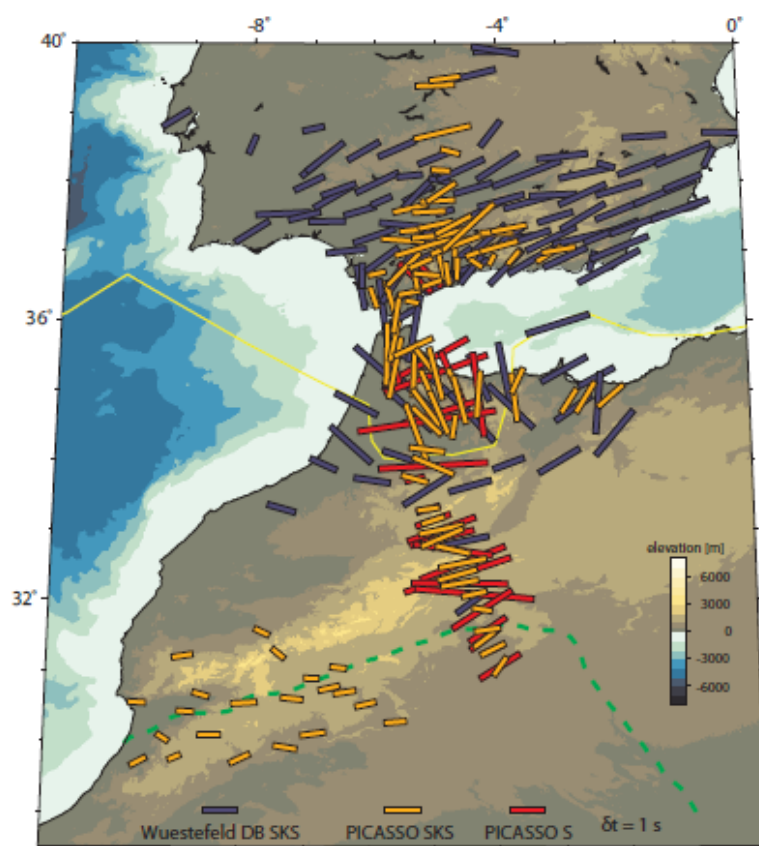


Figure 3.15.: Station-averaged SK(K)S splitting plotted centered at the station location from the [Wuestefeld et al. \(2009\)](#) updated database which includes the studies of [Buontempo et al. \(2008\)](#) and [Diaz et al. \(2010\)](#) (dark blue), new SK(K)S (orange), and direct S results from the deep (>600 km) focus earthquake, that occurred beneath Grenada on April 11, 2010). The bar azimuth denotes the direction of fast polarization, with delay time proportional to bar length. The dashed green line shows the approximate location of the West African Craton; *from* [Miller et al. \(2013\)](#).

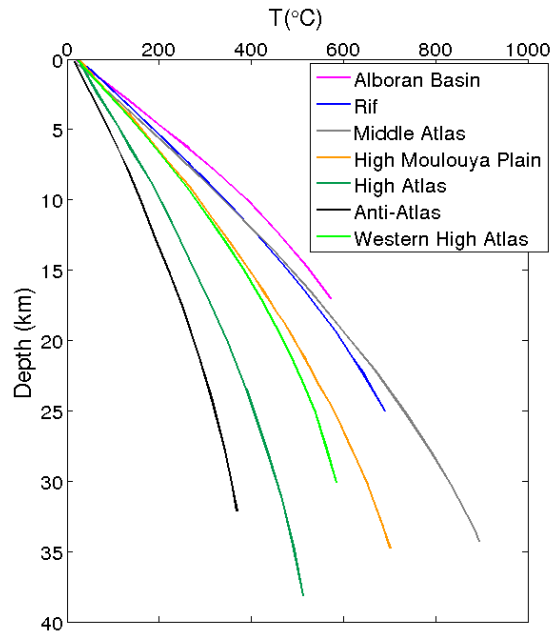


Figure 3.16.: Average crustal geotherms: Alboran Basin, Rif, Middle Atlas, High Moulouya Plain, High Atlas, Anti-Atlas, Western High Atlas and Anti-Atlas; *redrawn after Rimi (1999)*.

the strait of Gibraltar (Schwarz & Wigger, 1988). It comprises mostly shallow earthquakes ($0 < z < 50$ km) with small to moderate magnitude ($M \leq 5$). However, Hatzfeld & Frogneux (1981) confirmed that more than 30 events with small magnitude ($M \leq 3.5$) have a focal depth ≥ 40 km, especially in the High Atlas. In order to explain the occurrence of intermediate-depth earthquakes under the High Atlas and Middle Atlas and magmatism, delamination of Atlas lithosphere was also proposed by Ramdani (1998). The author suggested that the zone affected by delamination is assumed at depths 50-165 km, as 165 km corresponds to the deeper recorded earthquakes. In this case, the interpretation of Bezada et al. (2014) is in conflict with the reports of intermediate-depth earthquakes within what the authors consider to be the asthenosphere (Figure 3.12).

3.2.8 Integrated Geophysical and Petrological Modelling

In order to identify the geometry of the lithospheric structure beneath the Atlas Mountains, several authors have recently performed forward modelling of crustal and lithospheric thicknesses that integrates topography, geoid anomalies, surface heat flow data, and seismic data in a petrological-geophysical consistent manner (e.g., Teixell et al., 2005; Zeyen et al., 2005; Missenard et al., 2006; Fullea et al., 2010). Those authors all identified an anomalously thin lithosphere beneath the Mountains, but the magnitude, shape, and exact location of the lithospheric thinning vary significantly amongst their models due to the different crustal structure modelled in each case. The resulting map of Moho depths (Figure 3.18A) shows a moderately thick crust, with Moho

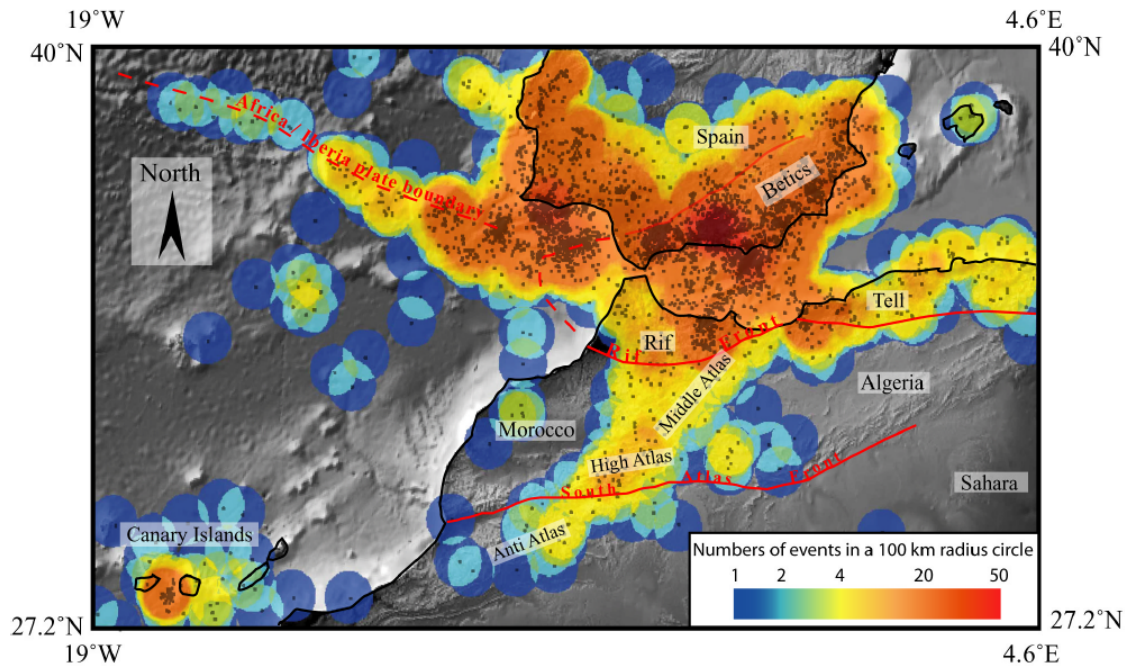


Figure 3.17.: Density map of seismicity in the Mediterranean-Atlantic transition zone calculated from ISC database for the 1995-2000 time interval; *from* Missenard et al. (2006). Grey points show epicenters.

depths of 38 km, below the most elevated parts of High Atlas, then decreasing southeastward down to 30 - 32 km. The map at the base of the purported lithosphere (Figure 3.18B) shows a prominent, NE-trending zone of thinned lithosphere beneath the Atlas Mountains. The thinnest lithosphere obtained in this model is in the Middle Atlas (<80 km) and in the central High Atlas, and eastern Anti-Atlas (90 km).

Fullea et al. (2010) compiled the lithospheric structure, which was described by the authors (e.g., Teixell et al., 2005; Zeyen et al., 2005; Missenard et al., 2006), along the southwestern Iberia-Gulf of Cadiz-Morocco NW-SE transect (Figure 3.19). The southern part of this transect crosses the geological domains of Morocco from the Middle Atlas in the north to the Anti-Atlas in the south. In the latter area, based on prior studies, the lithosphere thickness is thought to be ~140 km and ~70 km beneath the Middle Atlas. Missenard et al. (2006) associated this major lithospheric mantle thinning beneath the Atlas Mountains with Miocene to recent alkaline volcanism and seismicity. The authors proposed that this thermal anomaly is related to a shallow mantle plume, emplaced during middle to late Miocene time, during a period of relative tectonic quiescence. This view has also been proposed by other authors as well (Teixell et al., 2005; Zeyen et al., 2005; Fullea et al., 2010). Fullea et al. (2010) also claim that small-scale convection mechanism(s) can be responsible for the modelled lithospheric thinning beneath the Atlas, as the Atlas represents a relative thinned lithospheric region in comparison to the surrounding thick lithospheric domains of the West African Craton and Moroccan Atlantic Margin. Therefore, the undulation of the LAB topography would have enhanced small-scale convection of the sublithospheric mantle with a localized upward flow

3.2 PREVIOUS GEOPHYSICAL WORK IN THE ATLAS SYSTEM OF MOROCCO

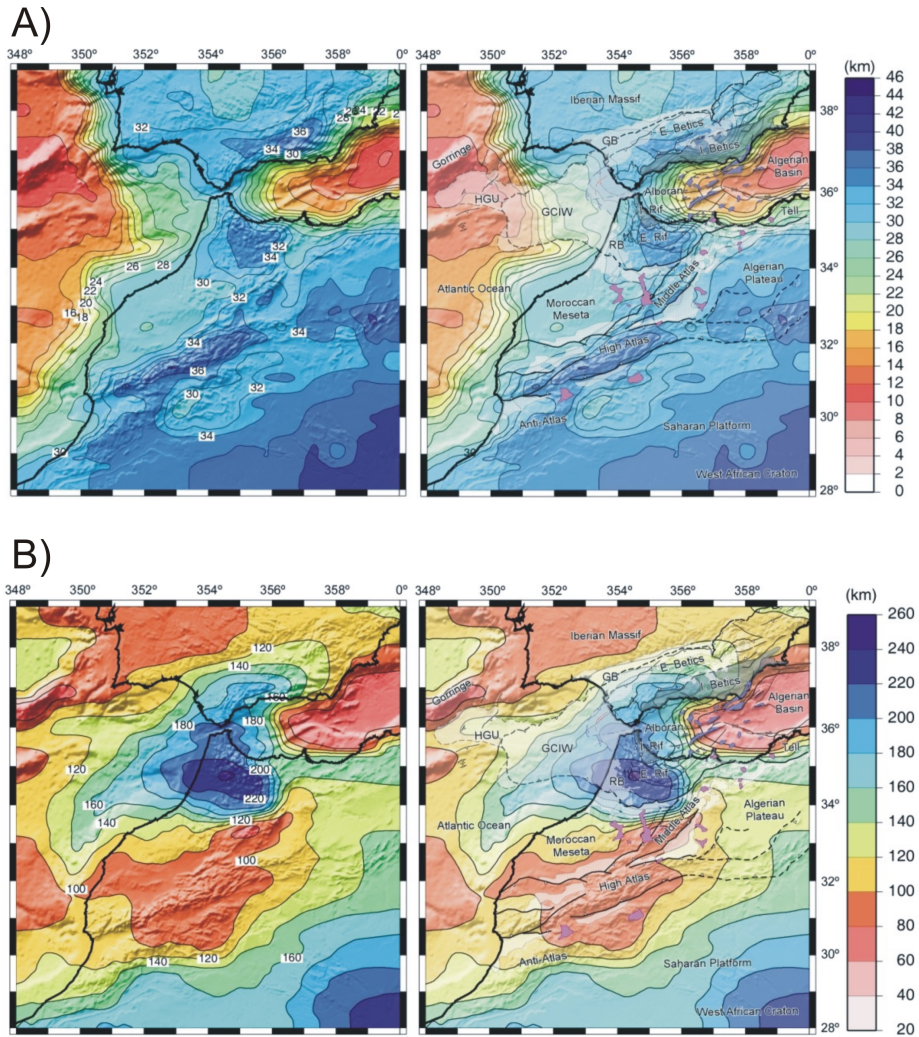


Figure 3.18.: Structure of the lithosphere of the Atlantic-Mediterranean Transition Region derived from topography, geoid anomalies, surface heat flow data, and seismic data modelling; *from Fullea et al. (2010)*. **A)** Maps of the Moho depths. Isolines every 2 km. **B)** LAB depth maps superimposed to the structural map with the main tectonic units and volcanism. Isolines every 20 km.

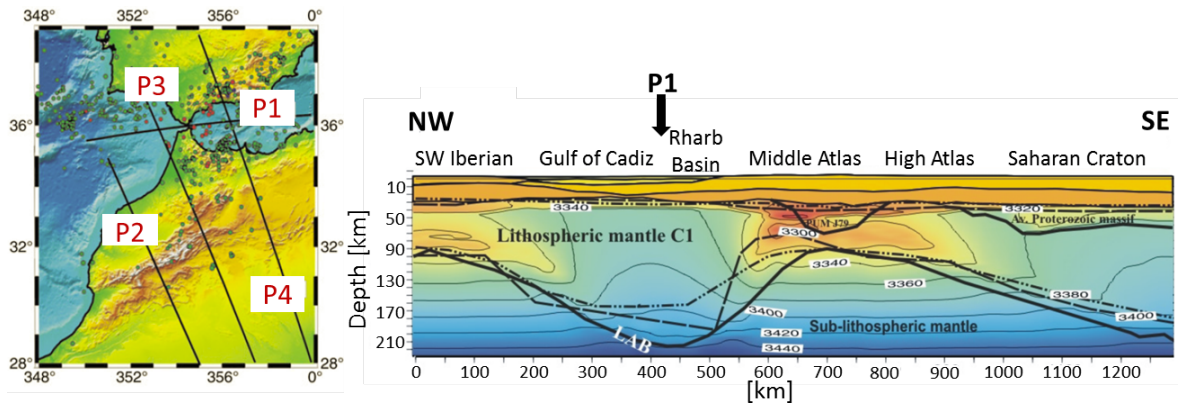


Figure 3.19.: Lithospheric model from [Fullea et al. \(2010\)](#) (thick solid line) along the profile P3 (coincides with the MT profile MEK, see [Figure 3.7](#) or [Figure 4.1](#)). Superimposed on the right-hand figure are the crust-mantle boundary and LAB geometries from previous works: dashed line ([Zeyen et al., 2005](#)), dash-dotted line ([Missenard et al., 2006](#)); *modified from Fullea et al. (2010)*.

beneath the Atlas. Note that this is entirely speculative - there has been no geodynamic modelling of this area that includes such small-scale convection cells.

Crustal and lithospheric-probing magnetotelluric (MT) data would provide a valuable additional information to previous and on-going studies in the study area. The MT imaging of the crustal and upper mantle structures has played an important role in the characterization of the active collision zones (such as the India-Asia collision zone and the Arabia-Eurasia collision zone) or the collision zones at later stage evolution (such as the European Alps and Pyrenees). The MT imaging is essential to distinguish between a strong, thick lithosphere and a weak lithosphere. While partial melting in the lower crust and upper mantle can cause 6 - 7% reduction in seismic velocity, the same amount of partial melting can increase the conductivity by two orders of magnitude ([Schilling et al., 1997](#)).

Part II

THE MAGNETOTELLURIC EXPERIMENT ACROSS THE ATLAS
MOUNTAINS OF MOROCCO

DATA ACQUISITION, PROCESSING AND ANALYSIS

This chapter describes the planning, data collection and processing steps of the 2009 - 2010 Magnetotelluric Experiment of the TopoMed Project, including the instrumentation and data acquisition parameters. Data imaging, analysis, and preliminary interpretation approaches, which can be used before any forward modelling or inversion tool, are also discussed and illustrated.

4.1 THE TOPOMED-PICASSO PROJECT

The PICASSO (Program to Investigate Convective Alboran Sea System Overturn) project, and the concomitant TopoMed (Plate re-organization in the western Mediterranean: Lithospheric causes and topographic consequences) project were funded by Science Foundation Ireland (SFI) and the Irish Research Council for Science Engineering and Technology (IRCSET), respectively. The two project consortia are multi-national, multi-disciplinary and multi-institutional academic collaborations. The principal, overarching objective of PICASSO/TopoMed projects is to determine the three-dimensional internal structure of the crust and the lithosphere of the Alboran Sea, Betics, Rif, Atlas Mountain belt and surrounding areas in the western Mediterranean, with special emphasis on the geometry of the upper mantle, in order to deduce the lithospheric processes that have and are taking place. A particular focus of PICASSO investigations is the Alboran Sea anomaly. Four competing models are proposed to explain it; retreating subduction, slab break-off, delamination, and convective removal (Calvert et al., 2000). However, the Alboran Sea, will never be fully understood without an intimate understanding of the roles of the Atlas and Rif-Betic Mountain systems. Therefore, the focus of PICASSO by the DIAS MT team is primarily Iberia, whereas the focus of TopoMed is the Atlas Mountains of Morocco.

The PICASSO project was primarily organized initially by Spanish (leader: Institut de Ciències de la Terra "Jaume Almera" (IJA), Barcelona, Spain) and then subsequently U.S. (leader: Rice University, Houston, Texas) investigators, and was a Cooperative Research Project within the EUROCORES TOPO-EUROPE project orchestrated by the European Science Foundation, with six Individual Projects (IPs), and was selected as a pilot program for the nascent EuroArray programs. Currently, PICASSO institutions include Rice University, the University of Oregon, the University of Southern California, and Woods Hole Oceanographic Institution in U.S., IJA, the University of

Barcelona, and the University of Salamanca in Spain, Dublin Institute for Advanced Studies in Ireland, GEOMAR and the University of Munster in Germany, and the Scientific Institute of Rabat, in Morocco.

The various projects included in PICASSO involves land and sea magnetotelluric measurements, active and passive seismic experiments, geochemical sampling, structural geology, and geodynamic investigations of the western Mediterranean, and particularly of the Betics, the Gibraltar Arc, the Alboran Sea, the Rif, and the Atlas Mountains. An active seismic component of the project, led by IJA and the University of Salamanca, is affiliated with SIMA¹/PICASSO projects. In April 2010, a ~500 km long seismic refraction survey extending from the Sahara Desert to the western edge of the Rif Mountains was conducted, which coincides with one of the MT profiles in Morocco (Figure 4.1a). An 85 element broad-band passive seismic array was deployed from 2009 through 2013 in a roughly north-south line from the Iberian Massif in central Spain, across the Betics, the Gibraltar Strait, the Rif Mountains, the Middle and the High Atlas and ending on the Sahara Platform (Figure 4.1b). In order to increase the density of the more regionally distributed IberArray and SIBERIA arrays, some of the seismic stations were also deployed in aerial arrays (Palomeras et al., 2014). Figure 4.1b shows the IberArray stations as well as the existing permanent seismic networks in the western Mediterranean region. Details of both active and passive seismic experiment results are discussed in detail in Section 3.2.2, Section 3.2.3, Section 3.2.4, and Section 3.2.5 (Chapter 3).

Similar multi-disciplinary projects have demonstrated the advantages of using an integrated geophysical approach to tectonic studies. For example, in 1992 the INDEPTH project (InterNational Deep Profiling Tibet and the Himalaya) was launched to develop a better understanding of the deep structure mechanics of the Himalaya-Tibet region (Nelson et al., 1996). While the first phase of the project involved primarily seismology, with a deep seismic reflection transect (Zhao et al., 1993), the geophysical techniques in the subsequent phases (II, III and IV) broadened with the introduction of passive seismic and magnetotelluric imaging as well as geological mapping (e.g., Tilmann et al., 2003; Unsworth et al., 2004; Le Pape, 2013). In the framework of the INDEPTH phase II, combining seismic and magnetotelluric observations, high electrical conductivity and low seismic velocity highlighted the presence of fluids and partially molten material in the crust of Southern Tibet. Those results initiated the development of the Himalayan channel flow and Tibetan crustal flow models.

As discussed in Chapter 3, the Atlas mountains apparently have an anomalously thin lithosphere beneath them, although the magnitude, shape, and exact location of this lithospheric thinning vary considerably amongst authors. Thus, there was a particular need to collect high quality deep sounding magnetotelluric data in this region in order to test the recent models constructed from seismic tomography, seismic SKS, and integrated geophysical observations. As well as providing structural information within the crust, the magnetotelluric method is particularly suited for imaging the lithosphere-asthenosphere (LAB), as electrical conductivity is highly sensitive to temperature and the onset of even small fractions of partial melt (Jones, 1999).

1 Seismic Investigations of the Moroccan Atlas

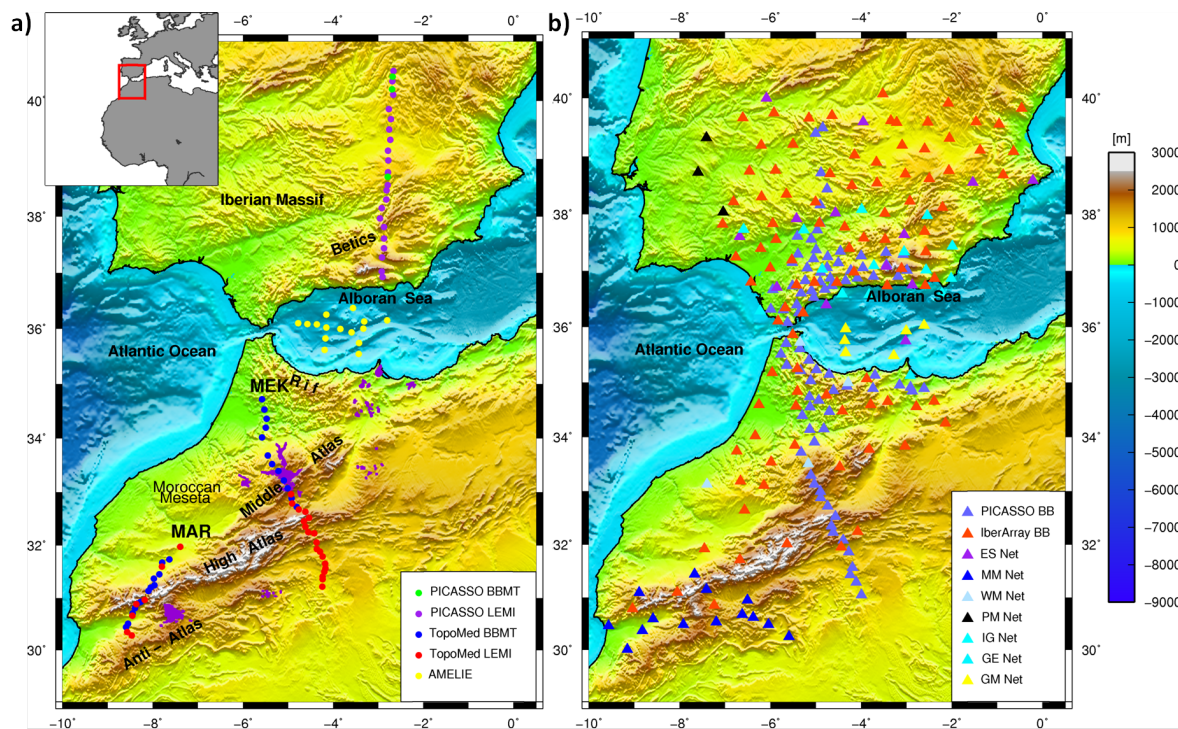


Figure 4.1.: Overview of all PICASSO-TopoMed MT and seismic site locations. **(a)** Topographic map (ETOPO2 Global Data Base; [Smith & Sandwell \(1997\)](#); [Sandwell & Smith \(1997\)](#)) of the study area showing MT site locations across the Iberian Massif, Alboran Sea, and Atlas Mountains, together with location of the Cenozoic alkaline volcanism outcrops (purple polygons). The periods of volcanic activity are compiled from [Missenard & Cadoux \(2012\)](#). For the TopoMed MT survey, the red solid circles represent broad-band only sites and the blue ones represent both broad-band and long-period sites. The map inset shows the study region of both PICASSO and TopoMed projects outlined by a red box. **(b)** Location of broad-band seismic stations and different networks are shown by coloured triangles.

The PICASSO/TopoMed projects initially proposed the collection of broad-band and long-period MT data on the three land-based transects following [Teixell et al. \(2003\)](#) to compare and contrast lithospheric structure and geometries with the models of [Teixell et al. \(2005\)](#). However, there were deviations from this ideal layout as a consequence of both road access and security issues. Therefore, MT data set were acquired along only two profiles ([Figure 4.1a](#)): a N-S oriented profile through the Middle Atlas to the east and a NE-SW profile through the Western High Atlas to the west.

4.2 BROAD-BAND AND LONG-PERIOD MT DATA ACQUISITION

The MT experiment across the Atlas mountains started in September, 2009 and ended in February, 2010. In total, 25 long-period (~ 15 s - 10,000+ s) and 42 broad-band measurements (~ 0.003 s - 5,000+ s) were made on two profiles across the mountains. These data acquired during two separate field campaigns, Phase I and Phase II, during late September 2009 and February 2010 in joint fieldwork by Dublin Institute for Advanced Studies, University of Barcelona, University of Bari, and University of Meknes.

TopoMed fieldwork – phase I

The first phase of MT measurements was carried out from late-September to mid-December, 2009 on profile MAR and the southern half of profile MEK. The first long-period MT station of the survey was deployed in the foothills of the Western High Atlas mountains, which is approximately 50 km away from Marrakesh city, on the tenth of October, 2009. A total of 13 long-period stations were subsequently deployed on the MAR profile between north of Marrakesh and south of Taroudant ([Figure 4.1a](#)). These sites recorded data at a 1 second sampling rate for approximately 2 weeks. Service checks on the sites were performed every week in order to verify the status of data acquisition and to check for potential problems with the site and the recorded time series. In addition, 20 broad-band MT stations were deployed at approximately 10 km intervals along the profile. Meanwhile, BBMT data were collected at 22 stations along the southern portion of the MEK profile which extends approximately 500 km from the Rif to the Sahara Platform ([Figure 4.1a](#)).

In mid-December, the LEMI acquisition started recording at 12 stations (blue circles along the MEK profile on [Figure 4.1a](#)) on the northern part of the MEK profile. These stations were extended for approximately 2 months, from a planned deployment time of 4 weeks to 8 weeks, due to the very low solar activity in 2009. According to the NASA report, there were no sunspots observed on 260 days (71%) of the year. [Figure 4.2](#) shows Daily International Sunspot Numbers which vary between 0 and 40 from October 2009 to February 2010.

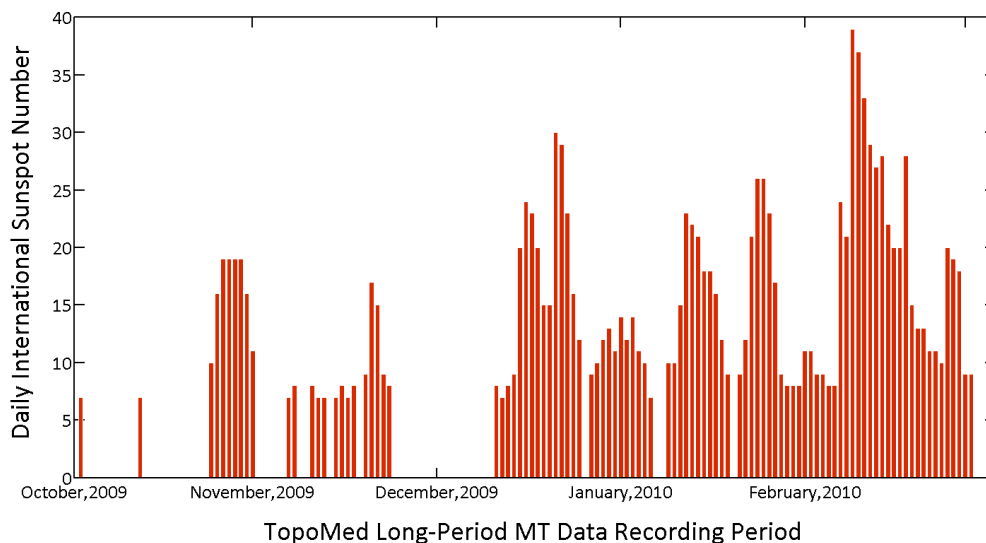


Figure 4.2.: Daily international sunspot numbers for the period during the acquisition of the long-period MT data. Sunspot data obtained from the Sunspot Index Data Centre maintained by the Royal Observatory of Belgium.

TopoMed fieldwork – phase II

The second phase of the field campaign took place in February 2010 to retrieve the LEMI stations and continue BBMT data collection along the northern part of the MEK profile. However, due to poor data quality, these BBMT data were not used.

4.3 INSTRUMENTATION

4.3.1 *Broad-Band MT System*

Within the TopoMed project, two different broad-band MT systems were used: a system built by Phoenix Geophysics (Figure 4.3) owned by DIAS and EMI's MT-24LF system owned by University of Bari. The recording boxes of the Phoenix system, MTU5s and MTU5As, are able to record data in the MT range (0,001 s - 50,000 s) and the AMT-MT range (0.00001 s - 50,000 s) respectively. The MTU5s/MTU5As record up to two electric channels and three magnetic channels simultaneously. A GPS antenna provides the geographic coordinates and the elevation of the site, and a continuous time signal that allows accurate recording of the time series to allow synchronization with remote reference stations. The sensors used for measuring time variations of horizontal electric fields were non-polarizing lead, lead-chloride (Pb - PbCl) electrodes in an X-configuration (Figure 4.4). Magnetic field variations were measured with three orthogonal 1,41 m long MTC-50 induction



Figure 4.3.: Phoenix V5-2000 MT system. From left to right: non-polarizing lead, lead-chloride (Pb - PbCl) electrodes, induction coil cables, MTC-50 induction coils, battery, recording unit, case for the unit, and GPS antenna. Photo courtesy Phoenix Geophysics.

coils that measure the temporal changes in the magnetic field through the voltage induced in a coil. According to manufacturer's specifications, these coils can provide high quality MT data in the range 0.0025 s to 50,000 s. However, the longest usable periods recorded in the TopoMed project are only a few 1,000 s, because of the short acquisition time of 3 days at each site, relative low signal due to cultural noise and a minimum in the solar cycle. The power required to run the MT system was provided by a 12 V 33 Ah battery.

Figure 4.4 shows a typical set-up used for the sites in the TopoMed project. A ground electrode was at the centre of the layout while four other electrodes were located in geographical orientation with respect to magnetic north - approximately 45 m, where possible, each - north, south, east and west of the ground electrode. The electrodes were put into buckets filled with mud made from local soil and salt water in order to lower the contact resistance with the ground and to keep the electrodes moist for longer in the hot and dry climate. These buckets were buried in the ground as deep as possible, as well as the magnetic sensors once they were aligned north-south or east-west (horizontal coils) and levelled (horizontal and vertical coils). The sensors were buried to protect them against human and animal interference, reduce movement caused by wind or animals dragging on the cables and to give thermal stability.

4.3.2 The Long-Period Magnetotelluric Instrumentation (LMTI, LEMI-417M)

Long-period MT data were recorded using the 22 Ukrainian Lviv long-period called LEMI-417M instruments owned by Dublin Institute for Advanced Studies (Figure 4.5). With these systems time variations of orthogonal horizontal electric (E_x , E_y) and magnetic (H_x , H_y , H_z) fields were measured at the Earth's surface, and all data were stored on a flash card. While the time variations of electric fields were measured by non-polarized copper, copper-sulphide (Cu - CuSO_4) electrodes

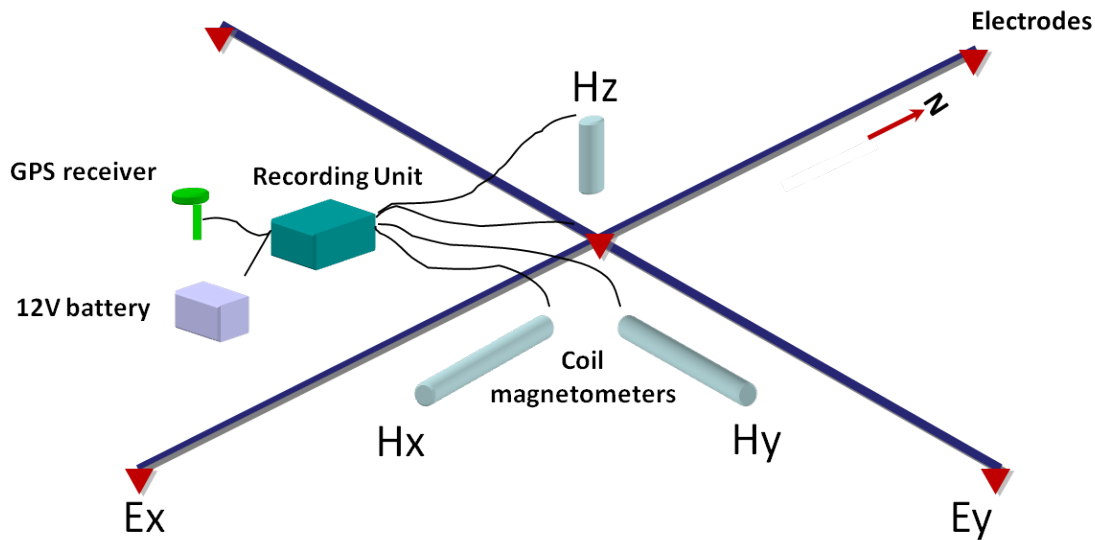


Figure 4.4.: Schematic layout of the broad-band MT recording system used during the TopoMed fieldwork campaigns.

(Figure 4.5), variations of Earth's magnetic fields were measured using fluxgate magnetometer. The sampling rate was 1 s and timing of the data collection was accurately determined from GPS signals.

4.4 TIME SERIES DATA PROCESSING

4.4.1 Time Series Data

Figure 4.6 displays 20 days of typical time series data recorded simultaneously at a location in the Middle Atlas and in the High Moulouya Plain along the MEK profile. Note the similarity of the horizontal magnetic fields recorded at these stations, even though they are separated by ~ 40 km. On the other hand, the electric and vertical magnetic fields data set show much greater variations from site to site since they depend on the electrical resistivity of the subsurface.

4.4.2 Data Processing

After visual inspection of the time series and removal of bad or null data, the data were processed with modern processing techniques (see Section 2.8 in Chapter 2) to ensure that the most accurate and reliable MT response curves are produced to the longest period possible for each site. Three different robust remote reference methods (those of Jones et al. (1989), Smirnov (2003), and Chave & Thomson (2004)) were tested to obtain optimum MT response for each LEMI site. Among these, the processing algorithm by Smirnov (2003) yielded superior results in terms of the usable period range and scattering of the impedance estimates, and was therefore used for further processing.



Figure 4.5.: The Long-period Magnetotelluric Instrument (LMTI) LEMI-417M. From left to right: fluxgate magnetometer with 10 m cable and installation platform, electronic unit (black box), the lead-free non-polarizing copper, copper-sulphide ($\text{Cu} - \text{CuSO}_4$) electrodes, electric lines terminal, and GPS antenna.

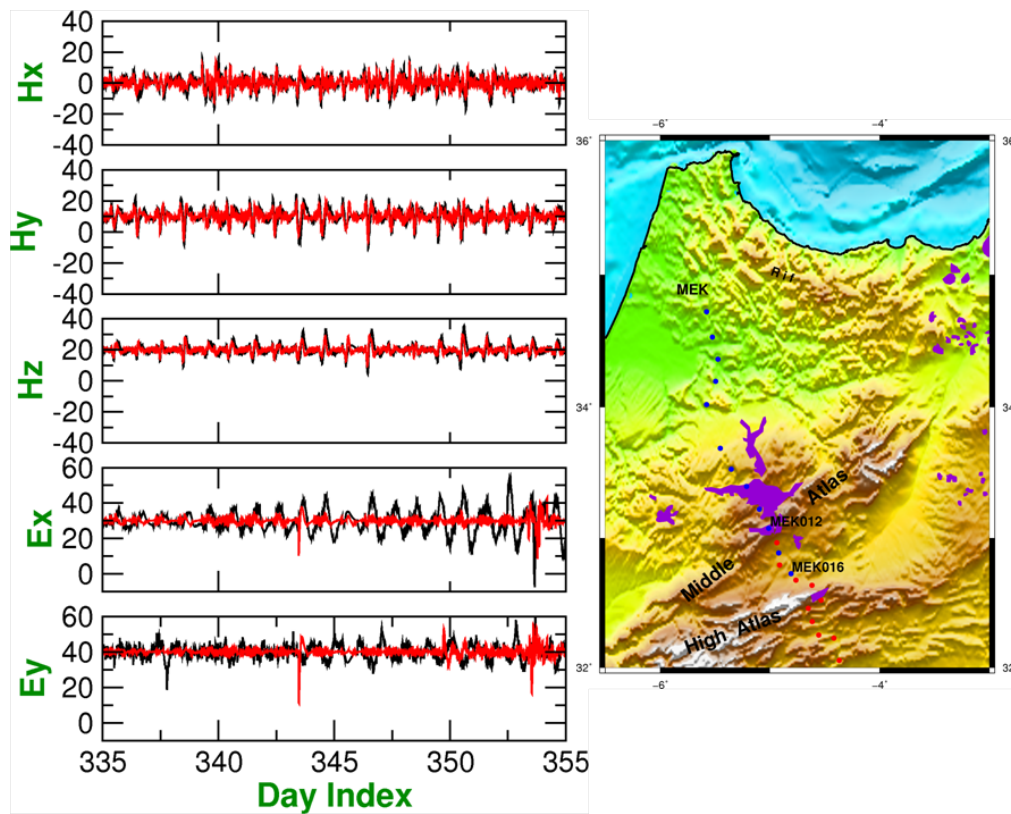


Figure 4.6.: Simultaneous time series data of magnetic and electric fields at station MEK012 (red) in Middle Atlas and at station MEK016 (black) in High Moulouya Plain.

The BBMT data were processed using remote referencing Phoenix processing software which is based on Jones & Jödicke (1984), and additionally the Egbert (1997) robust remote reference method. The long-period response curves were then merged with the BBMT response curves for stations where both data types were recorded to obtain apparent resistivity and phase estimates in the period range of ~ 0.003 s - 10,000+ s. At most of the sites (BBMT alone) along the MAR profile, data are good quality to 1,000 s and for merged (BBMT+LEMI) sites apparent resistivity and phase estimates in the period range of ~ 0.003 s - 5,000+ s. The sites located along the MEK profile over the Middle Atlas and further south have good quality data to periods of 3,000 s - 5,000 s and at merged sites even up to 15,000 s.

4.5 DATA ANALYSIS – DIMENSIONALITY AND DIRECTIONALITY

Once the MT impedance tensor has been estimated, the next step is to submit the data to comprehensive strike and dimensionality analysis. In order to determine if the MT responses require a 1-D, 2-D or 3-D interpretation, careful dimensionality analysis must be completed prior to modelling. Simplified analysis of MT responses, such as 1-D interpretation of 2-D and 3-D structures, or 2-D interpretation of 3-D structures (Ledo, 2005a; Ledo et al., 2002), can lead to artefacts in inversion results and therefore erroneous interpretation. In Morocco, geologic structures are largely 2-D, however, Morocco is located in a region of complex tectonics and is bounded by the Alboran Sea to the north, and Atlantic Ocean to the west Figure 4.1. These two factors necessitated a careful analysis to determine if a 2-D interpretation is valid or if 3-D interpretation is needed.

The apparent resistivity and phase curves for each MT site were plotted for all four components (XX, XY, YX and YY) of the impedance tensor shown in Appendix Section B.1 (Figure B.1 - Figure B.5).

4.5.1 Phase Tensor

The phase tensor was introduced in Section 2.8 (Chapter 2). Representation of MT data as phase tensor pseudo sections or maps provides an electric galvanic distortion free method of visualizing the conductivity gradient of the subsurface and allows qualitative determination of the major features of the conductivity structure (e.g., Heise et al., 2008; Hill et al., 2009).

Figure 4.7 and Figure 4.8 show phase tensor profiles of MEK and MAR line data, where the axes of the ellipses are normalized by Φ_{max} , and the colours represent the skew angle (β) (on the top) and the geometric mean (Φ_2) of the maximum and minimum phase differences between the magnetic and electric field (on the bottom).

The colour coding of the plots in both Figure 4.7 and Figure 4.8 (top) represents the phase tensor skew angle, which is a coordinate invariant measure of the asymmetry produced in the phase response by the presence of 3-D conductivity structures. In 1-D or isotropic 2-D case, the phase tensor is symmetric ($\beta=0$). As already noted in Section 2.8 and references therein, a large

skew angle is a robust indicator of 3-D regional conductivity structure, however a small skew angle is a necessary but not sufficient condition for the structure to be identified as 2-D. "Large" and "small" here are of course defined with reference to the errors within the data, something poorly considered by the original architects of the Phase Tensor method but considered in detail in Jones (2012c). For the phase tensor pseudo section of the MEK profile one can see that most of the sites and periods have high skew angles ($|\beta| \geq 5^\circ$), except sites, 8 - 16 and from 20 - 24. However, sites 10, 11, 12, and 13 have large skew angles at shorter periods whereas sites 22, 23, and 24 show large β values at longer periods. Caldwell et al. (2004) suggested that the consistency of the direction of the principal axes of the phase tensor with period and with location along strike is a much more reliable indicator of two-dimensionality (2-D). Therefore, one can conclude that a 2-D modelling and inversion approach may still be valid for this profile, as the principal axes directions of the ellipses are somewhat consistent over several periods and stations. The overall orientation of the major ellipse axes for MEK profile is roughly NE-SW. One interesting point is the major axes of the ellipses of the last six southern stations, particularly sites 24, 25 and 26, point towards the north direction with almost flat ellipses, reflecting a strong difference between Φ_{min} and Φ_{max} . Similarly, MAR profile phase tensor results show that high skew angles are present at each station especially for periods longer than ~ 1 s (Figure 4.8). Even though it is difficult to say that there is a consistent pattern in the orientation of the major axes of the phase tensor ellipses, an N-S and a NE-SW orientations are dominant in the results.

The colour of the phase tensor ellipses in both Figure 4.7 and Figure 4.8 (bottom) is related to the geometric mean (Φ_2). This parameter is an indicator of the vertical conductivity gradient, values greater than 45° indicating increasing conductivity with increasing depth. For the MEK profile (Figure 4.7), high Φ_2 values occur beneath the High Atlas (periods < 10 s), and the High Moulouya Plain (in the period range of 10 s - ~ 700 s), likely revealing the presence of a north dipping crustal conductor previously imaged by Schwarz et al. (1992) and Ledo et al. (2011). The other zone of high Φ_2 values that is located beneath the Anti-Atlas periods lower than ~ 10 s, could reflect the signature of thick deposits of Paleozoic sedimentary rocks, that can reach up to 4 km depth (Robert-Charue, 2006), also previously imaged as a high conductivity region in 2-D model of Ledo et al. (2011). Also, in the 2-D model, the Moulouya Plain upper crust showed high resistivity values that were interpreted to be due to the lack of important thrusting systems. That can provide an explanation for the observed low Φ_2 values beneath the region. The Anti-Atlas, which has been essentially stable since the beginning of Mesozoic, is defined by low Φ_2 for periods higher than ~ 2 s. Similarly, data at sites 1, 2 and 3 also show low Φ_2 values for the entire period range of ~ 20 s - $\sim 5,000$ s. For the MAR profile (Figure 4.8), the southern edge of the Souss Basin (sites 5, 6 and 7) and the Western High Atlas are characterized by high Φ_2 values, except the northern end of Western High Atlas. For sites 11, 12 and 13, Φ_2 values are low, as they are likely sensing a resistive structure beneath the region. The northern edge of the Haouz Basin and Anti-Atlas are defined by low Φ_2 values for the periods 0.003 s - 1 s.

4.5.2 Strike Analysis

Determination of a common strike direction for all sites and periods being modelled is essential for 2-D modelling along a profile. The *strike* program by McNeice & Jones (2001) based on the Groom and Bailey decomposition (Bailey & Groom, 1987; Groom, 1988; Groom & Bailey, 1989) was introduced in Section 2.8. The distortion decomposition code was applied to the MT response estimates for each of the MT site along both MEK and MAR profiles to analyse galvanic distortions and to determine the most consistent geo-electric strike direction over most sites and periods. The latest version of *strike* code allows comparative analyses in an approximate-depth domain (based on the Niblett-Bostick depth approximation) rather than the frequency domain. An example of this new version of the code's use is presented in the work of Miensopust et al. (2011), where the authors showed that geo-electric strike may vary not only along a profile but also with depth. Therefore, a multi-site, multi-frequency decomposition based on depth bands become more important and necessary when trying to determine the geo-electric strike direction for a number of sites, where the penetration depths vary strongly.

Initially, in order to determine a reasonable geo-electric strike for the crust and mantle lithosphere, the respective depth ranges were subdivided into two layers based on the results of seismic studies and integrated geophysical modelling studies discussed in Section 3.2 (Chapter 3). Single-site strike analysis was undertaken for different strike directions varying every 5° from 0° to 90° for each station at Niblett-Bostick depth ranges of 3 - 10 km (upper crust), 10 - 28 km (middle to lower crust), 40 - 90 km (lithospheric depth ranges), and 90 - 150 km (lithospheric depth ranges). Figure 4.9 shows a comparison of the average rms misfit values for different geo-electric strike directions (0° - 90°) of the stations. As a next step, multi-site, multi-frequency strike analysis was applied for these same defined depth ranges for all MEK profile sites together, and only for the sites in the southern Middle Atlas, High Moulouya Plain, High Atlas and Anti-Atlas (i.e., sites in the Tabular Middle Atlas (mek006 and mek008) and sites in the northern part of the profile (mek01a, mek02a and mek03a) were excluded). The results are indicated by dashed and dotted lines on each plot (Figure 4.9), respectively. Excluding those sites from the analysis did not change the resulting strike directions for defined depth bands. The sites in the Rif (mek01a, mek02a and mek01a), High Atlas (the sites mek021, mek022 and mek023) and Anti-Atlas (mek031, mek032, mek033 and mek034) exhibit higher rms values mostly in the crustal depths.

As a second step, the same approach as described above was applied to the depth ranges that are defined as crust and mantle lithosphere (and asthenosphere) spanning from 5 km to 35 km and 50 km to 150 km, respectively (Figure 4.10a). In this particular case, the strike analysis reveals two major trends in the estimates: an azimuth of $N50^\circ E$ characterizing the crust and an azimuth of $N22^\circ E$ for the mantle structures. In addition, multi-site multi-frequency strike was run for numerous groups of different sites and depth bands. The table in Figure 4.10b summarizes the resulting strike directions for different groups of sites for the crust and lithospheric mantle. While the analysis yields directions of $N62.5^\circ E$ and $N51.7^\circ$ for the folded Middle Atlas-High Moulouya

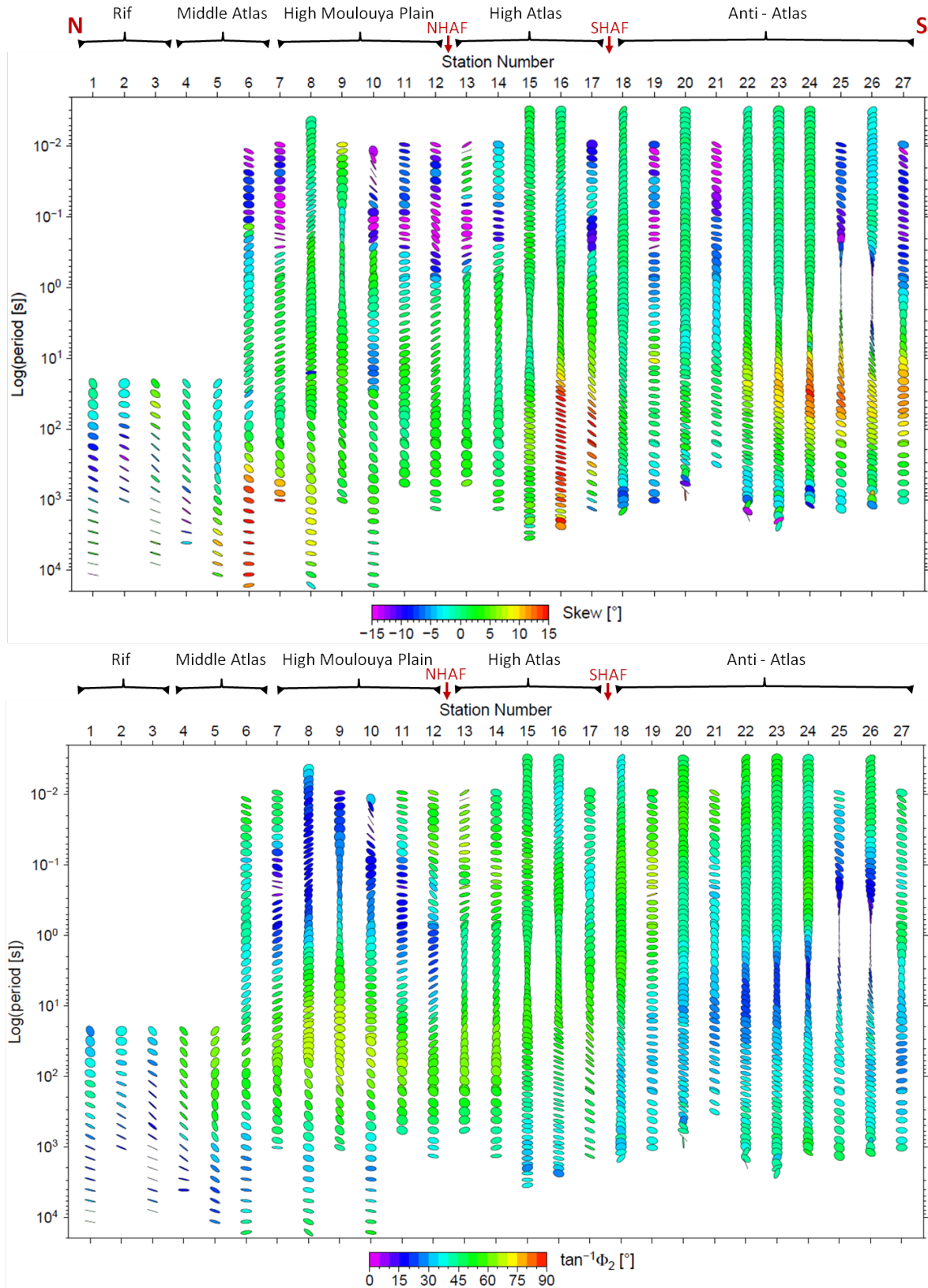


Figure 4.7.: Phase tensor ellipse pseudo-sections for each periods of each sites (except 4 sites: mek010, mek004, mek002 and mek001 due to poor data quality) along the MAR profile of measurements across the Middle Atlas. The axes of ellipses are normalized by Φ_{max} and the colours represent the skew angle β (on the top) and the geometric mean Φ_2 ($\sqrt{\Phi_{max}\Phi_{min}}$) (on the bottom). The ellipses are plotted so that the horizontal axis corresponds to an east-west orientation.

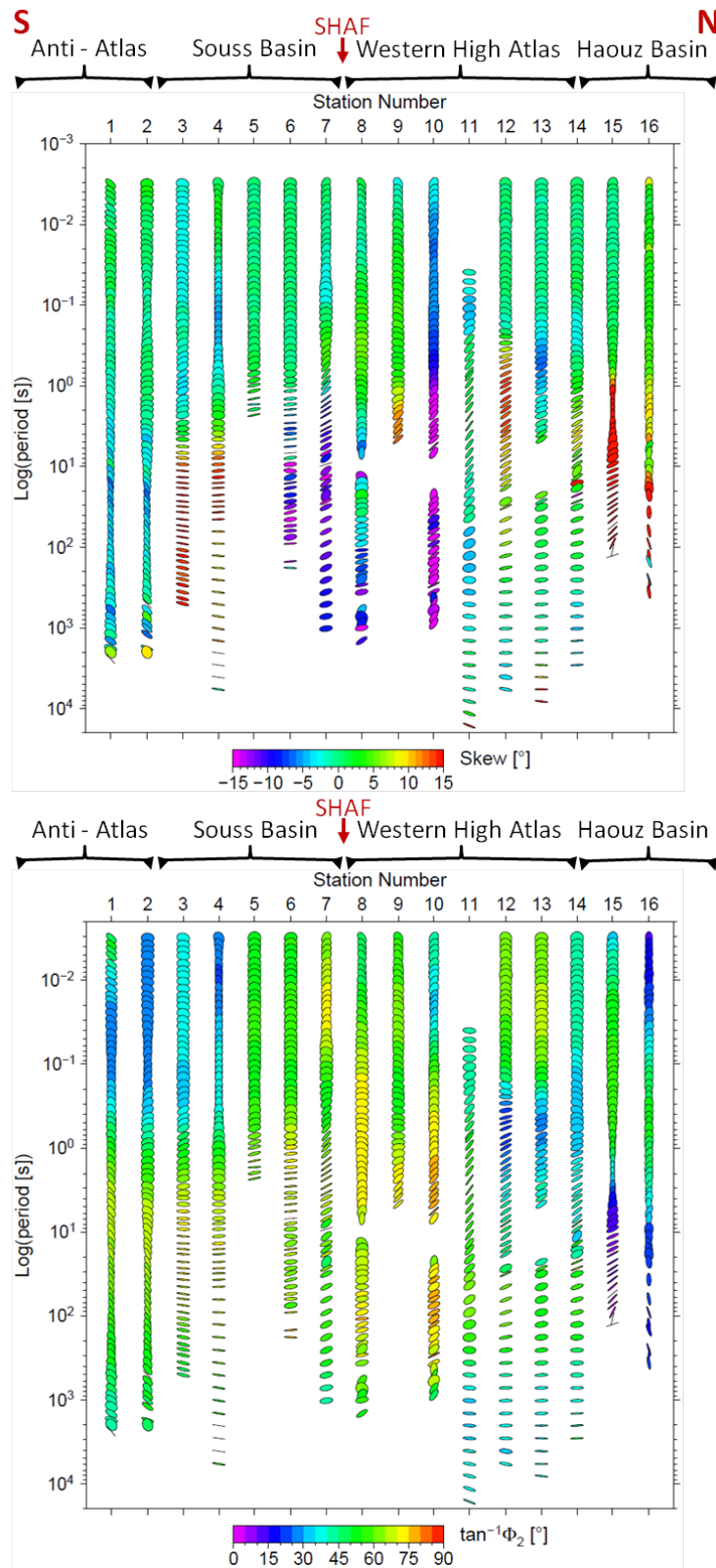


Figure 4.8.: Phase tensor ellipse pseudo-sections for each periods of each sites (except 4 sites: mar015, mar016, mar019 and mek020 due to poor data quality) along the MAR profile of measurements across the Middle Atlas. The axes of ellipses are normalized by Φ_{max} and the colours represent the skew angle β (on the top) and the geometric mean $\Phi_2 (\sqrt{\Phi_{max}\Phi_{min}})$ (on the bottom). The ellipses are plotted so that the horizontal axis corresponds to an east-west orientation.

Plain and High Atlas respectively, the sites in the Anti-Atlas prefer a strike direction of $N17^{\circ}E$. However, when including site mek025, which is located just on the southern edge of the SHAF, a strike direction of $N44.5^{\circ}E$ is obtained. Nevertheless, an overall strike direction of $N50^{\circ}E$ was chosen for crustal depths, in agreement with the results of Ledo et al. (2011). For lithospheric mantle depth ranges, the Middle Atlas-High Moulouya and the Anti-Atlas exhibit similar strike directions, whereas the High Atlas shows a strike direction of 4° . As shown in Figure 4.10a on the bottom, an overall strike direction of $N22^{\circ}E$ was chosen because it was a dominant direction for the lithospheric depths at all sites. Finally, the decomposition was performed for fixed strike angles, 50° and 22° , in addition to unconstrained individual strike decomposition to see the effect on the resulting rms misfit. Figure 4.11 illustrates the results. The orientation of the arrows represents the strike direction and their length is a measure of the average of the absolute phase difference. Colour coding of squares indicates rms misfit of the distortion model to the data (dark to light purple colours represent small average rms misfit). Forcing a strike angle to be 50° for crustal depths and 22° for mantle depths did not make a significant difference on the resulting rms misfit values. One can clearly see from the individual strike results (Figure 4.11a and Figure 4.11b), the preferred strike orientation is changing from NE-SW at crustal depths to NNE-SSW at lithospheric depths. Additionally, rms misfit and phase difference are indicators for dimensionality. Large phase differences ($> 30^{\circ}$) mean that a strongly 2-D or (3-D) environment is present. The sites in the Anti-Atlas and in the Tabular Middle Atlas show relatively large phase ($\sim 25^{\circ}$) compared to the rest of the sites along the profile, also supports the phase tensor results where those sites have higher $|\beta|$.

The dominant geo-electric strike orientation of $50^{\circ}E$ of north is in agreement with the NE-SW trend of the main geological structures. Therefore, this direction was adopted for inversion and interpretations of the crustal part of the MEK profile, and a strike direction of $22^{\circ}E$ of north for the lithospheric part of the MEK profile.

MAR profile multi-strike multi-depth strike analysis (Figure 4.12, dashed line) showed that the optimal strike direction varies between the upper crust (500 m - 3 km and 3 - 10 km) and middle to lower crust. In general, the average rms misfit values are not high, it does indeed change in between the stations at the requested depth range. In order to determine a reasonable/acceptable geo-electric strike direction for the crust, multi-strike analysis was run for the whole crust (3 - 30 km). A preferred strike azimuth of $N45^{\circ}E$ that was found to best fit most of the sites along the profile at most of the frequencies (the frequencies that fall into the requested depth range, 3 - 30 km in this case). This strike angle of $N45^{\circ}E$ is consistent with the general trend (NE-SW) of the Western High Atlas, so this geo-electric strike was chosen for further analysis.

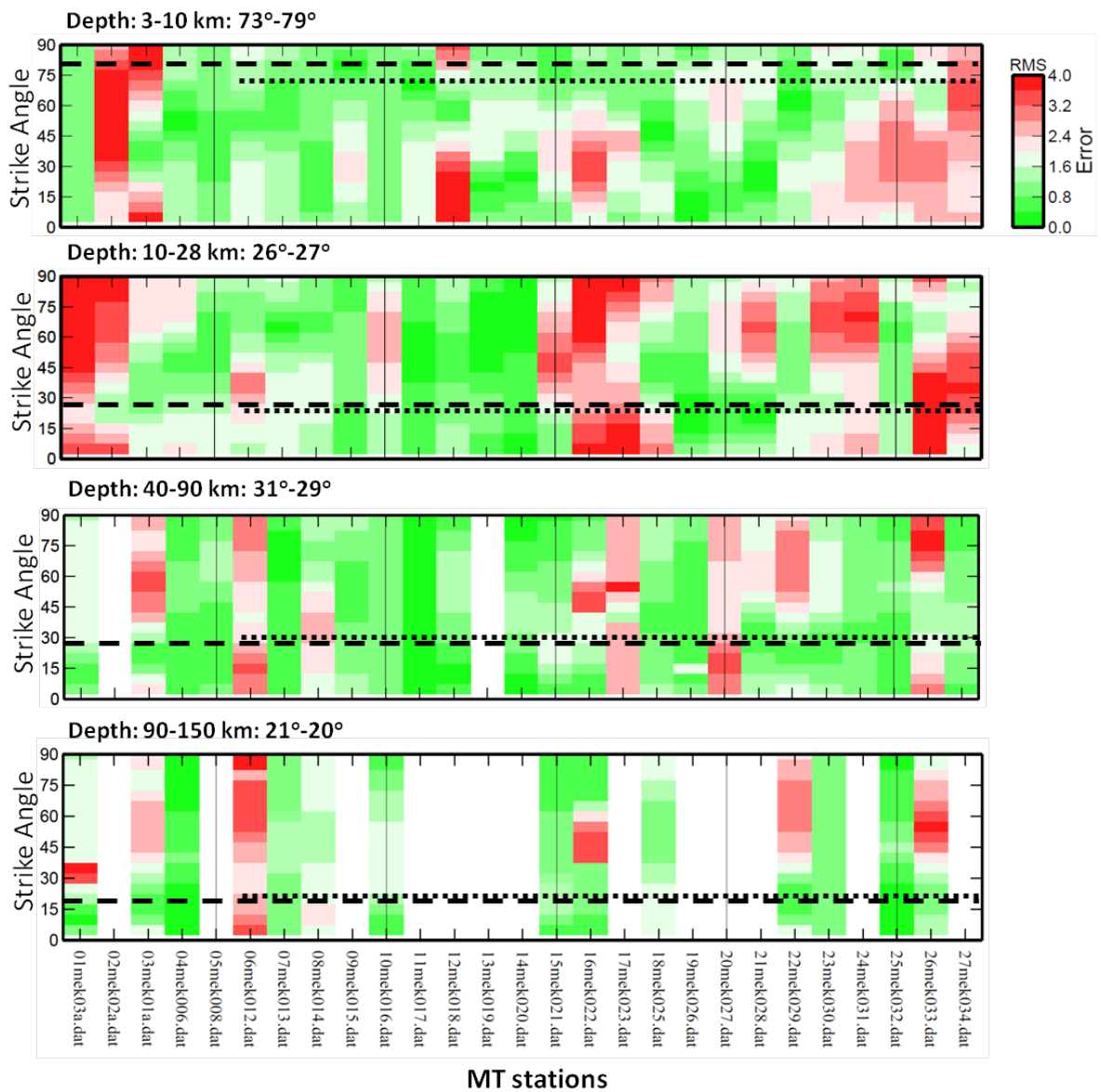
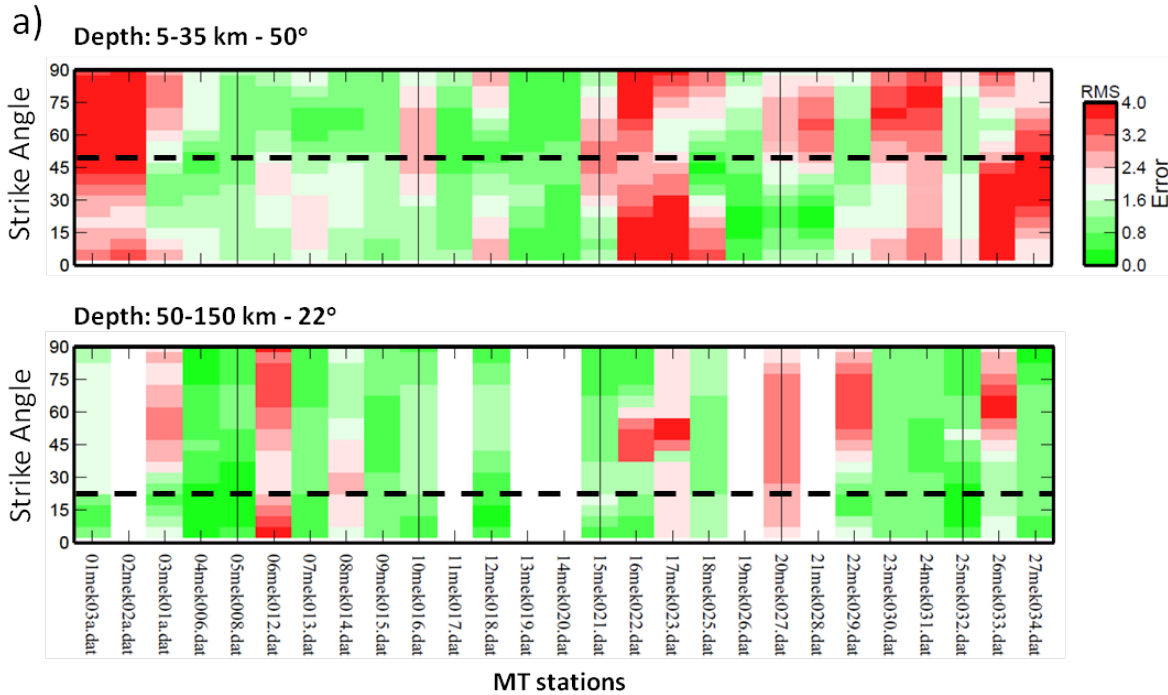


Figure 4.9.: Rms misfit values from decomposition models for each MT stations along the MEK profile with varying the geo-electric strike direction at the Niblett-Bostick depth ranges of 3 - 10 km, 10 - 28 km, 40 - 90 km, and 90 - 150 km. The optimal common geo-electric strike direction clockwise from North calculated for all stations for crustal and lithospheric depths; indicated by black dashed line on the plots. Also, the optimal geo-electric strike directions calculated for stations excluding the stations in the Tabular Middle Atlas (mek006 and mek008) and the stations in the northern part of the profile (mek01a, mek02a, and mek03a); indicated by black dotted line on the plots. Empty columns are due to insufficient data for this depth range at the respective station.



b)

	Middle Atlas – High Moulouya Plain	High Atlas	Anti-Atlas	
5 km	62.5° (rms = 1.1)	51.7° (rms = 1.9)	17° (rms = 2.0)	44.5° (rms = 2.0)
35 km	22.4° (rms = 1.4)	4° (rms = 0.8)	21° (rms = 1.1)	21.8° (rms = 1.1)
150 km	Sites: mek012- mek018	Sites: mek019- mek023	Sites: mek026- mek034	Sites: mek025- mek034

Figure 4.10.: Figure showing (a) rms misfit values from decomposition models for each MT stations along the MEK profile with varying the geo-electric strike direction for crustal (5 - 35 km) and lithospheric (50 - 150 km) depth ranges, respectively. The dashed line indicate overall strike directions for crustal and lithospheric depths. Empty columns are due to insufficient data for this depth range at the respective station. (b) a table of the different strike angles for crustal and lithospheric depth ranges and for different areas of the MEK profile.

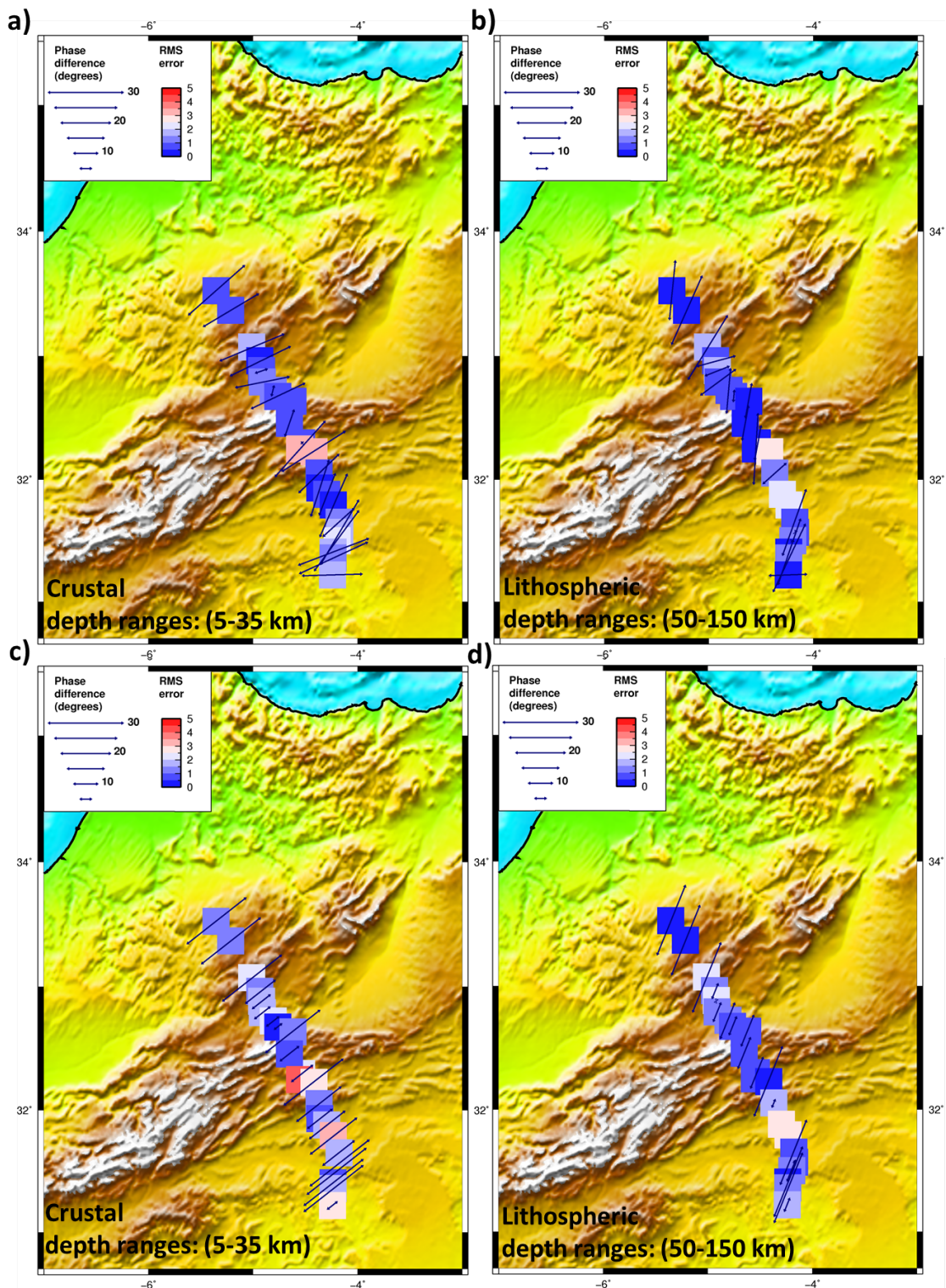


Figure 4.11.: Figures showing the comparison between the results of unconstrained (a & b) and constrained (c-50° & d-22°) single-site strike analysis along MEK profile (a & c) for crustal depth ranges (5-35 km) and (b & d) for lithospheric depth ranges (50 - 150 km). Double-headed arrows show 2-D geo-electric strike direction, scaled in length by phase difference between the XY and YX modes. A large phase indicates a stronger degree of dimensionality. Coloured squares show the rms misfit error, normalized by the observational errors in the observed MT response, at each site. By normalizing the rms error by observational errors, higher quality data with low errors are weighted more heavily in the decomposition. Low rms errors ($< \sim 2$) indicate MT responses in which the sub-surface structure is described as 2-D.

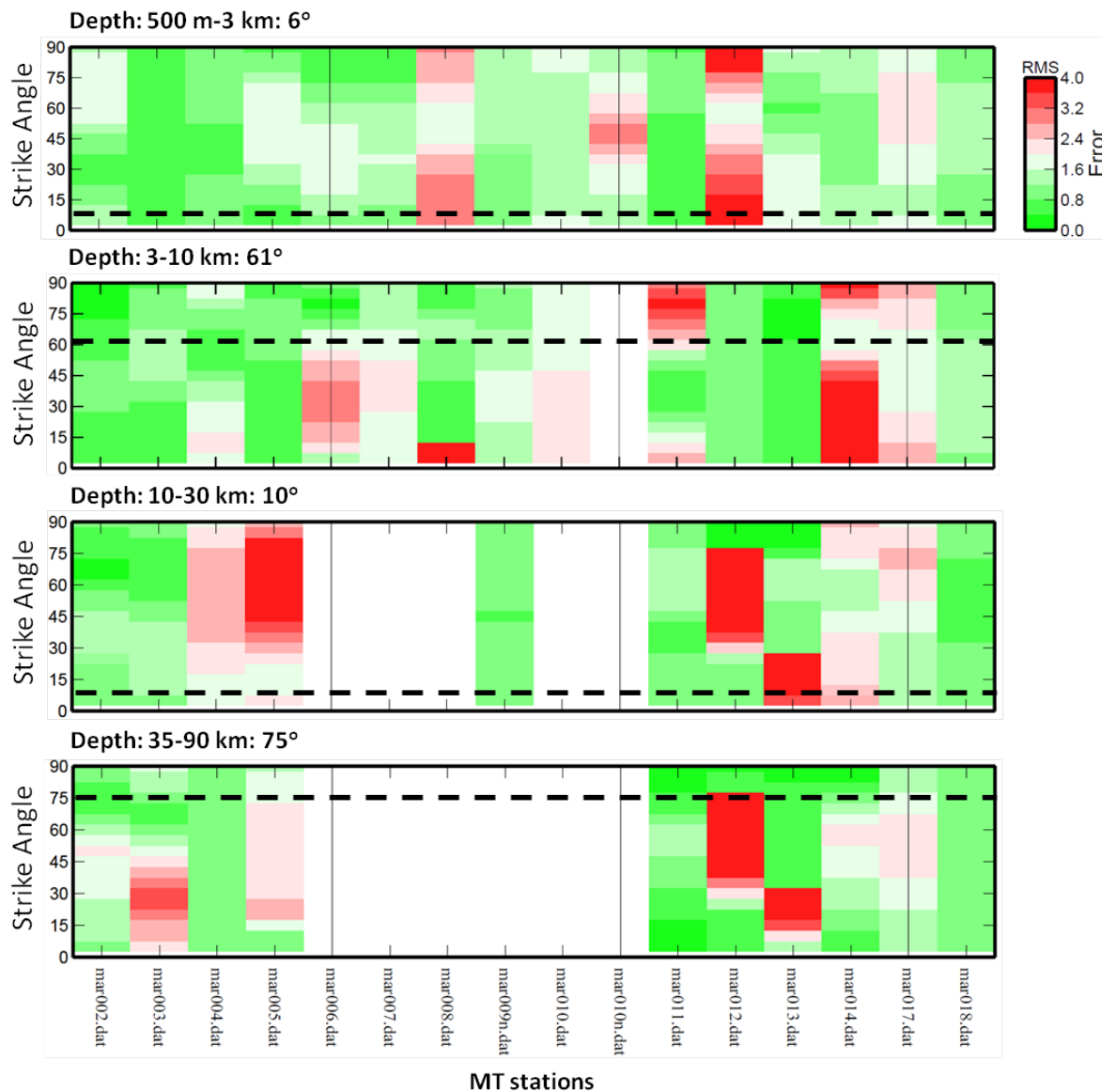


Figure 4.12.: Rms misfit values from decomposition models for each MT stations along the MAR profile with varying the geo-electric strike direction at Niblett-Bostick depth ranges of 300 m - 3 km, 3 - 10 km, 10 - 30 km, and 35 - 90 km. The dashed lines indicate overall strike direction for requested depth range. Empty columns are due to insufficient data for this depth range at the respective station.

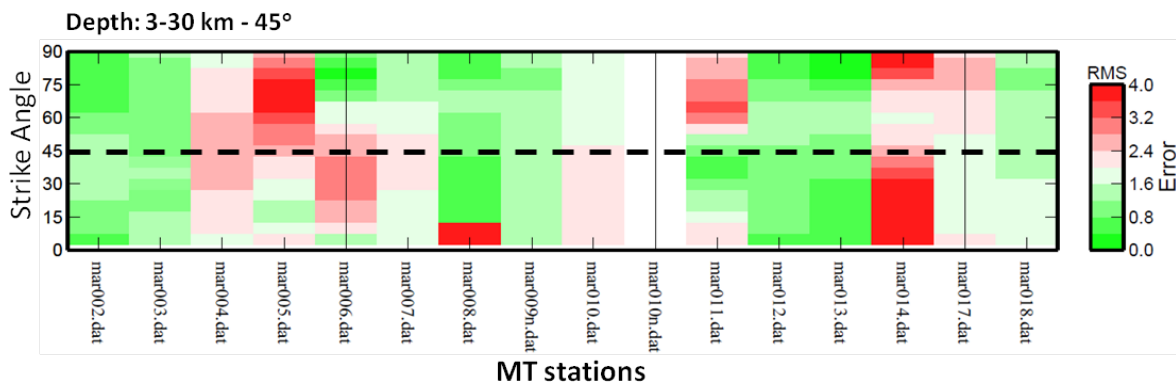


Figure 4.13.: Rms misfit values from decomposition models for each MT stations along the MAR profile with varying the geo-electric strike direction for crustal depth ranges (3 - 30 km). The dashed line indicates overall strike direction.

2-D INVERSION OF TOPOMED MT DATA

This chapter describes the two-dimensional (2-D) inversion of the TopoMed MT data set and illustrates and describes subsurface resistivity models obtained from the inversions using different parameters and data subsets. The results are compared to the other available information in the study area (see [Chapter 3](#), where the geology and previous research are discussed) and a geological interpretation of the modelled subsurface resistivity structures is discussed.

The 2-D inversion of the MEK profile data across the Atlas Mountains was performed using the 2-D finite difference, smooth model inversion code within the software package WinGLink® by Geosystem developed by [Rodi & Mackie \(2001\)](#), which assumes isotropic resistivity cells in the mesh (i.e., the same resistivity in the lateral and vertical directions in each cell), as well as a version of the code which solves for anisotropic conductivity structures ([Mackie, 2002](#); [Evans et al., 2005](#); [Baba et al., 2006](#)), (i.e., different conductivities in the three directions).

5.1 INVERSION PARAMETERS

Many different parameters need to be defined in the inversion code. All inversion results shown in the sections below are based on the following settings, unless stated otherwise:

For the crustal model:

- data period range: minimum periods 0.001 s to period related to ≤ 40 km depth
- invert for observed station data
- using data errors, otherwise the errors of the resistivity values and phase values were set to 10% and 5%, respectively.
- simultaneous inversion for phase and apparent resistivity for both TE and TM modes
- error floors: 50%, and 10% for resistivity and phases of both TE and TM modes for the first inversion run. Successively the error floors of phase and resistivity of both modes were reduced as follows: 5% for TM and TE phases and 10% for TM and TE resistivities.

For the lithospheric model:

- data period range: minimum period 0.001 s and 8 decades, if available, i.e., to 20,000 s.
- invert for observed station data
- using data errors, otherwise the errors of the resistivity values and phase values were set to 10% and 5%, respectively.
- simultaneous inversion for phase and apparent resistivity for both TE and TM modes
- error floors: 50%, and 10% for resistivity and phase of both TE and TM modes for the first inversion run. Successively the error floors of phase and resistivity of both modes were reduced as follows: 5% for TM and TE phases and 10% for TM resistivity and 15% for TE resistivity.

For all models shown in this chapter the inversions are started from a homogeneous half space of 100 Ωm , which is an average value for the resistivity in the Anti-Atlas (cratonic part, therefore older) and in the Middle Atlas, the High Moulouya Plain and the High Atlas (younger part). Also, another starting model, which is a homogeneous half space of 500 Ωm , is tested on the data subset like the Anti-Atlas part alone; it all yields similar results. The inversion scheme of the standard Laplacian regularisation and minimising the gradient of the model are chosen to derive the inversion models.

Influence of regularization parameter

Since the NLGG code of [Rodi & Mackie \(2001\)](#) is a regularized scheme, the regularization parameter (also called the smoothing operator), τ , has a significant effect on the resulting inversion models. τ controls the trade-off between fitting the data and the model smoothness, or more correctly roughness. Larger τ values result in smoother models at the expense of poorer fit. Therefore, a series of inversions are run to determine the most optimum solution, that ensures both a good data fit and a smooth model for the chosen model mesh, data set and subsurface structure. In order to avoid static shift problems, inversions are initiated to fit the phases only (50% for both TE and TM resistivities, and 5% for the phases of both TE and TM modes) using interpolated 5 samples per decade as input data. Note that once the optimum τ value is obtained, real field data are used as input data for the subsequent inversions.

[Figure 5.1](#) shows the resulting trade-off curves of rms versus τ values for the inversion of data subset at crustal levels (on the left) and for the inversion of the whole data set (on the right). During the inversion the smoothing weighting parameters (α , β , and H/V) are set to standard values, i.e., $\alpha = 1$, $\beta = 0$. The parameter, α is the factor to multiply the horizontal derivatives (the default $\alpha = 1$, larger values increase the horizontal smoothness). The second parameter, β is the exponent in the weighting function (the default $\beta = 0$). However, according to both theoretical studies and

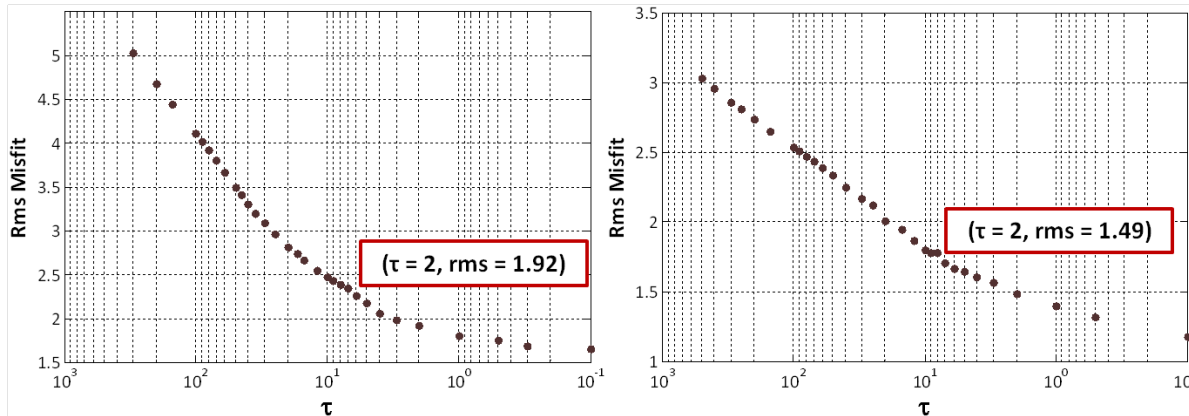


Figure 5.1.: Rms misfit versus τ trade-off curves for the crustal data set with a strike angle of 50° E of N and for the whole data set with a strike angle of 22° E of N, using default settings for the weighting parameters, i.e., $\alpha = 1$, $\beta = 0$.

empirical studies, one of the weighting parameters, β should be set to 1 if minimising the gradient of the model when standard Laplacian operator is chosen (Mackie (2002) and references therein). Following the suggestion of Mackie (2002), β is set to 1 for the subsequent inversion runs. A range of τ parameters from 0.1 to 300 and 0.1 to 500 are used in the test for crustal data set with a strike angle of 50° and the whole data set with a strike angle of 22° , respectively. A compromise between fitting the MT data and generating a smooth resistivity models are obtained when $\tau = 2$ for both data sets Figure 5.1 and Figure 5.2 illustrate a comparison of 2-D inversion results using three different τ values ($\tau = 0.1, 2$ and 100). During these trial inversions, error floors of 50% and 5% are set for apparent resistivity and phase data, respectively. A lower value of τ results in a rough model which has disconnected structures especially in the upper part of the model, up to 20 km in depth (Figure 5.2a). On the other hand, a high value of regularization parameter ($\tau = 100$) causes the roughness term in the penalty function to have more weight and data misfit is down-weighted. Therefore, the resulting model is very smooth, however, the measured data are not well fit, as small structures that are required by the data were smeared out (Figure 5.2c).

5.2 CRUSTAL STRUCTURES, MEK PROFILE – CRUSTAL STRIKE DIRECTION

2-D inversion results

The complete MEK profile data set is decomposed to a fixed strike direction 50° E of N using *strike* (McNeice & Jones, 2001), the data are imported into WinGLink® and D^+ consistency checks are performed to identify for removal inconsistent data points before the inversion. Niblett-Bostick penetration depths are estimated for both modes individually for each station and all data points at periods with penetration depths greater than 40 km are excluded. The inversion strategy described in Section 5.1 is used, that is TM and TE phases first, then TM and TE resistivities are included.

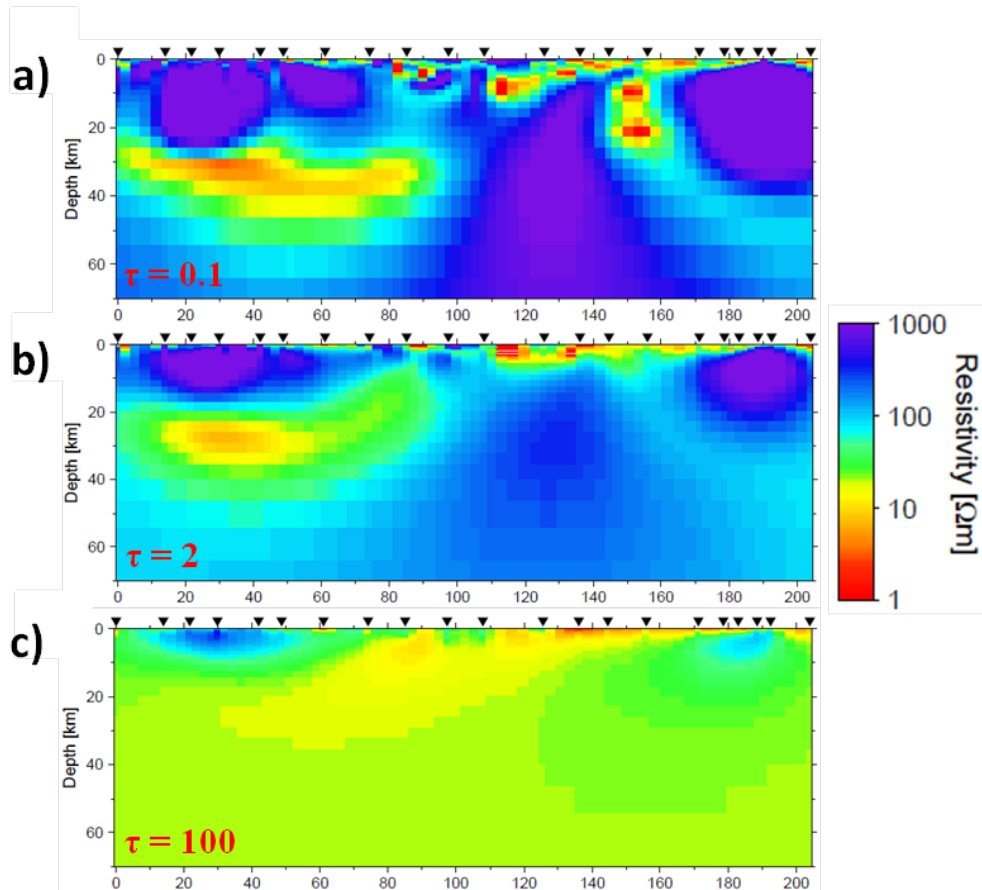


Figure 5.2.: Figure showing an example of inversion results using three different values 0.1 (a), 2 (b) and 100 (c) for τ , respectively. While the smallest value of $\tau = 0.1$ produces a rough model with an acceptable data fit (small rms value - 2.19), using larger value of $\tau = 100$ during the inversion process produces a very smooth model but an unacceptable data fit (high rms value - 5.25).

Figure 5.3b shows 2-D isotropic and anisotropic inversion results for the crust (depth ≤ 40 km) for the MEK profile, using a modified version of the 2-D magnetotelluric algorithm of Rodi & Mackie (2001) incorporating an additional isotropy regularization parameter for electrical anisotropy (τ_{iso}). The 2-D anisotropy problem is restrictively solved by assuming the anisotropy axes are parallel and perpendicular to the main axis of regional geo-electric strike (Baba et al., 2006). Anisotropic modelling defines three models; XX-horizontal resistivity across-profile, YY-horizontal resistivity along-profile and ZZ-vertical resistivity (the ZZ models were not included as they are very similar to XX). Setting $\tau_{iso} = 100$ (or higher) forces the models in all three directions to be similar, in other words, result in an isotropic solution, whereas small values allow the model to vary more in the three different directions (Mackie, 2002). For anisotropic inversion, three different anisotropy trade-off parameters ($\tau_{iso} = 3, 1$ and 0.1) are chosen to demonstrate the possible levels of anisotropy. For each site rms values are plotted on top of the model (Figure 5.3a). For an isotropy regularization parameter ($\tau_{iso} = 1,000$), the two models are basically identical, reducing the parameter to $\tau_{iso} = 3$ the models are almost similar, but the middle to lower crustal conductor located beneath the Anti-Atlas is more pronounced in the XX direction. To compare and to assess which structures are required by which data components, the isotropic inversion results of the TM mode only and TE mode only data are shown, respectively, in Figure 5.5a and b. Although these models are not identical to the anisotropic inversion results using $\tau_{iso} = 0.1$, they are very similar.

Pseudo-sections of both TM and TE mode data and isotropic model responses with apparent resistivities and phases are presented in Figure 5.4. The figure shows that a satisfactory fit to observed data was obtained for the period range used for the inversion (minimum period 0.001 s to period related to ≤ 40 km depth).

The resistivity structures obtained from TM only (Figure 5.5a), TE only (Figure 5.5b) and joint TM and TE inversion (Figure 5.3b, the model obtained using $\tau_{iso} = 1000$), however, clearly exhibit differences, as the two modes have different sensitivities (e.g., Unsworth et al., 1999; Ritter et al., 2003). Some authors are in favour of basing their interpretation of MT data solely on the TM data if the data show 3-D effects, as TM mode is sensitive to the electrical charge accumulations at the boundaries, thus, TM mode data generally will be less influenced by off-profile structures (e.g., Wannamaker et al., 1984). In the previous chapter, we pointed out that 3-D features have an effect on the data set given that the high skew angles are present almost at each station; particularly for the stations in Anti-Atlas there is a change in the direction of major axes of the phase tensor ellipses, pointing towards the north direction, reflecting a strong difference between Φ_{min} and Φ_{max} .

The best fitting TM mode model (Figure 5.5a) is dominated by a heterogeneous upper and middle crust (10 - 20 km) with much higher conductivity (1 - 10 Ωm) in the northern part of the profile than at the southern end. The lower crust (20 - 40 km) below 20 km appears to be less conductive, with resistivity values of 50 - 200 Ωm . The upper crust (0 - 5 km) beneath the High Atlas and Anti-Atlas has high conductivity (1 - 5 Ωm), as expected for the High Atlas which has experienced the greatest shortening in the Atlas system and the structure is interpreted to be dominated by thick-skinned thrusting and folding (e.g., Beauchamp et al., 1999; Benammi et al.,

5.2 CRUSTAL STRUCTURES, MEK PROFILE – CRUSTAL STRIKE DIRECTION

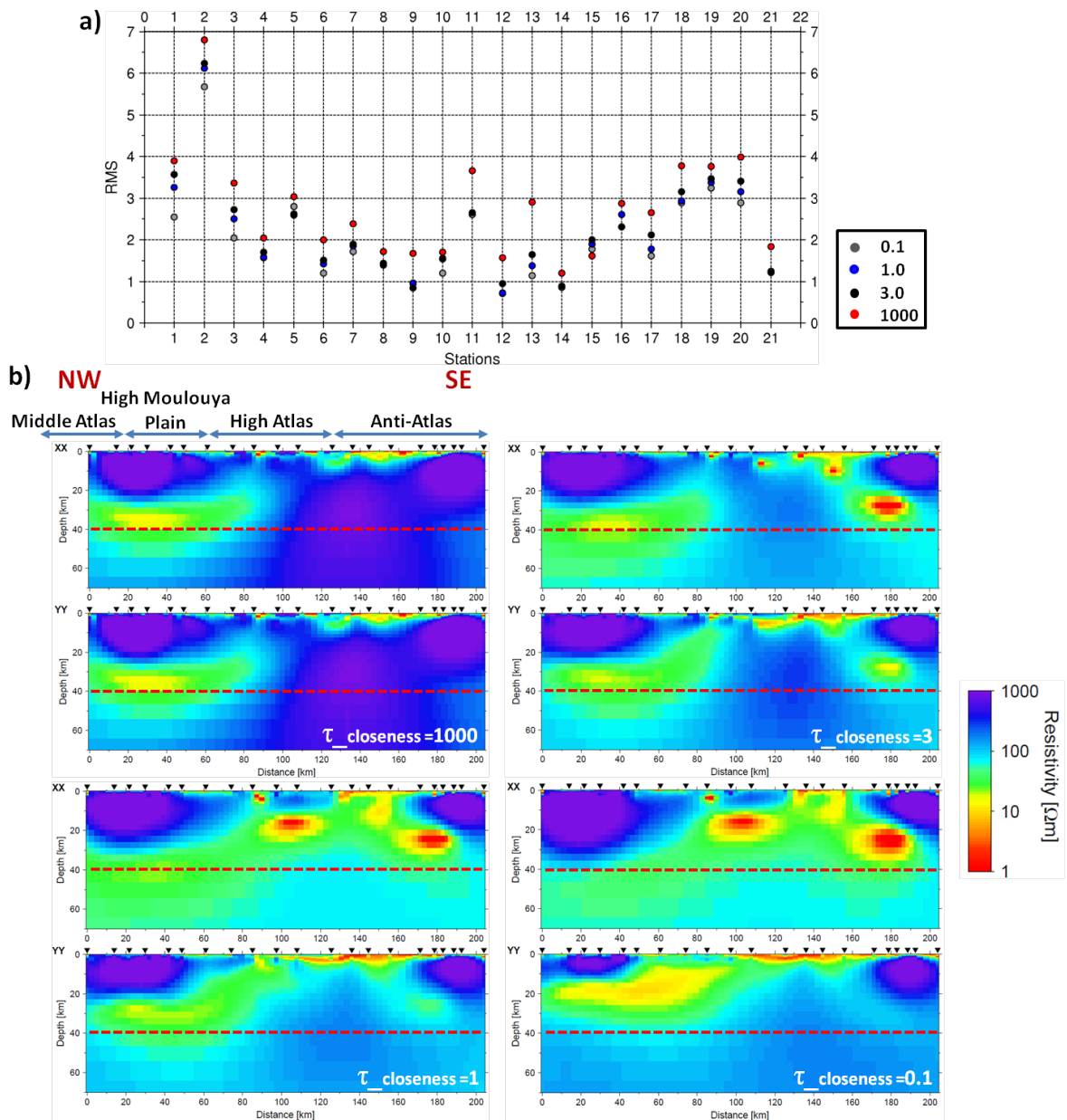


Figure 5.3.: Comparison of isotropic and anisotropic 2-D inversion results for the MEK profile data set. **(a)** The rms values for individual sites were plotted on top of the models; **(b)** resulting 2-D inversion models using different τ_{iso} values. For the first inversion run, error floor values of 50% and 10% were used for apparent resistivity and phase data, respectively. For the second inversion run, the values were reduced to 10% and 5%. Red dashed line indicates the maximum depth of penetration considered during the inversion runs.

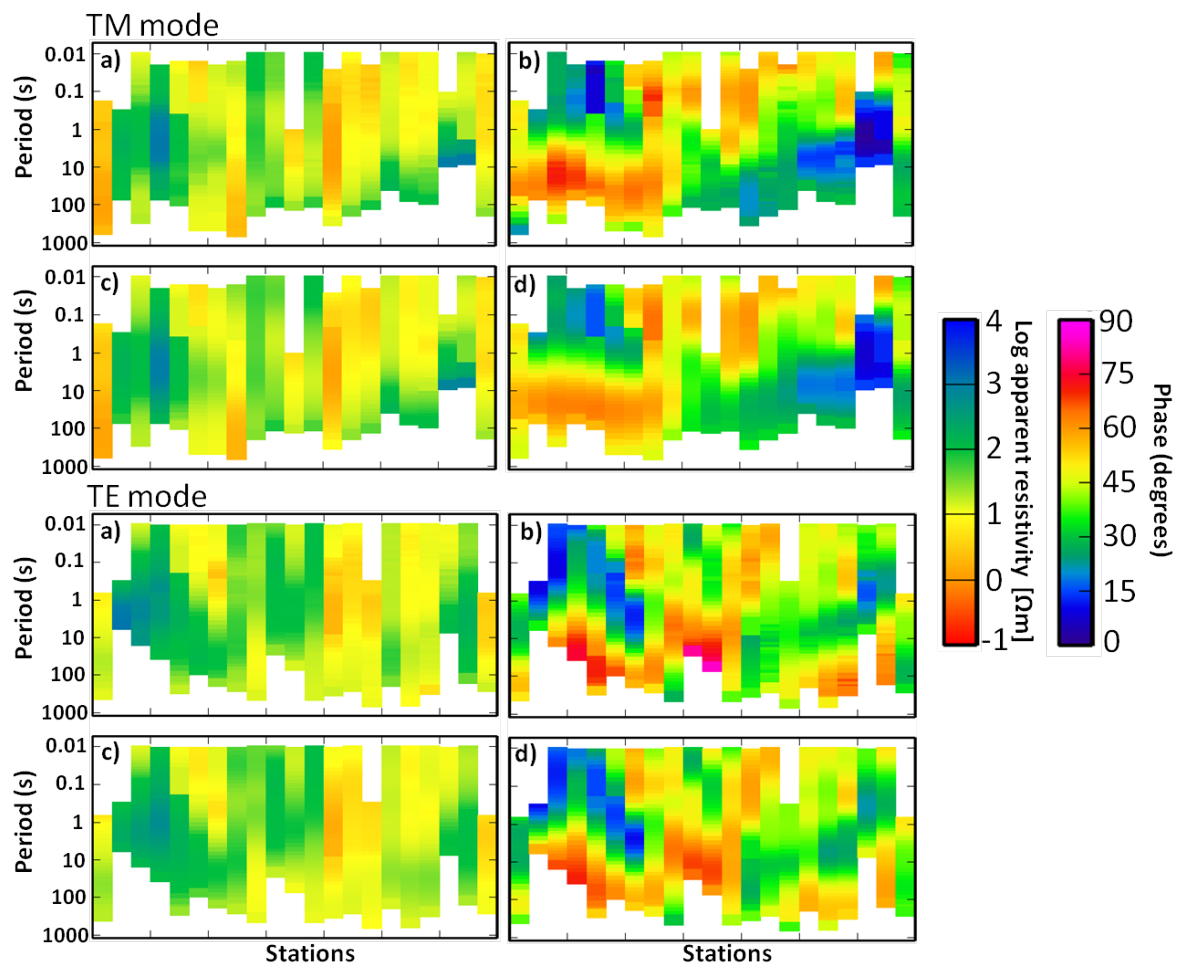


Figure 5.4.: The apparent resistivity and phase pseudo-sections of TM (on the top) and TE data (on the bottom). Panels showing (a&b) observed apparent resistivity and phase and (c&d) model responses with apparent resistivity and phase.

2001). In the Anti-Atlas, thick deposits of Paleozoic sedimentary rocks (Robert-Charue, 2006) are likely responsible for the conductive upper crust. Below the upper crust, the entire High Atlas and the Anti-Atlas appear to be homogeneous and resistive ($>100 \Omega\text{m}$). On the other hand, the best fitting TE model (Figure 5.5b) indicates a thicker resistive ($\geq 1000 \Omega\text{m}$) crust (0 - 40 km) below the northern end of the profile, whereas two prominent conductive bodies (1 - 10 Ωm) are imaged beneath the High Atlas at mid-crustal levels (10 - 23 km) and beneath the Anti-Atlas at lower crustal levels (20 - 40 km). As expected, the combined TE and TM mode isotropic model exhibits some features from the inversion of individual modes (Figure 5.3b, the model with $\tau_{iso} = 1000$). The position of the conductor beneath the Middle Atlas and the High Moulouya Plain moves to the middle to lower crustal levels and also the high conductivity is now confined to the northern part of the profile. Furthermore, a lower crustal conductor is imaged, if only the TE mode data are inverted and or if anisotropic inversions are performed with $\tau_{iso} = 3, 1$ and 0.1, beneath the Anti-Atlas disappeared.

To explore for the existence of the lower crustal conductor at the southern end of the profile, focused isotropic and anisotropic inversions are performed only for the stations in the Anti-Atlas using the strike direction of 22° E of N. As shown in the Chapter 4, this geo-electrical strike is obtained when performing multi-site multi-frequency strike analysis for only those sites. The resistivity models in Figure 5.6b are obtained when the TE and TM mode data are fit simultaneously. Anisotropic inversions are run using $\tau_{iso} = 1, 0.5$ and 0.1. The difference between the isotropic ($\tau_{iso} = 1000$) and anisotropic rms misfits are shown on top of the models (Figure 5.6a). As one can see, the fit is slightly better when the degree of anisotropy is increased, which is also observed for the previous crustal modelling using the strike direction of 50° E of N (Figure 5.3a). In all models, the entire Anti-Atlas is dominated by resistive crust (100 - 1000 Ωm), except the conductive layer (1 - 10 Ωm) for the top maximum 5 km. One interesting feature is a conductive body that is observed particularly emphasized in the XX direction if high levels of anisotropy are allowed (Figure 5.6c and Figure 5.6d). Unlike the inversion result of joint TM and TE mode data, the conductive structure is imaged at a shallower depth (5 - 10 km). Pseudo-section comparison of observed data and isotropic modelling result are presented in Figure 5.7. The TM mode apparent resistivities and phases fit better than the TE mode ones.

5.3 MANTLE STRUCTURES, MEK PROFILE – LITHOSPHERIC MANTLE STRIKE DIRECTION

2-D inversion results

The complete MEK profile data set is decomposed according to a fixed strike direction of 22° E of N using *strike* (McNeice & Jones, 2001) and subsequently the data are imported into WinGLink® and D^+ consistency checks are used as a guide to manually eliminate inconsistent data points prior

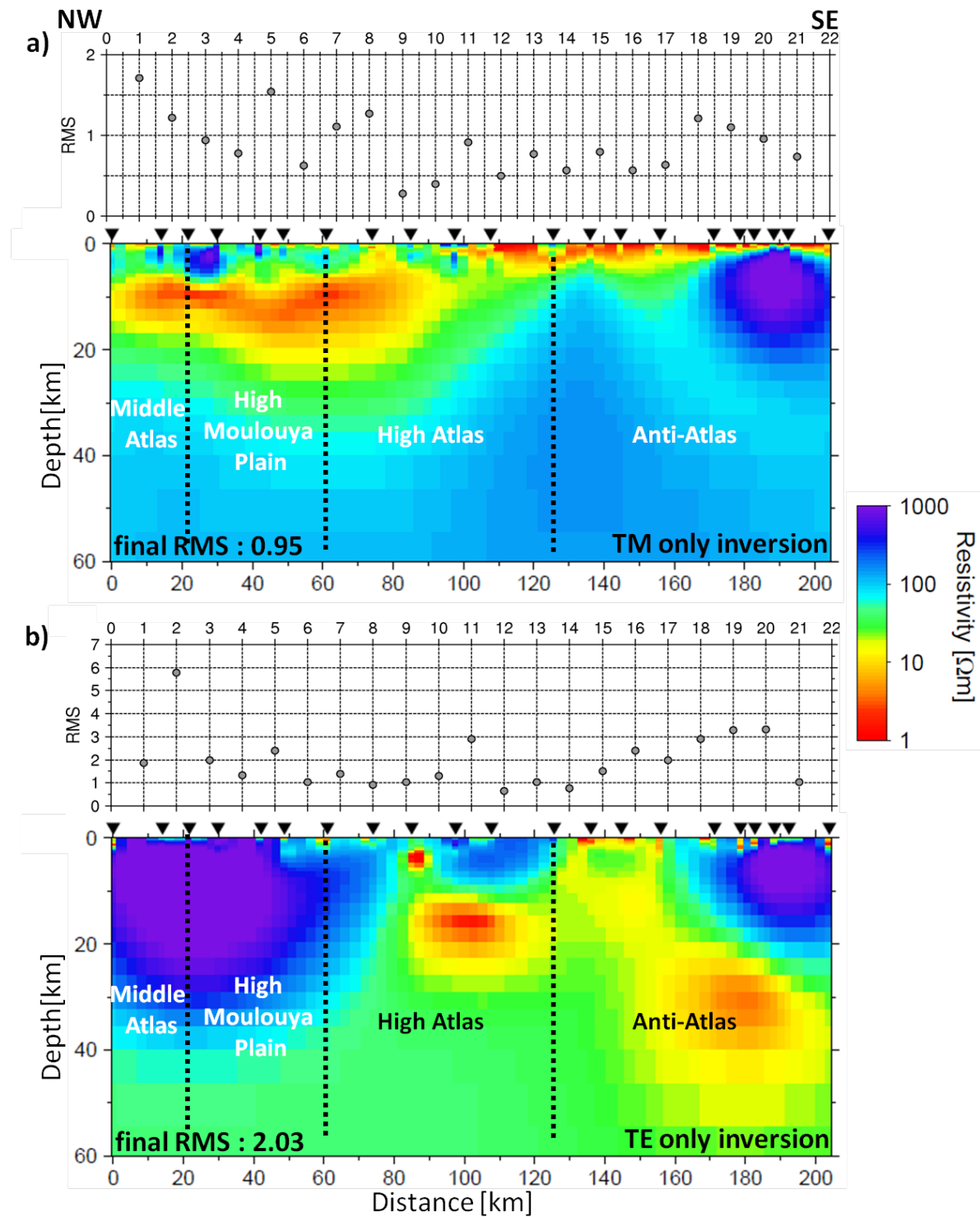


Figure 5.5.: Figure showing the inversion results of the crustal, MEK profile. Panels (a) show the results if only the TM mode data are used for the inversion, whereas in (b) only the TE mode data are taken into account during the inversion. For each inversion, $\alpha = 3$ and $\beta = 1$ are used. The rms values of the TM and TE modes with respect to the final models at each individual site are shown on top.

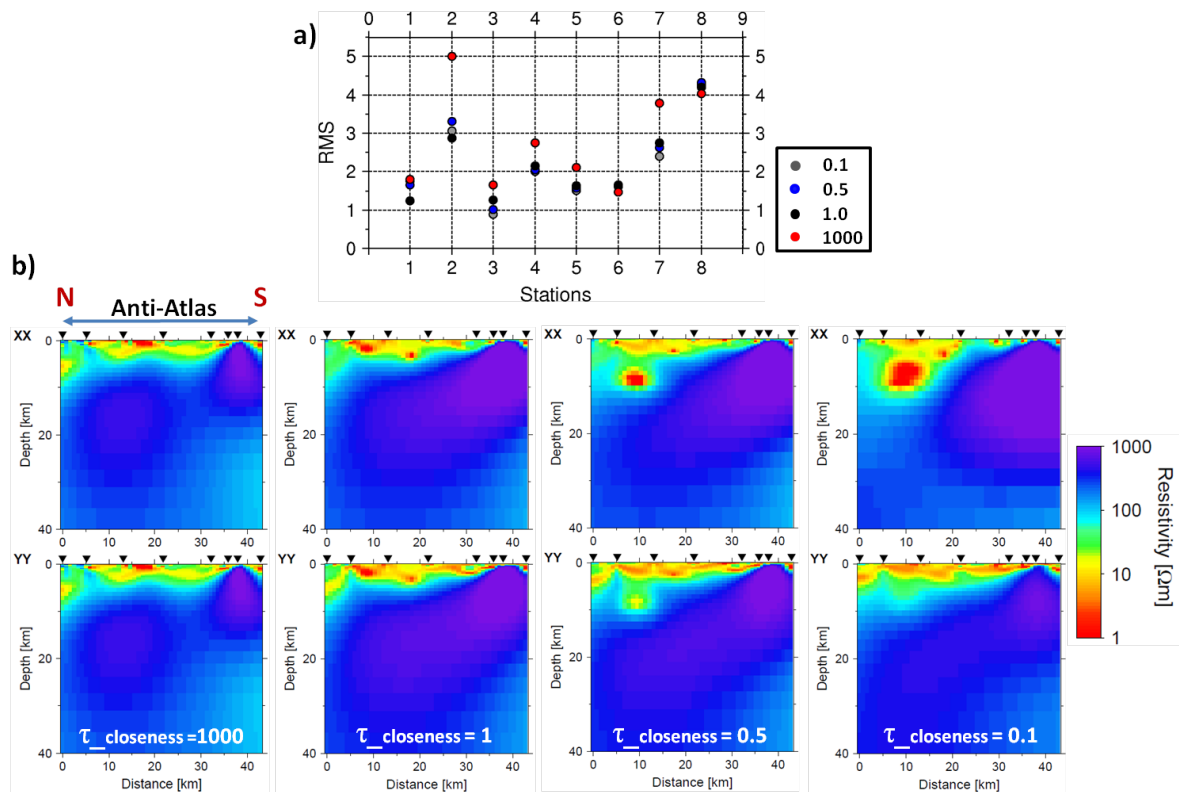


Figure 5.6.: Comparison of isotropic and anisotropic 2-D inversion results of the southern part of the MEK profile (only sites in the Anti-Atlas, mek025, mek026, mek027, mek028, mek029, mek030, mek033 and mek034). **(a)** The rms values for individual sites were plotted on top of the models; **(b)** resulting 2-D inversion models using different τ_{ISO} values. For the first inversion run, error floor values of 50% and 10% were used for apparent resistivity and phase data respectively. For the second inversion run, the values are reduced to 10% and 5%.

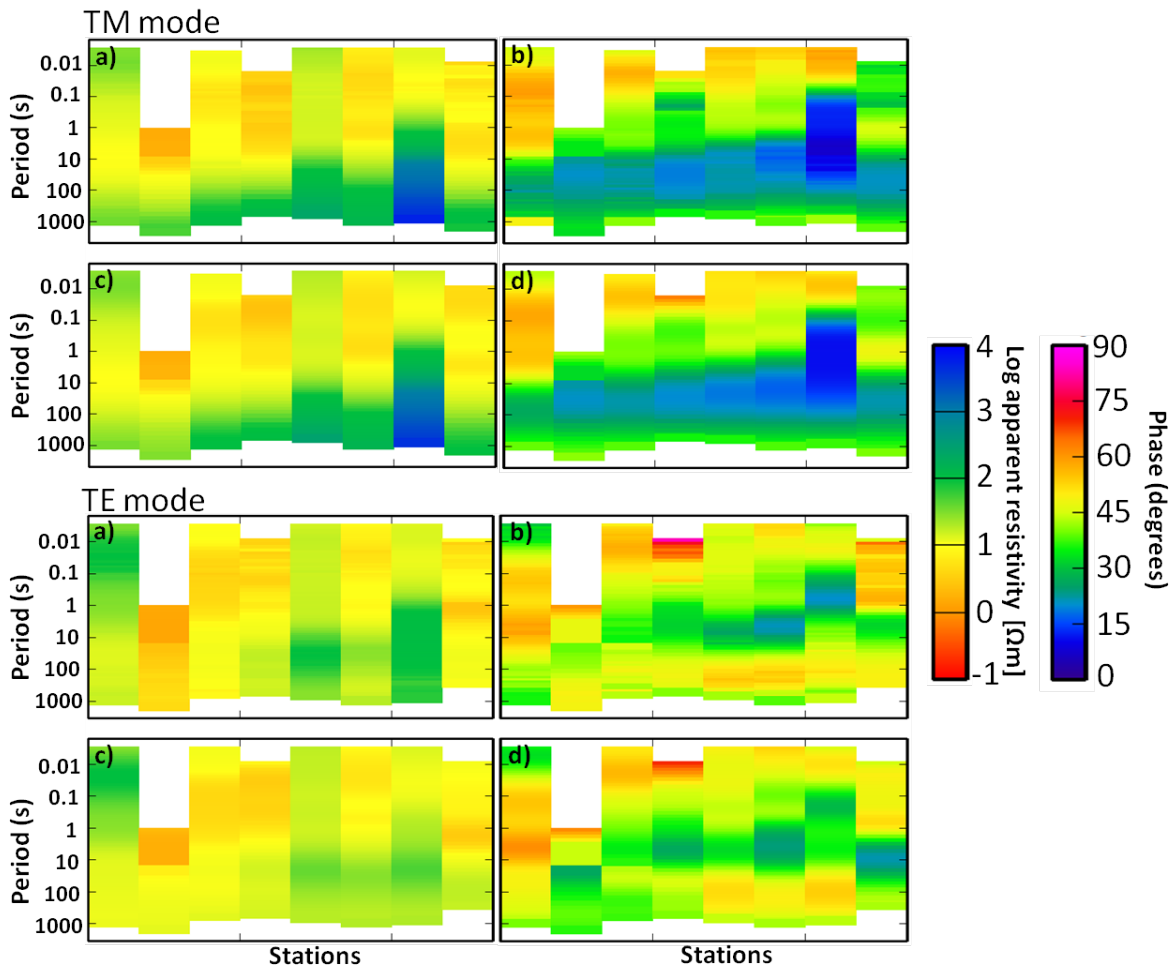


Figure 5.7.: The apparent resistivity and phase pseudo-sections of TM (on the top) and TE data (on the bottom). Panels showing **(a&b)** observed apparent resistivity and phase and **(c&d)** model responses with apparent resistivity and phase.

to inversion. The same inversion strategy as for the crustal part in [Section 5.2](#) and as described in [Section 5.1](#) is applied, that is TM and TE phases first, then TM and TE resistivities are introduced.

[Figure 5.8](#) shows the final 2-D isotropic smooth inversion model for the MEK profile. For each site the individual joint TM and TE rms values are plotted on top of the model, clearly showing that the sites in the northern end of the profile (the Middle Atlas and the High Moulouya Plain) have higher rms values compared to the rest of the stations. This could be the result of the choice of strike angle, 22°E of N, as those stations favour a strike angle of 50°E of N as shown in [Chapter 4](#). The previously observed conductive layer beneath the Middle Atlas and the High Moulouya Plain is now extended to upper mantle depths. The entire Atlas is characterized by a homogeneous, resistive mantle. However, one should bear in mind that the crustal part of the mantle model is not reliable. Pseudo-sections of both the TM and TE mode data and isotropic model response with apparent resistivities and phases are presented in [Figure 5.9](#). The figure shows that a satisfactory fit to observed data is obtained for the period range used for the inversion (0.001 to 10,000 s). It can also be clearly seen from the observed phase data, high phase values are observed between the periods of 10 s and 1000 s which are related to imaged high conductivity anomaly and periods >1000 s decrease in phase values are observed which means increase in resistivity.

In the case of 3-D effects in an MT data set, 3-D inversion of a single MT profile can be more reliable than a 2-D inversion of the same data set ([Siripunvaraporn et al., 2005a](#)). Including diagonal elements of the impedance tensor provides controlling information regarding the presence and geometries of off-profile structures. ([Siripunvaraporn et al., 2005a](#)) also illustrated that 2-D inversion of presumed TE mode data may introduce spurious features in the 2-D model, when the data are 3-D. Also, with 3-D inversion it is not necessary to make an assumption about the strike direction when the full impedance tensor data are used. This is one of the motivations for applying 3-D inversion to the TopoMed data set in this study. However, one should still be careful about the coordinate system used in 3-D inversion ([Kiyani et al., 2014](#)). Detailed discussion about coordinate system is given in the next chapter ([Chapter 6](#)) and the 3-D inversion results of the TopoMed MT data are discussed in [Chapter 7](#).

5.4 INTERPRETATION

The inversion model of the crustal model for the MEK profile reveals a number of significant features. The SHAF represents the main boundary between the resistive block on the south (associated with Anti-Atlas, West African Craton) and lower resistivity crustal features to the north ([Figure 5.10](#)).

The most dominant feature of this model is the low resistivity layer at middle to lower crustal depths (20 - 40 km) beneath the Middle and High Atlas Mountains, which was also imaged by [Schwarz et al. \(1992\)](#) and [Ledo et al. \(2011\)](#) ([Figure 5.11](#) and [Figure 5.12](#)). This zone is well correlated with a low seismic velocity zone (LVZ) and low Bouguer gravity anomaly (~ -110 mGal) ([Wigger et al., 1992](#); [Schwarz & Wigger, 1988](#); [Ayarza et al., 2005](#)) and is confined by NHAF to the south. As a possible explanation to address the origin of high conductive zone ([Figure 5.11](#)), which

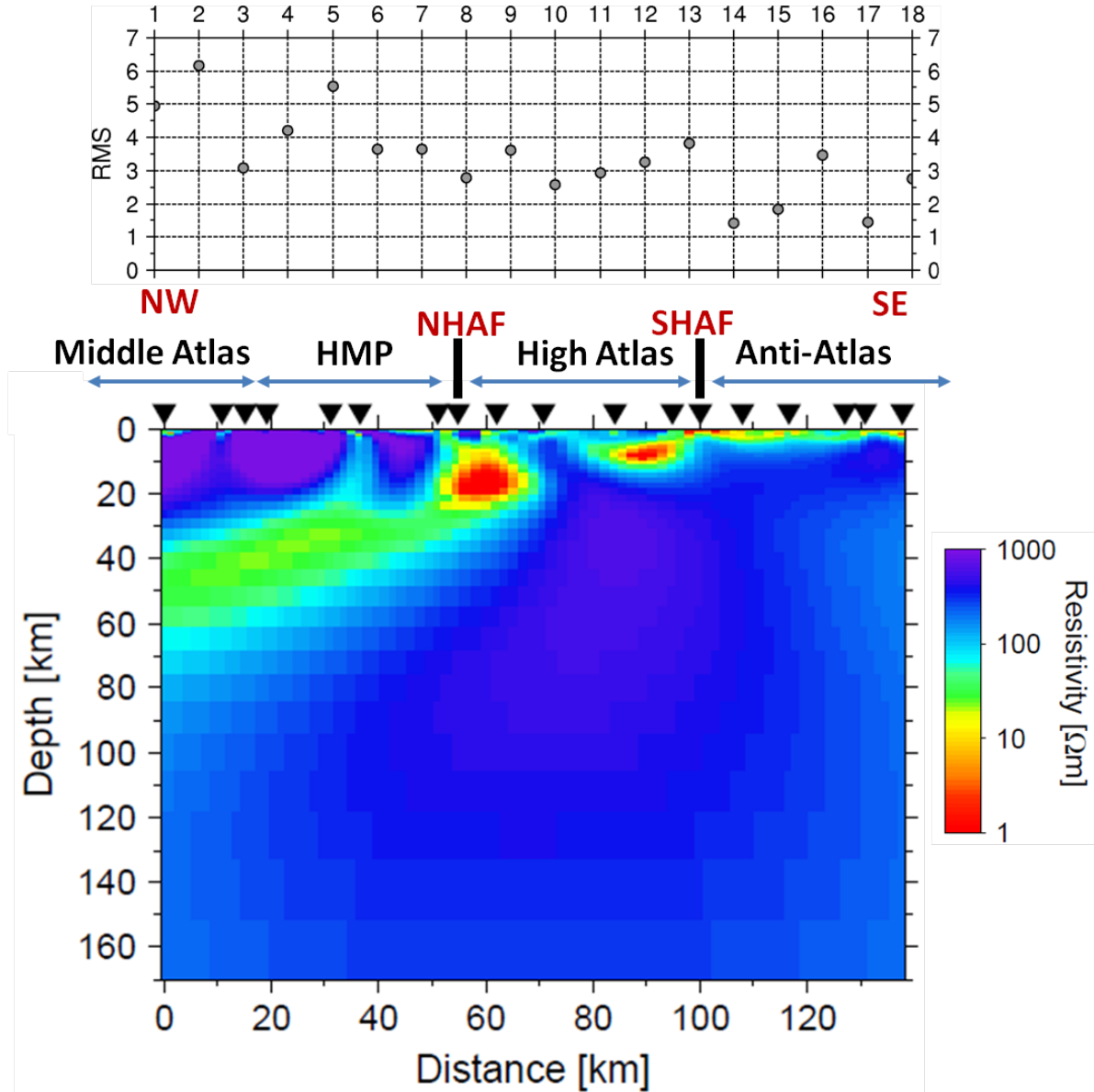


Figure 5.8.: Figure showing the inversion results of the mantle structures, MEK profile. For each inversion, $\alpha = 3$ and $\beta = 1$ are used. For the first inversion run, error floor values of 50% and 10% are used for apparent resistivity and phase data, respectively. For the second inversion run, the values are reduced to 10% and 5% for TM apparent resistivities and phases, respectively, and 15% and 5% for TE apparent resistivities and phases, respectively. The rms values of the TM and TE modes with respect to the final models at each individual site is shown on top.

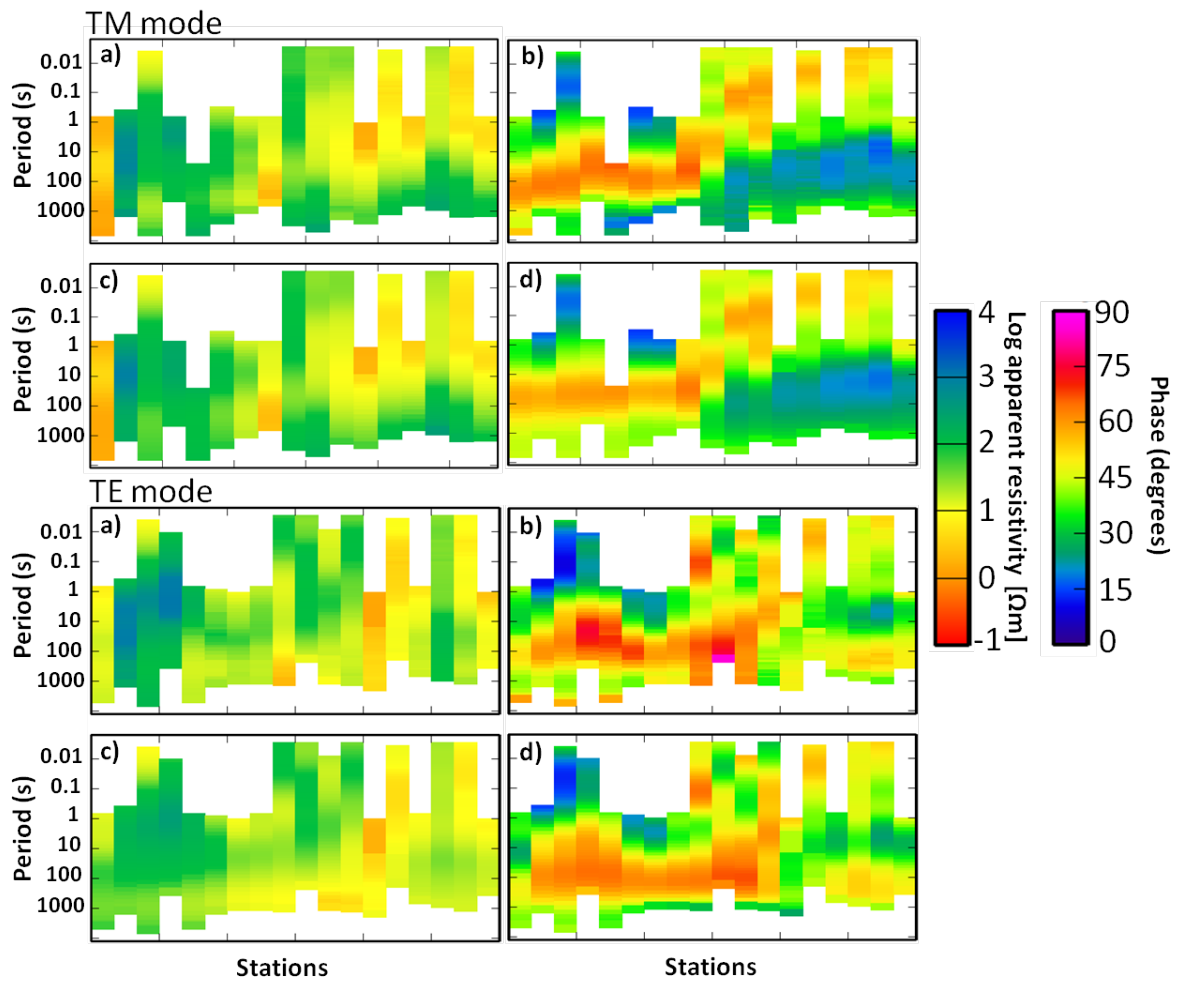


Figure 5.9.: The apparent resistivity and phase pseudo-sections of TM (on the top) and TE data (on the bottom). Panels showing (a&b) observed apparent resistivity and phase and (c&d) model responses with apparent resistivity and phase.

has a listric geometry and flattens beneath the High Moulouya Plain, Schwarz et al. (1992) proposed that fluids and volatiles within a connected system of porosity (e.g., with effective pore pressure close to zero) are responsible for the observed anomaly. Based on knowledge of the Cenozoic volcanic events in the study area, those authors argued that those fluids and their products would be activated from those volcanic events. On the other hand, Ledo et al. (2011) proposed that low degree partial melting of sub-lithospheric mantle sources could be the cause for that anomaly. The authors calculated the amount of partial melting necessary to explain the conductive anomaly is between 2% and 8% according to the Modified Brick Layer Model (MBLM). However, those proposed sublithospheric mantle sources (e.g., Ayarza et al., 2014; Bezada et al., 2014; Miller & Becker, 2014; Palomeras et al., 2014) are not imaged in their resistivity model ($\sim 1000 \Omega\text{m}$ at depth ≥ 40 km) and in the resistivity model with strike angle of 22°E of N (Figure 5.8).

Zones with low resistivity are often observed in the lower crust in many tectonic settings. The cause of a crustal conductive anomaly can be generally attributed to a range of mechanisms including conductive minerals such as graphite, sulphides, fluids or melt. Detailed discussion of this dominant feature is given in Chapter 8. The discussion involves the interpretation of the 2-D and 3-D inversion results of the TopoMed MT data set. This is followed by a discussion of the origin of low electrical resistivity in the crust and upper mantle as well as with the previous and ongoing seismological, geological and petrological work in the study area.

The resistive ($\geq 1000 \Omega\text{m}$) upper crust and middle crust (0 - 20 km) below the Middle Atlas and the High Moulouya Plain could be explained by a large volume of Paleozoic granites (Schwarz & Wigger, 1988) and lack of important thrusting systems (Ledo et al., 2011). Unlike the Middle Atlas and the High Moulouya Plain, the High Atlas and the Anti-Atlas are characterized by more homogeneous resistive crustal structures (Figure 5.10).

Comment on "Deep resistivity cross section of the intraplate Atlas Mountains (NW Africa): New evidence of anomalous mantle and related Quaternary volcanism" by Anahnah et al. (2011)

As discussed in Section 3.2 (of Chapter 3), the geoelectric structure of the Atlas Mountains was also investigated by Topolberia MT studies along the MEK profile (Anahnah et al., 2011). Figure 5.13 shows the resulting 2-D MT model of Anahnah et al. (2011) with a geological transect on top, which integrates their MT results with the previous geological and geophysical data. However, Jones et al. (2012a) contend that the presented 2-D model (Figure 5.13B) is highly suspect, particularly at mantle depths; therefore the corresponding tectonic interpretation (Figure 5.13A) based on that 2-D model has not been proven and cannot be trusted. The reasons for the contentions of Jones et al. (2012a) are as follows:

- Data analysis: Jones et al. (2012a) reproduced the responses from Site 15 (Fig. 1 in Jones et al. (2012a)), which lies almost above the purported anomalously conducting zone in the lithospheric mantle. The authors analyzed the data at Site 15 using the Rho+ algorithm of Parker & Booker (1996) and showed that the data are not internally consistent, (i.e., the

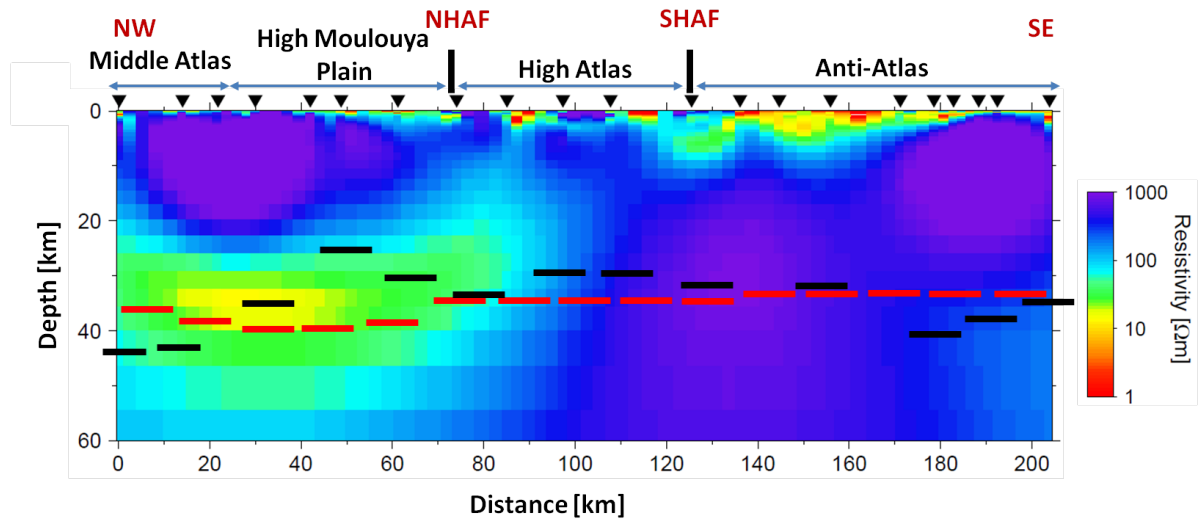


Figure 5.10.: Isotropic 2-D crustal resistivity model of the MEK profile across the Atlas Mountains are derived from inversion of joint TM and TE mode MT data. The main features of the resistivity model are the high conductivity of the middle to lower crust in the Middle Atlas and the High Moulouya Plain and the resistive Anti-Atlas. The Moho depth is highlighted by red dashed lines (Ayarza et al., 2005) and black dashed lines (Miller & Becker, 2014). NHAF: North High Atlas Fault; SHAF: South Atlas Fault.

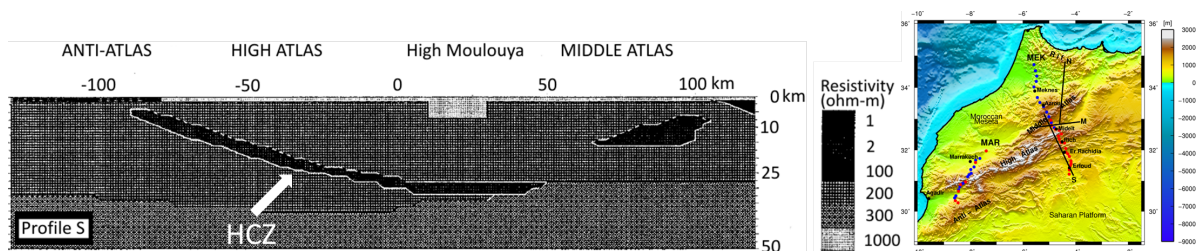


Figure 5.11.: Figure showing the first electrical resistivity model derived from forward modelling of 5-component MT data along the Profile S. Electrical resistivity of the middle and lower crust beneath the Anti-Atlas was determined to about 200 Ωm , the same as for the lower crust of the High and Middle Atlas. The model has a highly resistive (1000 Ωm) uppermost mantle. The model shows a rather steeply dipping high electrical conductivity zone (HCZ), stretching from the southern border of the High Atlas almost down to Moho depth (36 km) beneath the Moulouya Plain; *modified from (Schwarz et al., 1992).*

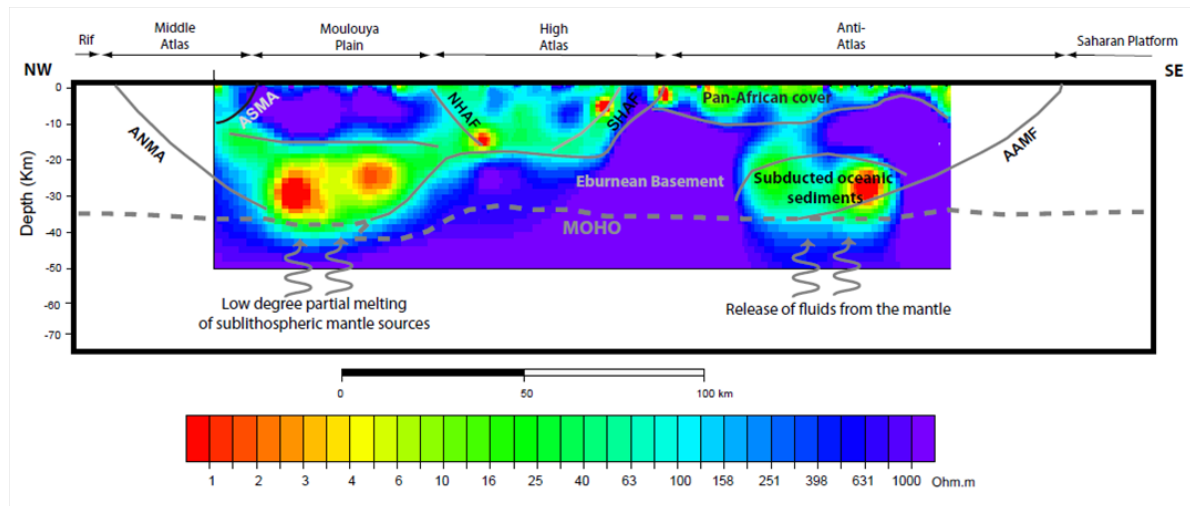


Figure 5.12.: Electrical resistivity model across the Atlas Mountains of Morocco obtained from 2-D inverse modelling. The high conductivity in the lower crust (20-40 km) beneath the High Moulouya Plain was attributed to low degree partial melting (between 2% and 8%) as a consequence of either the Canary mantle plume flow (Duggen et al., 2009) or thermal erosion of a metasomatized lithosphere (Berger et al., 2009). Another enhanced conductivity feature obtained in the Anti-Atlas was interpreted to be due to minerals precipitated from fluids released from the mantle during the Precambrian accretion of the Anti-Atlas to the West African super continent. ANMA: North Middle Atlas Fault; ASMA: South Middle Atlas Fault; NHAF: North High Atlas Front; SHAF: South Atlas Fault; AAMF: Anti-Atlas Major Fault. The Moho depth is based on the work of Ayarza et al. (2005); from Ledo et al. (2011).

apparent resistivities and phases do not obey the dispersion relations, in other words, they are not Hilbert transform pairs, as is formally required in 1-D (Parker & Booker, 1996) and in 2-D in the TM mode (Weidelt & Kaikkonen, 1994), and is usually the case in 2-D for the TE mode (Fischer & Schnegg, 1993; Parker, 2010) and for the off-diagonal terms of the MT impedance tensor in 3-D (Yee & Paulson, 1988, 1990)), (Fig. 2 in Jones et al. (2012a)).

- Geoelectric strike: Anahnah et al. (2011) conducted 2-D modelling of MT data that display 3-D effects. This 3-D nature is visibly evident in the phase tensor plots of their Fig. 3; the strikes of ellipses rotate with increasing period. The authors adopted a single strike direction for both the crust and the mantle of 80° E of north, which is 30° different from our own crustal value of 50° E of north and 58° different from our mantle value of $N22^\circ$ E (for details see Section 4.5 of Chapter 4). Either the data should be modelled fully in 3-D, or the crustal structures modelled in 2-D then the mantle structures modelled in 2-D in a different strike angle, after removing the crustal effects as a "distortion" on the mantle responses.
- Modelling: The 2-D model does not fit their data, either in a global (whole data set) sense or in a local (site specific, Fig. 4 in Anahnah et al. (2011)) one. Anahnah et al. (2011) showed the fit of the model to the data at only four sites. At Site 15, the data are very poorly fit particularly at periods greater than ~ 10 s, which are the mantle-probing periods. If the data at Site 15 are questionable in their internal consistency (as discussed above) and are

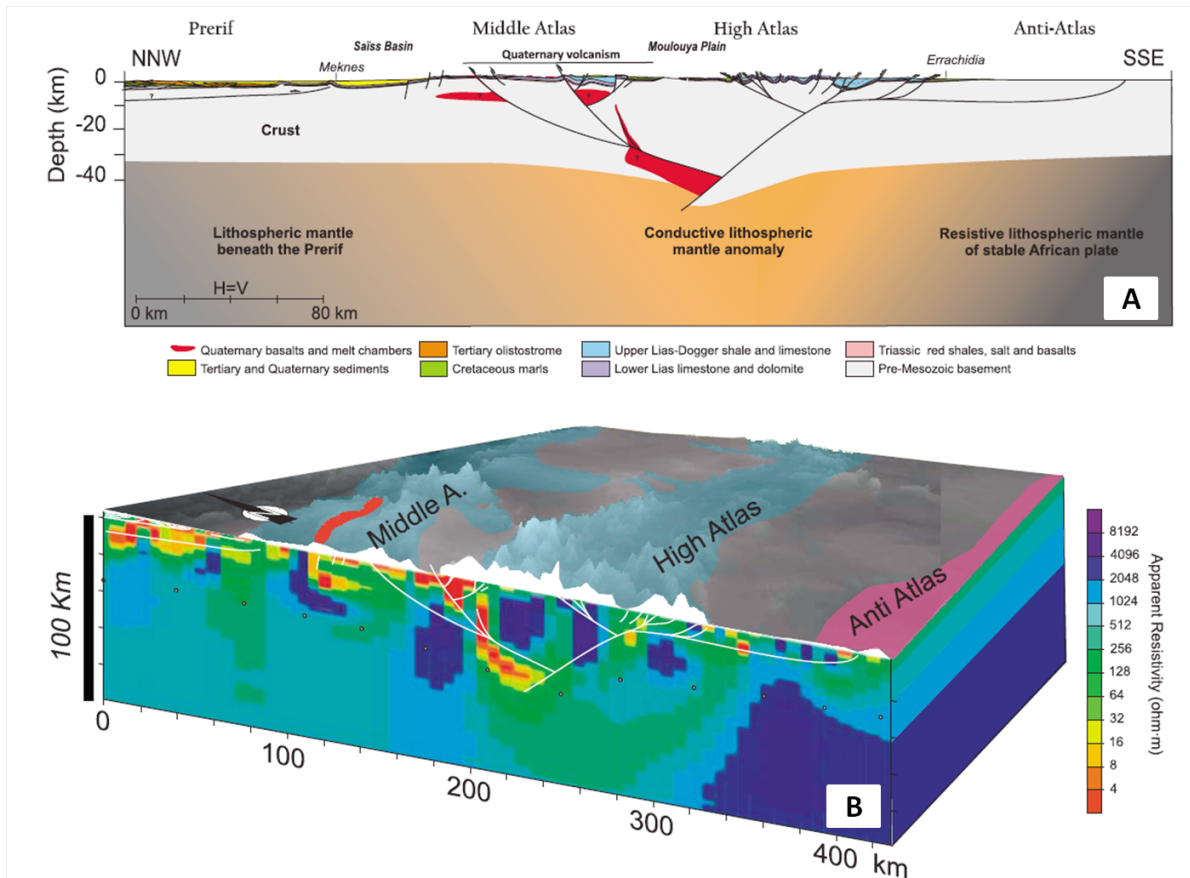


Figure 5.13.: **(A)** Geological transect across the Atlas Mountains integrating the MT (Anahnah et al., 2011) and the previous geological (Teixell et al., 2003; Arboleya et al., 2004) and geophysical data (Arboleya et al., 2004; Ayarza et al., 2005). **(B)** Present-day crustal and mantle structure derived from 2-D MT modelling; from Anahnah et al. (2011).

furthermore not being fit by the model, then the 2-D model is an inaccurate representation of the data, and one of the primary interpretive features, of thinned lithosphere indicated by the moderately conducting lithospheric mantle beneath the High Atlas, is not proven and highly questionable.

- In the model of Anahnah et al. (2011), the interpreted conductive lithospheric mantle (Figure 5.13) has a resistivity in the order of some hundred Ωm , which is not indicative of typical asthenospheric resistivity of 5 - 25 Ωm .

THE INABILITY OF MAGNETOTELLURIC OFF-DIAGONAL IMPEDANCE TENSOR ELEMENTS TO SENSE OBLIQUE CONDUCTORS IN THREE-DIMENSIONAL INVERSION

6.1 ABSTRACT

In this paper, we use synthetic data sets from a profile to demonstrate the importance of aligning the 3-D mesh and data coordinate system with the dominant geo-electrical strike direction in 3-D inverse modelling. The resistivity model investigated consists of a regional, elongated 2-D conductive structure at 45° to the profile. We compare the results of full impedance tensor inversion with the results from inversion of only off-diagonal components of the magnetotelluric impedance tensor. The 3-D inversion result obtained with the complete tensor elements yields the subsurface model closest to the original model, whereas the result of inverting only off-diagonal components is the poor imaging of the continuity of the conductive 2-D body. However, the conductor can be correctly recovered using only the off-diagonal components if the model mesh and the data are aligned with quasi-2-D geo-electrical strike.

6.2 INTRODUCTION

In recent years, with the availability of 3-D inversion codes (e.g., Farquharson et al., 2002; Siripunvaraporn et al., 2005a; Egbert & Kelbert, 2012), routine applications of 3-D inverse modelling of magnetotelluric (MT) data have become common in the EM community. However, logistics, acquisition costs and instrumentation availability still require MT field specialists to acquire data predominantly along 2-D profiles across geological terranes. One of the motivations for applying 3-D inversion instead of 2-D inversion is that no assumption about geo-electric strike direction or coordinate system has to be made. In some cases, it is difficult to determine a common geo-electric strike angle for whole period range and for all sites along the 2-D profile (e.g., Marquis et al., 1995;

This chapter has been published: Kiyani, D., Jones, A. G., & Vozar, J. The inability of magnetotelluric off-diagonal impedance tensor elements to sense oblique conductors in three-dimensional inversion. *Geophysical Journal International*, **196**, doi: 10.1093/gji/ggt470.

Kiyan et al., 2010; Miensoopust et al., 2011). Siripunvaraporn et al. (2005b) demonstrated the advantages of interpretation of 2-D MT profile data using 3-D inversion (Siripunvaraporn et al., 2005a) for a synthetic data set. Siripunvaraporn et al. (2005b) conclude that 3-D inversion of single profile data can provide a more meaningful picture of the subsurface geometry beneath the profile, particularly when using the full impedance tensor. Xiao et al. (2010), Patro & Egbert (2011), Bertrand et al. (2012), and Khoza et al. (2013b) present their 3-D models from MT profile field data set. Among these, Patro & Egbert (2011) present inversion results with data and a 3-D model grid aligned with the predominant geological strike direction of the study area, in order to force structures to have longer length scales along the strike direction. In addition, they compare full impedance tensor inversion results with results from only off-diagonal components, and they concluded that the main structural features inferred from 2-D and 3-D modelling are in good agreement, although there are differences regarding the positions and amplitudes of the main conductive features in the resulting models, particularly in the use of higher smoothing scale along geo-electric strike direction. Most recently, Tietze & Ritter (2013) investigated the influence of the orientation of the inversion coordinate system, data error bounds, and model regularization parameters, including using different components of the impedance tensor in the context of inverting a large, real 2-D array and complementary synthetic data sets via 3-D inversion. Our paper results from an examination of the differences found when applying 3-D compared to 2-D inversion.

In this paper, we present the limitations of 3-D interpretation of single MT profile data in the presence of a regional 2-D structure with a strongly oblique strike direction (45°) to the adopted 3-D grid. Our aims are (1) to demonstrate the importance of including the diagonal terms of the impedance tensor ($\mathbf{Z}_{xx}, \mathbf{Z}_{xy}, \mathbf{Z}_{yx}, \mathbf{Z}_{yy}$), and (2) to consider using a strike-aligned coordinate system when using off-diagonal impedance tensor elements ($\mathbf{Z}_{x'y'}, \mathbf{Z}_{y'x'}$) to map the right geometry and shape of the conductive structures, as most 3-D structures will have a dominant length direction with quasi 2-D strike. (Note on coordinate systems used: x and y are in the geographic coordinate system, with x directed north and y directed east. x' and y' define the coordinate system of the body, with x' parallel to the body direction, *i.e.*, directed NE for the particular example considered in this paper in a geographic reference frame, and y' directed perpendicular to the body, *i.e.*, NW.)

6.3 SYNTHETIC DATA: TEST MODEL

To simulate a 2-D case, we designed a simple model consisting of a $10 \Omega\text{m}$ conductive body of infinite extent embedded in a homogeneous, $1,000 \Omega\text{m}$ half space. Figure 6.1a shows the design of the structure in plan view. The width of the body is 28 km and its depth extent is from 20 to 40 km below the surface. The model is discretized on a $63 \times 63 \times 45$ mesh (including 10 air layers), with a horizontal centre cell size of $4 \text{ km} \times 4 \text{ km}$. The central part comprises a uniform horizontal mesh of 43×43 . On each of the north, south, east and west directions, the central part of the mesh was surrounded by 10 planes, where each successive padding cell was scaled by a factor of 1.5.

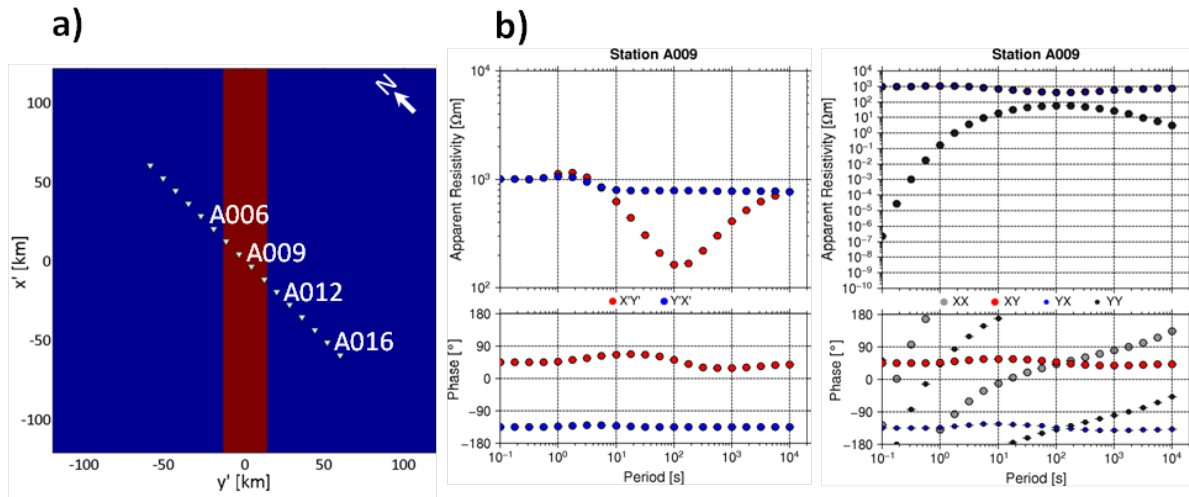


Figure 6.1.: a) Plan view of the synthetic model used to generate MT data. The white triangles represent the site locations. The model consists of 10 Ωm conductor with a strike direction of 45° east of north in a homogeneous half space of 1,000 Ωm . b) Resistivity and phase curves calculated at site A009, the forward response of the test model (x' -axis pointing parallel to strike direction) and in the geographic coordinate system (x -axis points towards north), respectively.

Instead of rotating the body with a strike direction of 45° east of north, which would introduce "corners" on the step-like edges of the body, we rotated the 3-D inversion mesh by 45° west of north. A profile of 16 sites, shown as white solid triangles in Figure 6.1a, is considered. The MT response of the model at 20 periods (four periods per decade), between 0.1 and 10,000 s, was calculated using the 3-D forward modelling code of Mackie et al. (1994) (implemented in Geosystem's WinGLink® package) to generate the four complex components ($\mathbf{Z}_{x'x'}$, $\mathbf{Z}_{x'y'}$, $\mathbf{Z}_{y'x'}$, $\mathbf{Z}_{y'y'}$) of the impedance tensor. In addition, we also calculated the 2-D forward responses of the test model to verify the 3-D forward solution (see Section A.1). 2.5% Gaussian-distributed random noise and scatter were added to the synthetic impedance data (equivalent to 5% to apparent resistivity and 1.5° to phase) and to the error estimates themselves. Figure 6.1b shows apparent resistivity and phase curves of site A009: (on the left) data are provided in a coordinate system that is aligned with the geo-electric strike direction (forward response of the test model, Figure 6.1a) and (on the right) data are shown in a coordinate system that is aligned with geographic directions, that is the x -axis points towards geographic north.

6.4 3-D INVERSE MODELLING

We inverted the synthetic data from the single profile employing the parallel version of Modular system for ElectroMagnetic inversion (ModEM; Egbert & Kelbert (2012)). We considered two different types of coordinate systems summarized below. For the geographic coordinate system, we performed two types of inversions: for the off-diagonal tensor elements only, and for the complete impedance tensor. For the geo-electric strike oriented coordinate system, we ran inversion with

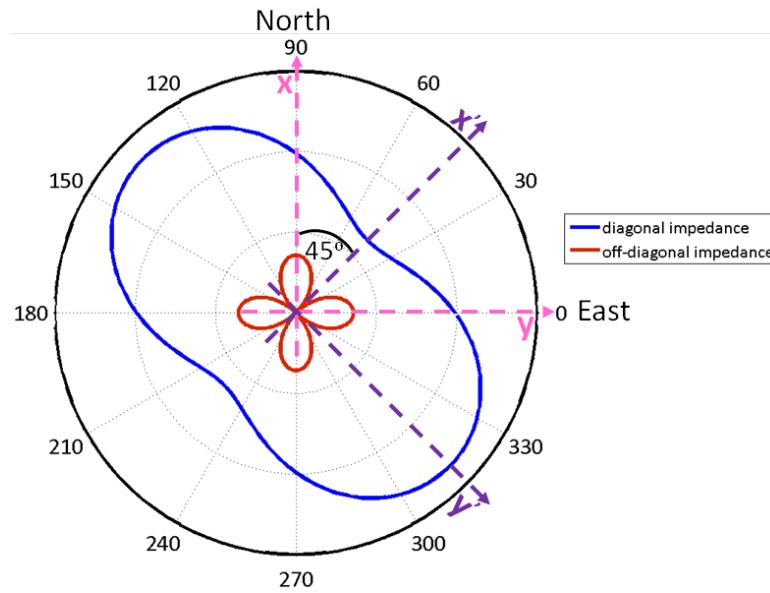


Figure 6.2.: Impedance magnitude rotation diagram ("peanut diagram") for site A009 is at 100 s. The blue solid curve represents the off-diagonal impedance element, and the red solid curve represents the diagonal impedance element.

off-diagonal components only, and with the complete tensor, but here we only report on the former (see below).

6.4.1 Model Set-up

In the first inversion set-up, we used a coordinate system with the x - and y -axis pointing towards geographic north and east, respectively. The 3-D solution mesh comprised $66 \times 67 \times 45$ cells in the north-south, east-west and vertical directions, with a horizontal cell size of $4 \text{ km} \times 4 \text{ km}$ in the area of interest. The lateral extent of the padding cells, 11 in each of north, south, east, and west directions, increased by factor of 1.5. The centre of the mesh, where the horizontal dimensions of the cells were all the same, comprised $45 \times 44 \times 45$ cells. The thickness of the top layer was 50 m, and the thickness of each subsequent layer increased with a vertical factor of 1.2. As input data, which were used in the geographic coordinate system shown in Figure 6.2 with pink colour, we ran the inversion twice, once with only the off-diagonal components and a second time with all four complex tensor elements.

In a second inversion set-up, we used the synthetic model configuration (Figure 6.1a) that was aligned with the regional geo-electric strike direction, that is x' points 45° east of x . Details of the 3-D mesh are described in Section 6.3. In this case, we considered inversion of only the off-diagonal terms, which were also rotated to the strike direction, presented in Figure 6.2 with purple colour.

For all the inversions presented in the framework of this paper, the starting model was a homogeneous half-space of $500 \Omega\text{m}$, and the error floors were set as an absolute value to 2.5% of

$(|\mathbf{Z}_{xy} \times \mathbf{Z}_{yx}|)^{1/2}$. Note that this error floor setting dominates over the assigned error floors for the diagonal terms and ensures that the diagonal terms are not unduly weighted.

6.4.2 Smoothing Parameter

Smoothing in ModEM is governed by the covariance parameter, which controls the decorrelation length scale, and therefore the resulting roughness of the model. This in effect defines the relative weighting coming from different wavelength features in the model.

ModEM allows smoothing over different length scales for the x -, y -, and z - directions, which is similar to WSINV3DMT (Siripunvaraporn et al., 2005a). If no further information is given, this parameter is set to 0.3 in all directions. We carried out tests with several variations on the model covariance to investigate the impact of it on the resulting inversions. Figure 6.3 summarizes the final inversion models for various values of model smoothing parameters. In all resulting inversion models, the linear conductive structure is present; however, the extent and intensity of the conductor varies depending on the choice of the smoothing values. Applying lower regularization in the vertical direction (Figure 6.3A and B) produces a less pronounced conductive feature at 30 km depth. In addition, with lower regularization in the horizontal directions the linear conductive feature tends to lean towards the NNW-SSE direction, whereas with higher smoothing (Figure 6.3E and F) it leans towards the NNE-SSW direction. The slight skewness of the conductor, that is the slightly the NNW to SSE orientation of the conductor, is because of the location of the stations (as the stations in the NW region, relative to the centre point are closer in proximity to the northern part of the conductor than the southern, as a result, the inversion is assigning the conductivity slightly closer to the station than it ideally should.)

For all inversions discussed in the following section, the same model smoothing (model covariance parameters) value of 0.4 was applied in the x - and y - directions and a value of 0.1 was applied in the z - direction.

6.4.3 3-D Inversion Results

The final models obtained by inverting (i) only the off-diagonal elements and (ii) the full impedance tensor elements, are shown in Figure 6.4. Whereas the 45° oblique structure has been recovered successfully when inverting the full impedance tensor, for the off-diagonal impedance tensor inversion results the structure is barely sensed, and has not been resolved. As we invert data from a single profile, the along-strike extent of the oblique conductivity structure imaged beneath the profile is resolved to some extent when using all elements. Figure 6.5A and B show a comparison of apparent resistivity and phase pseudo-sections for the observed data and the corresponding calculated data for the final inversion results using off-diagonal components and the complete impedance tensor, respectively. The total rms misfits of 1.26 and 1.00 were achieved for each case.

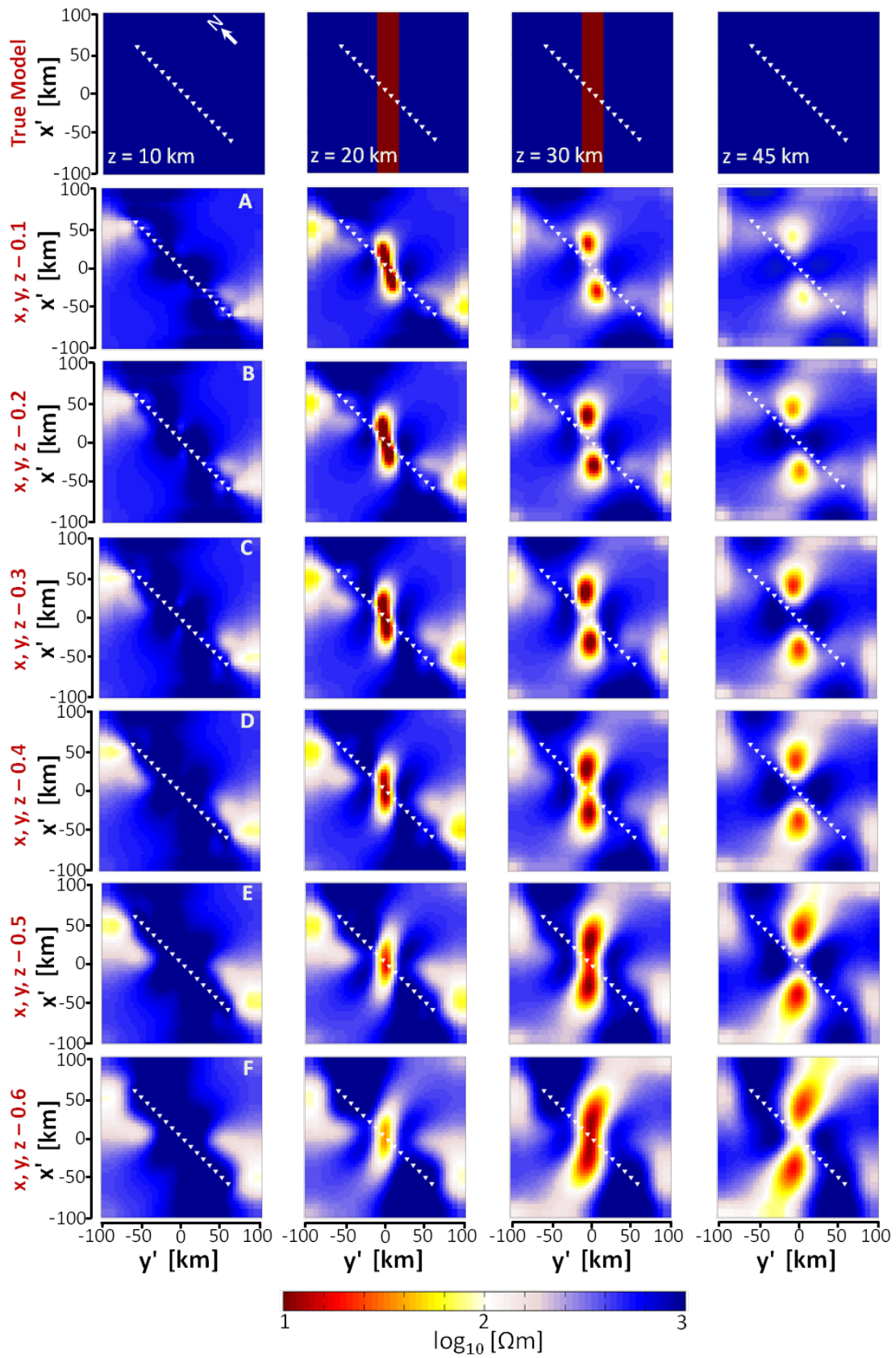


Figure 6.3.: 3-D inversion results of the test model using different smoothing parameters. As input data, only off-diagonal impedance components ($Z_{x'y'}$, $Z_{y'x'}$) were used. The white triangles represent the site locations.

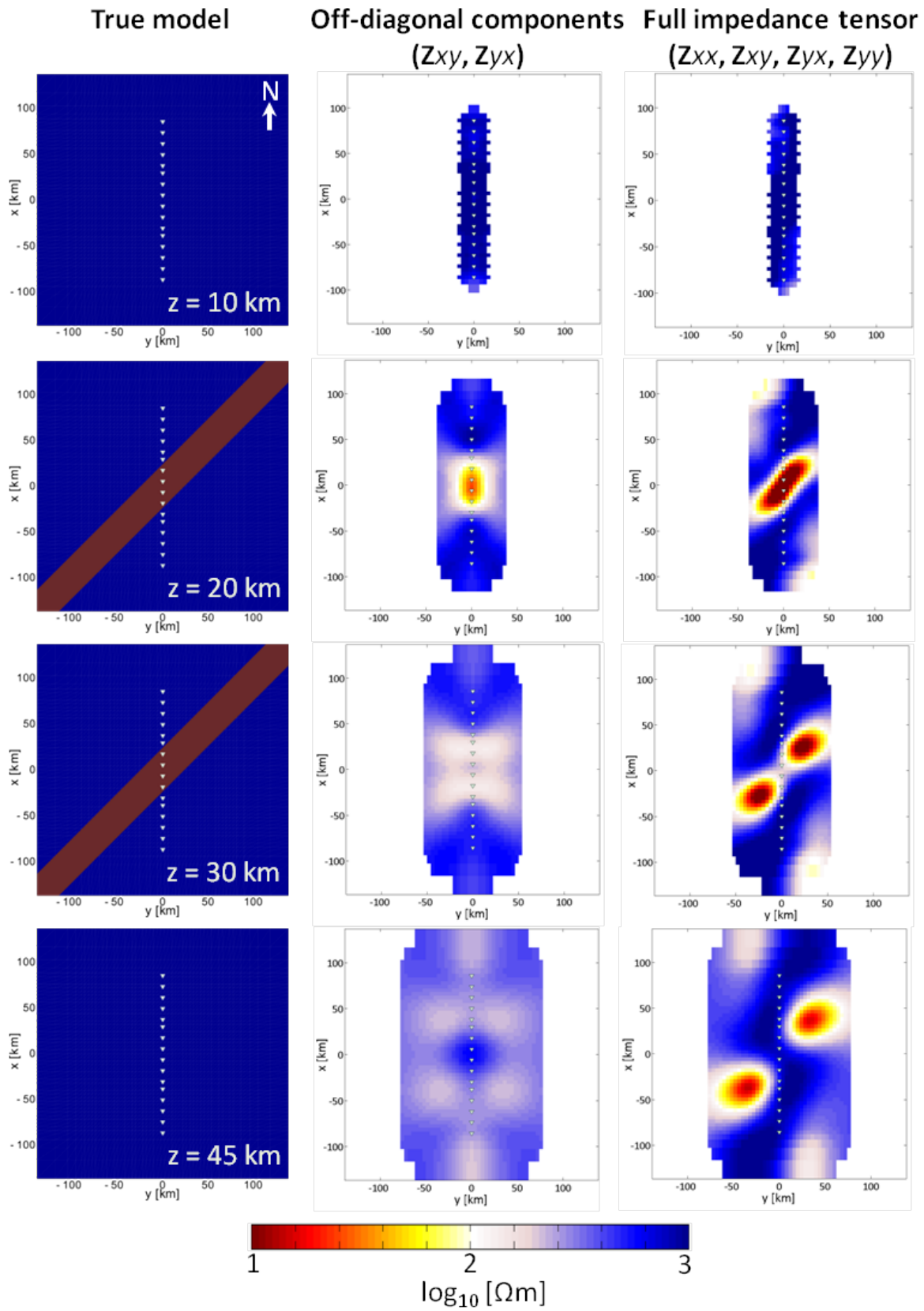


Figure 6.4.: 3-D inversion results of the test model obtained in geographic coordinate system. From left to right the true model and models obtained from inversion of off-diagonal tensor components and from inversion of full impedance tensor. The white triangles represent the site locations.

In order to recover the true model using only off-diagonal elements of the impedance tensor, the coordinate system must be considered, meaning that the data set and the model grid should be rotated to a specific coordinate system that is most consistent with a previously identified geo-electrical strike direction (Figure 6.6). Off-diagonal apparent resistivity and phase pseudo-sections for the inversion result shown in Figure 6.6 and for the observed data were summarized in Figure 6.7. An rms misfit of 1.03 was obtained for the model.

Figure 6.2 illustrates the polar diagram at 100 s of one of the stations located on top of the conductor. As expected for perfect 2-D geometry, the amplitude of the diagonal term displays a four-leaf clover pattern with zeros in the direction of strike and perpendicular to strike, whereas the off-diagonal term reaches maxima and minima in those directions. In our example, when we invert data in the coordinate frame 45° to strike, the off-diagonal terms reach their maximum and minimum values (Figure 6.2, purple dashed line), in which inversion with rotated data was able to recover the true structure well (Figure 6.6). In contrast, in the original coordinate system, shown by the pink dashed line, $|Z_{xy}|$ is almost the same as $|Z_{yx}|$, so the response of the conductive anomaly has disappeared.

Without data and mesh rotation, but with two additional profiles, the inversion results using off-diagonal terms can recover the right geometry of the oblique structure, although the resistivity value shows some discrepancies compared to the true model (Figure 6.8). As shown in Figure 6.2 (pink solid circles), this result can be explained by not using minimum and maximum values of the off-diagonal terms. Additionally, the model resulting from the inversion using full impedance tensor information from three profiles represent the true model successfully (Figure 6.9). Figure 6.10-Figure 6.13 illustrate the fits of predicted data for the inversion results shown in Figure 6.8 and Figure 6.9 to the observed data. The total rms misfits of 1.06 (only off-diagonal elements) and 1.02 (all impedance tensor elements) were obtained.

We also inverted all four elements of the data in the rotated coordinate frame. Not surprisingly, given that the diagonal terms are zero (plus error), we obtained exactly the same result as for inverting the off-diagonals only in the rotated reference frame.

6.5 CONCLUSIONS

We have applied 3-D MT inversion scheme using non-linear conjugate gradients inversion code of Egbert & Kelbert (2012) to MT profile data, considering the case of a dominant 2-D oblique conductor buried in a resistive host. Our numerical experiments with 3-D inversion suggest that, if only off-diagonal components are used, such as by Sasaki & Meju (2006), Tuncer et al. (2006), Newman et al. (2008), and Zhdanov et al. (2010), one has to rotate both the 3-D grid and the data to predominant strike to obtain the true resistivity and true geometry of the structure. On the other hand, if the complete impedance tensor is used in the inversion without rotation of coordinate system and data, such as by Farquharson & Craven (2009), the true structure can be clearly mapped, as in this case, the along-strike variation is defined by main diagonal terms.

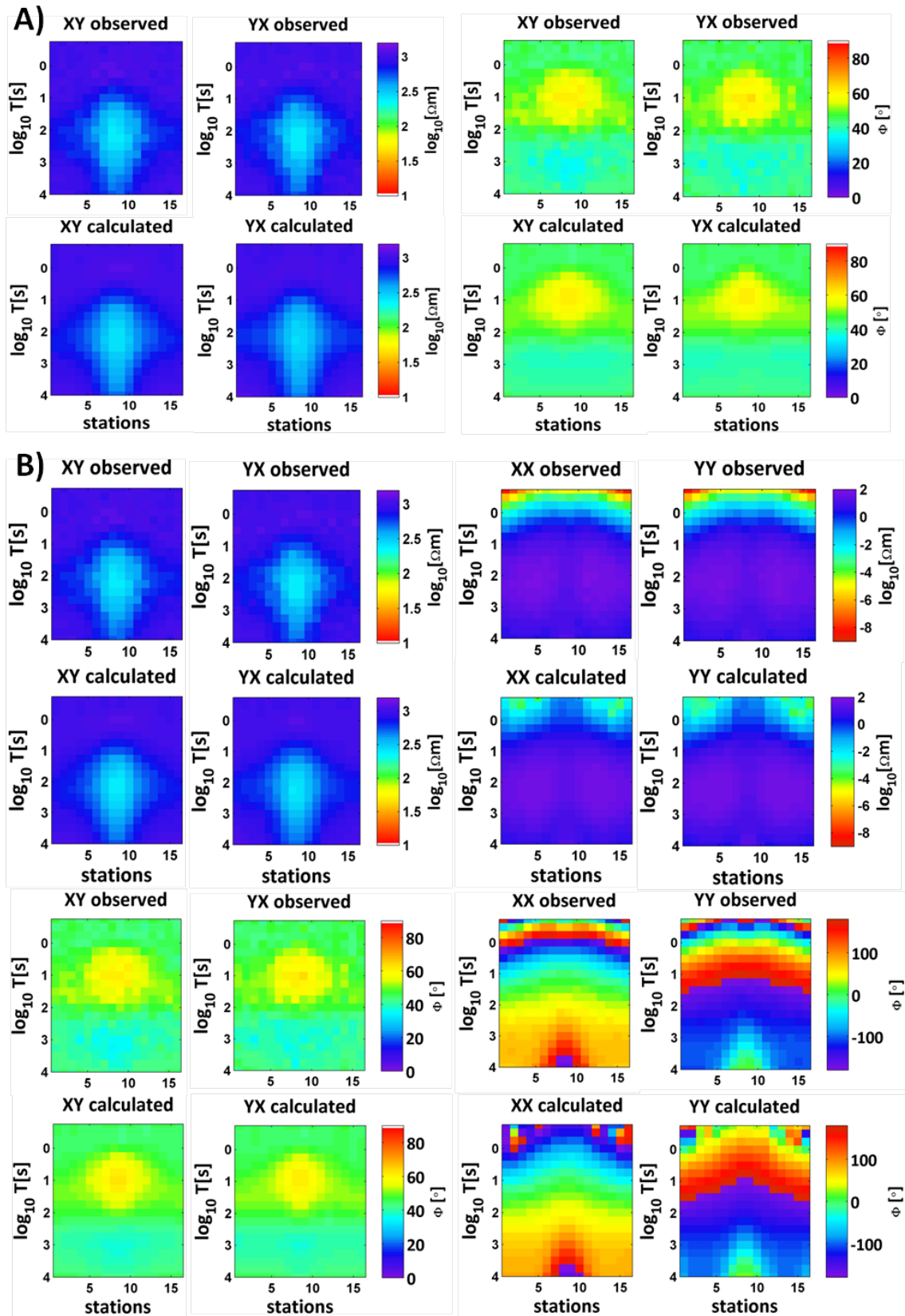


Figure 6.5.: **A)** Apparent resistivity and phase pseudo-sections of observed data, and the corresponding predicted data for the final 3-D inversion result fitting off-diagonal data only. **B)** Observed and predicted pseudo-sections from the full-tensor 3-D inversion. The total rms misfit of 1.26 and 1.00 were achieved respectively.

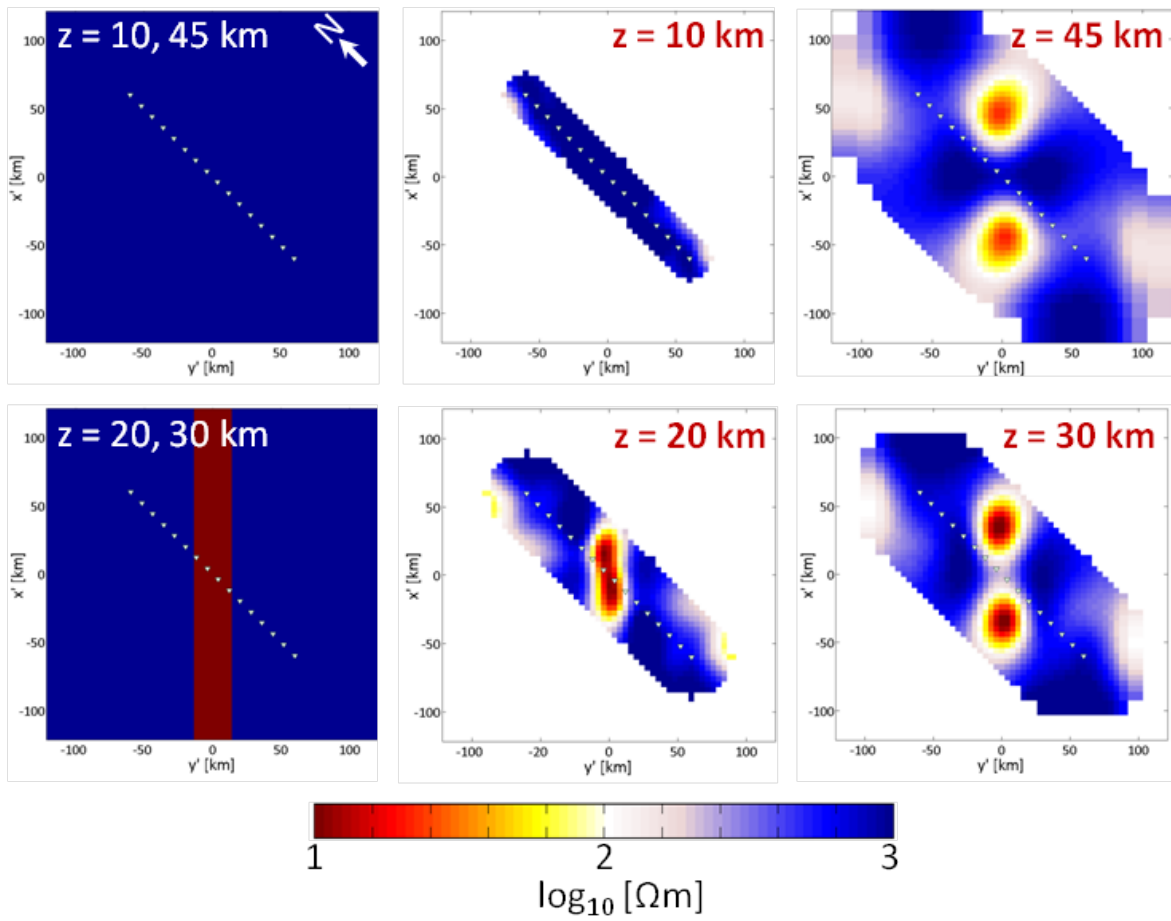


Figure 6.6.: Inversion results obtained using off-diagonal ($\mathbf{Z}_{x'y'}$, $\mathbf{Z}_{y'x'}$) tensor components after aligning both the 3-D mesh and the data with predominant strike direction.

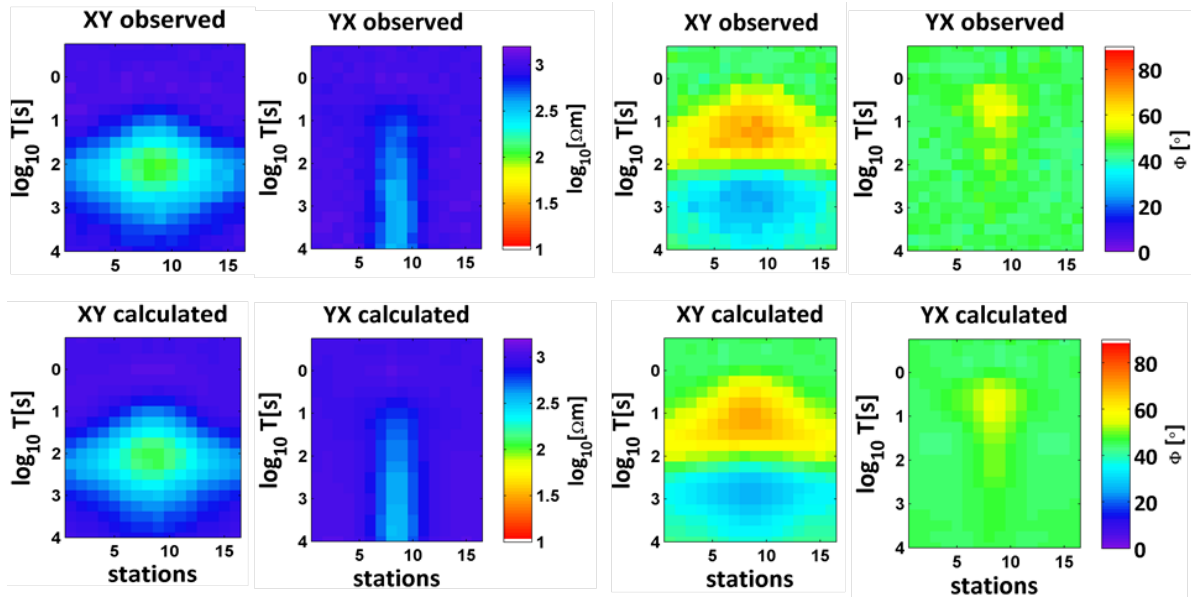


Figure 6.7.: Apparent resistivity and phase pseudo-sections for observed data, and the predicted data for the final 3-D inversion result obtained by fitting off-diagonal components. The total rms misfit of 1.03 was achieved.

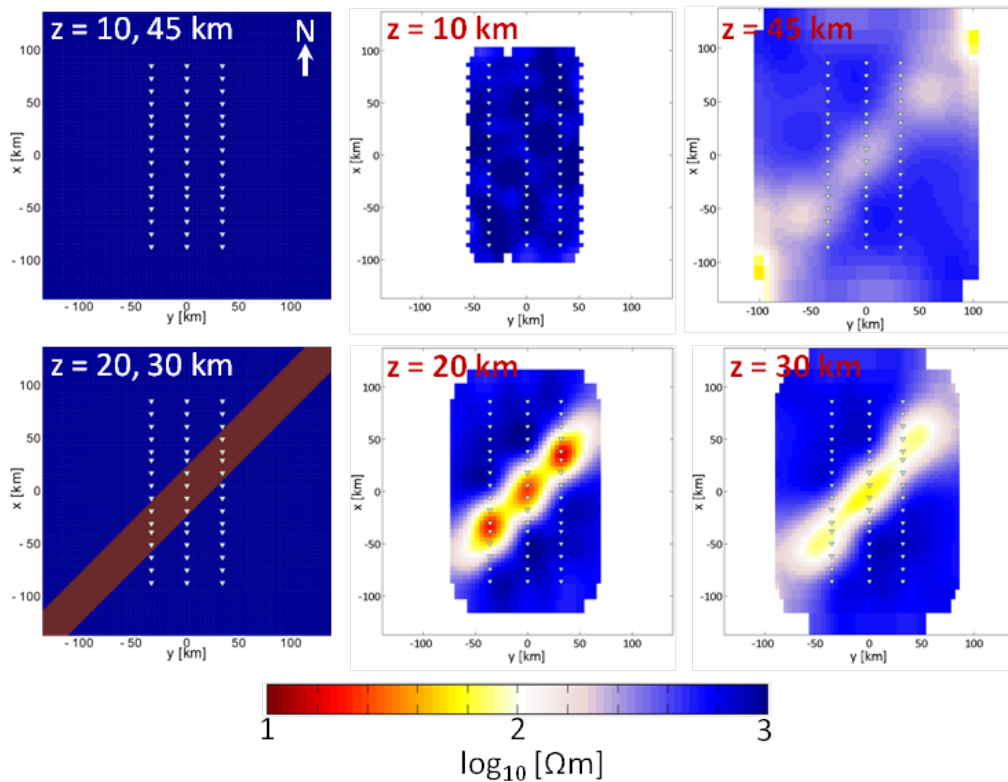


Figure 6.8.: Inversion results from three parallel profiles using only off-diagonal elements (Z_{xy} , Z_{yx}) of the impedance tensor. The white triangles represent the site locations.

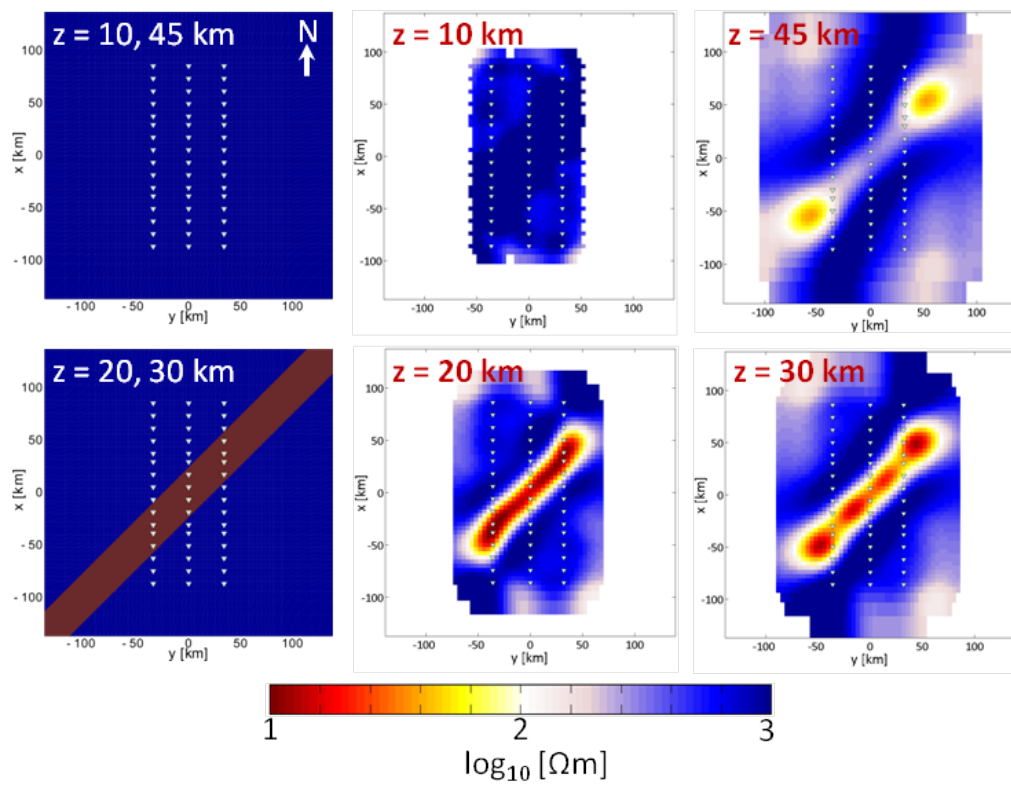


Figure 6.9.: Inversion results from three parallel profiles using complete impedance tensor elements (\mathbf{Z}_{xx} , \mathbf{Z}_{xy} , \mathbf{Z}_{yx} , \mathbf{Z}_{yy}). The white triangles represent the site locations.

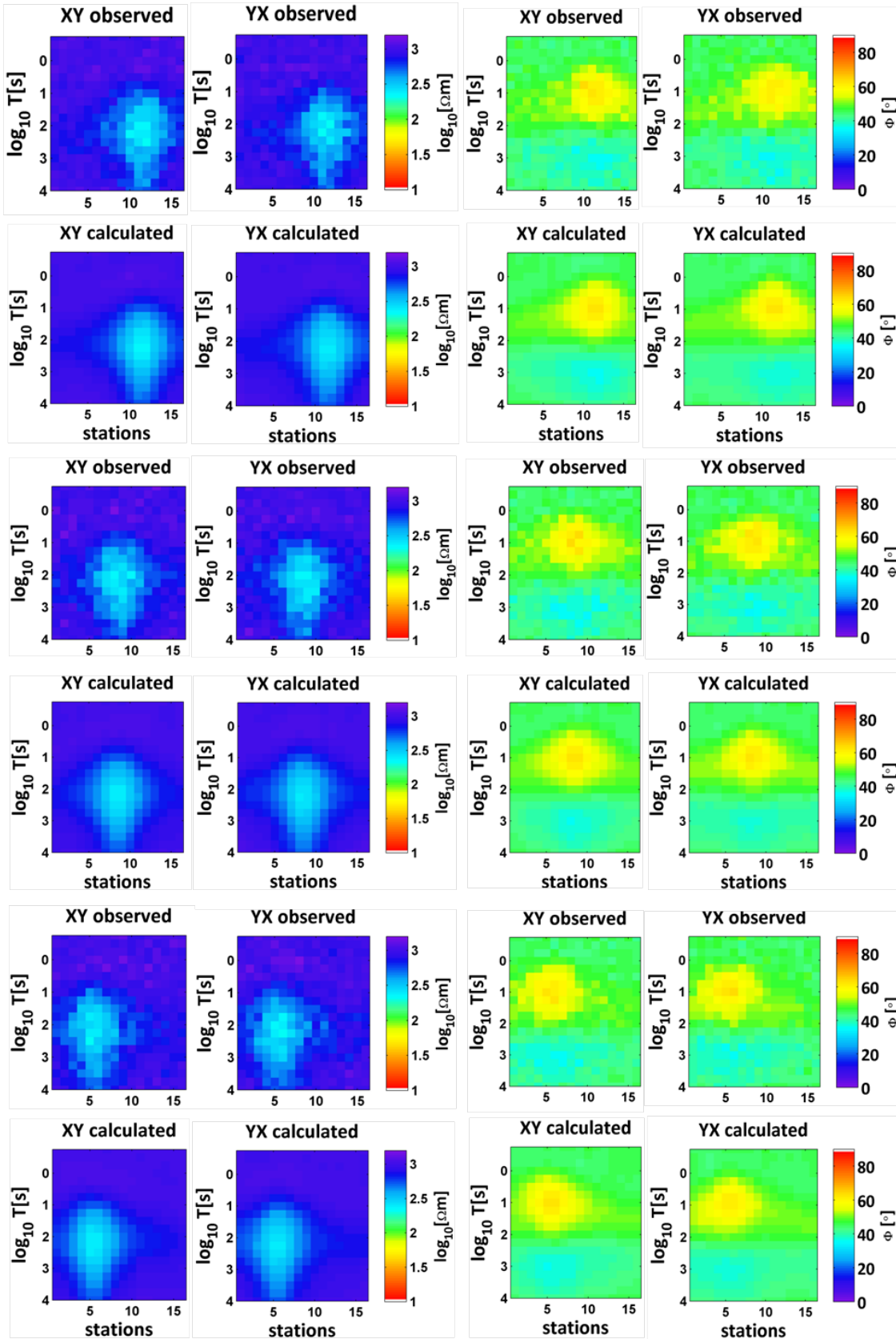


Figure 6.10.: From top to bottom, observed and the predicted pseudo-sections of apparent resistivity and phase for the inversion of the off-diagonal components for left-hand side, centre and right-hand side profiles, respectively. The total rms misfit of 1.06 was achieved.

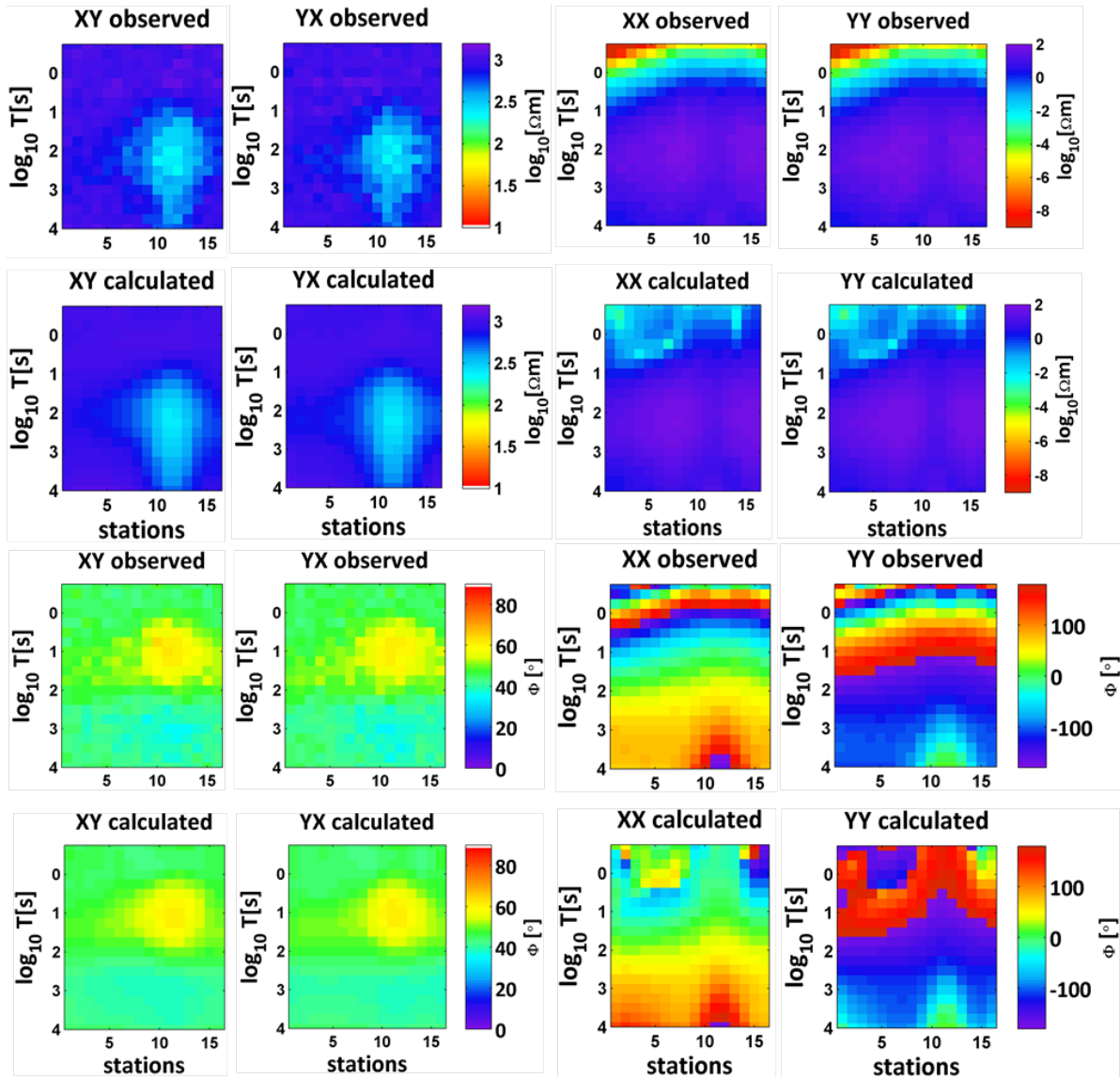


Figure 6.11.: Apparent resistivity and phase pseudo-sections of observed data, and the predicted data for the final 3-D inversion result fitting full-tensor components for the left-hand side profile. The total rms misfit of 1.02 was achieved.

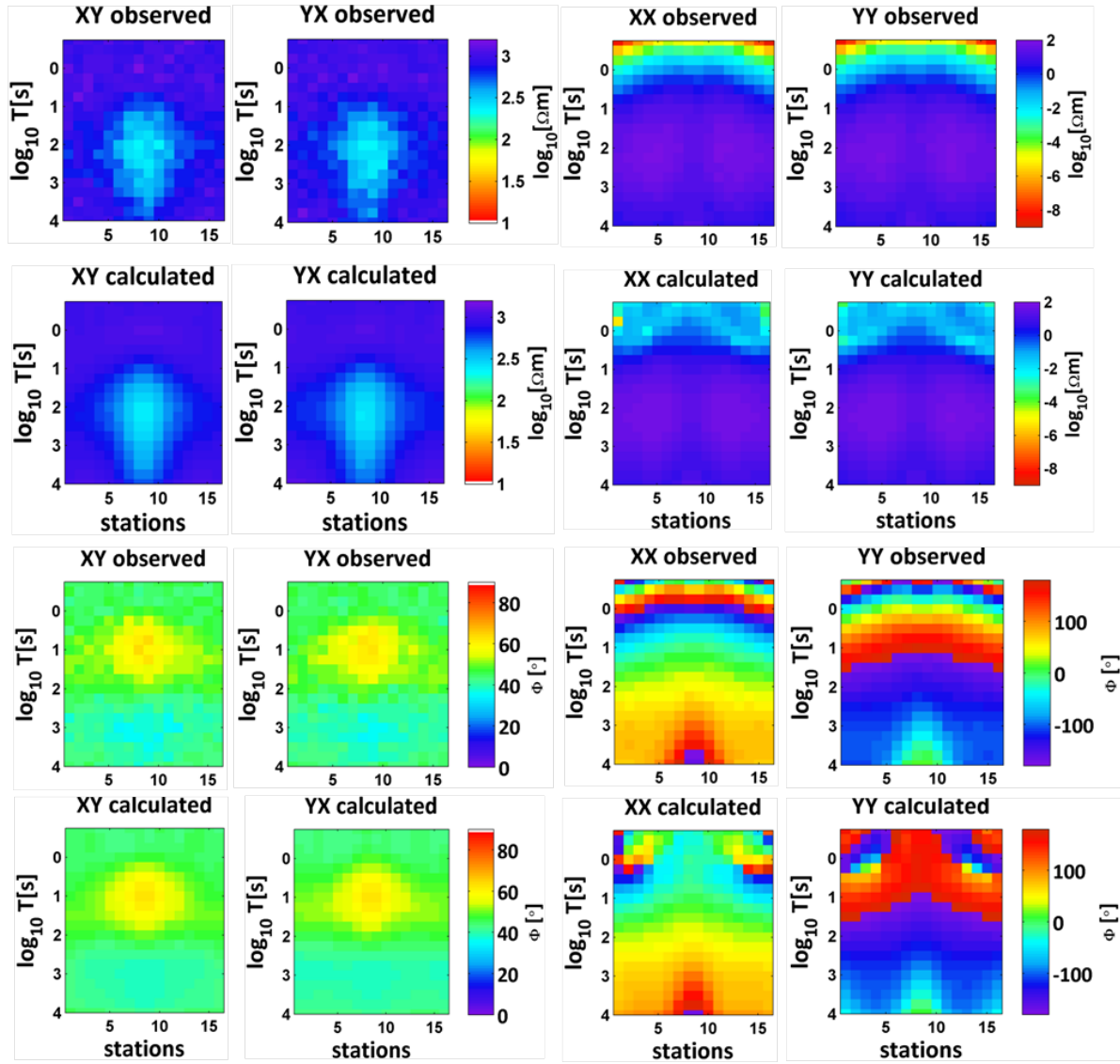


Figure 6.12.: As in Figure 6.11, but for the centre profile.

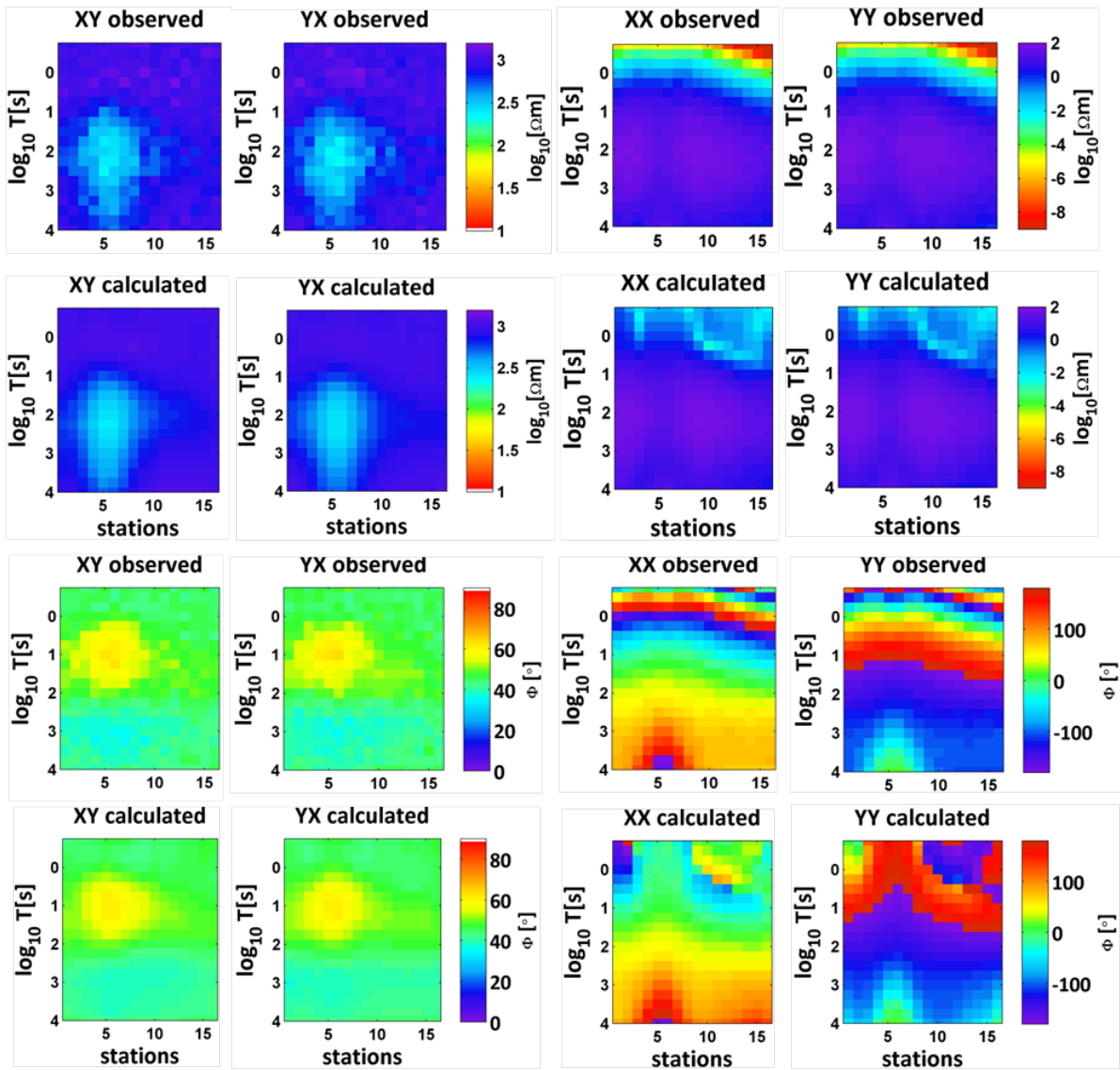


Figure 6.13.: As in Figure 6.11 & Figure 6.12, but for the right-hand side profile.

3-D INVERSION OF TOPOMED MT DATA

As discussed in [Chapter 6](#), during the past two decades, a number of 3-D inversion codes have been developed based on forward algorithms using finite-difference, finite-element and integral-equation approaches (e.g., [Smith & Booker, 1991](#); [Mackie et al., 1994](#); [Newman & Alumbaugh, 2000](#); [Zhdanov et al., 2000](#); [Sasaki, 2001](#); [Farquharson et al., 2002](#); [Siripunvaraporn et al., 2005a](#); [Avdeev & Avdeeva, 2009](#); [Egbert & Kelbert, 2012](#)). Nevertheless, full 3-D inversion of MT data remains a very challenging task numerically and practically due to large MT data sets, distortion in 3-D environments, and non-uniqueness of the inversion problem. The majority of the previous 3-D studies concentrated on geological features with modelling parameters of the computational grids extending up to a few tens of square kilometres for ore deposit explorations (e.g., [Tuncer et al., 2006](#); [Farquharson & Craven, 2009](#); [Xiao et al., 2010](#)), waste characterizations (e.g., [Newman et al., 2003](#)), hydrocarbon explorations (e.g., [Hautot & Tarits, 2009](#); [Zhanxiang et al., 2010](#)), investigations of geothermal areas (e.g., [Newman et al., 2008](#); [Arnason et al., 2010](#); [Cumming & Mackie, 2010](#)), and volcanic studies (e.g., [Spichak et al., 2007](#); [Heise et al., 2008](#); [Jones et al., 2008](#); [Hill et al., 2009](#); [Ingham et al., 2009](#)). Besides these, there are some more recent studies focussed on investigating larger scale tectonic structures (e.g., [Zhdanov et al., 2010](#); [Patro & Egbert, 2011](#); [Kelbert et al., 2012](#); [Khoza et al., 2013a](#); [Tietze & Ritter, 2013](#); [Bedrosian & Feucht, 2014](#)).

This chapter describes the 3-D MT inversion code and 3-D inversion of both the MAR and the MEK profiles data and illustrates and describes subsurface resistivity models obtained from the inversions using different parameter settings and data subsets. The results are compared to other available information in the area (see [Chapter 3](#), where the geology and previous geophysical work are reviewed) and a geological interpretation of the modelled subsurface resistivity structures is discussed.

7.1 MODULAR ELECTROMAGNETIC INVERSION SYSTEM

In the framework of this thesis, the Modular Electromagnetic Inversion System (ModEM) of [Egbert & Kelbert \(2012\)](#) and [Kelbert et al. \(2014\)](#) is used for 3-D inversion of the TopoMed MT data. The ModEM package comprises computer codes for modelling and inversion of frequency-domain electromagnetic data using gradient-based search methods. The 3-D MT modelling scheme used

in this study is based on a finite difference formulation forward solver, and the inverse algorithm employs a non-linear conjugate gradient (NLCG) scheme to minimize the objective or penalty function. For ModEM the penalty function Φ consists of data regularization and model regularization terms (Egbert & Kelbert, 2012; Kelbert et al., 2014)

$$\Phi(\mathbf{m}, \mathbf{d}) = (\mathbf{d} - \mathbf{f}(\mathbf{m}))^T \mathbf{C}_d^{-1} (\mathbf{d} - \mathbf{f}(\mathbf{m})) + \nu (\mathbf{m} - \mathbf{m}_0)^T \mathbf{C}_m^{-1} (\mathbf{m} - \mathbf{m}_0) , \quad (7.1)$$

where \mathbf{m} is the resistivity model of dimension M , \mathbf{d} is the observed data with the dimension N , \mathbf{m}_0 is the prior model, which is a model that incorporates additional constraints about the characteristics of \mathbf{m} , \mathbf{C}_m is the model covariance matrix, \mathbf{C}_d is the data covariance matrix, and ν is the trade-off parameter controlling the balance between data fit and model smoothness. To avoid long computational time, the inversion starts with a larger ν value and its value is reduced during the progress of inversion. By assigning larger ν , the data misfit is initially less important and therefore the model norm is minimized by generating a smoother resistivity model. On the other hand, the inversion tends to fit the data better by assigning smaller ν values. The data covariance is a diagonal matrix containing the inverse of the squared data errors for each data point

$$\mathbf{C}_d = \text{diag}(1/e_i^2) . \quad (7.2)$$

As discussed briefly and illustrated in Chapter 6, the model covariance matrix, \mathbf{C}_m , is constructed as a sequence of 1-D smoothing and scaling operators, which is comparable to optimal interpolation and similar to the scheme of Siripunvaraporn & Egbert (2000) (Egbert & Kelbert, 2012; Tietze, 2012), and is given by

$$\mathbf{C}_m = c_x c_y c_z c_x^T c_y^T c_z^T . \quad (7.3)$$

$\mathbf{C}_m = \mathbf{C}_m^{1/2} (\mathbf{C}_m^{1/2})^T$ is symmetric. The 1-D block-diagonal smoothing operators have the form (e.g., for the x- direction)

$$\mathbf{c}_x = \begin{pmatrix} c_{11}^x & & & \\ & c_{22}^x & & \\ & & \ddots & \\ & & & c_{N_y N_z}^x \end{pmatrix} \quad (7.4)$$

with one block for each x-yz cell pair of the model mesh with N_y and N_z cells in the y- and z-directions, respectively. Each block c_{jk}^x is constructed by an autoregression scheme:

$$c_{jk}^x = \begin{pmatrix} 1 & & & & \\ \alpha_x & 1 & & & \\ \alpha_x^2 & \alpha_x & 1 & & \\ \vdots & & & \ddots & \\ \alpha_x^{N_x-1} & & & \cdots & 1 \end{pmatrix} \quad (7.5)$$

where the model covariance parameter α_x , $0 \leq \alpha_x \leq 1$, defines the model smoothness in x direction. Similarly, smoothing is set up for y- and z- directions.

The penalty function can be minimized using a least-squares approach. The EM inversion problem is highly non-linear, so, the function $\mathbf{f}(\mathbf{m})$ must be linearized using first order Taylor-expansion around a starting model (\mathbf{m}_0). In this case, the linearized $\mathbf{f}(\mathbf{m})$ function can be written as

$$\mathbf{f}(\mathbf{m}_0 + \Delta\mathbf{m}) = \mathbf{f}(\mathbf{m}_0) + \frac{\partial\mathbf{f}(\mathbf{m}_0)}{\partial\mathbf{m}_0} \Delta\mathbf{m} = \mathbf{f}(\mathbf{m}_0) + \mathbf{J}\Delta\mathbf{m} \quad , \quad (7.6)$$

where $\Delta\mathbf{m}$ is a small perturbation around \mathbf{m}_0 and \mathbf{J} is the sensitivity or Jacobian matrix which describes the sensitivity of the predicted data with respect to small changes in the model parameters. With the NLCG inversion scheme, the gradient of the penalty function (Equation 7.1) with respect to variations in model parameters \mathbf{m} must be evaluated at each iteration n , and is given by

$$\left. \frac{\partial\Phi}{\partial\mathbf{m}} \right|_{\mathbf{m}_n} = -2\mathbf{J}^T \mathbf{r} + 2\nu \mathbf{C}_m^{-1} \Delta\mathbf{m}_n \quad , \quad (7.7)$$

where $\mathbf{r} = (\mathbf{f}(\mathbf{m}_n) - \mathbf{d})^T \mathbf{C}_d$ is the data residual and $\Delta\mathbf{m}_n = \mathbf{m}_n - \mathbf{m}_0$ is the distance of the current model \mathbf{m}_n to the prior model (Egbert & Kelbert, 2012). Subsequently, the gradient is used to calculate a new conjugate search direction in the model space for inversion step $n + 1$ which is given by the direction where the gradient is largest.

The ModEM package is implemented in a modular way that allows inversion codes developed for one purpose to be rapidly adapted to other problems, and facilitates the development of new capabilities (Egbert & Kelbert, 2012; Kelbert et al., 2014). As illustrated in Figure 7.1, the modules are organized in three layers. Components which define the basic discretization and numerical solution approach used for the forward problem are depicted on the left-hand side of the figure. On the right-hand side, the components are more generic which are directly applicable to a wide range of EM inverse problems. The interface layer, which separates these two layers, serves to hide problem and implementation details from the right-hand side modules. The inversion module does not depend on the type of electromagnetic data (e.g., MT, CSEM, CSMT) nor on the dimension of the problem (2-D, 3-D). Currently 2-D and 3-D MT, CSEM, and global induction

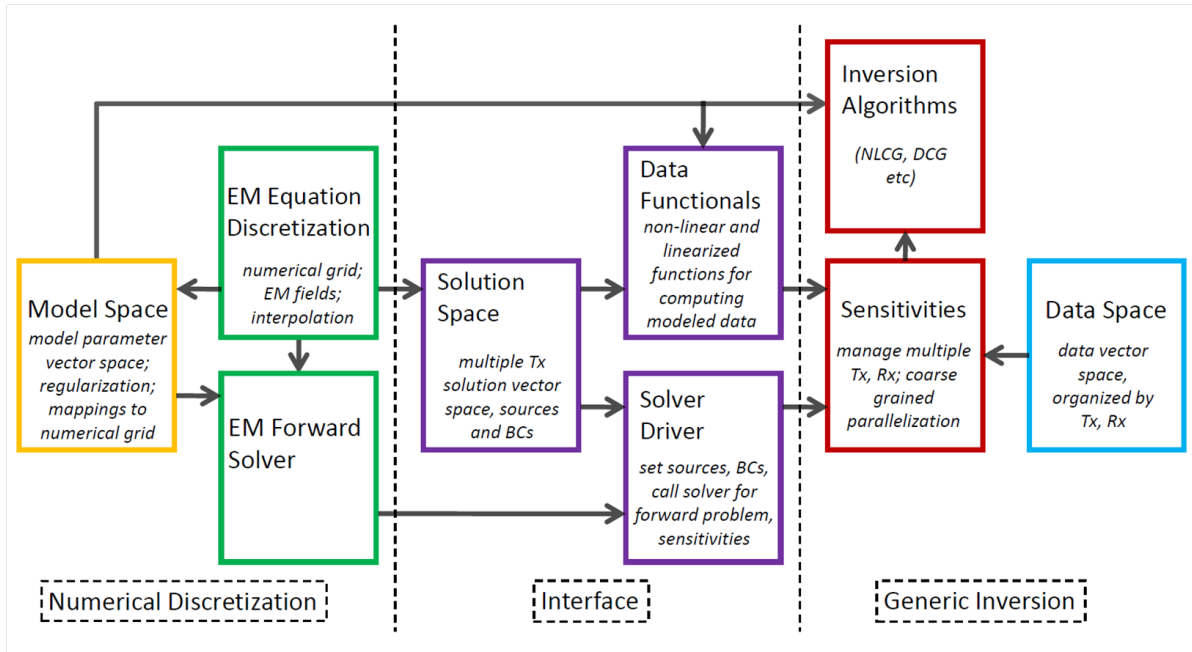


Figure 7.1.: Schematic overview of the Modular Electromagnetic Inversion (ModEM) system. Boxes represent modules (or group of modules, in actual implementation), with dependencies defined by arrows; *modified from Egbert & Kelbert (2012)*.

problems can be solved by the implemented inversion methods (Kelbert et al., 2014). The data types that are suitable for the current version of the 3-D inversion are full impedance tensor, full vertical components, full interstation magnetic transfer functions, off-diagonal apparent resistivities & phases, and phase tensor.

Within this study, a parallel version of the 3-D inversion code is used to reduce both memory requirements and total computation time. A coarse grained parallelization is implemented through forward modelling and sensitivity calculations. Minimum computation time is achieved by distributing the modelling problem over $2 \times N_p$ processors, where N_p is the number of periods used in both forward and inverse calculations. More details on development and implementation of the parallelization of 3-D MT forward and inverse modelling in ModEM can be found in Meqbel (2009), and a more detailed description of the implementation of apparent resistivities & phases and phase tensor can be found in Tietze (2012).

7.2 COAST EFFECT

The presence of deep oceans can have significant influence on land MT data due to the large contrast in electrical conductivity between land and seawater (Parkinson & Jones, 1979). Both the magnetic transfer function and MT impedances will be affected by this sharp conductivity contrast (e.g., Mackie et al., 1988; Santos et al., 2001; Munoz et al., 2008). In the presence of a conductive ocean, along-strike electric currents will preferentially flow within in the conductive ocean, thus

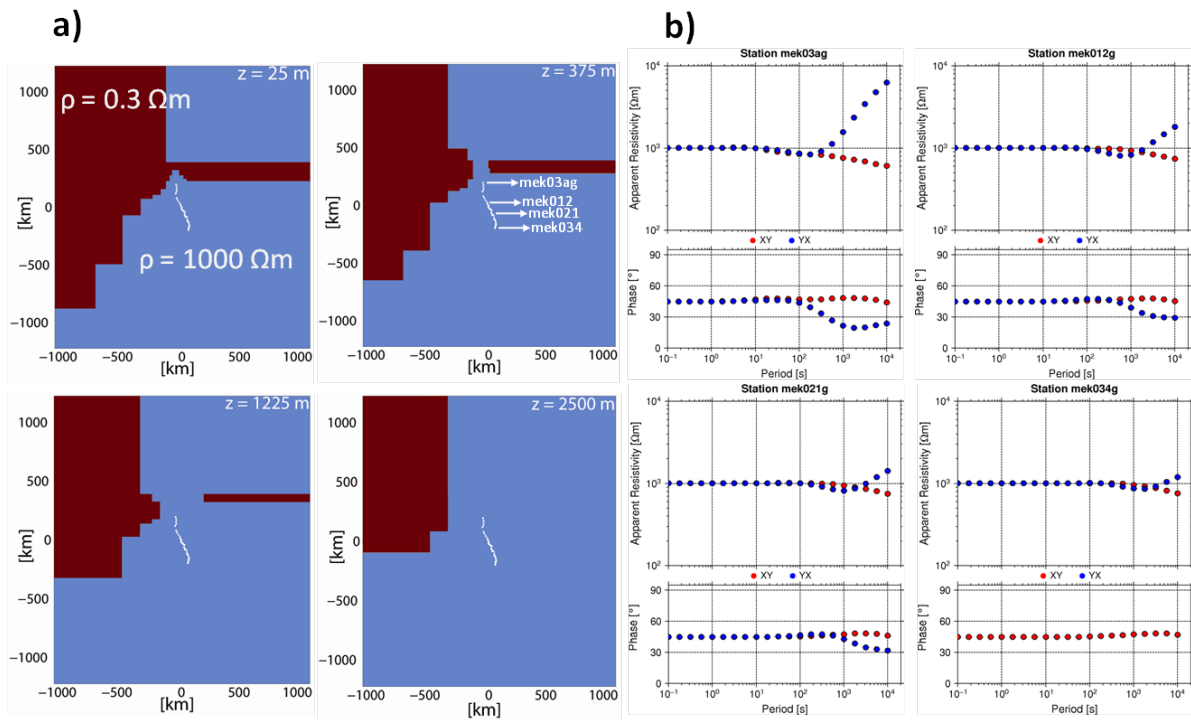


Figure 7.2.: **(a)** Plan view of the large-scale regional model used for the study of the ocean effect for the MEK profile, including the bathymetry. The land part is represented by a homogeneous half space of $1,000 \Omega\text{m}$ down to a depth of 2000 km , below which is a conducting half space of $10 \Omega\text{m}$. **(b)** The coast effect in the apparent resistivity and phase curves is portrayed for the stations mek03ag (its distance from Atlantic Ocean is $\sim 90 \text{ km}$, and $\sim 70 \text{ km}$ away from the Alboran Sea; located in the Rif), mek012g ($\sim 200 \text{ km}$; located in the Middle Atlas), mek021g ($\sim 290 \text{ km}$; located in the High Atlas), and mek034g ($\sim 400 \text{ km}$; located in the eastern Anti-Atlas). The white small dots indicate the location of MT stations along the MEK profile.

low apparent resistivities at longer periods in the TE mode will be observed. In contrast, higher values of apparent resistivity will be observed due to increased current flowing onshore in the near-surface. Therefore, MT data modelling from coastal areas must take into account the presence of surrounding ocean/seawater.

In Morocco, a coast effect might be expected from the presence of the Atlantic Ocean and the Alboran Sea. In order to assess the coast effect on the TopoMed MT data set, a simple 3-D resistivity model is designed with seawater resistivity values of $0.3 \Omega\text{m}$ extending the depths between 50 and $\sim 5000 \text{ m}$ and a uniform land resistivity values of $1,000 \Omega\text{m}$ underlain by a $10 \Omega\text{m}$ substratum (Figure 7.2 and Figure 7.3). However, this method is a very rough guide to determine coastal effects in the data set as a homogeneous resistive land subsurface structure is used rather than a layered or structured earth (Munoz et al., 2008), and also sedimentary overburden is not considered in the model. Structures that are of higher resistivity than that assumed ($1,000 \Omega\text{m}$) will create a larger anomalous response, whereas those smaller will attenuate the anomalous response. For Morocco, our modelling indicates that the crust is generally $< 1,000 \Omega\text{m}$, so this modelling describes the maximum likely effects.

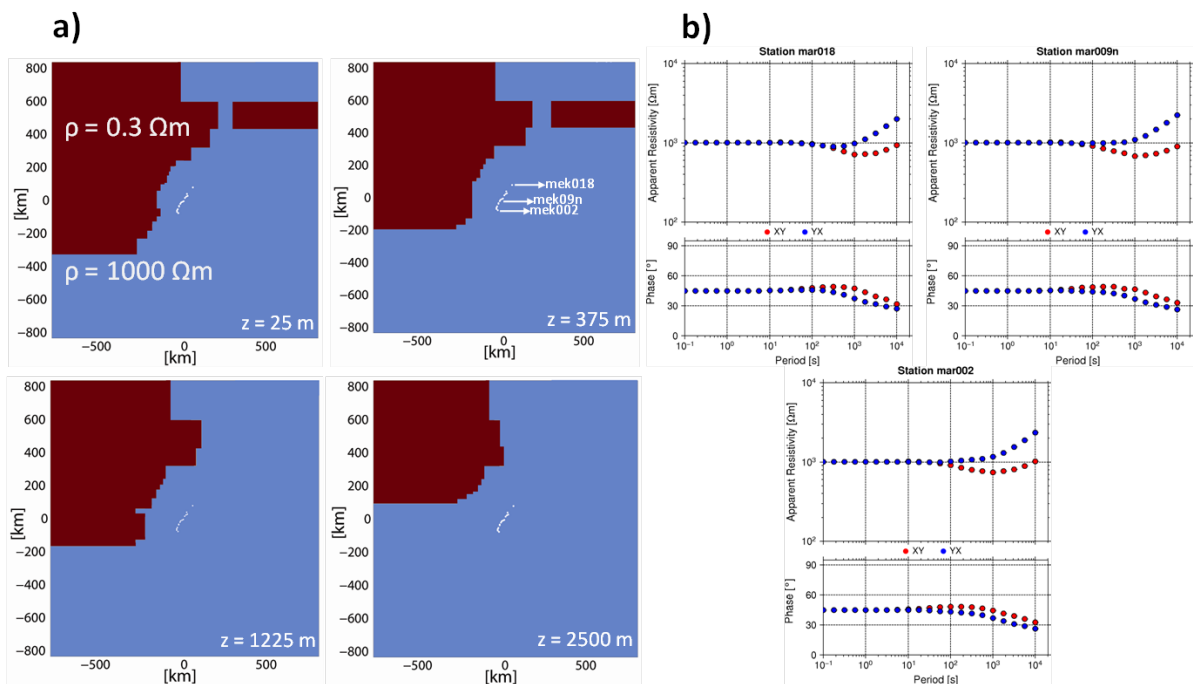


Figure 7.3.: **(a)** Plan view of the regional model used for the study of the ocean effect along the MAR profile, including the bathymetry. The land part is represented by a homogeneous half space of $1,000 \Omega\text{m}$ down to a depth of 1390 km, below which is a conducting half space of $10 \Omega\text{m}$. **(b)** Ocean effect in the apparent resistivity and phase curves for the stations mar002 (its distance from Atlantic Ocean is ~ 100 km; located in the Anti-Atlas), mar009 (~ 140 km; located in the Western High Atlas), and mar018g (~ 150 km; located in the Haouz Basin). The white small dots indicate the location of MT stations along the MAR profile.

For the MEK profile, the model discretized on a 122 (N-S) \times 56 (E-W) \times 45 (vertical) mesh (including 10 air layers), with a horizontal centre cell size of 4×4 km (Figure 7.2). The thickness of the top layer is 50 m, and the thickness of each subsequent layer increased with a vertical factor of 1.2. For the MAR profile, the mesh used for modelling consists of 71 (N-S) \times 61 (E-W) \times 48 (vertical) cells (including 10 air layers), with a horizontal centre size of 4×4 km (Figure 7.3). In the vertical direction, the thickness of the top layer is 30 m, and the thickness of each subsequent layer increases with a vertical factor of 1.2. Note that in order to account for perturbations in the magnetic fields from lateral current gradient those 10 air layers are added to the top of the model. These air layers should extend far above the earth. In the ideal case, since a plane wave source is assumed, the top boundary of the mesh should be at infinity. As this cannot be implemented, at least there should be sufficient distance between the air-Earth interface and the top boundary of the mesh to ensure that any magnetic field generated by induced currents in the ground has decayed to zero at the top boundary of the mesh (Mackie et al., 1993; Miensopust, 2010). The cell conductivity of air layers is set to 10^{-8} S/m. Figure 7.2 and Figure 7.3 show forward model responses for some representative sites. A typical coast effect is visible on both profiles, i.e., higher TM mode and lower TE mode resistivity are clearly observed, with the effect increasing with proximity to the coast. Thus, to include the effect of the coast on the field data set, the geometry of the Alboran Sea and Atlantic Ocean (seawater resistivity $0.3 \Omega\text{m}$) are provided as *a priori* information and are kept fixed for the 3-D inversions.

7.3 INVERSION OF MEK PROFILE DATA SET

As pointed out in the previous chapter, rotation of the input data and the model grid to a predominant strike angle is not required if the full impedance tensor data are used, and appropriate consideration is given to the diagonal tensor terms of the MT impedances. As discussed in Chapter 3, crustal-probing MT data from the MEK profile, crossing Middle Atlas, central High Atlas and Anti-Atlas are interpreted based on 2-D inversions of tensor decomposed data, with a strike angle of 50°E of north (Ledo et al., 2011). One of the most striking results of all the inversions is a conductive anomaly at lower crustal depths found below the Anti-Atlas. However, 3-D inversions of the same data set but in a geographic coordinate system supports instead a homogeneous, resistive subsurface, contrary to the 2-D results (Figure 7.4). Therefore, following the recommendations in Kiyan et al. (2014), 3-D inversions are conducted in two different types of coordinate systems: geographic, and geo-electric strike oriented coordinate systems.

For geographic coordinates, the inversion mesh consists of 74 (N-S) \times 52 (E-W) \times 45 (vertical) (including 10 air layers) with a horizontal cell size of $4 \text{ km} \times 4 \text{ km}$ in the area of interest. The lateral extent of the padding cells, 13 in the each of north and south directions, and 16 in the each of east and west directions, increases by factor of 1.5. The thickness of the top layer is 50 m, and the thickness of each subsequent layer increased with a vertical factor of 1.2. All inversions are started from a $100 \Omega\text{m}$ homogeneous half space down to a depth of 914 km, to which the

Alboran sea and Atlantic Ocean ($0.3 \Omega\text{m}$ seawater resistivity) are included as *a priori* structure using known bathymetry. Model smoothing parameter is set to the default value, 0.3, in the x -, y -, and z - directions and for all layers. The input data are decimated to 18 periods per site (in total 17 sites are used) with irregular distribution and denser selection for periods from 10 s to 5,623 s. Eighteen periods cover the period range from 0.03 s to 5,623 s. 3-D inversions are run for the full impedance tensor elements. Error floors are set as an absolute value to 5% of $(|\mathbf{Z}_{xy} \times \mathbf{Z}_{yx}|)^{1/2}$ (equivalent to 10% to apparent resistivity and 2.8° to phase). [Figure 7.4](#) shows the resulting 3-D model derived from inversion using only the off-diagonal components of the impedance tensor. An overall rms misfit of 1.37 is achieved. In addition to running inversions with only off-diagonal components, inversions with full impedance tensor components as well as with only off-diagonals are run using periods from 0.001 s to 2,000 s (18 periods are used). An overall rms of 2.1 and 1.57 are achieved, respectively.

For the strike-aligned coordinates, the corresponding model mesh consists of $42 \times 84 \times 45$ cells in the two horizontal and the vertical directions, respectively. The inner part comprises a uniform mesh of $18 \times 49 \times 45$ with a horizontal cell size of 4 km and a vertical size of 914 km. The lateral extent of the padding cells, 10, 14, 18, and 17 in the north, south, east, and west directions, respectively, increases by factor of 1.4. The vertical discretization is the same as for the model mesh in geographic coordinates. To allow different covariance length scales in along and across strike directions, the model grid is rotated into the predominant regional geo-electrical strike direction, that is, x points 50° west of North. The impedances are of course also rotated to be consistent with this coordinate system. This strike direction is consistent with the tensor decomposition analysis of [Ledo et al. \(2011\)](#) (see [Chapter 3](#)). The inversion again starts from a $100 \Omega\text{m}$ half space. Model covariance parameters are set to 0.2, 0.4, and 0.2 for x -, y -, and z - directions, respectively. Setting up anisotropic model covariance parameters will enforce inversion model to have more pronounced, smoother structures along the strike direction. Impedances are decimated to 4 periods per decade ranging from 0.001 s to 20,000 s. For the inversion, 22 periods are chosen covering the period range from 0.01 s to 5,623 s. Error floors are set as an absolute value to 5% of $(|\mathbf{Z}_{xy} \times \mathbf{Z}_{yx}|)^{1/2}$ (equivalent to 10% to apparent resistivity and 2.8° to phase). Using off-diagonal impedances, the final overall rms of 1.40 is obtained.

The final models obtained by inverting only the off-diagonal tensor elements in geographic coordinate and strike-aligned coordinate systems are presented in [Figure 7.4](#) & [Figure 7.5](#) together with the 2-D resistivity model of [Ledo et al. \(2011\)](#), and [Figure 7.7](#), respectively. The 3-D subsurface models largely match the main features in 2-D inversion model ([Figure 7.5](#)), except for the absence in the 3-D models of a conductor beneath the profile under the Anti-Atlas. [Figure 7.6](#) shows maps of observed values of phases, and the corresponding data computed for the final model in the geographic coordinate system.

Sensitivity to mantle resistivity & hypothesis testing

The Middle Atlas and High Moulouya conductor is located in the lower crust and upper mantle (20 km - \sim 55 km) with a resistivity of approximately 20 Ω m (Figure 7.5) and is underlain by a relatively resistive (\sim 100 - 200 Ω m) region. To show that the data are sensitive to geo-electric structure beneath the conductive layer, the resistivity of the underlying layer is perturbed. Figure 7.8 shows that when the resistivity is reduced to 25 Ω m, both XY and YX phase increase significantly and apparent resistivity values decrease at periods longer than 200 s. When the resistivity is increased to 500 Ω m, the fit to both phase and apparent resistivity becomes unacceptable at periods longer than 200 s.

Contrary to the previously proposed sub-lithospheric mantle geometry, which is described as deepening towards the southern margins of the Atlas Mountain belt (e.g., Teixell et al., 2003; Zeyen et al., 2005; Fullea et al., 2010) for the MEK profile, the recent S-receiver functions study of Miller & Becker (2014) image a flat LAB geometry (at \sim 70 km) beneath most of the profile, with localized deepening (to 100 km) to the south of the South Atlas Fault, and to the north of Middle Atlas (Figure 7.9a). To test if such a flat LAB is acceptable to the MT data set of the MEK profile, the preferred 3-D resistivity model (Figure 7.5) is perturbed by including a zone of 25 Ω m (even though the electrical resistivity of the asthenosphere is somewhat poorly defined, generally beneath active regions it lies in the range of 5 - 25 Ω m. The summary of selected global observations of the electrical resistivity of asthenosphere can also be found in Jones (1999).) The best-fitting 3-D model is altered by painting the zone with 25 Ω m resistivity value below the depth of 70 km, and the forward solution of this model is compared with the forward response of the best fitting model. Differences in apparent resistivity and phases are derived to illustrate the change. The responses show $>10 - 15\%$ (Figure 7.9b) change in apparent resistivities, and $5 - 15^\circ$ change in phase on the both XY and YX components (for periods >100 s, which are associated with lithospheric mantle depths). This test shows that the modified model has a significantly different MT response than the measured response, and the LAB geometry proposed by Miller & Becker (2014) is not supported in the electrical conductivity structure by the TopoMed MT data set.

A series of forward modelling tests are employed to investigate the range of LAB conditions that could generate plausible misfits based on TopoMed MT data set. The LAB depth is set at 60, 85, 102, 122, 147 km, with the along-profile geometry constrained to that of Fullea et al. (2010); sub-LAB electrical resistivity values are set at 25, 70, 100, 150, 300, and 500 Ω m, simulating conductive asthenosphere to resistive lithosphere. One should note here that the commonly-defined temperature for the LAB boundary is one of the order of 1300 - 1350 $^\circ$ C. At that temperature dry olivine has a resistivity of 100 Ω m (Jones et al., 2009). This value therefore is the maximum bound for the resistivity of the asthenosphere, as any conducting phase, such as water or partial melt, will significantly reduce the resistivity. However, there is no process that will lead to an increase in resistivity, except for lower temperatures.

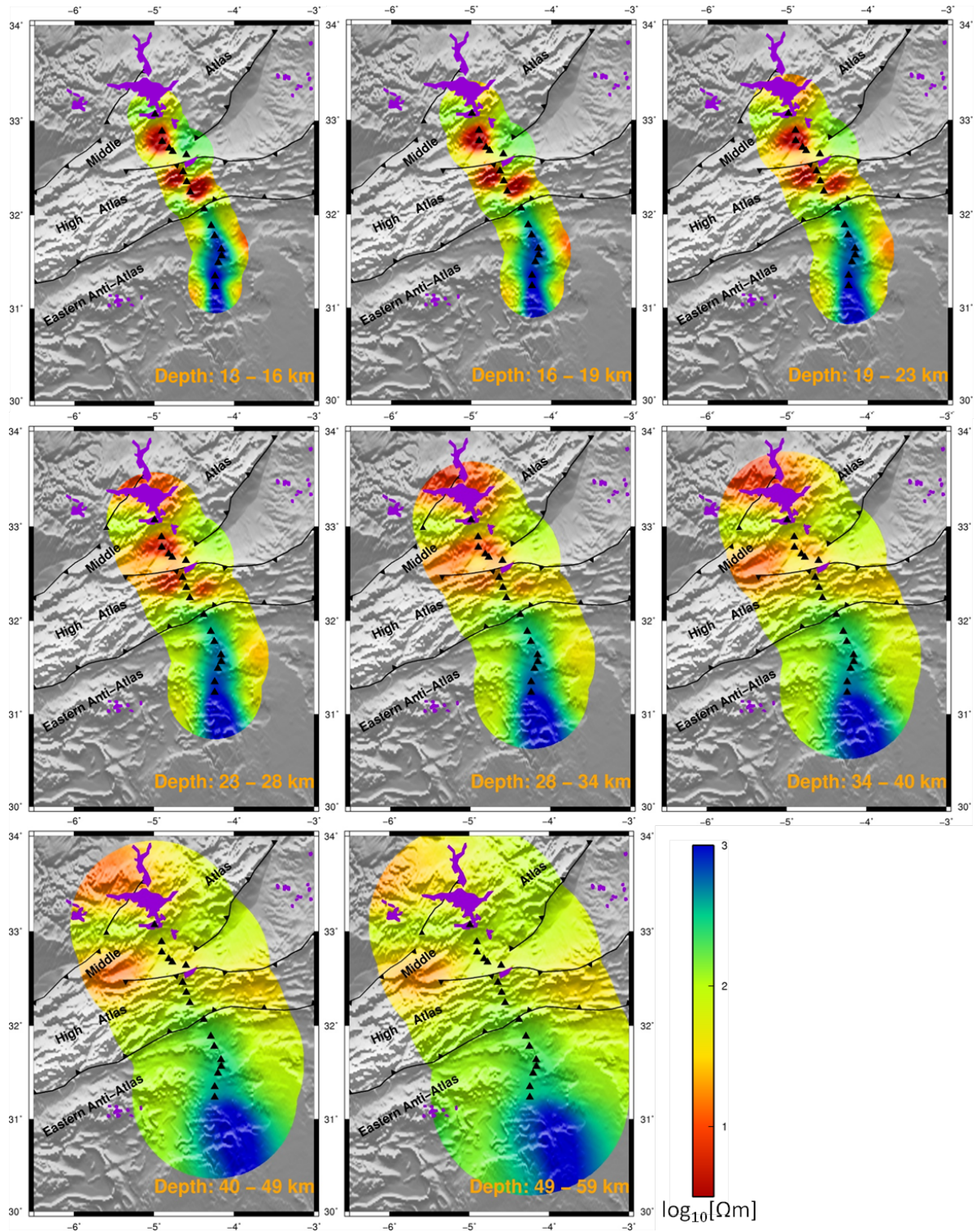


Figure 7.4.: Plan view of the preferred 3-D resistivity model obtained from the final 3-D inversion, which is the result of fitting only the components Z_{xy} and Z_{yx} , at depths middle crust (13 - 16km, 16 - 19 km, and 19 - 23 km), lower crust (23 - 28 km, and 28 - 34 km) and lithospheric mantle (34 - 40 km, 40 - 49 km, and 49 - 59 km). The triangles indicate the location of MT stations along the MEK profile. The part of the model which is well constrained by the data is shown only. The assumption is the unmasked region of the model is the area of the model is within the circles below each stations with radius two times of the depth of the presented horizontal slices.

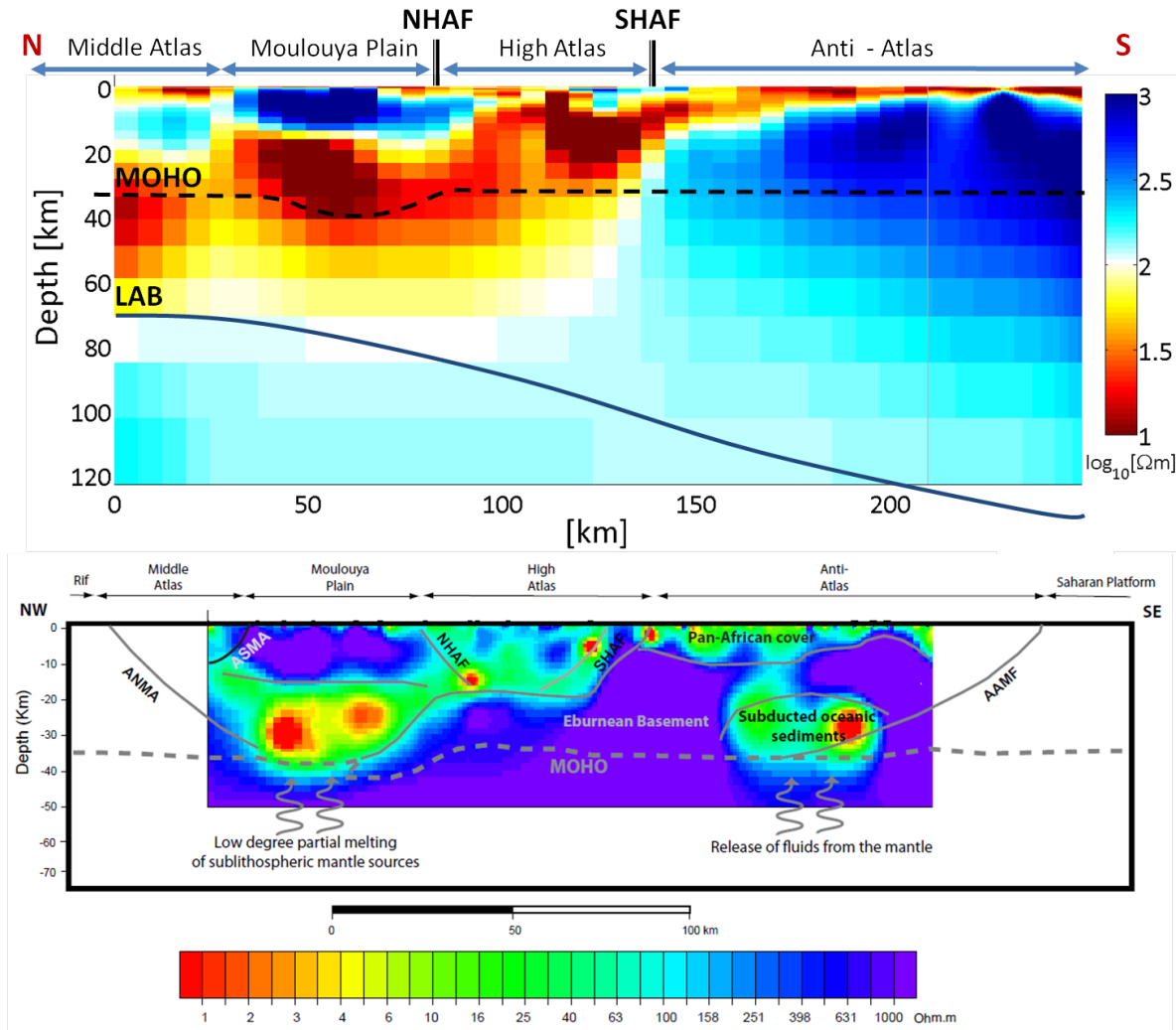


Figure 7.5.: (top) Representative cross-section from the representative 3-D resistivity model (see Fig. Figure 7.4). Superimposed crust-mantle boundary and LAB geometries are from previous works: Ayarza et al. (2005) and Fullea et al. (2010), respectively. The LAB geometry was obtained by forward modelling of topography, geoid anomalies, surface heat flow data, and seismic data. (bottom) 2-D electrical resistivity model of Ledo et al. (2011) along the MEK profile. 3-D and 2-D inversion results are in general consistent, in particular for the northern part of the profile.

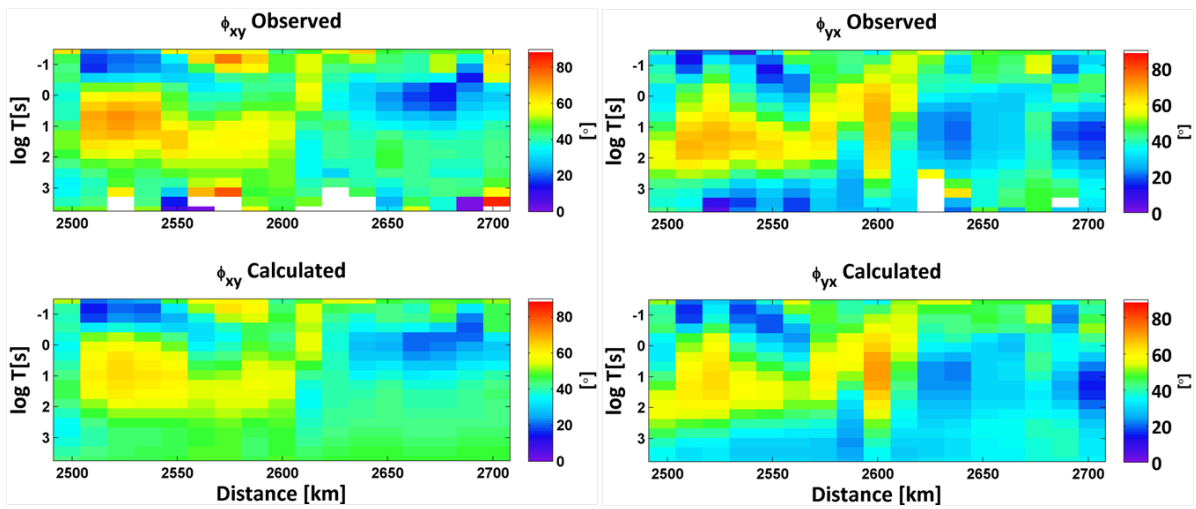


Figure 7.6.: Phase pseudo-sections of observed data, and the corresponding predicted data for the final 3-D inversion of the off-diagonal components only. The total rms misfit of 1.37 is achieved.

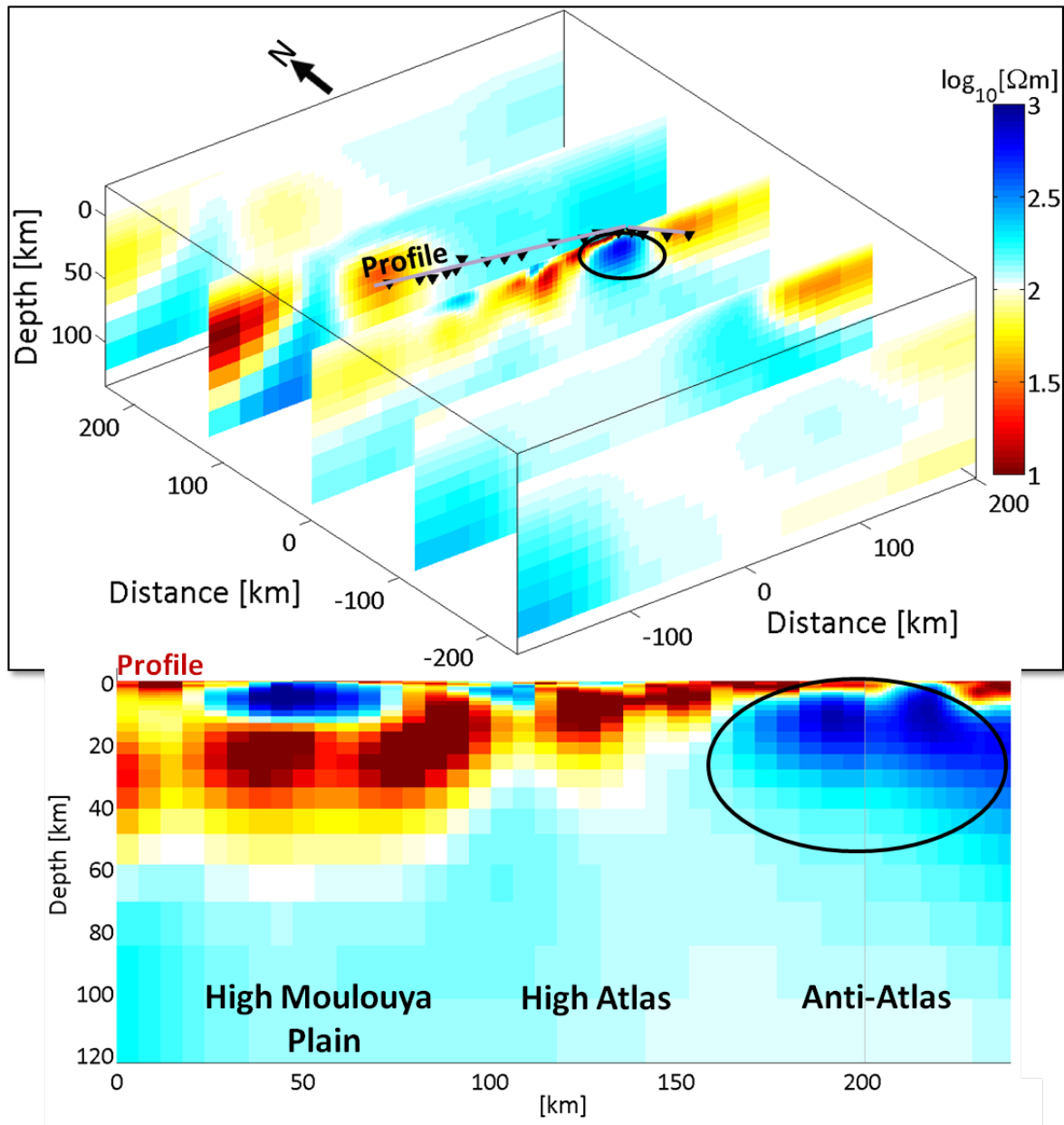


Figure 7.7.: Perspective view of 3-D inversion model, which is obtained from 3-D inversion of the southern part of the MEK profile data set, fitting only the off-diagonal (Z_{xy} and Z_{yx}) impedance tensor components, with E-W slices across the modelled space. The inverted triangles show the locations of MT stations (top). 2-D profile of the MEK transect extracted from 3-D inversion model on top (bottom). The total achieved rms misfit is 1.40.

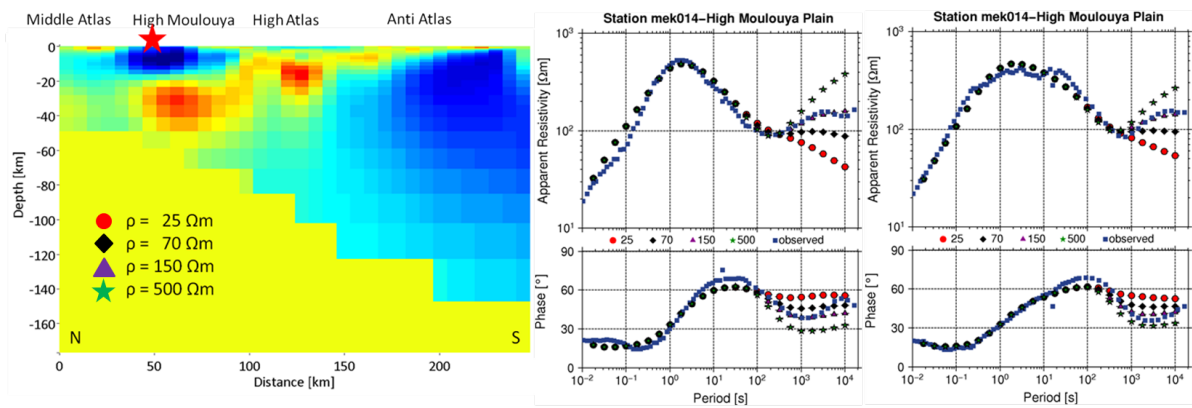


Figure 7.8.: Sensitivity test for 3-D MEK profile model (Figure 7.5): the right column shows comparison between the original data (blue squares) and the responses generated by forward modelling of perturbed models. MT apparent resistivity and phase responses (XY and YX, from left to right) at station 14, which is marked with red star, is located at the northern boundary of the Middle Atlas-High Moulouya Plain. The sub-lithospheric mantle geometry beneath the profile is drawn based on previously proposed models by (e.g., Teixell et al., 2003; Zeyen et al., 2005; Fullea et al., 2010).

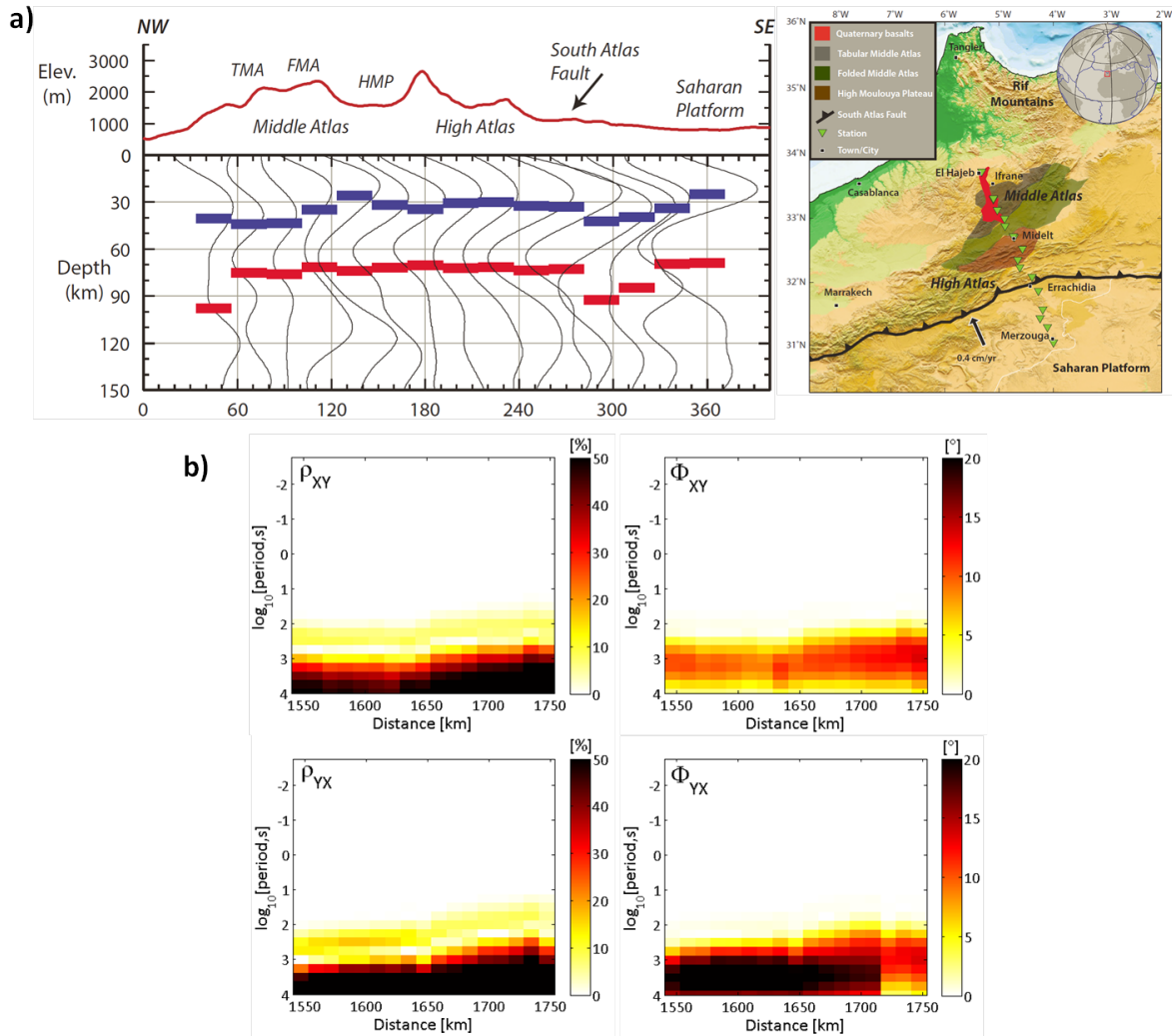


Figure 7.9.: **(a)** S-receiver function profile across Atlas mountains from north to south; top panel indicates tectonic features and elevation. HMP: High Moulouya Plain; FMA: Folded Middle Atlas; TMA: Tabular Middle Atlas. Receiver function stacks at 40 km spacing are shown for all stations within 20 km of profile and plotted evenly spaced for clarity. Blue and red dashes indicate Moho and LAB (sLABrf), respectively (on the left). Generalized tectonic map with seismic stations (green triangles), major cities and tectonic regions from (Gomez et al., 1998) (on the right); from Miller & Becker (2014). **(b)** Differences in apparent resistivities and phases of best fitting model and altered model response curves.

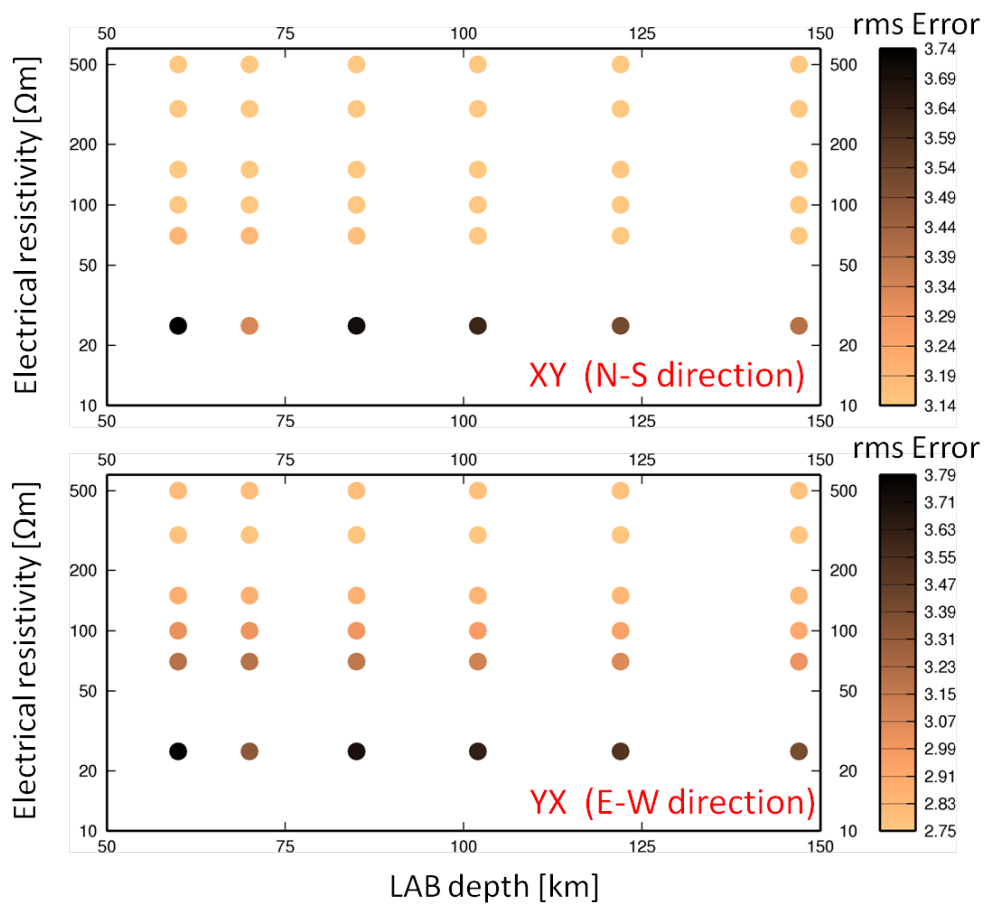


Figure 7.10.: Variation of rms error value with varying the LAB depth and the electrical resistivity value of the zone below the LAB depth.

The forward responses for the suite of models are calculated using the 3-D forward modelling code of Mackie et al. (1994) (implemented in Geosystem's WinGLink® package). The rms errors for both the XY and YX components are plotted, in Figure 7.10 for each of the models tested. The rms error values are then calculated using only the stations located in the Middle-Atlas and Moulouya Plain (namely mek014, mek015, mek016, mek017 and mek018), as they are the ones most sensitive to the LAB depth and sub-LAB resistivity. The main conclusion of this test is that an electrical resistivity value of 25 Ωm below the defined LAB depths is too low to be accepted by the MT data. The data certainly support a relatively resistive zone below the depth of 60 km. Note that values of 100 Ωm do lead to acceptable misfits, leading to the conclusion that if the S Receiver functions are defining the base of the lithosphere, and not a mid-lithosphere discontinuity (MLD, Fischer et al. (2010)), then the asthenosphere must be dry. Larger values than 100 Ωm can only exist if the temperature is less than 1300 $^{\circ}\text{C}$ and there are dry conditions. Lower temperatures would imply that the sLABrf events do not define the base of the thermal lithosphere.

7.4 INVERSION OF MAR PROFILE DATA SET

The 3-D solution mesh comprises $71 \times 61 \times 48$ cells in the north-south, east-west and vertical directions, respectively. The inner part comprises a uniform mesh of $39 \times 24 \times 48$ with a cell size of 4 km. The lateral extent of the padding cells, 16, 16, 19, 18 in the north, south, east and west directions, respectively. The thickness of the top layer is 30 m, and the thickness of each subsequent layer increases with a vertical factor of 1.2. A homogeneous model with $100 \Omega\text{m}$ resistivity is used as prior and starting model. The same model smoothing value of 0.3 is applied in x -, y -, and z - directions and for all layers. Impedances are decimated to 4 periods per decade ranging from 0.01 s to 3162 s (22 periods are used for each station during the inversion) for 15 MT stations. Error floors are set as an absolute value to 5% of $(|\mathbf{Z}_{xy} \times \mathbf{Z}_{yx}|)^{1/2}$ (equivalent to 10% to apparent resistivity and 2.8° to phase). 3-D inversions are performed with the complete impedance tensor elements, and the overall rms misfit of 1.39 is achieved.

[Figure 7.11](#) and [Figure 7.12](#) show the final inversion result obtained from fitting full impedance tensor elements. The preferred 3-D model shows that conductive ($1 - 20 \Omega\text{m}$) Western High Atlas is confined by two resistive basins ($>750 \Omega\text{m}$), namely the Souss basin to the south and Haouz basin to the north. At the southern boundary of the Western High Atlas, the conductor is located at a shallower depth and it is deepening to the north. However, due to the presence of the strong upper crustal conductor beneath the southern boundary of the mountains, the uppermost mantle structures ($>\sim 30$ km) could not be fully resolved by the existing data set. [Figure 7.13](#) shows a comparison of the input data (solid dots) and the responses from the preferred 3-D inversion result. The correspondence between the observed and predicted data is visually good.

Furthermore, [Figure 7.14](#) presents the final model obtained from inversion of the full impedance tensor elements (top panel) with the result of isotropic 2-D inversion modelling of [Siniscalchi et al. \(2014\)](#) (bottom panel). As discussed in [Chapter 4](#), geo-electric strike analysis reveals a regional strike direction of $N45^\circ\text{E}$, which is parallel to the general trend (NE-SW) of the Western High Atlas Mountains. Therefore, 45° is chosen for the decomposition of the MT responses, and the data set is modelled in 2-D ([Siniscalchi et al. \(2014\)](#)). The upper and middle crustal conductor which appears in the 2-D is found in 3-D inverse solutions. The greater difference between the two models are seen at the depths greater than ~ 10 km on the southwestern end of the profile, beneath the Souss Basin.

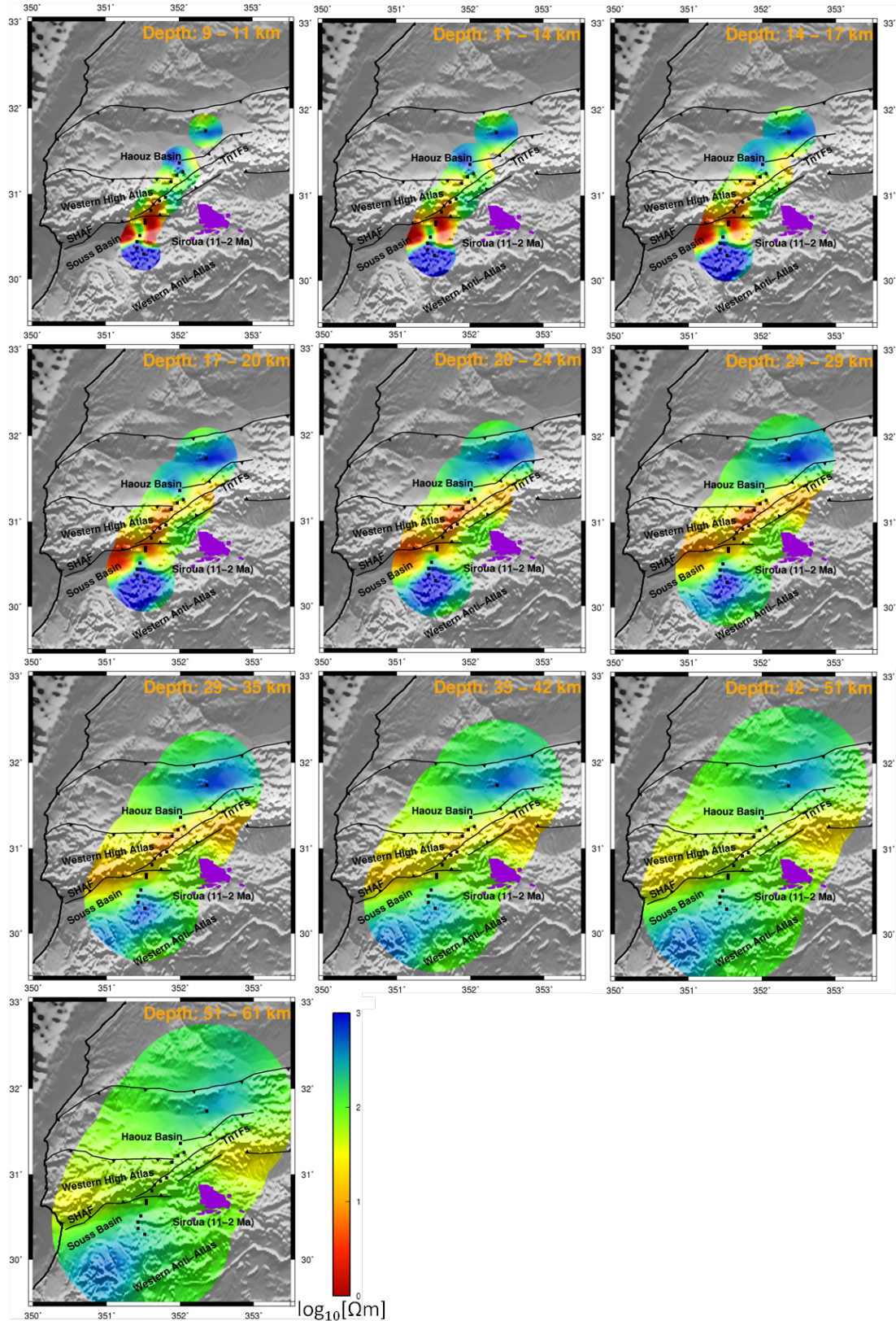


Figure 7.11.: Plan view of the preferred 3-D resistivity model obtained from the final 3-D inversion, which is the result of fitting full impedance tensor (Z_{xx} , Z_{xy} , Z_{yx} , and Z_{yy}), at depths upper crust (9 - 11 km, 11 - 14 km), middle crust (14 - 17 km, 17 - 20 km, and 20 - 24 km), lower crust (24 - 29 km, and 29 - 35 km) and lithospheric mantle (35 - 42 km, 42 - 51 km, and 51 - 61 km). The squares indicate the location of MT stations along the MAR profile. The part of the model which is well constrained by the data is shown only.

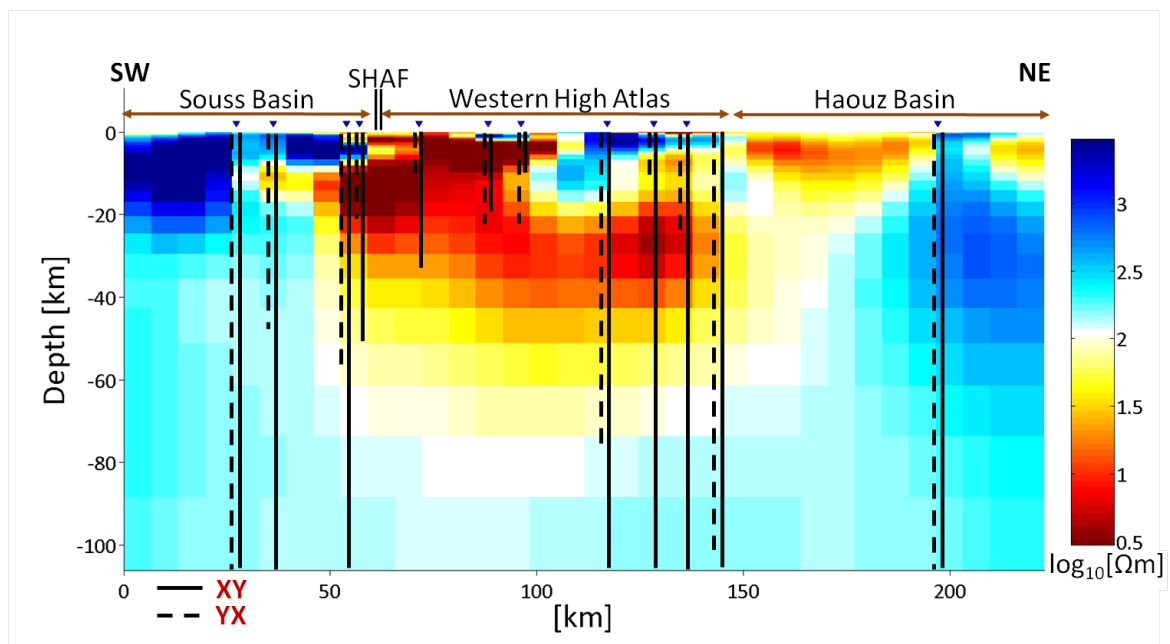


Figure 7.12.: 2-D profile of the MAR transect extracted from preferred 3-D inversion model is shown [Figure 7.11](#). The approximate Niblett-Bostick penetration depths ([Jones, 1983a](#)) of two modes (XY and YX) are plotted on top of the model.

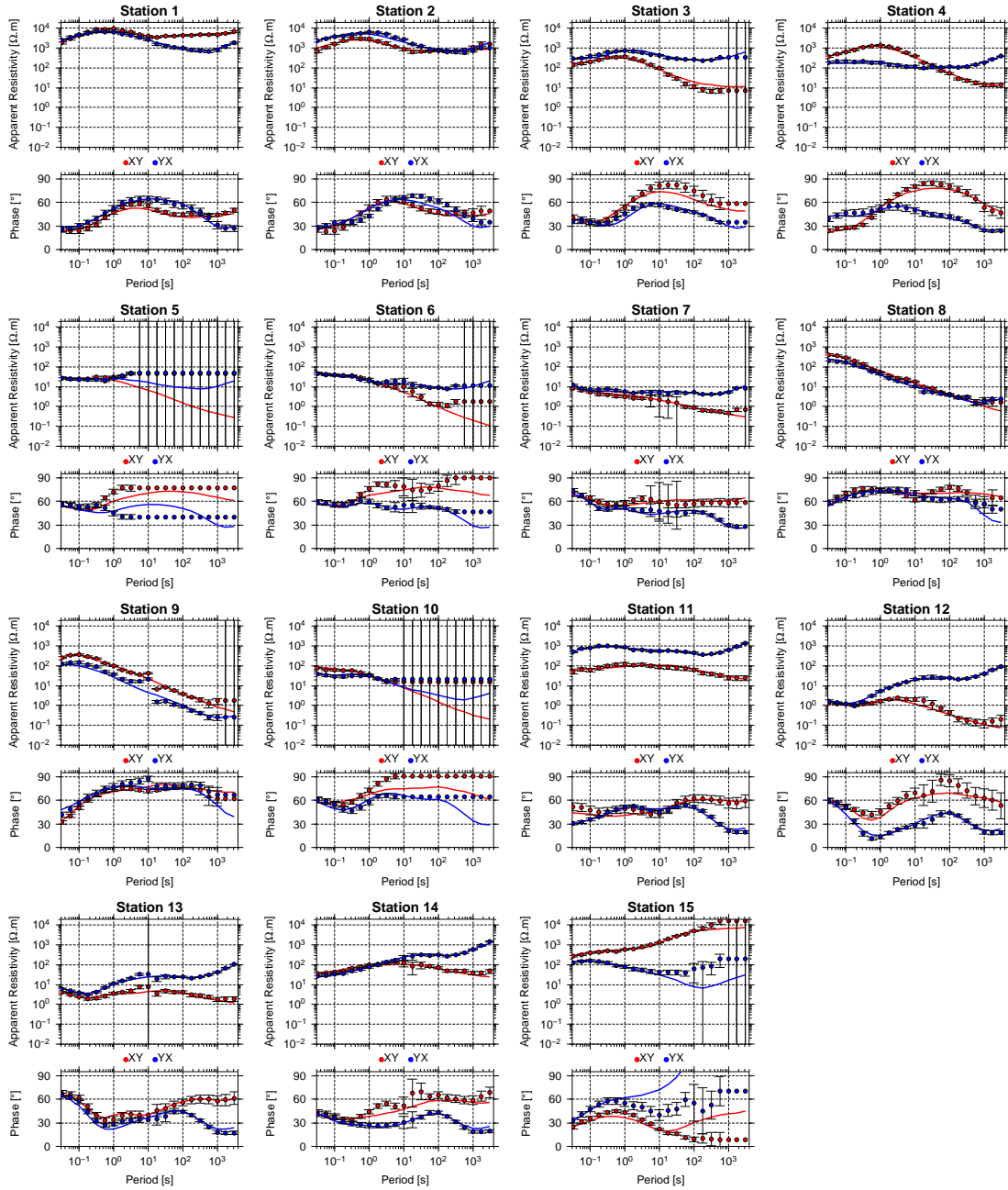


Figure 7.13.: This figure shows the comparison of the observed data (dots) and the response curves of the final 3-D inversion model (solid lines) of MAR profile for XY and YX components.

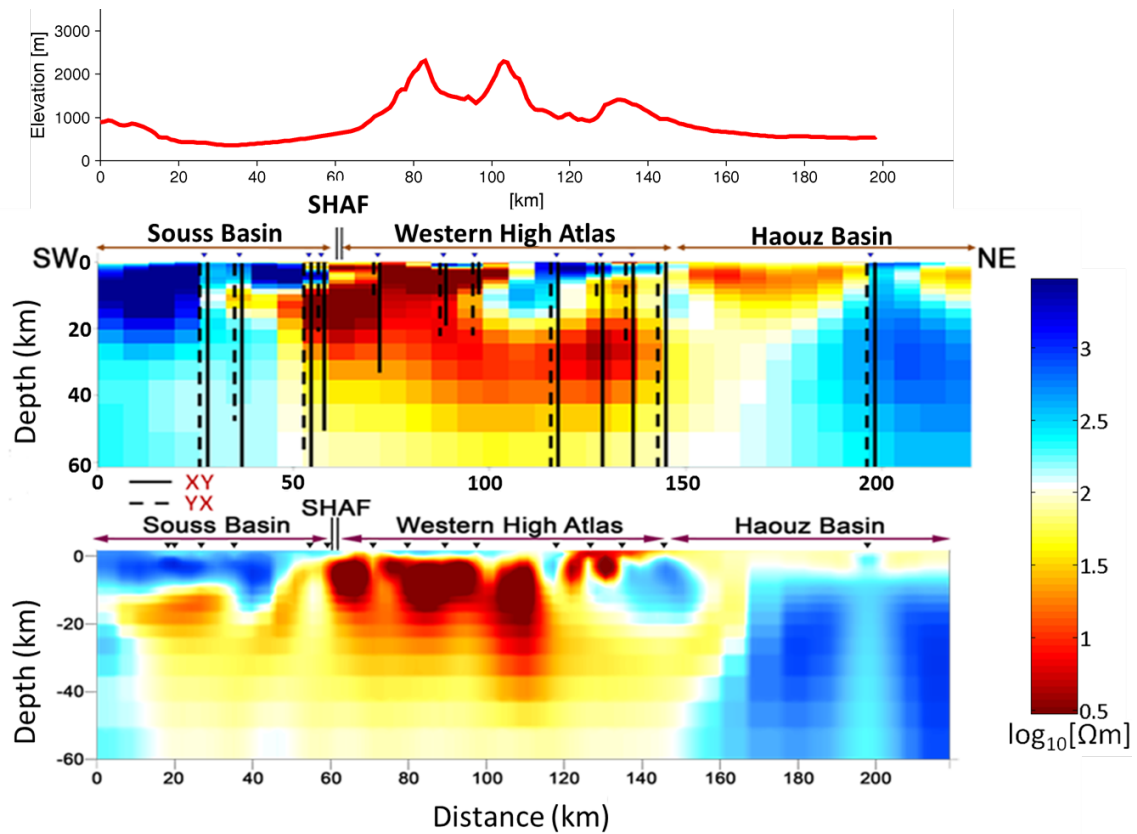


Figure 7.14.: Figure showing 2-D profile of the MAR transect extracted from preferred 3-D inversion model and the isotropic 2-D model obtained from joint inversion of TE and TM data using the NLCC algorithm of Rodi & Mackie (2001) along the MAR profile. Top panel shows the elevation profile along the MAR profile.

Part III

DISCUSSION, CONCLUSIONS AND REFERENCES

DISCUSSION

In this chapter, the origin of low electrical resistivity in the crust and uppermost mantle will be discussed and compared with the recent seismic results and previous geophysical and geological work in the study area. The results from several seismic experiments that have been carried out across the Atlas Mountains of Morocco have already been presented in detail in [Chapter 3](#).

8.1 COMPARISON WITH SEISMIC RESULTS

The 3-D inversion model reveals two resistive zones beneath the Anti-Atlas, which has been stable since the beginning of Mesozoic, and the High Moulouya Plain, and three zones of high electrical conductivity beneath the Middle Atlas, High Moulouya Plain, and the High Atlas ([Figure 8.1](#), on the bottom). The high conductivity material beneath the Tabular Middle Atlas is labelled as C1, beneath the southern end of the Tabular Middle Atlas, the Folded Middle Atlas and the High Moulouya Plain is labelled as C2, and beneath the central High Atlas is labelled as C3 between the depths of 30 - \sim 60 km, 17 - \sim 50 km, and 6 - \sim 25 km, respectively.

In the Anti-Atlas, the uppermost crust (\sim 2 km) is characterized by high conductivity values (5 - 20 Ω m), which are most likely related to Paleozoic sedimentary layers. [Robert-Charue \(2006\)](#) reported that thick deposits of Paleozoic sedimentary rocks can reach thicknesses up to 4 km below the Anti-Atlas. The middle and lower crust ($<$ 35 km) of the Anti-Atlas show high resistivities of 500 - 1500 Ω m. In the High Atlas, high conductivity structure (C3) with resistivity ($<$ 10 Ω m) is likely associated with the Triassic and Jurassic basin sequences and thrust fault systems of the North Atlas Fault (NHAf) and the South Atlas Fault (SHAf) (e.g., [Beauchamp et al., 1999](#); [Benammi et al., 2001](#)), ([Figure 8.1](#), on the bottom). Note that the distinct conductivity difference between the Middle-High Atlas and the Anti-Atlas correlates well with the SHAf, the depth extent of which appears to be limited to the uppermost mantle (\sim 50 km). In the High Moulouya Plain, the upper crustal high resistivity zone is approximately 17 km thick, with resistivity of 1000 Ω m, which is inferred to be the resistivity of Paleozoic granites ([Schwarz & Wigger, 1988](#)). Moreover, the lack of important thrusting systems in the region could also be an explanation for the observed high resistivity ([Ledo et al., 2011](#)).

8.2 ORIGIN OF HIGH CONDUCTIVITY IN THE LOWER CRUST AND UPPERMOST MANTLE

The most significant result of this study is the lower crustal and uppermost mantle conductor observed beneath the southern end of the Middle Atlas and the High Moulouya Plain (Figure 8.1, on the bottom; for the station locations, see Figure 8.5). The enhanced conductivity values correlate with the low V_p values in the lower crust (6.4 and 6.6 km/s characterize the top and bottom of the lower crust in the High Moulouya and in the Middle Atlas) and in the uppermost mantle of the Middle Atlas and the High Atlas (<7.8 km/s), Figure 8.1. Ayarza et al. (2014) concluded that these low velocity values must be due to high temperatures and partial melt at those depths, particularly given the presence of extensive Pliocene and Quaternary basaltic volcanism in the Middle Atlas and Eocene volcanism at the northern border of the High Atlas.

As for the mantle, in terms of seismic constraints teleseismic waves (Bezada et al., 2014; Bonnin et al., 2014) and surface waves (Palomeras et al., 2014) have shown evidence for strong low velocity anomalies, located at depths of 50 to ~ 150 km, beneath most of Morocco. In particular, Rayleigh wave tomography results have been taken to suggest that the lithosphere-asthenosphere boundary is as shallow as 45 - 50 km beneath the Middle Atlas and the High Atlas, both of which are characterized by very low shear wave velocities (~ 4.1 km/s between the depths of ~ 45 and 100 km). A comparison of the vertical section from the resulting shear-wave velocity model of Palomeras et al. (2014) and the 2-D profile of MEK transect extracted from the final 3-D resistivity model are shown in Figure 8.2. The interpreted Moho depths from Ayarza et al. (2014) and Miller & Becker (2014), and the LAB conversions from Fulla et al. (2010) and Miller & Becker (2014) are shown on the resistivity model. As seen from Figure 8.2, however, 3-D MT inversion results show relatively resistive ($\sim 100 - 150 \Omega\text{m}$) upper mantle beneath the Middle Atlas, the High Moulouya Plain, and the High Atlas at those depths. The relatively increased resistivities and low velocities observed in the mantle are highly unusual, since typically an increase in water content, partial melt, or temperature reduces the stiffness of the rocks in the mantle, thereby reducing both seismic velocity, and electrical resistivity. One could question the penetration depth of the data set in this region, owing to the widespread lower crustal conductor. However, running forward tests on this region showed that data are sensitive to structure beneath the conductive layer and certainly support a relatively resistive zone, (for further details, see Chapter 7).

8.2 ORIGIN OF HIGH CONDUCTIVITY IN THE LOWER CRUST AND UPPERMOST MANTLE

What is the origin of the observed high conductivity (low resistivity) layer in the lower crust? Many different mechanisms proposed to explain the cause of conductive anomaly observed in the crust, including conducting mineral phases such as sulphides (e.g., Jones et al., 1997; Ritter et al., 2003) and graphite (e.g., Mareschal et al., 1992; Khoza et al., 2013b), partial melt (e.g., Unsworth et al., 2005a; Le Pape et al., 2012) and aqueous fluids, (e.g., Li et al., 2003). In the mantle, however, electrical conductivity of mantle minerals (olivine, orthopyroxene and clinopyroxene) is primarily sensitive to temperature (e.g., Constable et al., 1992; Mareschal et al., 2000; Ledo &

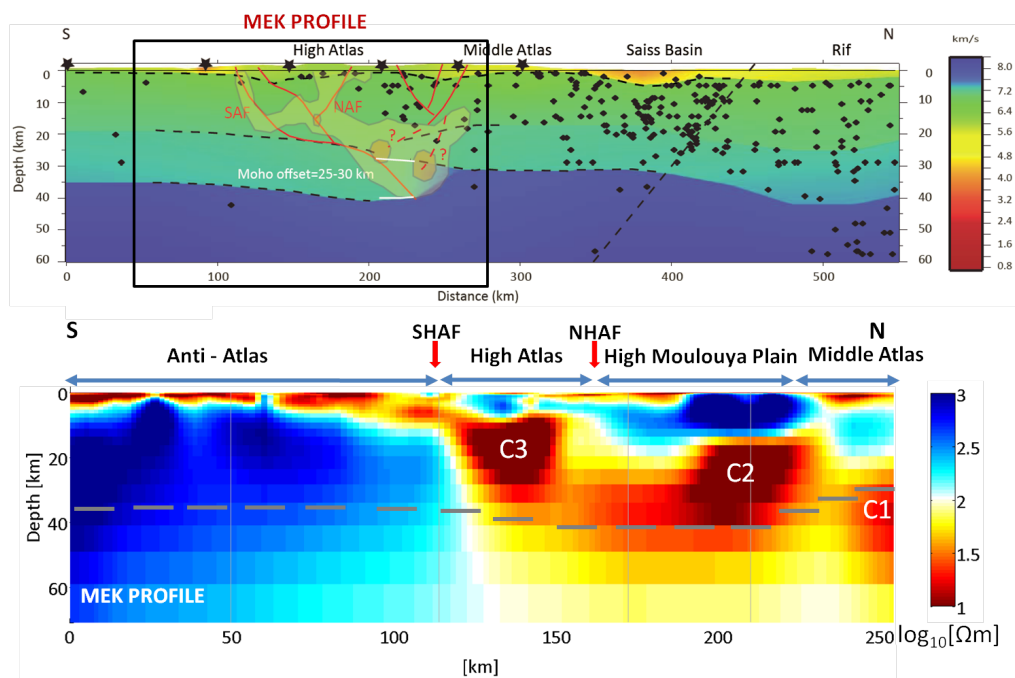


Figure 8.1.: Crustal resistivity models compared with the crustal velocity model obtained from long offset wide-angle seismic reflection data under the framwok of SIMA seismic experiment. **Top:** Velocity model with the tectonic interpretation; *modified from Ayarza et al. (2014)*. The area of interest, which coincides with the MEK profile, is outlined by a black box. On the velocity model, contours and semi-transparent colours represent the resistivity model by Ledo et al. (2011): while the outer contour indicates $\rho < 25 \Omega\text{m}$, the inner one indicates $\rho < 2 \Omega\text{m}$ (on the bottom). **Bottom:** Depth slice of electrical resistivity extracted from the final 3-D inversion model. The grey dashes indicate interpreted crust-mantle boundary (Moho) by Ayarza et al. (2014).

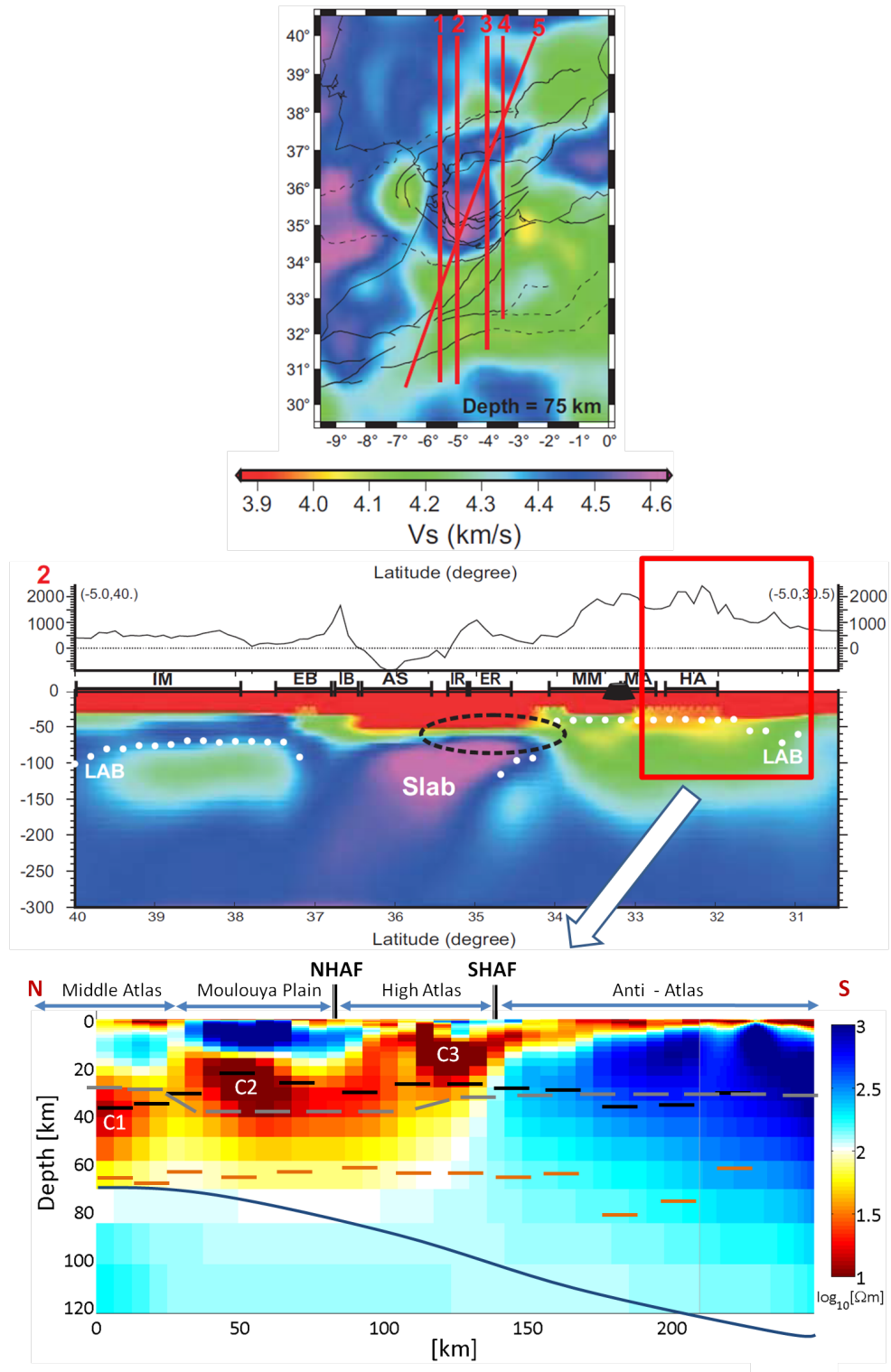


Figure 8.2.: **Top:** Cross sections showing shear wave velocity through the Atlas Mountains extracted from the 3-D shear wave velocity model; *from* (Palomeras et al., 2014). The area of interest, which coincides with the MEK profile, is outlined by a red box. **Bottom:** Depth slice of electrical resistivity extracted from the final 3-D inversion model. The black and grey dashes indicate interpreted crust-mantle boundary (Moho) by Miller & Becker (2014) and Ayarza et al. (2014), respectively. Lithosphere-asthenosphere boundary (LAB), based on S Receiver Function (SRF) analysis (Miller & Becker, 2014) and from Fullea et al. (2010) are indicated with red dashes and blue solid line, respectively.

Jones, 2005b), water content (e.g., Karato, 1990; Jones et al., 2009, 2012a) and, to a far lesser extent, compositional variations (e.g., Jones et al., 2009).

There are several arguments in favour of the existence of partial melt in the crust of the Middle Atlas and the High Moulouya Plain: (i) observed and modelled thin lithosphere (i.e., lithosphere-asthenosphere boundary (LAB) = $\sim 45 - 70$ km based on passive seismic (Palomeras et al., 2014), and potential field lithospheric forward modelling studies (Fullea et al., 2010; Teixell et al., 2005; Zeyen et al., 2005)), (ii) relatively high surface heat flow (70 mW/m^2 in the High Moulouya Plain, 83 mW/m^2 in the Middle Atlas, (Rimi, 1999)), (iii) presence of abundant Cenozoic to Quaternary alkaline dominated intraplate igneous activity (Tabular Middle Atlas — MT site mek012, Figure 8.5, on top — which is the loci of Quaternary alkali volcanism), and (iv) observed very low seismic velocities (e.g., Ayarza et al., 2014; Bezada et al., 2014; Bonnin et al., 2014). Using a modified brick layer model, Ledo et al. (2011) proposed estimates of the partial melt fraction ranging from 2 to 8 vol% at depths of 20 - 40 km in order to explain the enhanced conductivity anomaly beneath the Middle Atlas and High Moulouya Plain. New minimum estimates of the melt fraction that consider various geometrical models of electrical conductivity are presented below.

In order for the conductivity to be enhanced by the partial melt, the molten phase must form an interconnected network (Roberts & Tyburczy, 1999; Nover, 2005). The conductivity of pure melt depends on temperature, its composition, pressure, water content, interconnection geometry or texture, and weakly on pressure (Evans (2012), and references therein). Dry rocks begin to melt around $1200 \text{ }^\circ\text{C}$, with a melt conductivity range between 1 and 10 S/m (Tyburczy & Waff, 1983). Water-saturated rocks begin to melt at lower temperatures, about $650 \text{ }^\circ\text{C}$ (Thompson, 1992). For water-saturated rocks, melt conductivities are slightly higher between 1 and 20 S/m (Lebedev & Khitarov, 1964), Figure 8.4. For both dry and water saturated rocks, melt conductivity increases with temperature according to an Arrhenius relationship (Section 2.5.2).

8.2.1 *Temperature Regime in the Crust – crustal geotherm calculations*

Before estimating the possible melt that will be used to quantify the minimum melt fraction in the Middle Atlas and the High Moulouya Plain, the probable temperature within the lower crust ($\sim 20 - 35$ km) should be estimated. Rimi (1999) inferred temperatures of $890 \text{ }^\circ\text{C} \pm 84$ and $695 \text{ }^\circ\text{C} \pm 48$ at a depth of 35 km for the Middle Atlas and the High Moulouya Plain, respectively. In addition to existing geotherms published in the literature, crustal geotherms are also calculated in the framework of this thesis, and are presented in Figure 8.3.

The one-dimensional steady-state conductive geotherms are computed performing Monte Carlo (MC) simulations with a one-dimensional forward modelling code of Mottaghy & Rath (2006), and Rath & Mottaghy (2007). The forward modelling code requires thermal conductivity, heat production, basal heat flow, and recent temperature at the top of the first layer as inputs. The surface heat flow range is set to $70 - 85 \text{ mW/m}^2$ (Rimi, 1999), and $10 \text{ }^\circ\text{C}$ for the recent temperature at the surface for the Middle Atlas. Other input parameters are listed in Table 8.1. A three-layered

Table 8.1.: Properties of the different crustal bodies used in the geotherm calculation.

Layer	Heat Production [W/m^3]	Thermal conductivity [$W/m-K$]
Miocene-Quaternary Sediments	1.5 ± 0.5	2.2 ± 0.5
Upper-Middle Crust	1.5 ± 0.5	2.5 ± 0.5
Lower Crust	0.2 ± 0.1	2.1 ± 0.3

Earth model is assumed: Miocene-Quaternary sediments thickness of 2.7 km, upper and middle crustal total thickness of 20 km, and Moho depths of 32 km (represents Middle Atlas crustal thickness), 35 km (average crustal thickness), and 40 km (represents the crustal thickness for the High Moulouya Plain). However, the difference between the calculated geotherms varying Moho depths is negligible. According to the calculated geotherms, a temperature of $720 \text{ }^\circ\text{C} \pm 54$ at a depth of 30 km can be inferred. Temperature estimates in the lower crust (20 - 35 km) can be as low as $\sim 530 \pm 30 \text{ }^\circ\text{C}$ or as high as $810 \text{ }^\circ\text{C} \pm 58$.

Figure 8.5 shows a modelled lithospheric geotherm calculated by Fullea et al. (2010) (Moho depth = 32 km, LAB = 62 km) that matches surface heat flow and topography in the study area. As can be seen from the phase diagram in Figure 8.5, the presence of dry melt in the lower crust can be excluded as the dry solidus never crosses the geotherm. The depth at which the maximum conductivity beneath the Tabular Middle Atlas, Folded Middle Atlas, and High Moulouya Plain occurs within the lower crust (Figure 8.5, bottom-right), ~ 30 km, coincides with the depth where the modelled geotherm intersects the water-saturated granite/basalt solidus (pink region). Furthermore, the modelled geotherm suggests temperatures at those depths could be between $\sim 500 - 815 \text{ }^\circ\text{C}$. Therefore, temperatures in the lower crust are too low for dry melting, but wet melting is possible. As can be inferred from Figure 8.4, for a reference pressure ($P = 7 - 8$ kbar) and temperature ($T = 600 - 800 \text{ }^\circ\text{C}$, highlighted zone in Figure 8.4), a range of melt conductivity 1 - 10 S/m is to be expected. If we take a reference pressure value of 8 kbar (~ 27 km) and related temperature values of $625 \text{ }^\circ\text{C}$ (Figure 8.5) and $800 \text{ }^\circ\text{C}$ (upper limit of temperature), values of 3 S/m and 10 S/m for melt conductivity (Figure 8.4) can be used for melt fraction estimates.

8.2.2 Estimates of Melt Fraction

In order to estimate the minimum melt fraction required to explain the crustal conductor C2, whose conductivities ranges from 0.1 to 0.33 S/m, various geometrical models are used to calculate the bulk conductivity of the rock for the possible melt distributions. These include the modified brick layer model (Equation 8.1; Partzsch et al., 2000),

$$\sigma_{eff-MBLM} = \frac{1}{\frac{1-a}{\sigma_m} + \frac{a}{\sigma_m(1-a^2) + \sigma_s a^2}} \quad (8.1)$$

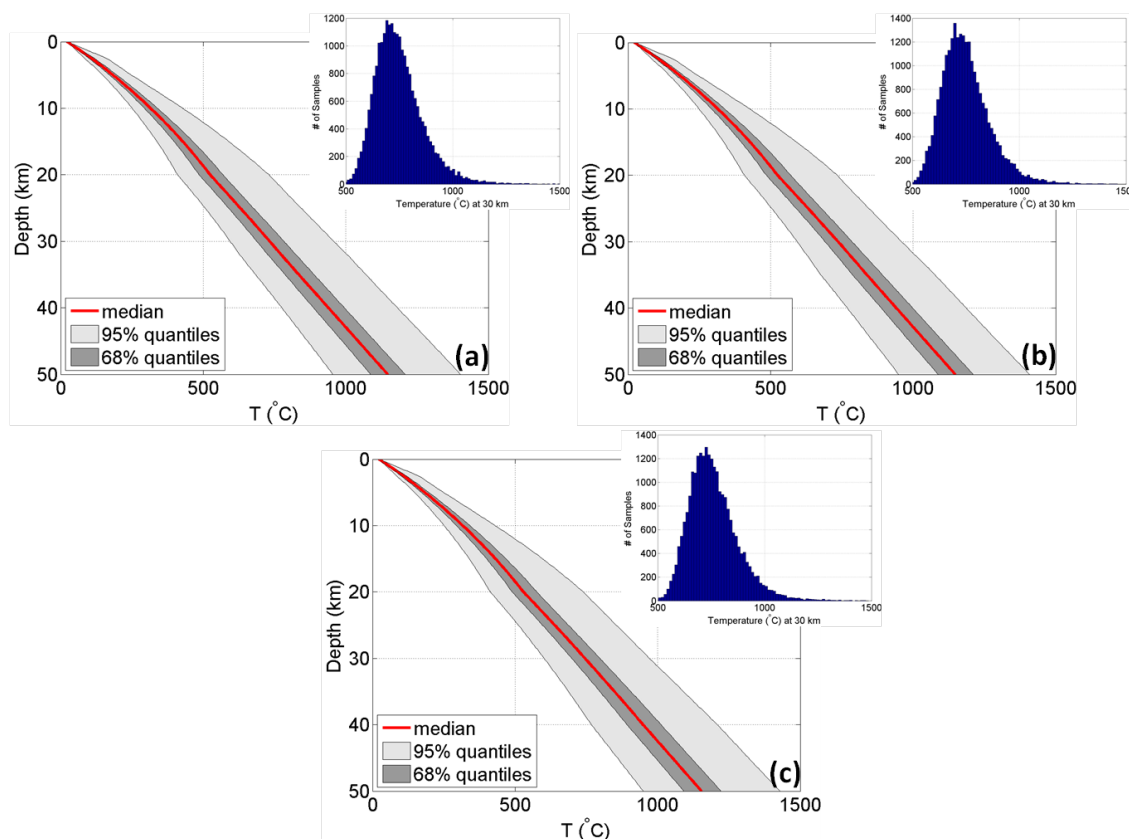


Figure 8.3.: Crustal geotherms for the Middle Atlas and the High Moulouya Plain with a plot showing temperature distribution at 30 km depth. The one-dimensional steady-state conductive geotherm is computed performing Monte Carlo (MC) simulations with a one-dimensional forward modelling code of Mottaghy & Rath (2006) and Rath & Mottaghy (2007), which requires thermal conductivity, heat production, basal heat flow, and recent temperature at the top of the first layer, which is ~ 10 °C for the Middle Atlas (<http://www.pages-igbp.org/old/about/national/morocco/highlight.html>). The surface heat flow range is set to 70 - 85 mW/m^2 (Rimi, 1999). Other physical parameters are listed in Table 8.1. Moho depths of 32 km (represents Middle Atlas crustal thickness), 35 km (average crustal thickness), and 40 km (represents the crustal thickness for High Moulouya Plain) are used. The difference between the calculated geotherms is negligible. According to the calculated geotherms, temperature of 720 °C ± 54 at a depth of 30 km can be inferred. Temperature estimates in the lower crust (20 - 35 km) range from 530 °C ± 30 to 810 °C ± 58 .

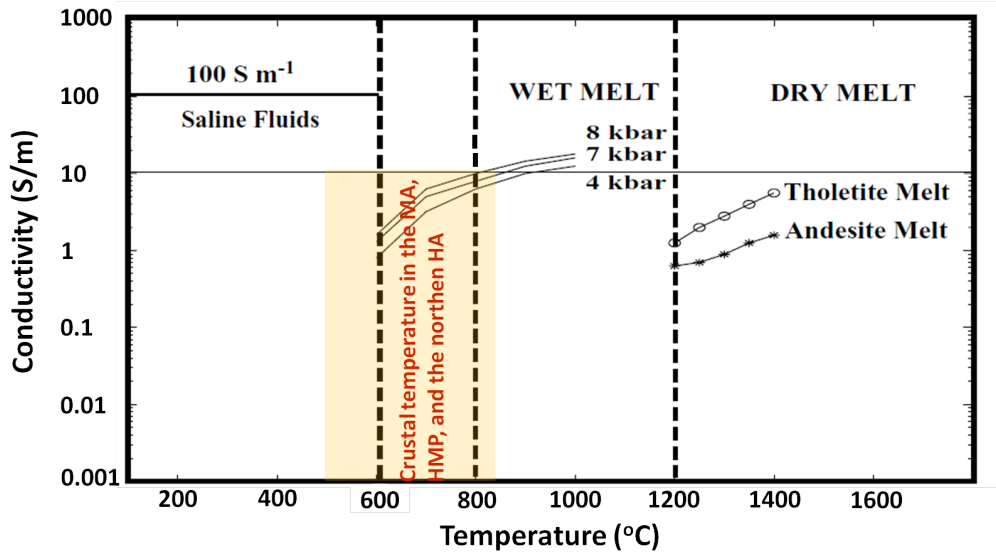


Figure 8.4.: Electrical conductivity of saline fluids compared with wet (Lebedev & Khitarov, 1964) and dry (Tyburczy & Waff, 1983) partial melt; *modified from Li et al. (2003).*

with σ_{eff} conductivity of the composite, σ_m conductivity of the melt, σ_s conductivity of the solid rock, and

$$a = (1 - X_m)^{1/3} \quad (8.2)$$

with X_m the melt fraction. Hashin-Shtrikman upper bound (refeq:melt-hsupper; Hashin & Shtrikman, 1962),

$$\sigma_{eff-HS+} = \sigma_m + \frac{(1 - X_m)}{1/(\sigma_s - \sigma_m) + X_m/3\sigma_m} \quad (8.3)$$

equally spaced conducting tubes model (Equation 8.4; Schmeling, 1986),

$$\sigma_{eff-TUBES} = \frac{1}{3}X_m\sigma_m + (1 - X_m)\sigma_s \quad (8.4)$$

parallel conduction model (Equation 8.5; Roberts & Tyburczy, 1999; ten Grotenhuis et al., 2005),

$$\sigma_{eff-PARALLEL} = \sigma_m X_m + \sigma_s X_r \quad (8.5)$$

where $X_r = 1 - X_m$, and Archie's Law (Equation 8.6; ten Grotenhuis et al., 2005),

$$\sigma_{eff-Archie'sLaw} = C X_m^n \sigma_m \quad (8.6)$$

These geometrical models and the Archie's law are described in Section 2.5 (of Chapter 2). As discussed above, highly conducting ($\sigma_{melt} = 10$ S/m) and an intermediate conducting ($\sigma_{melt} = 3$

S/m) melt conductivities can be used to define upper and lower limits of the melt fraction with a fixed host rock conductivity (σ_s) value of 0.001 S/m (1000 Ω m). Note that the conductivity of the host rock has a minimal effect on the calculations since the melt is interconnected and its conductivity is much higher. Following the study of [ten Grotenhuis et al. \(2005\)](#), values of $C = 1.47$ and $n = 1.3$ are used for the melt estimations using Archie's law. The resulting bulk conductivity as a function of the melt fraction is plotted in [Figure 8.6](#). According to [Figure 8.6](#), 0.8 - 3 vol% ($\sigma_{melt} = 10$ S/m) and 3.3 - 10 vol% ($\sigma_{melt} = 3$ S/m) can be taken as minimum melt fractions to explain the observed conductivity of 0.33 - 0.1 S/m beneath the Tabular and the Folded Middle Atlas, and the High Moulouya Plain, if we assume a parallel conduction model. If we consider Archie's law, melt fractions of 2 - 5 vol% ($\sigma_{melt} = 10$ S/m) and 5.7 - 12 vol% ($\sigma_{melt} = 3$ S/m) will be needed to explain the enhanced conductivity.

Alternatively, the web based application SIGMELTS can be used to estimate the conductivity of the silicate melts in the Middle Atlas given the melt composition (SiO_2 and Na_2O contents), temperature, pressure, and water content ([Pommier & Le-Trong, 2011](#)). Major and trace element analyses of Middle Atlas lavas are discussed in [El Azzouzi et al. \(2010\)](#) and [Bosch et al. \(2014\)](#). The results of those works are considered for melt composition ([Table 8.2](#)). Different combinations of composition, temperature, pressure, and water content are tested to understand their influence on the estimated melt conductivity. Estimated melt conductivities are listed in [Table 8.2](#). According to the test results, the conductivity of the melt is highly sensitive to temperature as well as water content, but relatively insensitive to composition and pressure. Note that SiO_2 and Na_2O contents in melt compositions used in the calculations do not vary significantly, therefore observing less influence of melt composition on electrical conductivity is not surprising in this case. The computed conductivity values are too low compared to the assumptions described above due to assigned temperature values during the calculations. If melt conductivity is assumed to be 1.5 S/m (water content = 5 wt%), the parallel conduction model gives volume fractions of 9 - 32 vol% for the lower crustal conductive body C2 with bulk conductivity suggested by the MT model. If we take the value of 0.8 S/m (water content = 2 wt%) for melt conductivity, a melt fraction between 17 - 46 vol% would be taken as a minimum estimate of the partial melt to explain the enhanced conductivity of C2. However, these value ranges of the estimated partial melt fractions are too high to be reasonable. A recent review of experimental studies on the strength of partially molten crustal rocks (granite) by [Rosenberg & Handy \(2005\)](#) showed that a factor of ten strength reduction occurs between 0 and 7 vol% melt fractions. Therefore, melt fractions of 3.3 - 10 vol% is required to account for the high conductivity to reduce the strength of the crust beneath the High Moulouya Plain by a factor of ten.

Regardless of the specific melt fraction, the source of the fluids which facilitates partial melting in the lower crust at lower temperatures remain a key question. Mantle xenoliths from the volcanic district of Azrou-Timahdite as well as with mafic lavas from the Middle Atlas and Central Morocco volcanic provinces ([Raffone et al., 2009](#); [El Azzouzi et al., 1999](#); [Bosch et al., 2014](#)) were examined. The volcanic district of Azrou-Timahdite is located ~ 25 km to the north of the last MT station

Table 8.2.: Parameters (i.e., melt composition, temperature, pressure and water content) used for the computation of electrical conductivity of pure melt – Effect of each parameter on the electrical conductivity of melt are tested, respectively. For the melt compositions, nephelinites, basanites, alkali basalts, and subalkaline basalts are used, respectively, (El Azzouzi et al., 2010; Bosch et al., 2014). Melt conductivity values of 0.796 and 1.564 are used in the melt fraction estimates.

<i>SiO₂</i> (wt%)	<i>Na₂O</i> (wt%)	T (°C)	P (MPa)	<i>H₂O</i> (wt%)	σ_{melt} (S/m)
39.91	4.07	800	1080	0	0.032
43.73	3.18	800	1080	0	0.032
48.17	3.19	800	1080	0	0.020
52.00	3.15	800	1080	0	0.032
<i>SiO₂</i> (wt%) (average)	<i>Na₂O</i> (wt%)	T (°C)	P (MPa)	<i>H₂O</i> (wt%)	σ_{melt} (S/m)
45.95	3.39	800	1080	0	0.032
45.95	3.39	890	1080	0	0.079
45.95	3.39	974	1080	0	0.166
<i>SiO₂</i> (wt%) (average)	<i>Na₂O</i> (wt%) (average)	T (°C)	P (MPa)	<i>H₂O</i> (wt%)	σ_{melt} (S/m)
45.95	3.39	800	1080	0	0.032
45.95	3.39	800	900	0	0.047
<i>SiO₂</i> (wt%) (average)	<i>Na₂O</i> (wt%) (average)	T (°C)	P (MPa)	<i>H₂O</i> (wt%)	σ_{melt} (S/m)
45.95	3.39	974	1080	0	0.166
45.95	3.39	974	1080	1	0.698
45.95	3.39	974	1080	2	0.796
45.95	3.39	974	1080	3	1.047
45.95	3.39	974	1080	4	1.475
45.95	3.39	974	1080	5	1.564
45.95	3.39	974	1080	6	1.640

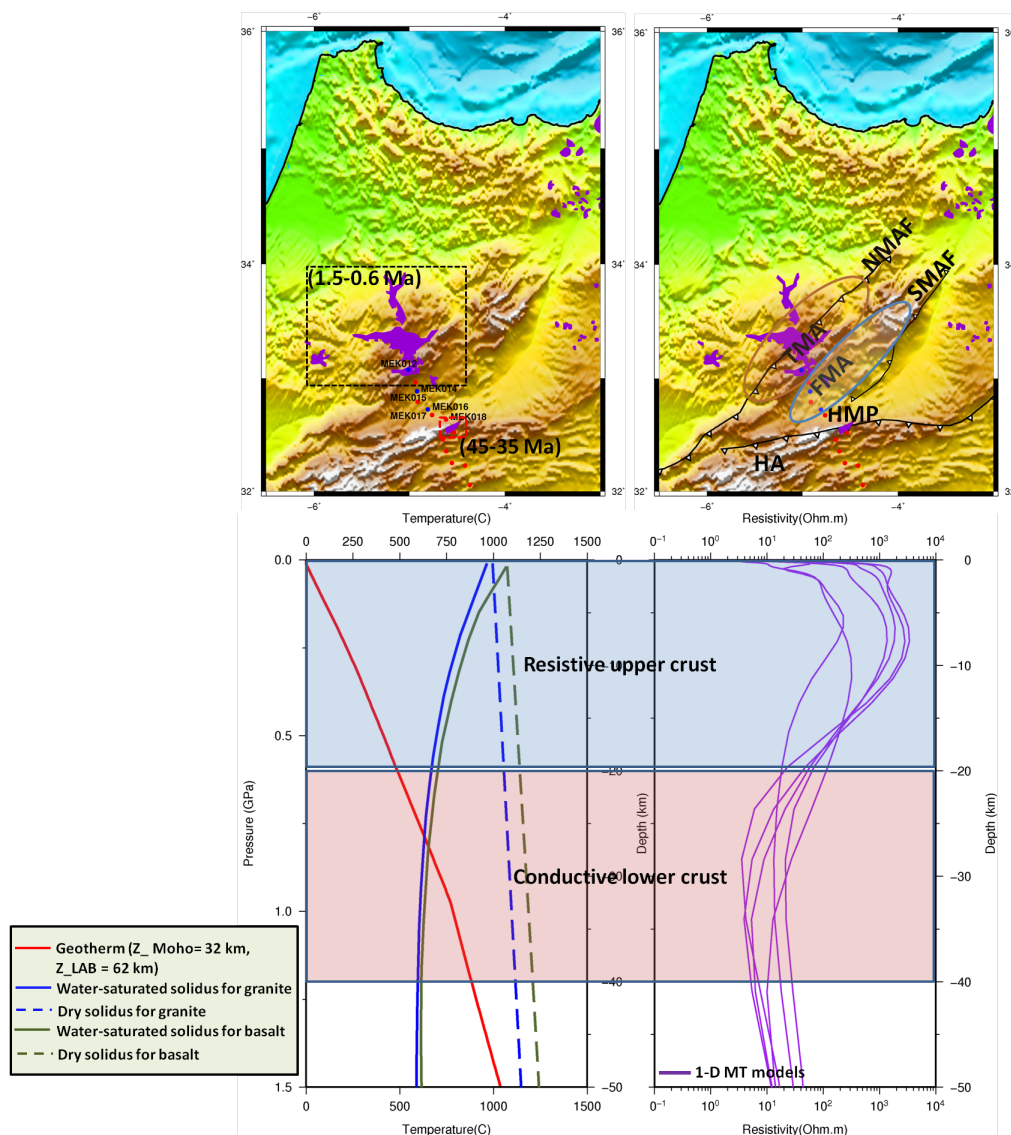


Figure 8.5.: Figure showing (on the bottom-left) a modelled geotherm (red solid line) corresponds to a lithospheric structure that matches measured surface heat flow and topography (LAB = 65 - 70 km, Moho depth = 32 - 34 km) in the study area, (Fullea et al., 2010). Phase diagram emphasizing the role of water in magma source rock showing a comparison between the dry and water-saturated solidi for granite and basalt (*digitized from (Murphy, 2006)*), and (on the bottom-right) 1-D MT models, which are from the stations located in the Middle Atlas (southern end of TMA-MEK012, FMA-MEK014 and MEK015) and HMP (MEK016, MEK017 and MEK018), extracted from the final 3-D model (Figure 7.5, Chapter 7). NMAF: North Middle Atlas Fault; SMAF: South Middle Atlas Fault; TMA: Tabular Middle Atlas; FMA: Folded Middle Atlas; HMP: High Moulouya Plain; HA: High Atlas.

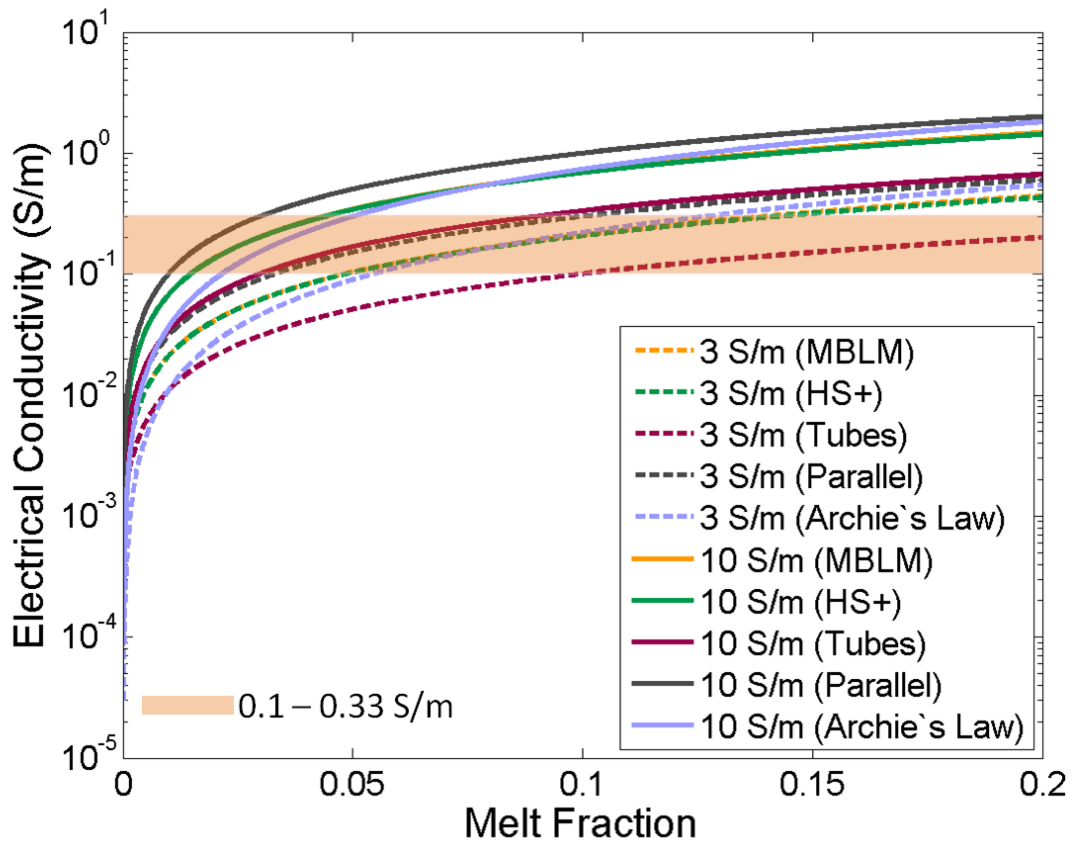


Figure 8.6.: Electrical conductivity of a partially molten rock as a function of melt fraction calculated using modified brick layer model (Partzsch et al., 2000), Hashin-Shtrikman upper bound (Hashin & Shtrikman, 1962), equally spaced conducting tubes model (Schmeling, 1986), parallel conduction model (Roberts & Tyburczy, 1999; ten Grotenhuis et al., 2005), and Archie's Law (Watanabe & Kurita, 1993), respectively. The conductivity of solid rock is set to 0.001 S/m. The melt conductivity is 3 S/m for dashed lines and 10 S/m for solid lines. Between 3.3 - 10 vol% ($\sigma_{melt} = 3$ S/m) and 0.8 - 3 vol% ($\sigma_{melt} = 10$ S/m) melt is necessary to obtain observed conductivity of 0.1 - 0.33 S/m beneath the Tabular and Folded Middle Atlas, and High Moulouya Plain if we assume a parallel conduction model.

(MEK012, Figure 8.5) used in the 3-D inversion. The results show extensive reactions with silicate and carbonate melts that led to the formation of a range of lithologies characterized by substantial olivine, clinopyroxene, or hydrous mineral (i.e., amphibole and pargasite) enrichments, as well as incompatible trace element enrichments (Raffone et al., 2009; Wittig et al., 2010; El Azzouzi et al., 2010; Natali et al., 2013; Bosch et al., 2014). The enriched geochemical characteristic of the volcanic rocks of this area suggests that Atlas lithosphere has experienced alkaline and carbonatite melt-induced metasomatic episodes since the late Cretaceous or Eocene (Raffone et al., 2009). Subsequent partial melting of the metasomatized Iherzolitic Atlas mantle could generate the silica-undersaturated alkali magmas in the Middle Atlas (Bosch et al., 2014). Therefore, supercritical fluids, i.e., $H_2O - CO_2$ rich, stemming from metasomatic alteration of the Atlas lithosphere during its partial melting process, may have migrated to the permeable lower crust and initiated its partial melting, therefore enhancing the electrical conductivity. It was suggested that the first alkaline and carbonatitic melts, which caused metasomatized Atlas lithosphere, could be originating from the Central Atlantic plume, the ancestor of the Canary plume (Bosch et al., 2014; Piromallo et al., 2008) or from the interplay between reactivation of inherited geological structures during Africa-Europe convergence since the Upper Cretaceous (Rosenbaum et al., 2002).

8.3 GEODYNAMIC IMPLICATIONS

One single mechanism is in general not solely responsible for the uplift history of any given region. For example, the Altiplano-Puna Plateau of the central Andes, where crustal thickening is responsible for the uplift of the plateau in a combination of tectonic shortening and magmatic addition (e.g., Allmendinger et al., 2014), the East Anatolian High Plateau, where a combination of crustal shortening and emplacement of buoyant asthenosphere beneath the plateau was proposed to be responsible for the total topography (Şengör & Kidd, 1979; Şengör et al., 2003). Similar to these examples, our study region, the Atlas Mountains of Morocco, where not only crustal shortening, but also a sub-lithospheric thermal component are thought to be responsible for the uplift in the mountains (Teixell et al., 2005; Zeyen et al., 2005; de Lamotte et al., 2008; Missenard et al., 2006; Fullea et al., 2010).

In order to explain the origin of the Cenozoic alkaline volcanism and the uncompensated Moroccan Atlas crust, several models have been proposed, including: (1) slab induced asthenospheric flow (Teixell et al., 2005); (2) delamination of the Atlas lithospheric mantle as a result of lithospheric overthickening with lateral transport of Canary mantle plume material (Duggen et al., 2009) or (3) without Canary mantle plume (Ramdani, 1998); (4) a large sheet-like mantle upwelling extends from the eastern North Atlantic to the western Mediterranean and central Europe (Hoernle et al., 1995); (5) a small Cenozoic asthenospheric plume, which causes thermal erosion of the Atlas lithosphere, similar to those mapped under the French Massif Central or the Eifel in Germany (Zeyen et al., 2005); (6) small-scale convection involving the deep mantle reservoir or baby-plume (Fullea et al., 2010); (7) edge-driven convection due to a difference in lithospheric thickness between the

West African Craton and the Moroccan Atlas Mountains (King & Ritsema, 2000; Missenard & Cadoux, 2012; Kaislaniemi & van Hunen, 2014).

The most recent body-wave tomography results (Bezada et al., 2014; Bonnín et al., 2014) reject the hypothesis of a lateral connection of the Moroccan Atlas low-velocity anomaly with the Canary plume (Duggen et al., 2009). Furthermore, Bonnín et al. (2014) suggested that a large-scale deep mantle anomaly, from a which small-scale plume could rise, can be ruled out since the slow anomalies in their tomography models do not extend deeper than ~ 300 km. Bezada et al. (2014), who used additional data from PICASSO seismic networks, suggest the occurrence of a delaminated lithospheric feature at ~ 400 km beneath the Middle Atlas. The authors proposed that the high velocity body is overlain by a corridor of hot mantle extending from 50 km to 90 km depths below the High Atlas, and the Anti-Atlas, and to 160 km beneath the Middle Atlas. Contrary to those listed geodynamic models and the most recent seismic results, the presence of a shallow asthenosphere beneath the Atlas mountains is not substantiated by the TopoMed MT data. As discussed in Chapter 7, we tested the LAB geometries suggested by Miller & Becker (2014) and Fulla et al. (2010) by perturbing the resulting model with a resistivity of $25 \Omega\text{m}$. (Note that generally beneath the active regions, the resistivity of the asthenosphere ranges from 5 - $25 \Omega\text{m}$ (Jones, 1999)). The main conclusion drawn from these tests is that an electrical resistivity value of $25 \Omega\text{m}$ below the defined LAB depths is too low to be accepted by the MT data (Note that observed resistivities are $\sim 150 \Omega\text{m}$ for the lithospheric mantle). Nevertheless, as evidenced by our preferred MT model (Figure 8.2), which represents the present day situation, the lower crust and the uppermost mantle of the southern Middle Atlas and High Moulouya Plain, as well as the upper-middle crust of the High Atlas have been characterized as a zone of rheological weakness, whereas the crust and the uppermost mantle of the Anti-Atlas is highly resistive and uniform.

CONCLUSIONS AND OUTLOOK

The thesis work presented here consists of two parts: (i) processing, analysis, modelling and interpretation of an MT data set in the Atlas Mountains of Morocco as a part of both PICASSO and TopoMed projects, and (ii) exploring the role of diagonal impedance tensor elements (Z_{xx} and Z_{yy}) and the orientation of the 3-D mesh coordinate system and the data set, particularly in the presence of a dominant regional 2-D conductivity structures, in 3-D MT inverse modelling.

9.1 MODELLING AND INTERPRETATION OF BOTH THE MEK AND THE MAR PROFILE DATA

9.1.1 *Insights into the Crustal and Mantle Structures of the Atlas Mountains of Morocco*

In the framework of TopoMed/PICASSO projects, magnetotelluric (MT) data were acquired along two profiles: a N-S oriented profile through Middle Atlas to the east and a NE-SW profile through Western High Atlas to the west. The main conclusions from the MT results are summarised as follows:

MEK Profile

- The TopoMed MT models show a low resistivity (high conductivity) layer observed in the middle to lower crust of the southern end of Tabular Middle Atlas, Folded Middle Atlas, and High Moulouya Plain. The preferred resistivities of 3 - 10 Ωm can be explained with the presence of a few percent (3.3 - 10 vol%) partial melt.
- Temperature of $720\text{ }^{\circ}\text{C} \pm 54$ at 30 km depth is estimated. In the lower crust (20 - 35 km), temperature estimates can be as low as $530\text{ }^{\circ}\text{C} \pm 30$ or as high as $810\text{ }^{\circ}\text{C} \pm 58$. Since the estimated temperatures in the lower crust are low, the presence of dry melt (Ayarza et al., 2014) can be ruled out. Instead, the TopoMed MT results are in favour of wet melting in the lower crust, which must be initiated by the mantle-derived H_2O - CO_2 rich supercritical fluids which are originating from metasomatized Iherzolithic Atlas mantle during its partial melting.

- The 3-D resistivity models are compared with the wide-angle seismic reflection results, confirming the presence of melt in the middle to lower crust beneath the Middle Atlas (southern end of the Tabular Middle Atlas and Folded Middle Atlas), and the High Moulouya Plain.
- 3-D modelling inversion results and sensitivity tests using forward modelling indicate that the preferred resistivity for the present day Atlas lithospheric mantle is $\sim 150 \Omega\text{m}$, which does not support an anomalous (hot) mantle beneath the Atlas Mountains.
- The distinct conductivity difference between between the Middle and High Atlas and the Anti-Atlas Mountains is marked by the South Atlas Fault, which is a major tectonic feature that extends from Western High Atlas to Tunisia. The southern side of the South Atlas Fault, the Anti-Atlas mountains, is characterized by the most resistive (and therefore potentially coldest and thickest) lithospheric structure.

MAR Profile

The magnetotelluric 3-D subsurface resistivity models of the MAR profile presented in this thesis provide first insights into the crustal structure of the Western High Atlas.

- 2-D and 3-D modelling of the TopoMed MT data set from an approximately 225 km long MAR profile confirm the presence of a strong conductive structure beneath the Western High Atlas at crustal depths (< 30 km).
- Western High Atlas is confined by two resistive ($> \sim 500 - 750 \Omega\text{m}$) basins, namely Souss Basin to the south and Haouz basin to the north. At the southern boundary of the Western High Atlas, the conductor is located at a shallower depth and than to the north.
- A series of forward modelling sensitivity tests show that the upper mantle structures ($> \sim 30$ km) could not fully be resolved by the existing data set due to the presence of the strong crustal conductor.
- The enhanced conductivity zone is mainly parallel to the early Mesozoic rifting geological structures and could be linked to the presence of fluids, presence of clay ions or possible mineralization along the fault zones.

9.2 3-D MT INVERSION – IMPORTANCE OF INCLUDING DIAGONAL IMPEDANCE TENSOR ELEMENTS AND ORIENTATION OF THE COORDINATE SYSTEM

As part of the TopoMed/PICASSO project, the crustal-probing MT data from the so-called MEK profile in Morocco were first interpreted by Ledo et al. (2011) based on 2-D inversions of tensor decomposed data, with a strike angle of 50°E of north. One of the most striking results of all the

inversions results is a conductive anomaly at middle to lower crustal depths found below the Anti-Atlas. However, 3-D inversion of the same data in a geographic coordinate system supports instead a homogeneous, resistive subsurface [Kiyani et al. \(2012\)](#). Absence of this conductive anomaly motivated us to explore inversion parameters such as the alignment of the coordinate system and the input data (i.e., full impedance tensor elements and only off-diagonal tensor elements) in 3-D.

In order to demonstrate the importance of aligning the 3-D mesh and data coordinate system with the dominant geo-electrical strike direction in 3-D inverse modelling, a synthetic MT profile data set is generated. The test model investigated comprises a regional, elongated 2-D conductive structure at 45° to the profile. The highly conductive, $10 \Omega\text{m}$, body is embedded in a homogeneous, $1000 \Omega\text{m}$ half space. The width of the body is 28 km and its depth extent is from 20 km to 40 km below the surface. Two different types of coordinate system are considered during the inversions: (1) geographic coordinate system, with x directed north and y directed east, and (2) geo-electric strike oriented coordinate system, with x' parallel to the body direction, i.e., directed NE for the particular example considered in this work in a geographic reference frame, and y' directed perpendicular to the body, i.e., NW. For both coordinate systems, inversion of both the off-diagonal tensor elements only, and the complete impedance tensor are performed, however, only the inversion results of off-diagonal components are reported for the strike-aligned coordinate system.

The numerical tests with applying 3-D MT inversion scheme using non-linear conjugate gradients inversion code of [Egbert & Kelbert \(2012\)](#) and [Kelbert et al. \(2014\)](#) to MT profile data shows that the recovery of the regional 2-D conductive structure in the inversion of only the off-diagonal impedance tensor elements depends on the coordinate system. Both the 3-D grid and the data set have to be aligned with quasi-2-D geo-electrical strike direction to obtain the true resistivity and true geometry of the structure. On the other hand, inverting complete impedance tensor components without rotation (i.e., geographic coordinate system) of both the 3-D mesh and the data set yields the subsurface model closest to the true model. Additionally, the influence of the model regularization parameter on the inversion results is briefly discussed.

9.3 SUGGESTIONS FOR FUTURE WORK

- This study provided the first 3-D images of the electrical resistivity structure of the Atlas Mountains of Morocco. However, additional 2-D MT profiles will be valuable in order to fully understand the geo-electric structure of the region and its tectonic significance, which is also important for developing a 3-D electrical resistivity model for the study region. Furthermore, acquiring more 2-D profiles will be helpful to constrain the lateral continuation of the observed high conductivity zone beneath the Middle Atlas and High Moulouya Plain and the High Atlas.
- As already mentioned in [Section 3.2 \(Chapter 3\)](#), the first MT data acquisition and geomagnetic deep sounding were performed in 1980s ([Schwarz & Wigger, 1988](#); [Schwarz et al., 1992](#)). We now have an access to this data set collected along the so-called M profile ([Figure 3.9](#),

Section 3.2; V. Rath, pers. comm.). We are planning to perform 3-D inversion using those MT sites together with the TopoMed MT data set which will facilitate investigation of detailed geo-electrical structures of the High Moulouya basin. Moreover, we will have more knowledge about the orientation/direction of the conductivity structure obtained by inversion of TopoMed MT data set.

- Due to very low solar activity in 2009, long-period data acquisition at 12 stations (blue circles along the MEK profile on Figure 4.1a) on the northern part of the MEK profile left on the ground for 8 weeks. Unfortunately, several problems were encountered during the service checks as the winter was so severe, particularly in the Middle Atlas Mountains. In February 2011, when we returned to Morocco to retrieve those LEMI sites and install BBMT sites, sites MEK010 and MEK001 flooded and little data, which unfortunately are of poor quality, were recovered from them. Based on these issues, future fieldwork campaigns should only be scheduled for spring/summer term in Morocco.
- Since the data quality is poor along the northern part of the MEK profile, which starts from the southern Tabular Middle Atlas to the Rif, both the broad-band and the long-period MT measurements should be repeated. Logistics issues and low solar activity led the TopoMed MT team to acquire the long-period MT data before the broad-band data. However, in general BBMT data should be acquired before LEMI data to assess the data quality from a station. Once the BBMT data are of good quality, then LEMI acquisition should be initiated.
- Qualitative interpretation of seismic wide angle results and MT results (Bedrosian et al., 2007). As part of the SIMA project, a crustal velocity model obtained from a wide-angle seismic reflection profile which coincides with one of the MT profiles, MEK profile. Therefore, a direct comparison between the crustal MT model and seismic model is possible. Bedrosian et al. (2007) successively applied a qualitative interpretation method to a 10 km long profile crossing the Dead Sea Transform in Jordan. The authors combined independently derived inverse models (i.e., MT and seismic models) using a classification approach to provide clear delineation of stratigraphy in accordance with geologic structure. The method comprises: (i) interpolation of models onto a common mesh, (ii) construction of a probability density function describing the physical parameter (i.e., electrical conductivity and velocity) distribution, (iii) identification of classes and class boundaries in the joint parameter space, and (iv) mapping class inclusions onto the original depth sections.
- An application of a coupled integrated geophysical-petrological inversion of surface-wave dispersion curve data (Palomeras et al., 2014) and topography data, with supplementary constraints from gravity data, xenolith data, surface heat flow data and crustal seismic model (Ayarza et al., 2014). The integrated inversion scheme is based on the software package LitMod (Afonso et al., 2008; Fulla et al., 2009), which combines petrological and geophysical modelling of the lithosphere and sub-lithospheric mantle within a self-consistent thermodynamic framework.

REFERENCES

- Afonso, J. C., Fernandez, M., Ranalli, G., Griffin, W. L., & Connolly, J., 2008. Combined geophysical-petrological modelling of the lithospheric-sublithospheric upper mantle: methodology and applications, *Geochemistry, Geophysics, Geochemistry*, **9**, Q05008. (Cited on page [173](#).)
- Akasofu, S. I., 1968. *Polar and magnetospheric substorms*, D. Reidel Pub. Co., Dordrecht, Holland. (Cited on page [22](#).)
- Allmendinger, R. W., Jordan, T. E., Kay, S. M., & L, I. B., 2014. The evolution of the Altiplano-Puna plateau of the Central Andes, *Annual Review of Earth and Planetary Sciences*, **25**, 139–174. (Cited on page [168](#).)
- Anahnah, F., Zaldívar, J. G., Chalouan, A., Pedrera, A., Ruano, P., Pous, J., Heise, W., Constan, A. R., Benmakhlof, M., Carlos, A., Garrido, L., Ahmamou, M. F., Galdeano, C. S. D., Arzate, J., Ibarra, P., Castillo, L. G., Bouregba, N., Corbo, F., & Asensio, E., 2011. Deep resistivity cross section of the intraplate Atlas Mountains (NW Africa): new evidence of anomalous mantle and related Quaternary volcanism, *Tectonics*, **30**, 1–9. (Cited on pages [xi](#), [7](#), [65](#), [114](#), [116](#), and [117](#).)
- Andersen, D. & Fuller-Rowell, T., 1999. The ionosphere, in *Space environment topics*, National Oceanic and Atmospheric Administration (NOAA), U.S. Department of Commerce, 325 Broadway, Boulder, CO 8033-3326. (Cited on pages [vi](#) and [21](#).)
- Andersen, F., Boerner, D. B., Harding, K., Jones, A. G., Kurtz, R. D., Parmelee, J., & Trigg, D., 1988. LIMS: Long period intelligent magnetotelluric system, in *9th Workshop on EM Induction Soschi, USSR*. (Cited on page [5](#).)
- Arboleya, M. L., Teixell, A., Charroud, M., & Julivert, M., 2004. A structural transect through the High and Middle Atlas of Morocco, *Journal of African Earth Sciences*, **39**, 319–327. (Cited on pages [4](#), [60](#), and [117](#).)
- Arnason, K., Eysteinnsson, H., & P, H. G., 2010. Joint 1D inversion of TEM and MT data and 3D inversion of MT data in the Hengill area, SW Iceland, *Geothermics*, **39**, 13–34. (Cited on page [134](#).)
- Avdeev, D. & Avdeeva, A., 2009. 3D magnetotelluric inversion using a limited-memory quasi-Newton optimization, *Geophysics*, **74**(3), F45–F57. (Cited on page [134](#).)
- Ayarza, P., Alvarez-lobato, F., Teixell, A., Arboleya, M. L., Teson, E., Julivert, M., & Charroud, M., 2005. Crustal structure under the central High Atlas Mountains (Morocco) from geological

- and gravity data, *Tectonophysics*, **400**, 67–84. (Cited on pages [x](#), [4](#), [70](#), [111](#), [115](#), [116](#), [117](#), and [144](#).)
- Ayarza, P., Carbonell, R., Teixell, A., Palomeras, I., Marti, D., Kchikach, A., Harnafi, M., Levander, A., Gallart, J., Arboleya, M. L., Alcalde, J., Charroud, M., & Amrhar, M., 2014. Crustal thickness and velocity structure across the Moroccan Atlas from long offset wide-angle reflection seismic data: the SIMA experiment, *Geochemistry, Geophysics, Geosystems*, **160**. (Cited on pages [xiii](#), [6](#), [66](#), [70](#), [114](#), [157](#), [158](#), [159](#), [160](#), [170](#), and [173](#).)
- Baba, K., Chave, A. D., Evans, R. L., Hirth, G., & Mackie, R. L., 2006. Mantle dynamics beneath the East Pacific Rise at 17: insights from the mantle electromagnetic and tomography (MELT) experiment, *Journal of Geophysical Research*, **111**, B02101. (Cited on pages [50](#), [51](#), [100](#), and [104](#).)
- Babault, J., Teixell, A., Arboleya, M. L., & Charroud, M., 2008. A late Cenozoic age for the long-wavelength surface uplift of the Atlas Mountains of Morocco, *Terra Nova*, **20**, 102–107. (Cited on page [4](#).)
- Bahr, K., 1988. Interpretation of the magnetotelluric impedance tensor: regional induction and local telluric distortion, *Journal of Geophysics*, **62**, 119–127. (Cited on page [43](#).)
- Bailey, R. C. & Groom, R. W., 1987. Decomposition of the magnetotelluric impedance tensor which is useful in the presence of channeling, in *SEG Expanded Abstract*. (Cited on pages [43](#) and [91](#).)
- Beauchamp, W., Allmendinger, R. W., Barazangi, M., Demnati, A., El Alji, M., & Dahmani, M., 1999. Inversion tectonics and the evolution of the High Atlas mountains, Morocco, based on a geological geophysical transect, *Tectonics*, **18**, 163–184. (Cited on pages [59](#), [104](#), and [156](#).)
- Becken, M., Ritter, O., & Burkhardt, H., 2008. Mode separation of magnetotelluric responses in three-dimensional environments, *Geophysical Journal International*, **172**, 67–86. (Cited on page [43](#).)
- Bedrosian, P. A. & Feucht, D. W., 2014. Structure and tectonics of the northwestern United States from EarthScope USArray magnetotelluric data, *Earth and Planetary Science Letters*, **402**, 275–289. (Cited on page [134](#).)
- Bedrosian, P. A., Maercklin, N., Weckmann, U., Bartov, Y., Ryberg, T., & Ritter, O., 2007. Lithology derived structure classification from the joint interpretation of magnetotelluric and seismic models, *Geophysical Journal International*, **170**, 737–748. (Cited on page [173](#).)
- Benammi, M., Toto, E. A., & Chakiri, S., 2001. Les chevauchements frontaux du Haut Atlas central Marocain: styles structuraux et taux de raccourcissement différentiel entre les versants nord et sud, *C R Acad Sci Paris*, **333**, 241–247. (Cited on pages [59](#), [104](#), and [156](#).)

- Berdichevsky, M. N. & Zhdanov, M. S., 1984. *Advanced theory of deep geomagnetic sounding*, Elsevier, Amsterdam. (Cited on page 8.)
- Berdichevsky, M. N., Vanyan, L. L., & Dmitriev, V. I., 1973. Methods used in the USSR to reduce near-surface inhomogeneity effects on deep magnetotelluric soundings, *Physics of the Earth and Planetary Interiors*, **53**, 194–206. (Cited on page 37.)
- Berger, J., Liégeois, J. P., Ennih, N., & Bonin, B., 2009. Velocity-conductivity relationships for mantle mineral assemblages in Archean cratonic lithosphere based on review of laboratory data and Hashin-Shtrikman extremal bounds, *Geology*, **38**, e202. (Cited on page 116.)
- Bertrand, E. a., Unsworth, M. J., Chiang, C.-W., Chen, C.-S., Chen, C.-C., Wu, F. T., TürkoÄŖlu, E., Hsu, H.-L., & Hill, G. J., 2012. Magnetotelluric imaging beneath the Taiwan orogen: An arc-continent collision, *Journal of Geophysical Research*, **117**(B1), B01402. (Cited on page 119.)
- Bezada, M. J., Humphreys, E. D., Toomey, D. R., Harnafi, M., Dávila, J. M., & Gallart, J., 2013. Evidence for slab rollback in westernmost Mediterranean from improved upper mantle imaging, *Earth and Planetary Science Letters*, pp. 51–60. (Cited on pages vii, 66, 67, and 68.)
- Bezada, M. J., Humphreys, E. D., Dávila, J. M., Carbonell, R., Harnafi, M., Palomeras, I., & Levander, A., 2014. Piecewise delamination of Moroccan lithosphere from beneath the Atlas Mountains, *Geochemistry, Geophysics, Geosystems*, **15**, 975–985. (Cited on pages 6, 67, 69, 75, 114, 157, 160, and 169.)
- Boerner, D. E., Kurtz, R. D., & Craven, J. A., 2000. A summary of electromagnetic studies on the Abitibi-Grenville transect, *Canadian Journal of Earth Sciences*, **37**, 427–437. (Cited on page 37.)
- Bonnin, M., Nolet, G., Villasenor, A., Gallart, J., & Thomas, C., 2014. Multiple-frequency tomography of the upper mantle beneath the African/Iberian collision zone, *Geophysical Journal International*, **198**, 1458–1473. (Cited on pages 6, 157, 160, and 169.)
- Bosch, D., René, C. M., El Azzouzi, M., Bollinger, C., Bellon, H., & Verdoux, P., 2014. Lithospheric origin for Neogene–Quaternary Middle Atlas lavas (Morocco): Clues from trace elements and Sr–Nd–Pb–Hf isotopes, *Lithos*, **205**, 40–53. (Cited on pages xv, 164, 165, and 168.)
- Bouabdellah, M., Hoernle, K. A. J., Kchit, A., Duggen, S., Hauff, F., Lowry, D., Beaudoin, G., & Klu, A., 2010. Petrogenesis of the Eocene Tamazert continental carbonatites (Central High Atlas, Morocco): implications for a common Source for the Tamazert and Canary and Cape Verde Island carbonatites, *Petrology*, **51**(8). (Cited on page 62.)
- Brede, R., 1992. Structural aspects of Middle and the High Atlas (Morocco) - phenomena and causalities, *Geol. Rundsch.*, **81**, 171–184. (Cited on page 53.)
- Buontempo, L., Bokelmann, G. H. R., Barruol, G., & Morales, J., 2008. Seismic anisotropy beneath southern Iberia from SKS splitting, *Earth and Planetary Science Letters*, **273**, 237–250. (Cited on pages vii and 74.)

- Burton, R. K., McPherron, R. L., & Russell, C. T., 1975. An empirical relationship between interplanetary conditions and D_{st} , *Journal of Geophysical Research*, **80**, 4204–4214. (Cited on page [22](#).)
- Cagniard, L., 1953. Basic theory of the magnetotelluric method of geophysical prospecting, *Geophysics*, **18**, 605–645. (Cited on pages [8](#), [10](#), and [16](#).)
- Caldwell, T. G., Bibby, H. M., & Brown, C., 2004. The magnetotelluric phase tensor, *Geophysical Journal International*, **158**, 457–469. (Cited on pages [43](#), [46](#), [47](#), [48](#), [49](#), and [90](#).)
- Calvert, A., Sandvol, E., Seber, D., Barazangi, M., Roecker, S., Mourabit, T., Vidal, F., Alguacil, G., & Jabour, N., 2000. Geodynamic evolution of the lithosphere and upper mantle beneath the Alboran region of the western Mediterranean: Constraints from travel time tomography, *Journal of Geophysical Research*, **105**, 10,871 – 10,898. (Cited on pages [3](#) and [80](#).)
- Chave, A. D. & Jones, A. G., 2012a. *The magnetotelluric method: theory and practice*, Cambridge University Press, Cambridge, UK. (Cited on page [8](#).)
- Chave, A. D. & Jones, A. G., 2012b. Introduction to the magnetotelluric method, in *The magnetotelluric method: theory and practice*, chap. 1, pp. 16–32, Cambridge University Press, Cambridge, UK. (Cited on page [8](#).)
- Chave, A. D. & Smith, J. T., 1994. On electric and magnetic galvanic distortion tensor, *Journal of Geophysical Research*, **99**(B3), 4669–4682. (Cited on page [39](#).)
- Chave, A. D. & Thomson, D. J., 2004. Bounded influence magnetotelluric response function estimation, *Geophysical Journal International*, **157**, 988–1006. (Cited on pages [42](#) and [86](#).)
- Chave, A. D. & Weidelt, P., 2012. The theoretical basis for electromagnetic induction, in *The magnetotelluric method: theory, practice*, chap. 4, pp. 33–64, Cambridge University Press, Cambridge, UK. (Cited on page [35](#).)
- Constable, S., Shankland, T. J., & Duba, A., 1992. The electrical conductivity of an isotropic olivine mantle, *Journal of Geophysical Research*, **97**, 3397–3404. (Cited on page [157](#).)
- Constable, S. C., Parker, R. L., & Constable, C. G., 1987. Occam's inversion: A practical algorithm for generating smooth models from electromagnetic sounding data, *Geophysics*, **52**(3), 289–300. (Cited on page [50](#).)
- Şengör, A., Özeren, S., Genç, T., & Zor, E., 2003. East Anatolian High Plateau as a mantle-supported, north-south shortened domal structure, *Geophysical Research Letters*, **30**(24), 8045. (Cited on page [168](#).)
- Şengör, A. M. C. & Kidd, W. S. F., 1979. The post-collisional tectonics of the Turkish-Iranian Plateau and a comparison with Tibet, *Tectonophysics*, **55**, 361–376. (Cited on page [168](#).)

- Cumming, W. & Mackie, R., 2010. Resistivity imaging of geothermal resources using 1D, 2D and 3D MT inversion and TDEM static shift correction illustrated by a Glass Mountain case history, in *World geothermal congress*. (Cited on page [134](#).)
- de Lamotte, D. F., Bezar, S. B., Bracene, R., & Mercier, E., 2000. The two main steps of the Atlas building and geodynamics of the western Mediterranean, *Tectonics*, **19**(4), 740–761. (Cited on pages [4](#), [53](#), [56](#), [59](#), and [60](#).)
- de Lamotte, D. F., Leturmy, P., Missenard, Y., Khomsi, S., Ruiz, G., Saddiqi, O., Guillocheau, F., & Michard, A., 2009. Mesozoic and Cenozoic vertical movements in the Atlas system (Algeria, Morocco, Tunisia): An overview, *Tectonophysics*, **475**(1), 9–28. (Cited on pages [4](#), [5](#), [60](#), and [63](#).)
- de Lamotte, F., Zizi, M., Missenard, Y., Hafid, M., El Azzouzi, M., Maury, R. C., Charriere, A., Taki, Z., Benammi, M., & Michard, A., 2008. The Atlas System, in *Continental evolution: the geology of Morocco*, pp. 133–202. (Cited on pages [vi](#), [53](#), [56](#), [58](#), and [168](#).)
- Diaz, J. & Gallart, J., 2014. Seismic anisotropy from the Variscan core of Iberia to the Western African craton: new constraints on upper mantle flow at regional scales, *Earth and Planetary Science Letters*, **394**, 48–57. (Cited on page [73](#).)
- Diaz, J., Gallart, J., Villaseñor, A., Mancilla, F., Pazos, A., Córdoba, D., Pulgar, J. A., Ibarra, P., & Harnafi, M., 2010. Mantle dynamics beneath the Gibraltar Arc (western Mediterranean) from shear-wave splitting measurements on a dense seismic array, *Geophysical Research Letters*, **37**, 1–5. (Cited on pages [vii](#) and [74](#).)
- Dresnay, R. D., 1988. Recent data on the geology of the Middle-Atlas (Morocco), in *The Atlas system of Morocco*, pp. 293–320, ed. Jacobshagen, V., Springer-Verlag, Berlin. (Cited on page [58](#).)
- Duba, A. & Shankland, T. J., 1982. Free carbon and electrical conductivity in the Earth's mantle, *Geophysical Research Letters*, **9**, 1271–1274. (Cited on page [27](#).)
- Duggen, S., Hoernle, K. A., Hauff, F., Klügel, A., Bouabdellah, M., & Thirlwall, M. F., 2009. Flow of Canary mantle plume material through a subcontinental lithospheric corridor beneath Africa to the Mediterranean, *Geology*, **37**, 283–286. (Cited on pages [4](#), [62](#), [64](#), [67](#), [116](#), [168](#), and [169](#).)
- Egbert, G., 1997. Robust multiple-station magnetotelluric data processing, *Geophysical Journal International*, **130**, 475–496. (Cited on pages [42](#) and [89](#).)
- Egbert, G. D. & Booker, J. R., 1986. Robust estimation of geomagnetic transfer functions, *Geophysical Journal of the Royal Astronomical Society*, **87**(2), 173–194. (Cited on page [42](#).)
- Egbert, G. D. & Kelbert, A., 2012. Computational recipes for electromagnetic inverse problems, *Geophysical Journal International*, **189**, 251–267. (Cited on pages [7](#), [118](#), [120](#), [125](#), [134](#), [135](#), [136](#), [137](#), and [172](#).)

- El Azzouzi, M., Bernard-Griffiths, J., Bellon, H., Maury, C. R., Piqué, A., Fourcade, S., Cotten, J., & Hernandez, J., 1999. Evolution of the sources of Moroccan volcanism during the Neogene, *Comptes Rendus de l'Académie des Sciences*, **329**, 95–102. (Cited on pages [60](#) and [164](#).)
- El Azzouzi, M., Reneé, C. M., Bellon, H., Youbi, N., Cotten, J., & Kharbouch, F., 2010. Petrology and K-Ar chronology of the Neogene-Quaternary Middle Atlas basaltic province, Morocco, *Bulletin de la Société Géologique de France*, **181**, 243–257. (Cited on pages [xv](#), [60](#), [164](#), [165](#), and [168](#).)
- Ellero, A., Ottria, G., Malusa, M. G., & Ouanaïmi, H., 2012. Structural geological analysis of the High Atlas (Morocco): evidences of a transpressional fold-thrust belt, *Intech*, pp. 229–257. (Cited on page [59](#).)
- Ennih, N. & Lie, J.-p., 2001. The Moroccan Anti-Atlas: the west African craton passive margin with limited Pan-African activity . Implications for the northern limit of the craton, *Precambrian Research*, **112**, 289–302. (Cited on pages [vii](#), [59](#), [60](#), and [61](#).)
- Evans, R. L., 2012. Conductivity of Earth's material, in *The magnetotelluric method: theory and practice*, chap. 3, pp. 50–95, Cambridge University Press, Cambridge, UK. (Cited on pages [6](#), [27](#), [29](#), [31](#), and [160](#).)
- Evans, R. L., Sinha, M. C., Constable, S. C., & Unsworth, M. J., 1994. On the electrical nature of the axial melt zone on the East Pacific Rise near 13N, *Journal of Geophysical Research*, **99**, 577–589. (Cited on page [29](#).)
- Evans, R. L., Hirth, G., Baba, K., Forsyth, D., Chave, A., & Mackie, R., 2005. Geophysical controls from the MELT area compositional controls on oceanic plates, *Nature*, **437**, 249–952. (Cited on pages [37](#) and [100](#).)
- Faccenna, C., Piromallo, C., Crespo-Blanc, L., & Rossetti, F., 2004. Lateral slab deformation and the origin of the western Mediterranean arcs, *Tectonics*, **23**, TC1012. (Cited on page [2](#).)
- Farquharson, C., Oldenburg, D., Haber, E., & Shekhtman, R., 2002. An algorithm for the three-dimensional inversion of magnetotelluric data, in *SEG Technical Program Expanded Abstracts*. (Cited on pages [118](#) and [134](#).)
- Farquharson, C. G. & Craven, J. A., 2009. Three-dimensional inversion of magnetotelluric data for mineral exploration: An example from the McArthur River uranium deposit, Saskatchewan, *Journal of Applied Geophysics*, **68**, 450–458. (Cited on pages [125](#) and [134](#).)
- Fedan, B., 1988. Evolution géodynamique d'un bassin intraplaque sur dtcrochements: le Moyen Atlas (Maroc) durant le Meso-Cénozoïque, *Sérié Géologie et Géographic Physique*, **18**. (Cited on page [58](#).)

- Fischer, G. & Schnegg, P. A., 1993. The magnetotelluric dispersion-relations over 2-D structures, *Geophysical Journal International*, **115**(3), 1119–1123. (Cited on page [116](#).)
- Fischer, K. M., Ford, H. A., Abt, D. L., & Rychert, C. A., 2010. The lithosphere-asthenosphere boundary, *Annual Review of Earth and Planetary Sciences*, **38**(1), 551–575. (Cited on page [149](#).)
- Fullea, J., Afonso, J. C., Connolly, J. A. D., M, F., Garcia-Castellanos, D., & Zeyen, H., 2009. LitMod3D: an interactive 3D software to model the thermal, compositional, density, seismological and rheological structure of the lithosphere and sublithospheric upper mantle, *Geochemistry, Geophysics, Geochemistry*, **10**, Q08019. (Cited on page [173](#).)
- Fullea, J., Fernández, M., Afonso, J., Vergés, J., & Zeyen, H., 2010. The structure and evolution of the lithosphere-asthenosphere boundary beneath the Atlantic-Mediterranean transition region, *Lithos*, **120**(1-2), 74–95. (Cited on pages [viii](#), [xiii](#), [4](#), [5](#), [6](#), [60](#), [63](#), [73](#), [75](#), [76](#), [77](#), [78](#), [142](#), [144](#), [147](#), [157](#), [159](#), [160](#), [161](#), [166](#), [168](#), and [169](#).)
- Gaillard, F., Malki, M., Iacono-Marziano, G., Pichavant, M., & Scaillet, B., 2008. Carbonatite melts and electrical conductivity in the asthenosphere, *Science*, **28**, 1363–1365. (Cited on page [37](#).)
- Gamble, T. D., Goubau, W. M., & Clarke, J., 1979. Magnetotelluric with a remote magnetic reference, *Geophysics*, **44**, 53–68. (Cited on page [42](#).)
- Garcia, X. & Jones, A. G., 2002a. Atmospheric sources for audio-magnetotelluric (AMT) sounding, *Geophysics*, **67**, 448–458. (Cited on pages [16](#), [23](#), [24](#), and [43](#).)
- Garcia, X. & Jones, A. G., 2002b. Decomposition of three-dimensional magnetotelluric data, in *Three-dimensional electromagnetics*, chap. 13, pp. 235–250, Elsevier. (Cited on page [40](#).)
- Garcia, X., Chave, A. D., & Jones, A. G., 1997. Robust processing of magnetotelluric data from the auroral zone, *Journal of Geomagnetism and Geoelectricity*, **49**, 1451–1468. (Cited on page [25](#).)
- Giese, P. & Jacobshagen, V., 1992. Inversion tectonics of intracontinental ranges: High and Middle Atlas, Morocco, *Geol. Rundsch.*, **81**, 249–259. (Cited on page [59](#).)
- Glover, P. W. J., Hole, M. J., & Pous, J., 2000. A modified Archie's law for two conducting phases, *Earth and Planetary Science Letters*, **180**(3-4), 369–383. (Cited on page [29](#).)
- Goes, S., Spakman, W., & Bijwaard, H., 1999. A lower mantle source for central European volcanism, *Science*, **286**, 1928–1931. (Cited on page [4](#).)
- Gomez, F., Muawia, B., & Bensaid, M., 1996. Active tectonism in the intracontinental Middle Atlas Mountains of Morocco: synchronous crustal shortening and extension, *Journal of Geological Society, London*, **153**, 389–402. (Cited on pages [vii](#) and [58](#).)

- Gomez, F., Allmendinger, R., Barazangi, M., Er-Raji, A., & Dahmani, M., 1998. Crustal shortening and vertical strain partitioning in the Middle Atlas Mountains of Morocco, *Tectonics*, **17**(4), 520–533. (Cited on pages [4](#), [58](#), [60](#), and [148](#).)
- Gomez, F., Beauchamp, W., & Barazangi, M., 2000. Role of the Atlas Mountains (northwest Africa) within the African-Eurasian plate-boundary zone, *Geology*, **28**, 775–778. (Cited on pages [2](#) and [67](#).)
- Görler, K., Helmdach, F. F., Gaemers, P., Hessig, K., Hinsch, W., Mädler, K., Schwarzahns, W., & Zucht, M., 1988. The uplift of the Central High Atlas as deduced from Neogene continental sediments of the Quarzazate province, Morocco, *The Atlas System of Morocco Lect. Notes Earth Sci.*, pp. 361–414. (Cited on page [59](#).)
- Goubau, W. M., Gamble, T. D., & Clarke, J., 1978. Magnetotelluric data analysis: removal of bias, *Geophysics*, **43**, 379–388. (Cited on page [42](#).)
- Grant, F. S. & West, G. F., 1965. *Introduction to the electrical methods*, McGraw-Hill, New York, pp. 385–401. (Cited on page [30](#).)
- Groom, R. W., 1988. *The effects of inhomogeneities on magnetotellurics*, Dissertation, University Toronto, Canada. (Cited on pages [43](#) and [91](#).)
- Groom, R. W. & Bahr, K., 1992. Corrections for near surface effects: decomposition of the magnetotelluric impedance tensor and scaling corrections for regional resistivities: A tutorial, *Surveys in Geophysics*, **13**, 341–379. (Cited on page [40](#).)
- Groom, R. W. & Bailey, C. R., 1989. Decomposition of magnetotelluric impedance tensors in the presence of local three dimensional galvanic distortion, *Journal of Geophysical Research*, **94**, 1913–1925. (Cited on pages [43](#), [44](#), and [91](#).)
- Hafid, M., Zizi, M., Bally, A. W., & Ait, A., 2006. Structural styles of the western onshore and offshore termination of the High Atlas, Morocco, *Comptes Rendus Geoscience*, **338**, 50–64. (Cited on pages [vii](#), [54](#), [56](#), and [57](#).)
- Hampel, R., Ronchetti, M., Rousseeuw, P., & Stahel, W., 1986. *Robust statistics. The approach based on influence functions*, Wiley, New York. (Cited on page [43](#).)
- Harfi, A. E., Lang, J., Salomon, J., & Chellai, E. H., 2001. Cenozoic sedimentary dynamics of the Quarzazate foreland basin (Central High Atlas Mountains, Morocco), *International Journal of Earth Sciences*, **90**, 393–411. (Cited on page [59](#).)
- Harfi, A. E., Guiraud, M., & Lang, J., 2006. Deep-rooted "thick skinned" model for the High Atlas Mountains (Morocco). Implications for the structural inheritance of the southern Tethys passive margin, *Journal of Structural Geology*, pp. 1958 – 1976. (Cited on page [59](#).)

- Hashin, Z. & Shtrikman, S., 1962. A variational approach to the theory of the effective magnetic permeability of multiphase materials, *Journal of Applied Geophysics*, **33**, 3125–3131. (Cited on pages [27](#), [29](#), [30](#), [163](#), and [167](#).)
- Hatzfeld, D. & Frogneux, M., 1981. Intermediate depth seismicity in the western Mediterranean unrelated to subduction of oceanic lithosphere, *Nature*, **292**, 443–445. (Cited on page [75](#).)
- Hautot, S. & Tarits, P., 2009. A new coarse-to-fine 3-D magnetotelluric inversion method - application to field data for hydrocarbon exploration, in *Society of petroleum engineers - 71st European association of geoscientists and engineers conference and exhibition*. (Cited on page [134](#).)
- Heinson, G. S., Direen, N. G., & Gill, R. M., 2006. Magnetotelluric evidence for a deep-crustal mineralizing system beneath the Olympic Dam iron oxide copper-gold deposit, southern Australia, *Geology*, **34**(7), 573–576. (Cited on page [6](#).)
- Heise, W., Caldwell, T. G., Bibby, H. M., & Brown, C., 2006. Anisotropy and phase splits in magnetotellurics, *Physics of the Earth and Planetary Interiors*, **158**, 107–121. (Cited on pages [35](#) and [36](#).)
- Heise, W., Caldwell, T. G., Bibby, H. M., & Bannister, S. C., 2008. Three-dimensional modelling of magnetotelluric data from the Rotokawa geothermal field, Taupo Volcanic Zone, New Zealand, *Geophysical Journal International*, **173**, 740–750. (Cited on pages [46](#), [89](#), and [134](#).)
- Hill, G. J., Caldwell, T. G., Heise, W., Chertkoff, D. G., Bibby, H. M., Burgess, M. K., Cull, J. P., & Cas, R. A. F., 2009. Distribution of melt beneath Mount St Helens and Mount Adams inferred from magnetotelluric data, *Nature Geoscience*, **2**, 785–789. (Cited on pages [89](#) and [134](#).)
- Hoepffner, C., Soulaïmani, A., & Piqué, A., 2005. Moroccan Hercynides, *Journal of African Earth Science*, **43**, 144–165. (Cited on page [57](#).)
- Hoernle, K., Zhang, Y. S., & D, G., 1995. Seismic and geochemical evidence for large-scale mantle upwelling beneath the eastern Atlantic and western central Europe, *Nature*, **374**, 34–39. (Cited on pages [4](#) and [168](#).)
- Houari, M. R. & Hoepffner, C., 2003. Late Carboniferous dextral wrench-dominated transpression along the North African craton margin (Eastern High Atlas, Morocco), *Journal of African Earth Science*, **37**, 11–24. (Cited on page [57](#).)
- Huber, P., 1981. *Robust statistics*, Wiley, New York. (Cited on page [42](#).)
- Ingham, M. R., Bibby, H. M., Heise, W., Jones, K. A., Cairns, P., Dravitzki, S., Bennie, S. L., Caldwell, T. G., & Ogawa, Y., 2009. A magnetotelluric study of Mount Ruapehu volcano, New Zealand, *Geophysical Journal International*, **179**, 887–904. (Cited on page [134](#).)

- Jacobshagen, V., Gorler, K., & Giese, P., 1988. Geodynamic evolution of the Atlas system (Morocco) in post-palaeozoic times, in *The Atlas system of Morocco*, vol. 15, pp. 481–499. (Cited on pages [2](#), [53](#), and [59](#).)
- Jiracek, G. R., 1990. Near-surface and topographic distortions in electromagnetic inductions, *Surveys in Geophysics*, **11**, 163–203. (Cited on pages [37](#), [38](#), [39](#), and [40](#).)
- Jolivet, L. & Faccenna, C., 2000. Mediterranean extension and the Africa-Eurasia collision, *Tectonics*, **19**(6), 1095–1106. (Cited on page [2](#).)
- Jones, A. G., 1977. *Geomagnetic induction studies in southern Scotland*, Dissertation, University of Edinburgh. (Cited on page [41](#).)
- Jones, A. G., 1986. Parkinson's pointers' potential perfidy!, *Geophysical Journal of the Royal Astronomical Society*, **87**, 1215–1224. (Cited on page [15](#).)
- Jones, A. G., 1992. Electrical properties of the continental lower crust, in *Continental lower crust*, chap. 3, pp. 81–143, Elsevier, New York. (Cited on page [37](#).)
- Jones, A. G., 2012c. Distortion of magnetotelluric data: its identification and removal, in *The magnetotelluric method: theory, practice*, chap. 6, pp. 219–302, Cambridge University Press, Cambridge, UK. (Cited on pages [40](#), [44](#), and [90](#).)
- Jones, A. G. & Groom, R. W., 1993. Strike angle determination from the magnetotelluric tensor in the presence of noise and local distortion: rotate at your peril!, *Geophysical Journal International*, **113**, 524–534. (Cited on page [39](#).)
- Jones, A. G. & Jödicke, H., 1984. Magnetotelluric transfer function estimation improvement by a coherence-based rejection technique, in *Society of exploration geophysics annual general meeting*. (Cited on page [89](#).)
- Jones, A. G. & Price, A. T., 1970. The perturbations of alternating geomagnetic fields by conductivity anomalies, *Geophysical Journal of the Royal Astronomical Society*, **20**, 317–334. (Cited on page [15](#).)
- Jones, A. G. & Spratt, J., 2002. A simple method for deriving the uniform field MT responses in auroral zones, *Earth, Planets and Space*, **54**, 443–450. (Cited on pages [16](#) and [25](#).)
- Jones, A. G., Chave, A. D., Egbert, G., Auld, D., & Bahr, K., 1989. A comparison of techniques for magnetotelluric response function estimation, *Journal of Geophysical Research*, **94**(10), 14,201–14,213. (Cited on pages [40](#) and [86](#).)
- Jones, A. G., Katsube, J. T., & Schwann, P., 1997. The longest conductivity anomaly in the world explained: sulphides in fold hinges causing very high electrical anisotropy, *Journal of Geomagnetism and Geoelectricity*. (Cited on pages [6](#), [37](#), and [157](#).)

- Jones, A. G., Ledo, A. G., & Ferguson, I. J., 2005. Electromagnetic images of the Trans Hudson Orogen: the North American Central Plains anomaly revealed, *Canadian Journal of Earth Sciences*, **42**, 495–515. (Cited on page 37.)
- Jones, A. G., Evans, R. L., & Eaton, D. W., 2009. Velocity-conductivity relationships for mantle mineral assemblages in Archean cratonic lithosphere based on review of laboratory data and Hashin-Shtrikman extremal bounds, *Lithos*, **109**, 131–143. (Cited on pages 142 and 160.)
- Jones, A. G., Fullea, J., Evans, R. L., & Muller, M., 2012a. Water in cratonic lithosphere: calibrating laboratory-determined models of electrical conductivity of mantle minerals using geophysical and petrological observations, *Geochemistry, Geophysics, Geosystems*, **13**(6), Q06010. (Cited on pages 6, 114, 116, and 160.)
- Jones, A. G., Kiyani, D., Fullea, J., Ledo, J., Queralt, P., Marcuello, A., Siniscalchi, A., & Romano, G., 2012b. Comment on "Deep resistivity cross section of the intraplate Atlas Mountains (NW Africa): new evidence of anomalous mantle and related Quaternary volcanism" by Anahnah et al. (2011)., *Tectonics*, **31**. (Cited on pages 65 and 66.)
- Jones, G. A., 1983a. On the equivalence of the "Niblett and Bostick" transformations in the magnetotelluric method, *Journal of Geophysics*, **53**, 72–73. (Cited on page 152.)
- Jones, G. A., 1983b. The problem of current channelling: a critical review, *Geophysical Surveys*, **6**, 79–122. (Cited on pages 33 and 37.)
- Jones, G. A., 1999. Imaging the continental upper mantle using electromagnetic methods, *Lithos*, **48**, 57–80. (Cited on pages 81, 142, and 169.)
- Jones, K. A., Ingham, R. A., & Bibby, H. M., 2008. The hydrothermal vent system of Mount Ruapehu, New Zealand - a high frequency MT survey of the summit plateau, *Journal of Volcanology and Geothermal Research*, **176**, 591–600. (Cited on page 134.)
- Kaislaniemi, L. & van Hunen, J., 2014. Dynamics of lithospheric thinning and mantle melting by edge-driven convection: application to Moroccan Atlas mountains, *Geochemistry, Geophysics, Geosystems*, **15**, 3175–3189. (Cited on page 169.)
- Karato, S., 1990. The electrical conductivity of an isotropic olivine mantle, *Nature*, **347**, 272–273. (Cited on page 160.)
- Kaufman, A. A. & Keller, G. V., 1981. *The magnetotelluric sounding method*, Elsevier, Amsterdam. (Cited on page 8.)
- Kelbert, A., Egbert, G. D., & deGroot Hedlin, C., 2012. Crust and upper mantle electrical conductivity beneath the Yellowstone Hotspot Track, *Geology*, **40**, 447–450. (Cited on page 134.)

- Kelbert, A., Meqbel, N., Egbert, G. D., & Tandon, K., 2014. ModEM: A modular system for inversion of electromagnetic geophysical data, *Computers and Geosciences*, **66**(4), 40–53. (Cited on pages [7](#), [46](#), [134](#), [135](#), [136](#), [137](#), and [172](#).)
- Kellet, R. L., Mareschal, M., & Kurtz, R. D., 1992. A model of lower crustal electrical anisotropy for the pontiac subprovince of the Canadian Shield, *Geophysical Journal International*, **111**, 141–150. (Cited on page [37](#).)
- Khoza, D., Jones, A. G., Muller, M. R., Evans, R. L., Miensopust, M., & Webb, S. J., 2013a. Lithospheric structure of an Archean craton and adjacent mobile belt revealed from 2-D and 3-D inversion of magnetotelluric data: example from southern Congo craton in northern Namibia, *Journal of Geophysical Research*, **118**, 4378–4397. (Cited on page [134](#).)
- Khoza, D., Jones, A. G., Muller, M. R., Evans, R. L., Webb, S. J., Miensopust, M., & the SAMTEX team, 2013b. Tectonic model of the Limpopo belt: constraints from magnetotelluric data, *Precambrian Research*, **226**, 143–156. (Cited on pages [6](#), [119](#), and [157](#).)
- King, S. D. & Ritsema, J., 2000. African hot spot volcanism: small-scale convection in the upper mantle beneath cratons, *Science*, **290**, 1137–1140. (Cited on pages [4](#) and [169](#).)
- Kiyan, D., Jones, A. G., Fulla, J., Hogg, C., Ledo, J., & Sinischalchi, A., 2010. Crustal and lithospheric imaging of the Atlas Mountains of Morocco inferred from magnetotelluric data, in *AGU Fall Meeting*. (Cited on page [119](#).)
- Kiyan, D., Jones, A. G., Fulla, J., Ledo, J., Sinischalchi, A., & Romano, G., 2012. Crustal and uppermost mantle structures of Atlas Mountains of Morocco inferred from electromagnetic imaging, in *AGU Fall Meeting*. (Cited on page [172](#).)
- Kiyan, D., Jones, A. G., & Vozar, J., 2014. The inability of magnetotelluric off-diagonal impedance tensor elements to sense oblique conductors in 3-D inversion, *Geophysical Journal International*, **196**, 1351–1364. (Cited on pages [111](#) and [140](#).)
- Kurtz, R. D., Craven, J. A., Niblett, E. R., & Stevens, R. A., 1993. The conductivity of the crust and mantle beneath the Kapuskasing uplift: electrical anisotropy in the upper mantle, *Geophysical Journal International*, **113**, 483–498. (Cited on page [37](#).)
- Lapenta, G., 2011. Lecture notes on space weather. (Cited on pages [vi](#) and [17](#).)
- Le Pape, F., 2013. *Characterization of a crustal transition zone in the northern Tibet using magnetotelluric Modelling*, Dissertation, National University of Ireland, Galway. (Cited on page [81](#).)
- Le Pape, F., Jones, A. G., Vozar, J., & Wenbo, W., 2012. Penetration of crustal melt beyond the Kunlun Fault into Northern Tibet, *Nature Geoscience*, **5**, 330–335. (Cited on pages [5](#), [6](#), [28](#), [37](#), and [157](#).)

- Lebedev, E. B. & Khitarov, N. I., 1964. Dependence on the beginning of melting of granite and the electrical conductivity of its melt on high vapour pressure, *Geochemistry International*, pp. 193–197. (Cited on pages [160](#) and [163](#).)
- Ledo, J., 2005a. 2-D versus 3-D magnetotelluric data interpretation, *Surveys in Geophysics*, pp. 511–543. (Cited on page [89](#).)
- Ledo, J. & Jones, A. G., 2005b. Upper mantle temperature determined from combining mineral composition, electrical conductivity laboratory studies and magnetotelluric field observations: application to the Intermontane Belt, Northern Canadian Cordillera, *Earth and Planetary Science Letters*, **236**, 258–268. (Cited on page [157](#).)
- Ledo, J., Queralt, P., Marti, A., & Jones, A. G., 2002. Two-dimensional interpretation of three-dimensional magnetotelluric data: an example of limitations and resolution, *Geophysical Journal International*, pp. 127–139. (Cited on page [89](#).)
- Ledo, J., Jones, A. G., Siniscalchi, A., Campyà, J., Kiyani, D., Romano, G., & Rouai, M., 2011. Electrical signature of modern and ancient tectonic processes in the crust of the Atlas mountains of Morocco, *Physics of the Earth and Planetary Interiors*, **185**, 82–88. (Cited on pages [xi](#), [xii](#), [xiii](#), [7](#), [90](#), [94](#), [111](#), [114](#), [116](#), [140](#), [141](#), [144](#), [156](#), [158](#), [160](#), and [171](#).)
- Lezaeta, P., Chave, A D, Jones, A. G., & Evans, R., 2007. Source field effects in the auroral zone: evidence from the Slave craton (NW Canada), *Physics of Earth and Planetary Sciences*, **164**, 323–329. (Cited on page [25](#).)
- Li, S., Unsworth, M. J., Booker, J. R., Wei, W., Handong, T., & Jones, A. G., 2003. Partial melt or aqueous fluid in the mid-crust of Southern Tibet? Constraints from INDEPTH magnetotelluric data, *Geophysical Journal International*, pp. 289–304. (Cited on pages [6](#), [157](#), and [163](#).)
- Long, M. D. & Becker, T. W., 2010. Mantle dynamics and seismic anisotropy, *Earth and Planetary Science Letters*, **297**, 341–354. (Cited on page [73](#).)
- Lustrino, M. & Wilson, M., 2007. The circum-Mediterranean anorogenic Cenozoic igneous province, *Earth-Science Reviews*, **81**, 1–65. (Cited on page [67](#).)
- Lviv Centre of Institute for Space Research, 2009. Long-period magnetotelluric instrument LEMI-417M: User Manual, Tech. rep., 5-A Naukova St., Lviv, 79000, Ukraine. (Cited on page [5](#).)
- Mackie, R. L., 2002. *User manual and software documentation for two dimensional inversion of magnetotelluric data. Anisotropy version 6.7*, GSY-USA, Inc., San Francisco, CA, USA. (Cited on pages [50](#), [52](#), [100](#), [102](#), and [104](#).)
- Mackie, R. L., Bennett, B. R., & Madden, T. R., 1988. Long-period magnetotelluric measurements near the central California coast: a land-locked view of the conductivity structure under the Pacific Ocean, *Geophysical Journal*, **95**, 181–194. (Cited on pages [51](#) and [137](#).)

- Mackie, R. L., Madden, T. R., & Wannamaker, P. E., 1993. Three-dimensional magnetotelluric modelling using difference equations-theory and comparison to the integral equations, *Geophysics*, **58**(2), 215–226. (Cited on page [140](#).)
- Mackie, R. L., Smith, J. T., & Madden, T. R., 1994. Three-dimensional electromagnetic modeling using finite difference equations: the magnetotelluric example, *Radio Science*, **29**(4), 923–935. (Cited on pages [120](#), [134](#), and [149](#).)
- Madden, T. R. & Nelson, P., 1964. A defense of Cagniard's magnetotelluric method, *Geophys. Lab. ONR proj. NR-371-401, MIT, Cambridge, Massachusetts*. (Cited on page [8](#).)
- Mareschal, A. G., Evans, R. L., & Eaton, D. W., 2000. Pressure effect on electrical conductivity of mantle olivine, *Physics of the Earth and Planetary Interiors*, **118**, 149–161. (Cited on page [157](#).)
- Mareschal, M., 1986. Modelling of natural sources of magnetospheric substorms, *Surveys in Geophysics*, **8**, 261–300. (Cited on page [16](#).)
- Mareschal, M., Fyfe, W. S., Percival, J., & T, C., 1992. Grain-boundary graphite in Kapuskasing gneisses and implications for lower-crustal conductivity, *Nature*, **357**, 674–676. (Cited on pages [6](#) and [157](#).)
- Mareschal, M., Kurtz, R. D., & Bailey, R. C., 1994. A review of electromagnetic investigations in the Kapuskasing uplift and surrounding regions: electrical properties of key rocks, *Canadian Journal of Earth Sciences*, **31**, 1042–1051. (Cited on page [37](#).)
- Mareschal, M., Kellet, R. L., Kurtz, R. D., Ludden, J. N., Ji, S., & Bailey, R. C., 1995. Archean cratonic roots, mantle shear zones and deep electrical anisotropy, *Nature*, **375**, 134–137. (Cited on page [37](#).)
- Marquis, G., Jones, A. G., & Hyndman, R. D., 1995. Coincident conductive and reflective middle and lower crust in southern British Columbia, *Geophysical Journal International*, **120**, 111–131. (Cited on page [118](#).)
- Marti, A., Pilar, Q., Jones, A. G., & Ledo, J., 2005. Research note: improving Bahr's invariant parameters using the WAL approach, *Geophysical Journal International*, **163**(2), 38–41. (Cited on page [43](#).)
- Martin, J., 1981. Le Moyen-Atlas central. Etude geomorphologique. Notes et Memoirs du Service Geologique du Maroc, Tech. rep. (Cited on page [58](#).)
- McNeice, W. G. & Jones, G. A., 2001. Multisite, multifrequency tensor decomposition of magnetotelluric data, *Geophysics*, **66**(1), 158–173. (Cited on pages [44](#), [91](#), [102](#), and [107](#).)
- McPherron, R. L., 1970. Growth phase of magnetospheric substorms, *Journal of Geophysical Research*, **75**, 5592. (Cited on page [22](#).)

- McPherron, R. L., 1979. Magnetospheric substorms, *Review of Geophysics and Space Physics*, **17**(4), 675–681. (Cited on page 22.)
- McPherron, R. L., 2005. Magnetic pulsations: their sources and relation to solar wind and geomagnetic activity, *Surveys in Geophysics*, **26**, 545–592. (Cited on pages 17 and 22.)
- Meqbel, M. N., 2009. *The electrical conductivity structure of the Dead Sea Basin derived from 2D and 3D inversion of magnetotelluric data*, Ph.D. thesis. (Cited on page 137.)
- Michard, A., Hoepffner, C., Soulimani, A., & Baidder, L., 2008. The Variscan Belt, in *Continental evolution: the geology of Morocco*, pp. 65–132, Springer-Verlag Berlin Heidelberg. (Cited on pages 57 and 60.)
- Miensopust, M. P., 2010. *Multi dimensional magnetotellurics: a 2D case study and a 3D approach to simultaneously invert for resistivity structure and distortion parameters*, Dissertation, National University of Ireland, Galway. (Cited on page 140.)
- Miensopust, M. P., Jones, a. G., Muller, M. R., Garcia, X., & Evans, R. L., 2011. Lithospheric structures and Precambrian terrane boundaries in northeastern Botswana revealed through magnetotelluric profiling as part of the Southern African Magnetotelluric Experiment, *Journal of Geophysical Research*, **116**(B2), 1–21. (Cited on pages 46, 91, and 119.)
- Miller, M. S. & Becker, T. W., 2014. Reactivated lithospheric-scale discontinuities localize dynamic uplift of the Moroccan Atlas Mountains, *Geology*, **42**(1), 35–38. (Cited on pages x, xiii, 114, 115, 142, 148, 157, 159, and 169.)
- Miller, M. S., Allam, A. A., Becker, T. W., Di Leo, J. F., & Wookey, J., 2013. Constraints on the tectonic evolution of the westernmost Mediterranean and northwestern Africa from shear wave splitting analysis, *Earth and Planetary Science Letters*, pp. 1–10. (Cited on pages vii, 70, 73, and 74.)
- Missenard, Y. & Cadoux, A., 2012. Can Moroccan Atlas lithospheric thinning and volcanism be induced by Edge-Driven Convection?, *Terra Nova*, pp. 27–33. (Cited on pages 4, 63, 82, and 169.)
- Missenard, Y., Zeyen, H., Lamotte, D. F. D., Leturmy, P., Petit, C., Se, M., & Saddiqi, O., 2006. Crustal versus asthenospheric origin of relief of the Atlas Mountains of Morocco, *Journal of Geophysical Research*, **111**, 1–13. (Cited on pages viii, 4, 5, 53, 60, 63, 67, 70, 73, 75, 76, 78, and 168.)
- Missenard, Y., Taki, Z., de Lamotte, D. F., Benammi, M., Hafid, M., Leturmy, P., & Sebrier, M., 2007. Tectonic styles in the Marrakesh High Atlas (Morocco): the role of heritage and mechanical stratigraphy, *Journal of African Earth Sciences*, **48**, 247–266. (Cited on pages 56 and 59.)

- Mottaghy, D. & Rath, V., 2006. Latent heat effects in subsurface heat transport modelling and their impact on palaeotemperature reconstructions, *Geophysical Journal International*, **164**, 236–245. (Cited on pages [160](#) and [162](#).)
- Munoz, G., Mateus, A., Pous, J., Santos, M. F., & Almeida, E., 2008. Unraveling middle-crust conductive layers in Paleozoic Orogens through 3D modeling of magnetotelluric data: the Ossa-Morena zone case study (SW Iberian Variscides, *Journal of Geophysical Research*, **B6**. (Cited on pages [137](#) and [138](#).)
- Murphy, B. J., 2006. Arc magmatism I: relationship between subduction and magma genesis, *Journal of the Geological Association of Canada*, **33**. (Cited on page [166](#).)
- Mustaphi, H., Medina, F., Jabour, H., & C, H., 1997. Le bassin du Souss (Zone de faille du Tizi n'Test, Haut Atlas occidental, Maroc): resultat d'une inversion tectonique controlee par une faille de d'etachement profonde, *Journal of African Earth Sciences*, **24**, 153–168. (Cited on page [57](#).)
- Natali, C., Beccaluva, L., Bianchini, G., Ellam, R. M., Siena, F., & Stuart, F. M., 2013. Carbonated alkali-silicate metasomatism in the North Africa lithosphere: evidence from Middle Atlas spinel-lherzolites, Morocco, *Journal of South American Earth Sciences*, **41**, 113–121. (Cited on page [168](#).)
- Nelson, K. D., Zhao, W., Brown, L. D., Kuo, J., Che, J., Liu, X., Klemperer, S. L., Makovsky, Y., Meissner, R., Mechie, J., Kind, R., Wenzel, F., Ni, J., Nabelek, J., Leshou, C., Tan, H., Wei, W., Jones, A. G., Booker, J., Unsworth, M., Kidd, W. S. F., Hauck, M., Alsdorf, D., Ross, A., Cogan, M., Wu, C., Sandvol, E., & Edwards, E., 1996. Partially molten middle crust beneath southern Tibet: an initial synthesis of Project INDEPTH results, *Science*, **274**, 1684–1688. (Cited on page [81](#).)
- Neves, A. S. D., 1957. *The generalized magnetotelluric method*, Dissertation, Massachusetts Institute of Technology. (Cited on page [8](#).)
- Newman, G. a. & Alumbaugh, D. L., 2000. Three-dimensional magnetotelluric inversion using non-linear conjugate gradients, *Geophysical Journal International*, **140**(2), 410–424. (Cited on page [134](#).)
- Newman, G. A., Recher, S., Tezkan, B., & Neubauer, F. M., 2003. Case history 3D inversion of a scalar radio magnetotelluric field data set, *Geophysics*, **68**, 791–802. (Cited on page [134](#).)
- Newman, G. A., Gasperikova, E., Hoversten, G. M., & Wannamaker, P. E., 2008. Three-dimensional magnetotelluric characterization of the Coso geothermal field, *Geothermics*, **37**, 369–399. (Cited on pages [125](#) and [134](#).)

- Nover, G., 2005. Electrical Properties of crustal and mantle rocks: a review of laboratory measurements and their explanation, *Surveys in Geophysics*, **26**, 593–651. (Cited on pages 27, 28, and 160.)
- Osipova, I. L., Hjelt, S. E., & Vanyan, L. L., 1989. Source field problems in northern parts of the Baltic Shield, *Physics of the Earth and Planetary Interiors*, **53**, 337–342. (Cited on page 16.)
- Ouanaimi, H. & Petit, J. P., 1992. The southern limit of the Hercynian belt in the High Atlas (Morocco): reconstitution of an undeformed projecting block, *Bulletin de la Société Géologique de France*, **163**, 63–72. (Cited on page 57.)
- Padilha, A. L., 1999. Behaviour of magnetotelluric source fields within the equatorial zone, *Earth Planet Space*, **51**, 1119–1125. (Cited on pages 16 and 25.)
- Padilha, A. L., Vitorello, I., & Rijo, L., 1997. Effects of the equatorial electrojet on magnetotelluric surveys: field results from Northwest Brazil, *Geophysical Research Letters*, **24**, 89–92. (Cited on pages 16, 24, and 25.)
- Palomeras, I., Thurner, S., Levander, A., Liu, K., Villasenor, A., Carbonell, R., & Harnafi, M., 2014. Finite-frequency Rayleigh wave tomography of the western Mediterranean: mapping its lithospheric structure, *Geochemistry, Geophysics, Geosystems*, **15**, 140–160. (Cited on pages vii, xiii, 6, 66, 67, 68, 69, 71, 81, 114, 157, 159, 160, and 173.)
- Park, K., Hirasuna, B., Jiracek, G. R., & Kinn, C., 1996. Magnetotelluric evidence of lithospheric mantle thinning beneath the southern Sierra Nevada, *Journal of Geophysical Research*, **101**(B7), 16,241–16,255. (Cited on page 28.)
- Park, S. K., 1985. Distortion of magnetotelluric sounding curves by three-dimensional structures, *Geophysics*, **50**, 785–797. (Cited on page 37.)
- Parker, R. L., 1980. The inverse problem of electromagnetic induction: existence and construction of solutions based on incomplete data, *Journal of Geophysical Research*, **85**, 4421–4425. (Cited on page 49.)
- Parker, R. L., 2010. Can a 2-D MT frequency response always be interpreted as a 1-D response?, *Geophysical Journal International*, **181**(1), 269–274. (Cited on page 116.)
- Parker, R. L. & Booker, J. R., 1996. Optimal one-dimensional inversion and bounding of magnetotelluric apparent resistivity and phase measurements, *Physics of the Earth and Planetary Interiors*, **98**, 269–282. (Cited on pages 49, 114, and 116.)
- Parker, R. L. & Whaler, K. A., 1981. Numerical methods for establishing solutions to the inverse problem of electromagnetic induction, *Journal of Geophysical Research*, **86**, 9574–9584. (Cited on page 49.)

- Parkinson, D. W. & Jones, W. F., 1979. The geomagnetic coast effect, *Reviews of Geophysics and Space Physics*, **17**, 1999 – 2015. (Cited on page [137](#).)
- Parkinson, W., 1983. *Introduction to geomagnetism*, Elsevier. (Cited on pages [vi](#) and [21](#).)
- Parkinson, W. D., 1959. Directions of rapid geomagnetic fluctuations, *Geophysical Journal of the Royal Astronomical Society*, **2**, 1–14. (Cited on page [15](#).)
- Parkinson, W. D., 1962. The influence of continents and oceans on geomagnetic variations, *Geophysical Journal of the Royal Astronomical Society*, **6**, 441–449. (Cited on page [15](#).)
- Partzsch, G. M., Schilling, F. R., & Arndt, J., 2000. The influence of partial melting on the electrical behaviour of crustal rocks: laboratory examinations, model calculations and geological interpretations, *Tectonophysics*, **317**(3-4), 189–203. (Cited on pages [xv](#), [28](#), [29](#), [30](#), [31](#), [161](#), and [167](#).)
- Patro, P. K. & Egbert, G. D., 2011. Application of 3D inversion to magnetotelluric profile data from the Deccan Volcanic Province of Western India, *Physics of the Earth and Planetary Interiors*, **187**(1-2), 33–46. (Cited on pages [119](#) and [134](#).)
- Patro, P. K., Uyeshima, M., & Siripunvaraporn, W., 2012. Three-dimensional inversion of magnetotelluric phase tensor data, *Geophysical Journal International*, **192**, 58–66. (Cited on page [46](#).)
- Pek, J. & Santos, F. A. M., 2002. Magnetotelluric impedances and parametric sensitivities for 1-D anisotropic layered media, *Computers and Geosciences*, **28**, 939–950. (Cited on pages [35](#) and [36](#).)
- Pek, J. & Verner, T., 1997. Finite-difference modelling of magnetotelluric fields in two-dimensional anisotropic media, *Geophysical Journal International*, **128**, 505–521. (Cited on page [35](#).)
- Pirjola, R., 1992. On magnetotelluric source effects caused by an auroral electrojet system, *Radio Science*, **27**, 463–468. (Cited on page [16](#).)
- Piomallo, C., Gasperini, D., Macera, P., & Facenna, C., 2008. A late Cretaceous contamination episode of the European-Mediterranean mantle, *Earth and Planetary Science Letters*, **268**, 15–27. (Cited on page [168](#).)
- Poe, B. T., Romano, C., Nestola, F., & Smyth, J. R., 2010. Electrical conductivity anisotropy of dry and hydrous olivine at 8 GPa, *Physics of the Earth and Planetary Interiors*, **181**, 103–111. (Cited on page [37](#).)
- Pommier, A. & Le-Trong, E., 2011. "SIGMELTS": A web portal for electrical conductivity calculations in geosciences, *Computer and Geosciences*, **37**, 1450–1459. (Cited on page [164](#).)

- Pommier, A., Gaillard, F., Pichavant, M., & Scaillet, B., 2008. Laboratory measurements of electrical conductivities of hydrous and dry Mount Vesuvius melts under pressure, *Journal of Geophysical Research*, **113**, B0205. (Cited on page 28.)
- Price, A. T., 1962. The theory of magnetotelluric methods when the source field is considered, *Journal of Geophysical Research*, **67**(5), 1907–1918. (Cited on pages 8 and 10.)
- Proust, F., P, P. J., & Tapponnier, P., 1977. L'accident de Tizi n'Test et le rôle des décrochements dans la tectonique du Haut Atlas occidental (Maroc), *Bulletin de la Société Géologique de France*, **7**, 541–551. (Cited on page 57.)
- Raffone, N., Chazot, G., Pin, C., Vannucci, R., Zanetti, A., Di, D., & Della, S., 2009. Metasomatism in the lithospheric mantle beneath Middle Atlas (Morocco) and the origin of Fe- and Mg-rich wehrlites, *Journal of Petrology*, **50**(2), 197–249. (Cited on pages 164 and 168.)
- Ramdani, F., 1998. Geodynamic implications of intermediate-depth earthquakes and volcanism in the intraplate Atlas mountains (Morocco), *Physics of the Earth and Planetary Interiors*, **108**, 245–260. (Cited on pages 4, 62, 67, 75, and 168.)
- Rangarajan, G. K., 1989. Indices of geomagnetic activity, in *Geomagnetism*, vol. 3, pp. 323–384, Academic Press, London. (Cited on page 22.)
- Rastogi, R. G., 1992. Critical problems of equatorial electrojet, *Advances in Space Research*, **28**, 13–21. (Cited on page 20.)
- Rastogi, R. G. & Iyer, K. N., 1976. Quiet day variation of geomagnetic h-field at low latitudes, *Journal of Geomagnetism and Geoelectricity*, **28**, 461–479. (Cited on page 20.)
- Rath, V. & Mottaghy, D., 2007. Smooth inversion for ground surface temperature histories: estimating the optimum regularization parameter by generalized cross-validation, *Geophysical Journal International*, **171**(3), 1440–1448. (Cited on pages 160 and 162.)
- Rimi, A., 1999. Mantle heat flow and geotherms for the main geologic domains in Morocco, *International Journal Earth Sciences*, **88**, 458–466. (Cited on pages vii, 73, 75, 160, and 162.)
- Ritter, O., Weckmann, U., Vietor, T., & V, H., 2003. A magnetotelluric study of the Damara Belt in Namibia - 1. regional scale conductivity anomalies, *Physics of the Earth and Planetary Interiors*, **138**, 71–90. (Cited on pages 6, 104, and 157.)
- Robert-Charue, C., 2006. *Géologie structurale de l'Anti-Atlas oriental*, Ph.D. thesis. (Cited on pages 90, 107, and 156.)
- Roberts, J. J. & Tyburczy, J. A., 1999. Partial melt electrical conductivity: influence of melt composition, *Journal of Geophysical Research*, **104**, 7055–7065. (Cited on pages 28, 160, 163, and 167.)

- Rodi, W. & Mackie, R. L., 2001. Nonlinear conjugate gradients algorithm for 2-D magnetotelluric inversion, *Geophysics*, **66**(1), 174–187. (Cited on pages [xii](#), [50](#), [51](#), [52](#), [100](#), [101](#), [104](#), [154](#), and [202](#).)
- Rosenbaum, G., Lister, G. S., & Duboz, C., 2002. Reconstruction of the tectonic evolution of the western Mediterranean since the Oligocene, *Journal of the Virtual Explorer*, **8**, 107–130. (Cited on pages [2](#) and [168](#).)
- Rosenberg, C. L. & Handy, M. R., 2005. Experimental deformation of partially melted granite revisited: implications for the continental crust, *Journal of Metamorphic Geology*, **23**, 19–28. (Cited on page [164](#).)
- Sandvol, E., Seber, D., & Barazangi, M., 1998. Grid search modeling of receiver functions: implications for crustal structure in the Middle East and North Africa, *Journal of Geophysical Research*, **103**, 26,899–26,917. (Cited on page [70](#).)
- Sandwell, D. T. & Smith, W. H. F., 1997. Global sea floor topography from satellite altimetry and ship depth soundings., *Science*, **227**, 1957–1962. (Cited on page [82](#).)
- Santos, F. A. M., Nolasco, M., & Pous, J., 2001. Coast effects on magnetic and magnetotelluric transfer functions and their correction: application to MT soundings carried out in SW Iberia, *Earth and Planetary Science Letters*, **186**, 283–295. (Cited on page [137](#).)
- Sasaki, Y., 2001. Full 3-D inversion of electromagnetic data on PC, *Journal of Applied Geophysics*, **46**(1), 45–54. (Cited on page [134](#).)
- Sasaki, Y. & Meju, M. A., 2006. Three-dimensional joint inversion for magnetotelluric resistivity and static shift distributions in complex media, *Journal of Geophysical Research*, **111**(B5), B05101. (Cited on page [125](#).)
- Schaer, J. P., 1987. Evolution and structure of the high atlas of morocco, in *The anatomy of mountain ranges*, pp. 107–127, Princeton University Press, Princeton, N J. (Cited on page [2](#).)
- Schilling, F. R., Partzsch, G. M., Brasse, H., & Schwarz, G., 1997. Partial melting below the magmatic arc in the central Andes deduced from geoelectromagnetic field experiments, *Annals of Geophysics*, **103**, 17–31. (Cited on pages [28](#) and [78](#).)
- Schmeling, H., 1986. Numerical models on the influence of partial melt on elastic, anelastic and electrical properties of rocks, Part II: electrical conductivity, *Physics of the Earth and Planetary Interiors*, **43**, 123–136. (Cited on pages [30](#), [163](#), and [167](#).)
- Schmucker, U., 1973. Regional induction studies: a review of methods and results, *Physics of the Earth and Planetary Interiors*, pp. 365–378. (Cited on page [13](#).)

- Schmucker, U., 1985. Geophysics of the solid Earth, the Moon and the Planets, in *Numerical Data and Functional Relationships in Science and Technology*, vol. 2, pp. 31–73, Springer-Verlag, Berlin-Heidelberg. (Cited on pages [vi](#), [xv](#), [17](#), [20](#), [21](#), [23](#), and [24](#).)
- Schwarz, G. & Wigger, J. P., 1988. *Geophysical studies of the Earth's crust and upper mantle in the Atlas system of Morocco*, pp. 339–357. (Cited on pages [75](#), [111](#), [114](#), [156](#), and [172](#).)
- Schwarz, G., Mehl, H. G., Ramdani, F., & Rath, V., 1992. Electrical resistivity structure of the eastern Moroccan Atlas System and its tectonic implications, *Gelogische Rundschau*, pp. 221–235. (Cited on pages [vii](#), [x](#), [5](#), [7](#), [62](#), [65](#), [90](#), [111](#), [114](#), [115](#), and [172](#).)
- Seber, D., Barazangi, M., Tadili, B. A., Ramdani, M., Ibenbrahim, A., & Sari, D. B., 1996. Three-dimensional upper mantle structure beneath the intraplate Atlas and interplate Rif mountains of Morocco, *Journal of Geophysical Research*, **101**, 3125–3138. (Cited on pages [4](#) and [67](#).)
- Sebrier, M., Siame, L., Zoine, E. M., Winter, T., Missenard, Y., & Leturmy, P., 2006. Active tectonics in the Moroccan High Atlas, *Comptes Rendus Geoscience*, **338**, 65–79. (Cited on page [56](#).)
- Shankland, T. J. & Waff, H. S., 1977. Partial melting and electrical conductivity anomalies in the upper mantle, *Journal of Geophysical Research*, **82**, 5409–5417. (Cited on page [28](#).)
- Siegel, A., 1982. Robust regression using repeated medians, *Biometrika*, **69**, 801–809. (Cited on page [43](#).)
- Simpson, F., 2002. Intensity and direction of lattice-preferred orientation of olivine: are electrical and seismic anisotropies of the Austrian mantle reconcilable?, *Earth Planetary Science Letters*, **203**, 535–547. (Cited on page [37](#).)
- Simpson, F. & Bahr, K., 2005. *Practical magnetotellurics*, Cambridge University Press. (Cited on pages [vi](#), [8](#), [10](#), [15](#), [29](#), [33](#), [41](#), and [45](#).)
- Siniscalchi, A., Kiyani, D., Romano, G., Ledo, J., Jones, A. G., & the TopoMed MT Team, 2014. Electrical signature of the Marrakech High Atlas inferred by 3D MT modelling, in *22nd EM Workshop Weimar*. (Cited on page [150](#).)
- Siripunvaraporn, W. & Egbert, G., 2000. An efficient data-subspace inversion method for 2D magnetotelluric data, *Geophysics*, **65**, 791–803. (Cited on pages [50](#) and [135](#).)
- Siripunvaraporn, W., Egbert, G., Lenbury, Y., & Uyeshima, M., 2005a. Three-dimensional magnetotelluric inversion: data-space method, *Physics of the Earth and Planetary Interiors*, **150**(1-3), 3–14. (Cited on pages [46](#), [111](#), [118](#), [119](#), [122](#), and [134](#).)
- Siripunvaraporn, W., Egbert, G., & Uyeshima, M., 2005b. Interpretation of two-dimensional magnetotelluric profile data with three-dimensional inversion: synthetic examples, *Geophysical Journal International*, **160**, 804–814. (Cited on page [119](#).)

- Sizova, S., 2002. The field-aligned currents effects on the equatorial geomagnetic field variations, *Advances in Space Research*, **30**, 2247–2252. (Cited on page 20.)
- Smirnov, M. Y., 2003. Magnetotelluric data processing with a robust statistical procedure having a high breakdown point, *Geophysical Journal International*, **152**(1), 1–7. (Cited on pages 42, 43, and 86.)
- Smith, J. T., 1997. Estimating galvanic-distortion magnetic fields in magnetotellurics, *Geophysical Journal International*, **130**, 65–72. (Cited on pages 38 and 39.)
- Smith, J. T. & Booker, J. R., 1991. Rapid inversion of two- and three-dimensional magnetotelluric data, *Journal of Geophysical Research*, **96**(B3), 3905. (Cited on page 134.)
- Smith, W. H. F. & Sandwell, D. T., 1997. Bathymetry prediction from dense satellite altimetry and sparse shipborne bathymetry., *Journal of Geophysical Research*, **99**, 21803–21824. (Cited on page 82.)
- Solon, K., Jones, A. G., Nelson, K. D., Unsworth, M. J., & the INDEPTH MT team, 2005. Geophysical transect across a Paleoproterozoic continent-continent collision zone: the Trans-Hudson Orogen, *Journal of Geophysical Research*, **110**, B10102. (Cited on page 5.)
- Spichak, V. V., Borisova, V. P., Fainberg, E. B., Khalezov, A. A., & Goidina, A. G., 2007. Electro-magnetic 3D tomography of the Elbrus volcanic center according to magnetotelluric and satellite data, *Journal of Volcanology and Seismology*, **1**, 53–66. (Cited on page 134.)
- Spieker, K., Wölbern, I., Thomas, C., Harnafi, M., & El Moudnib, L., 2014. Crustal and upper-mantle structure beneath the western Atlas Mountains in SW Morocco derived from receiver functions, *Geophysical Journal International*, **198**, 1474–1485. (Cited on page 70.)
- Spratt, J., Jones, A. G., Nelson, K. D., Unsworth, M. J., & the INDEPTH MT team, 2005. Crustal structure of the India-Asia collision zone, southern Tibet, from INDEPTH MT investigations, *Physics of the Earth and Planetary Interiors*, **150**, 227–237. (Cited on pages 5 and 49.)
- Srivastava, S. P., 1965. Method of interpretation of magnetotelluric data when the source field is considered, *Journal of Geophysical Research*, **70**, 945–954. (Cited on page 8.)
- Stampfli, G. M. & Borel, G. D., 2002. A plate tectonic model for the Paleozoic and Mesozoic constrained by dynamic plate boundaries and restored synthetic oceanic isochrons, *Earth and Planetary Science Letters*, **196**, 17–33. (Cited on pages vi and 55.)
- Sugiura, M., 1964. Hourly values of equatorial D_{st} for the IGY, *Annals of the International Geophysical Year*, **35**, 945–948. (Cited on page 22.)
- Sugiura, M., 1991. On D_{st} index, *IAGA Bulletins*, (40). (Cited on page 22.)

- Swift, C. M., 1967. *A magnetotelluric investigation of an electrical conductivity anomaly in the southwestern United States*, Dissertation, Massachusetts Institute of Technology. (Cited on pages [8](#) and [43](#).)
- Tadili, B., Ramdani, M., Bensari, D., Chapochnikov, K., & Bellot, A., 1986. Structure de la croûte dans le Nord du Maroc., *Annales Geophysicae*, **4**(1), 99–104. (Cited on page [66](#).)
- Tanskanen, E., 2002. Terrestrial substorms as a part of global energy flow, in *Finnish Meteorological Institute Contributions*. (Cited on page [22](#).)
- Tarantola, A., 2006. Popper, Bayes and the inverse problem, *Nature Physics*, **2**, 492–494. (Cited on page [50](#).)
- Teixell, A., Arboleya, M.-I., Julivert, M., & Charroud, M., 2003. Tectonic shortening and topography in the central High Atlas, *Tectonics*, **22**(5). (Cited on pages [4](#), [59](#), [60](#), [83](#), [117](#), [142](#), and [147](#).)
- Teixell, A., Ayarza, P., Zeyen, H., & Ferna, M., 2005. Effects of mantle upwelling in a compressional setting: the Atlas Mountains of Morocco, *Terra Nova*, **17**, 456–461. (Cited on pages [4](#), [5](#), [6](#), [60](#), [70](#), [73](#), [75](#), [76](#), [83](#), [160](#), and [168](#).)
- Telford, W. M., Geldart, L. P., & Sheriff, R. E., 1990. *Applied Geophysics*, Cambridge University Press. (Cited on page [26](#).)
- ten Grotenhuis, S. M., Drury, M. R., Spiers, C. J., & Peach, C. J., 2005. Melt distribution in olivine rocks based on electrical conductivity measurements, *Journal of Geophysical Research: Solid Earth*, **110**, B12201. (Cited on pages [xv](#), [29](#), [30](#), [163](#), [164](#), and [167](#).)
- Thompson, A. B., 1992. Metamorphism and fluids, in *Understanding the Earth*, chap. 12, pp. 244–247, Cambridge University Press, Cambridge, UK. (Cited on page [160](#).)
- Tietze, K., 2012. *Investigating the electrical conductivity structure of the San Andreas fault system in the Parkfield-Cholame region, central California, with 3D magnetotelluric inversion*, Dissertation, Freie Universität Berlin. (Cited on pages [46](#), [135](#), and [137](#).)
- Tietze, K. & Ritter, O., 2013. Three-dimensional magnetotelluric inversion in practice—the electrical conductivity structure of the San Andreas Fault in Central California, *Geophysical Journal International*, **195**, 130–147. (Cited on pages [119](#) and [134](#).)
- Tikhonov, A. N., 1950. On determining electric characteristics of the deep layers of the earth's crust, *Dolk. Acad. Nauk, SSR*, **73**, 295–297. (Cited on pages [8](#) and [16](#).)
- Tikhonov, A. N. & Arsenin, V. Y., 1977. *Solutions of ill-posed problems*, V. H. Winston and Sons. (Cited on page [51](#).)

- Tilmann, F., Ni, J., & Team, I., 2003. Seismic imaging of the downwelling Indian lithosphere beneath central Tibet, *Science*, **300**, 1424–1427. (Cited on page [81](#).)
- Tuncer, V., Unsworth, M. J., Siripunvaraporn, W., & Craven, J. A., 2006. Exploration for unconformity-type uranium deposits with audiomagnetotelluric data: a case study from the McArthur River mine, Saskatchewan, Canada, *Geophysics*, **71**(6), B201–B209. (Cited on pages [125](#) and [134](#).)
- Türkoğlu, E., Unsworth, M., Çağlar, I., & Avşar, U., 2008. Lithospheric structure of the Arabia-Eurasia collision zone in eastern Anatolia: magnetotelluric evidence for widespread weakening by fluids?, *Geology*, **36**(8), 619–622. (Cited on pages [5](#) and [28](#).)
- Tyburczy, J. A. & Waff, H. S., 1983. Electrical conductivity of molten basalt and andesite to 25 kbar pressure: geophysical significance and implications for charge transport and melt structure, *Journal of Geophysical Research*, **88**, 2413–2430. (Cited on pages [160](#) and [163](#).)
- Uchida, T., 1993. Smooth 2-D inversion for magnetotelluric data based on statistical criterion, ABIC, *Journal of Geomagnetism and Geoelectricity*, **45**, 841–858. (Cited on page [50](#).)
- Unsworth, M., 2010. Magnetotelluric studies of active continent-continent collisions, *Surveys in Geophysics*, **31**, 137–161. (Cited on page [5](#).)
- Unsworth, M., Wei, W., Jones, A. G., Li, S., Bedrosian, P., Booker, J., Jin, S., Deng, M., & Tan, H., 2004. Crustal and upper mantle structure of northern Tibet imaged with magnetotelluric exploration, *Journal of Geophysical Research*, **109**, B02403–1–B02403–18. (Cited on page [81](#).)
- Unsworth, M. J., 2005b. Developments in conventional hydrocarbon exploration with EM methods, *CSEG Recorder*. (Cited on page [8](#).)
- Unsworth, M. J. & Rondenay, S., 2012. Mapping the distribution of fluids in the crust and lithospheric mantle utilizing geophysical methods, in *Metasomatism and metamorphism: the role of fluids in crustal and upper mantle processes*, pp. 535–598, Springer-Verlag, Berlin, Heidelberg. (Cited on page [26](#).)
- Unsworth, M. J., Egbert, G., & Booker, J., 1999. High-resolution electromagnetic imaging of the San Andreas fault in Central California, *Journal of Geophysical Research*, **104**(B1), 1131–1150. (Cited on page [104](#).)
- Unsworth, M. J., Jones, A. G., Wei, W., Marquis, G., Gokarn S, G., Spratt, J. E., & the INDEPTH-MT Team, 2005a. Crustal rheology of the Himalaya and Southern Tibet inferred from magnetotelluric data, *Nature*, **438**, 78–81. (Cited on pages [5](#), [6](#), and [157](#).)
- Utada, H. & Munekane, H., 2000. On galvanic distortion of regional three-dimensional magnetotelluric impedances, *Geophysical Journal International*, **142**, 385–398. (Cited on page [43](#).)

- van der Meijde, M., Lee, S. V. D., & Giardini, D., 2003. Crustal structure beneath broad-band seismic stations in the Mediterranean region, *Geophysical Journal International*, **739**, 729–739. (Cited on page [70](#).)
- Viljanen, A., 2012. Description of the magnetospheric/ionospheric sources, in *The magnetotelluric method*, chap. 3B, pp. 96–111, Cambridge University Press, Cambridge, UK. (Cited on pages [17](#) and [22](#).)
- Villeneuve, M. & Cornee, J. J., 1994. Structure, evolution and paleogeography of the west African craton and bordering belts during the Neoproterozoic, *Precambrian Research*, **69**, 307–326. (Cited on page [59](#).)
- Vozoff, K., 1991. The magnetotelluric method, in *Electromagnetic methods in applied geophysics*, chap. 8, pp. 641–752, Society of Exploration Geophysicists, Tulsa, OK. (Cited on pages [8](#), [10](#), [16](#), and [24](#).)
- Waff, H. S., 1974. Theoretical considerations of electrical conductivity in a partially molten mantle and implications for geothermometry, *Journal of Geophysical Research*, **79**(26), 4003–4010. (Cited on page [30](#).)
- Wait, J. R., 1954. On the relation between telluric currents and the earth's magnetic field, *Geophysics*, **19**, 281–289. (Cited on page [8](#).)
- Wannamaker, P. E., 2005. Anisotropy versus heterogeneity in continental solid earth electromagnetic studies: fundamental response characteristics and implications for physicochemical state, *Surveys in Geophysics*, **26**, 733–765. (Cited on pages [35](#), [36](#), and [37](#).)
- Wannamaker, P. E., Hohmann, G. W., & Ward, S. H., 1984. Magnetotelluric responses of three-dimensional bodies in layered earth, *Geophysics*, **37**, 1517–1553. (Cited on page [104](#).)
- Wannamaker, P. E., Jiracek, G. R., Stodt, J. A., Caldwell, T. G., Porter, A. D., Gonzalez, V. M., & McKnight, J. D., 2002. Fluid generation and movement beneath an active compressional orogen, the New Zealand Southern Alps, inferred from magnetotelluric (MT) data, *Journal of Geophysical Research*, **107**(B6), ETG6 1–22. (Cited on page [37](#).)
- Wannamaker, P. E., Hasterok, D. P., Johnston, J. M., Stodt, J. A., Hall, D. B., Soderdgen, T. L., Pellerin, L., Maris, V., Doerner, W. M., Groenewold, K. A., & Unsworth, M. J., 2008. Fluid generation and movement beneath an active compressional orogen, the New Zealand Southern Alps, inferred from magnetotelluric (MT) data, *Geochemistry, Geophysics, Geosystems*, **9**(5), Q05019. (Cited on pages [27](#) and [37](#).)
- Ward, S. H. & Hohmann, G. W., 1987. Electromagnetic theory for geophysical applications, in *Electromagnetic methods in applied geophysics*, chap. 4, pp. 131–311, Society of Exploration Geophysicists, Tulsa, OK. (Cited on page [11](#).)

- Watanabe, T. & Kurita, K., 1993. The relationship between electrical conductivity and melt fraction in a partially molten system: Archie's law behaviour, *Physics of the Earth and Planetary Sciences*, **78**, 9–17. (Cited on pages [31](#) and [167](#).)
- Weaver, J. T., Agarwal, A. K., & Lilley, F. E. M., 2000. Characterization of the magnetotelluric tensor in terms of its invariants, *Geophysical Journal International*, **141**(2), 321–336. (Cited on pages [15](#) and [43](#).)
- Weidelt, P., 1972. The inverse problem of geomagnetic induction, *Zeitschrift für Geophysik*, **38**, 257–289. (Cited on pages [13](#) and [41](#).)
- Weidelt, P. & Kaikkonen, P., 1994. Local 1-D interpretation of magnetotelluric B-polarization impedances, *Geophysical Journal International*, **117**(3), 733–748. (Cited on page [116](#).)
- Wessel, P. & Smith, W. H. F., 2005. New version of the generic mapping tools released, *Eos, Transaction American Geophysical Union*, **76**(33), 329. (Cited on page [xxiii](#).)
- White, D. J., Jones, A. G., Hope, J., Nemeth, B., & Hajnal, Z., 2005. Geophysical transect across a Paleoproterozoic continent-continent collision zone: the Trans-Hudson Orogen, *Canadian Journal of Earth Sciences*, **42**, 385–402. (Cited on page [5](#).)
- Wiese, H., 1962. Geomagnetische Tiefentellurik. II. Die Streichrichtung der Untergrundstrukturen des elektrischen Widerstandes, erschlossen aus geomagnetischen Variationen, *Geofis. Pura Appl.*, **52**, 83–103. (Cited on page [15](#).)
- Wigger, P., Asch, G., Giese, P., Heinsohn, W. D., El Alami, S. O., & Ramdani, F., 1992. Crustal structure along a transverse across the Middle and High Atlas Mountains derived from seismic refraction studies, *Geologische Rundschau*, **81**, 237–248. (Cited on pages [vii](#), [66](#), [70](#), and [111](#).)
- Wilson, J. T., 1966. Did the Atlantic close and then re-open?, *Nature*, **211**, 676–681. (Cited on page [2](#).)
- Wittig, N., Pearson, D. G., Baker, J. A., Duggen, S., & Hoernle, K., 2010. A major element, PGE and Re-Os isotope study of Middle Atlas (Morocco) peridotite xenoliths: evidence for coupled introduction of metasomatic sulphides and clinopyroxene, *Lithos*, **115**(1-4), 15–26. (Cited on page [168](#).)
- Wustefeld, A., Bokelmann, G. H. R., Barruol, G., & Montagner, J. P., 2009. Identifying global seismic anisotropy patterns by correlating shear-wave splitting and surface-wave data, *Physics of the Earth and Planetary Interiors*, **176**, 198–212. (Cited on pages [vii](#) and [74](#).)
- Xiao, Q., Cai, X., Xu, X., Liang, G., & Zhang, B., 2010. Application of the 3D magnetotelluric inversion code in a geologically complex area, *Geophysical Prospecting*, **58**, 1177–1192. (Cited on pages [119](#) and [134](#).)

- Yee, E. & Paulson, K. V., 1988. Concerning dispersion-relations for the magnetotelluric impedance tensor, *Geophysical Journal International*, **95**(3), 549–559. (Cited on page [116](#).)
- Yee, E. & Paulson, K. V., 1990. Concerning dispersion-relations for the magnetotelluric impedance tensor—Reply, *Geophysical Journal International*, **102**(1), 549–559. (Cited on page [116](#).)
- Yoshino, T., 2010. Laboratory electrical conductivity measurement of mantle materials, *Surveys in Geophysics*, **31**, 163–206. (Cited on page [28](#).)
- Yoshino, T., Matsuzaki, T., Yamashita, S., & Katsura, T., 2006. Hydrous olivine unable to account for conductivity anomaly at the top of the asthenosphere, *Nature*, **443**, 973–976. (Cited on page [37](#).)
- Zeyen, H., Ayarza, P., Fernandez, M., & Rimi, A., 2005. Lithospheric structure under the western African-European plate boundary: a transect across the Atlas Mountains and the Gulf of Cadiz, *Tectonics*, **24**. (Cited on pages [viii](#), [4](#), [5](#), [6](#), [60](#), [73](#), [75](#), [76](#), [78](#), [142](#), [147](#), [160](#), and [168](#).)
- Zhanxiang, H., Hu, Z., & Luo, W., 2010. Mapping reservoirs based on resistivity and induced polarization derived from continuous 3D magnetotelluric profiling: case study from Qaidam basin, China, *Geophysics*, **75**, B25–B33. (Cited on page [134](#).)
- Zhao, W., Nelson, K. D., & INDEPTH, P., 1993. Deep seismic reflection evidence for continental underthrusting beneath southern Tibet, *Nature*, **366**(5), 557–559. (Cited on page [81](#).)
- Zhdanov, M. S. & Keller, G. V., 1994. *The geoelectrical methods in geophysical exploration*, Elsevier, Amsterdam. (Cited on page [8](#).)
- Zhdanov, M. S., Green, A., Gribenko, A., & Cuma, M., 2010. Large-scale three-dimensional inversion of EarthScope MT data using the integral equation method, *Physics of the Solid Earth*, **46**, 670–678. (Cited on pages [125](#) and [134](#).)
- Zhdanov, S. M., Sheng, F., & Hursan, G., 2000. Electromagnetic inversion using quasi-linear approximation, *Geophysics*, **65**(5), 1501–1513. (Cited on page [134](#).)

Part IV

APPENDICES

A

FORWARD MODELLING RESULTS OF OBLIQUE CONDUCTOR

A.1 COMPARISON OF 2-D AND 3-D FORWARD RESPONSES

To compare the responses of 3-D forward modelling with 2-D solutions, the same structure was simulated using a 2-D forward algorithm, the code of [Rodi & Mackie \(2001\)](#) (implemented in Geosystem's WinGLink® package). Calculated 2-D responses were rotated by 45° to gain the diagonal components ($|\mathbf{Z}_{xx}|$, $|\mathbf{Z}_{yy}|$) of the impedance tensor. All four components of the rotated 2-D (blue circle) and 3-D (red star) are shown in [Figure A.1](#).

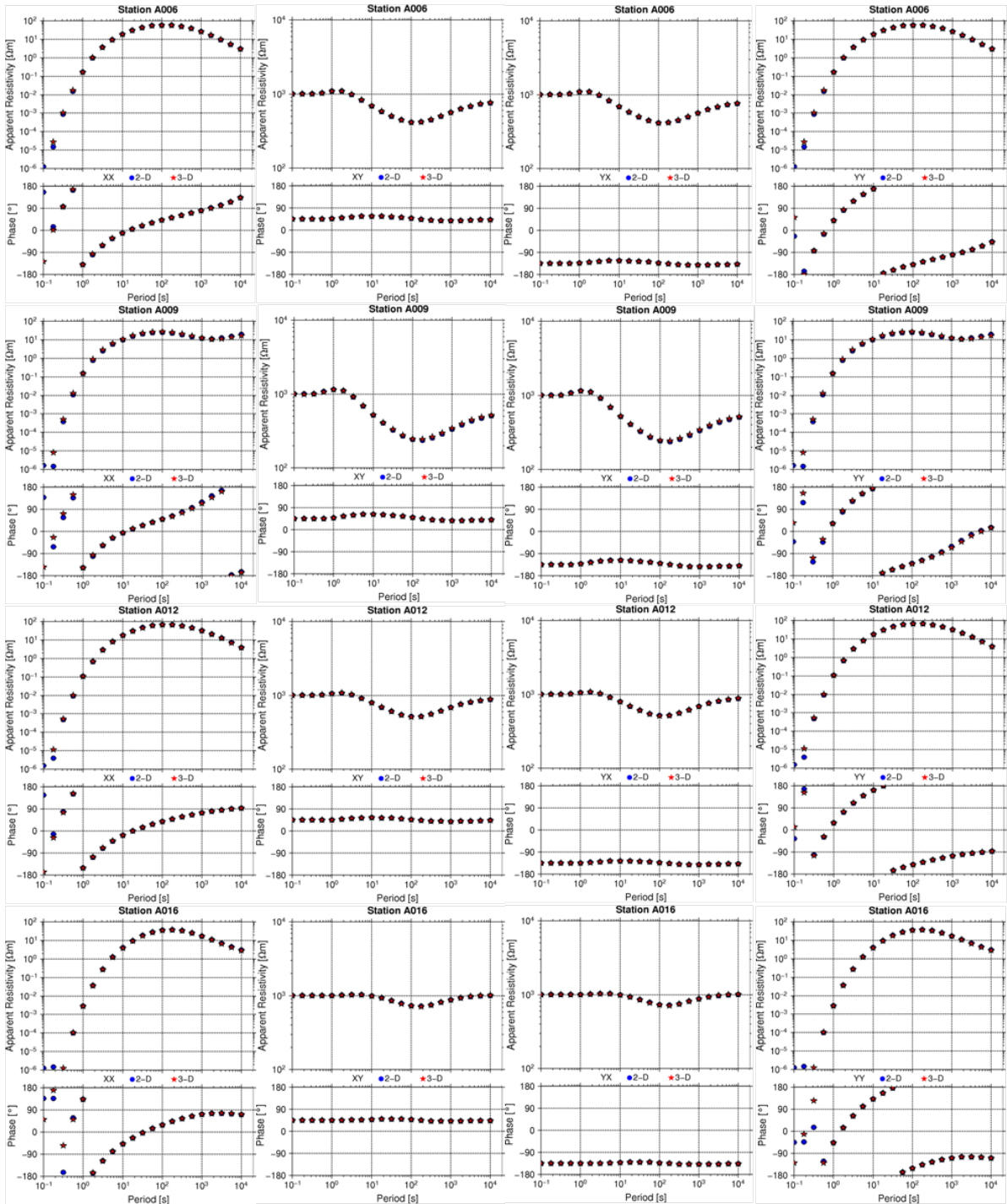


Figure A.1.: Comparison of the rotated 2-D and 3-D responses. Resistivity and phase curves for all four components calculated at stations A006, A009, A012, and A016 (for station locations see Figure 6.1a in Section 6.3) The blue circles represent the rotated 2-D responses into strike angle of 45° and the red stars are the 3-D responses.

B

PICASSO/TOPOMED - SUPPLEMENTARY FIGURES

B.1 TOPOMED MAGNETOTELLURIC DATA

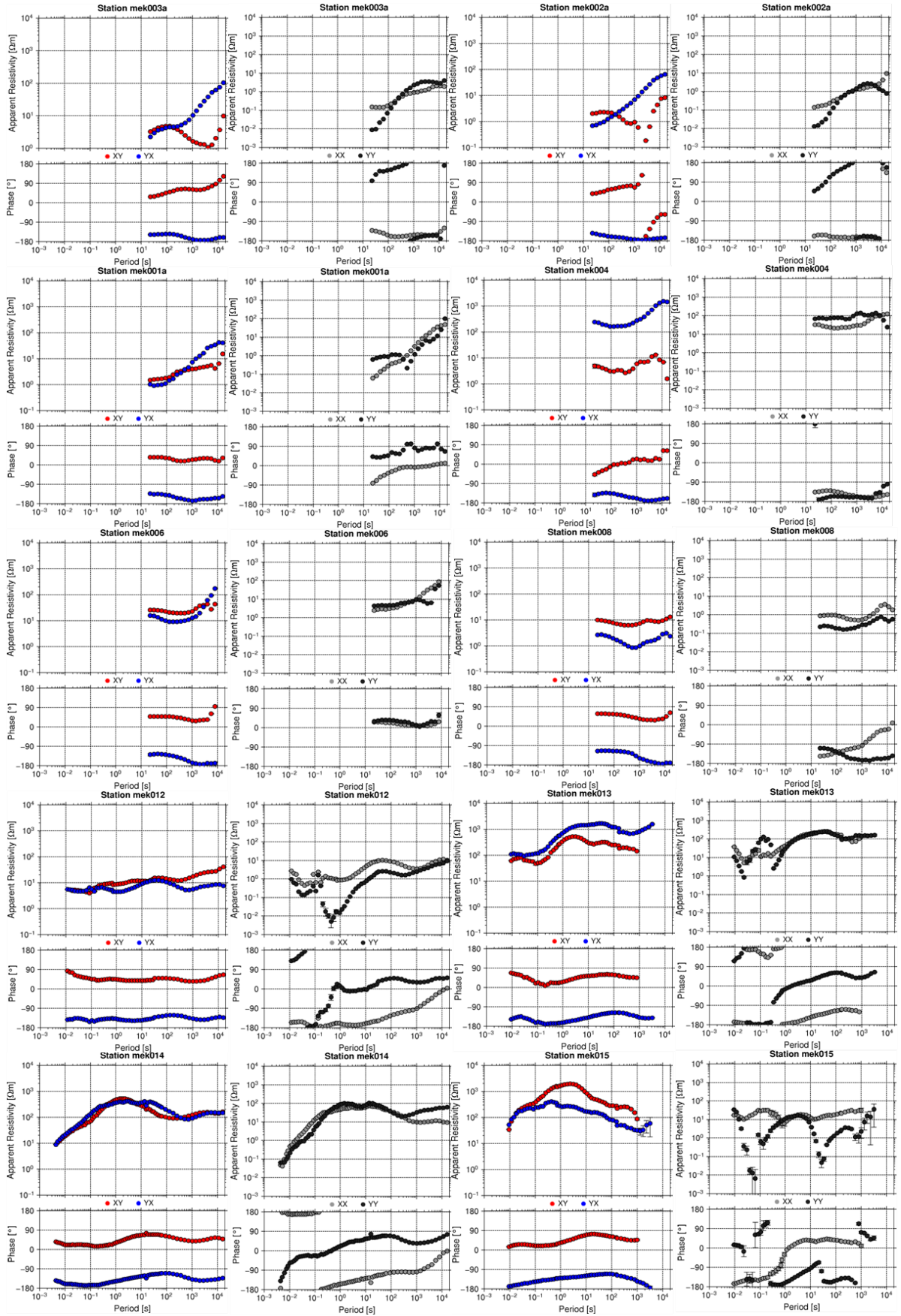


Figure B.1.: PICASSO/TopoMed MEK profile original data for plotted for all four components (XX, XY, YX and YY) of the impedance tensor.

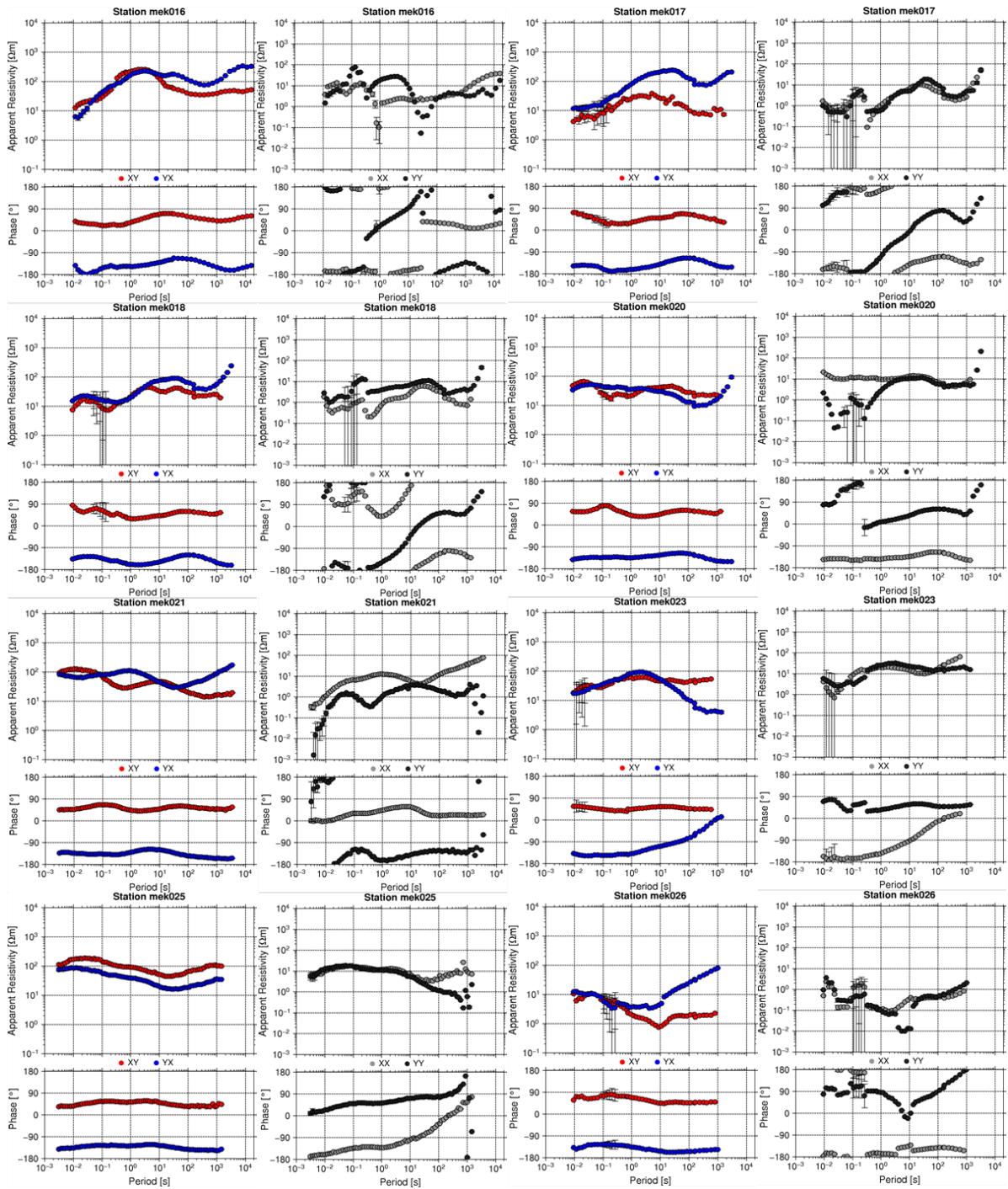


Figure B.2.: PICASSO/TopoMed MEK profile original data for plotted for all four components (XX, XY, YX and YY) of the impedance tensor.

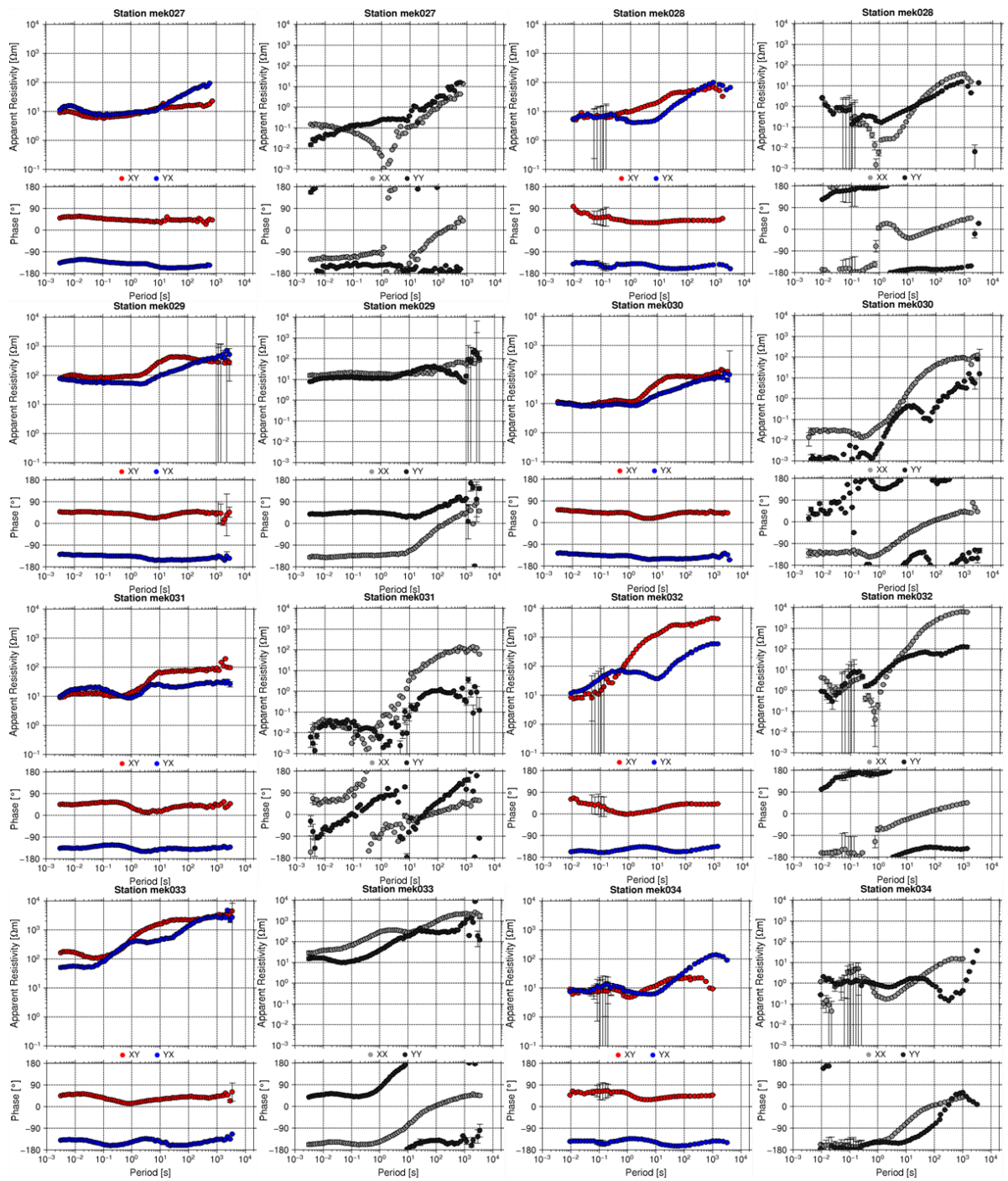


Figure B.3.: PICASSO/TopoMed MEK profile original data for plotted for all four components (XX, XY, YX and YY) of the impedance tensor.

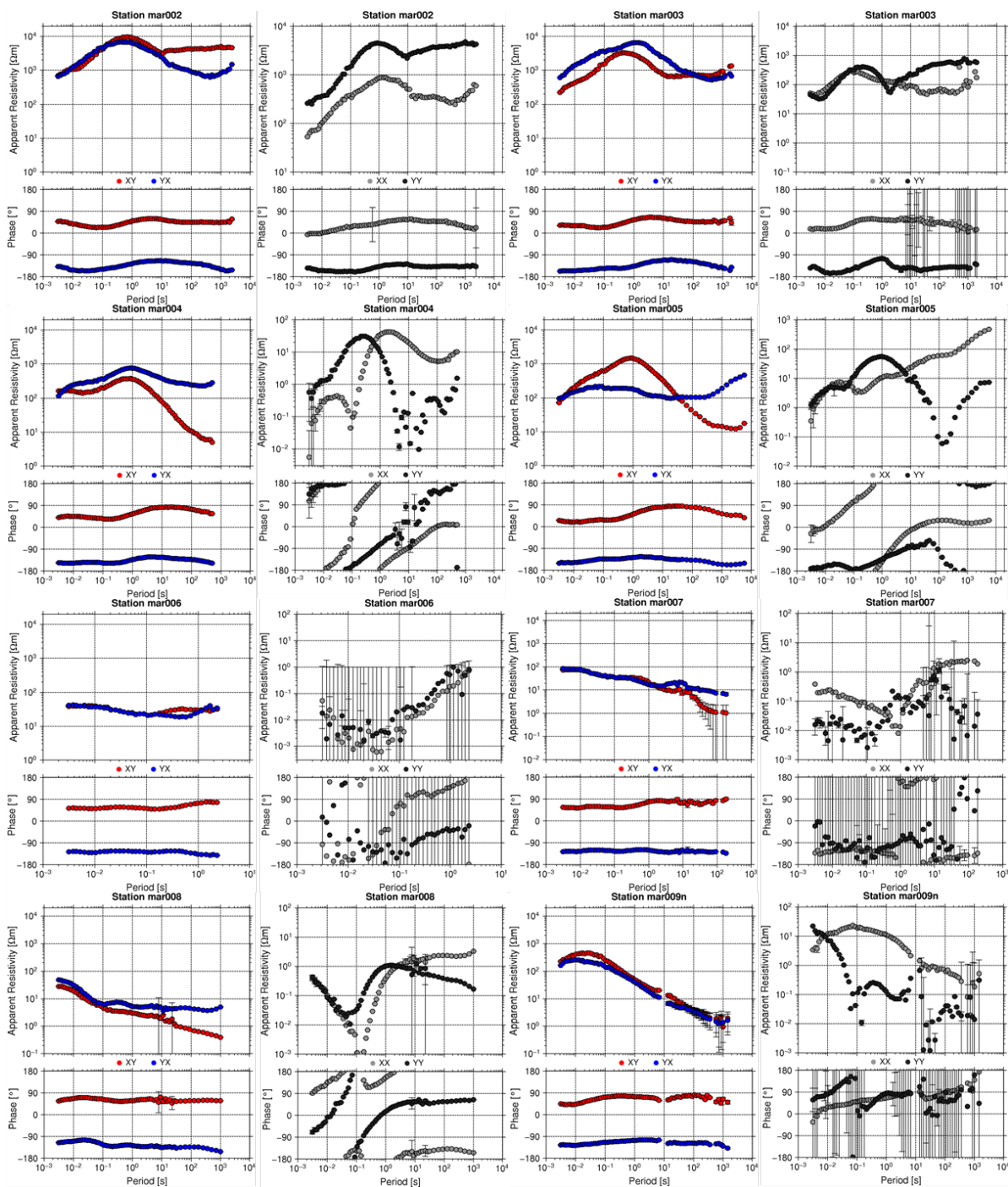


Figure B.4.: PICASSO/TopoMed MAR profile original data for plotted for all four components (XX, XY, YX and YY) of the impedance tensor.

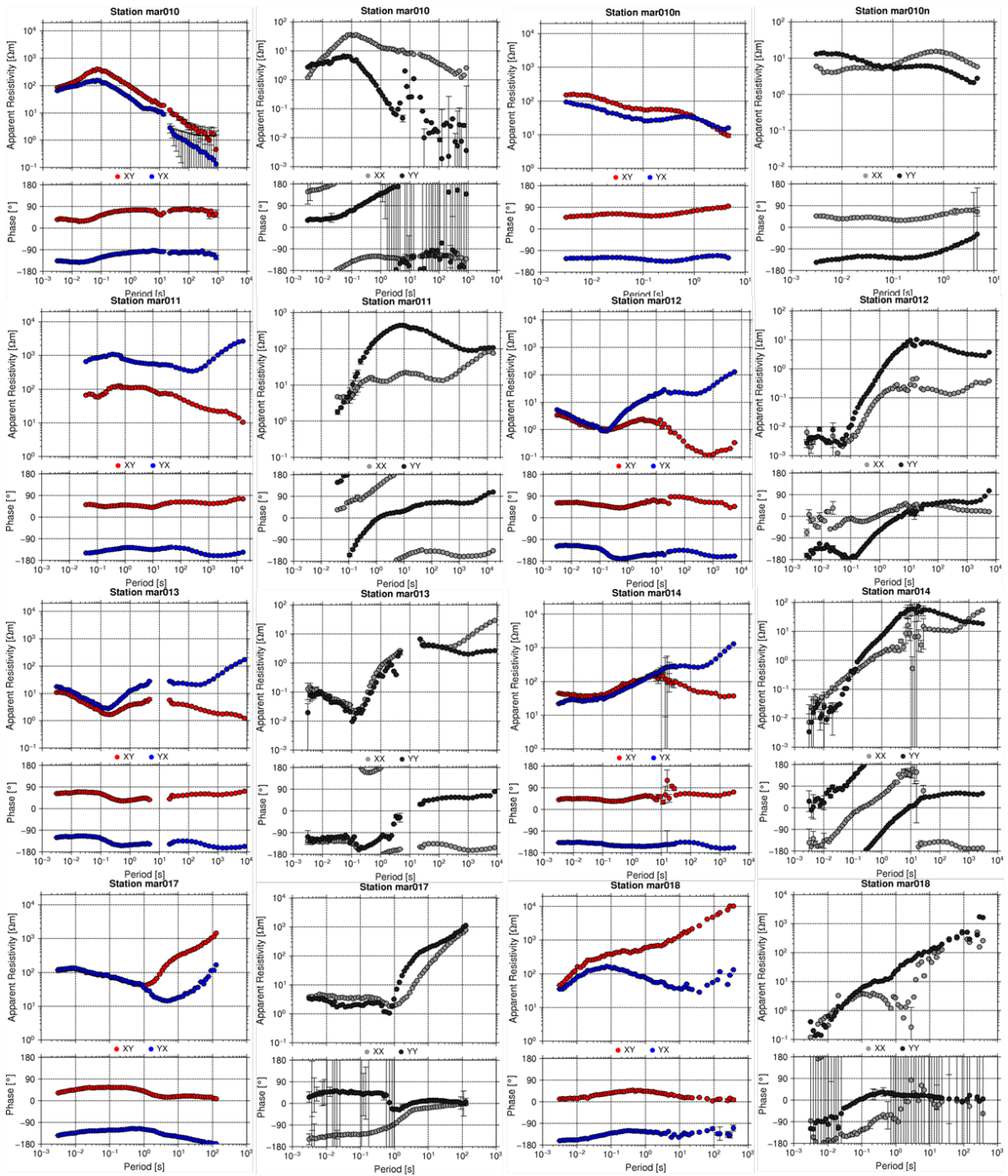


Figure B.5.: PICASSO/TopoMed MAR profile original data plotted for all four components (XX, XY, YX and YY) of the impedance tensor.